Important Notice

THE UNIVERSITY OF CALGARY

Analyzing Converted-Wave Seismic Data:

Statics, Interpolation, Imaging, and P-P Correlation

by

Wai-kin Chan

A DISSERTATION

SUBMITTED TO THE FACULTY OF GRADUATE STUDIES

IN PARTIAL FULFILLMENT OF THE REQUIREMENTS FOR THE

DEGREE OF DOCTOR OF PHILOSOPHY

DEPARTMENT OF GEOLOGY AND GEOPHYSICS

CALGARY, ALBERTA

OCTOBER, 1998

THE UNIVERSITY OF CALGARY

FACULTY OF GRADUATE STUDIES

The undersigned certify that they have read, and recommend to the Faculty of Graduate Studies for acceptance, a dissertation entitled "Analyzing Converted-Wave Seismic Data: Statics, Interpolation, Imaging, and P-P Correlation" submitted by Wai-kin Chan in partial fulfillment of the requirements for the degree of Doctor of Philosophy.

_____

Supervisor, Dr. R. R. Stewart, Department of Geology and Geophysics

_____

Dr. E. S. Krebes, Department of Geology and Geophysics

_____

Dr. J. C. Bancroft, Department of Geology and Geophysics

_____

Dr. M. A. Slawinski, Department of Mechanical Engineering

_____

External Examiner
Dr. P. W. Cary, Sensor Geophysical Ltd.

_____

Date

Abstract

Converted-wave (P-S) seismic processing requires a specialized approach due to its mixed wavetype. To facilitate this approach, a set of algorithms has been developed starting from data preparation and ending with the correlation techniques for P-P and P-S time sections.

A new statics estimation algorithm is developed to estimate S-wave receiver statics. This algorithm operates in the common-offset domain and relies on f-x prediction to generate pilot traces. Good results using the f-x statics estimation on the synthetic Marmousi example with random statics suggests that this technique is very useful especially in complex structural regimes. This is especially true where hyperbolic velocity assumption is violated or velocity estimation before statics is not possible. These features of the new technique are important for the converted-wave data and are demonstrated with Blackfoot data.

After statics corrections are applied, I use f-x prediction filters to interpolate missing traces. At this stage, the prestack data are assumed to be evenly sampled and are ready for further multi-channel processing.

Some fundamental equations for converted-wave traveltimes are derived and implemented in a velocity analysis method based on P-S prestack migration. This analysis uses the previously estimated P-wave background velocity to create the pseudo S-wave velocity

field.

Based on both velocity fields I use a new Asymmetric MoveOut Correction (AMOC) technique to transform the P-S data into pseudo P-P reflection data. With this approach, S-wave receiver statics can be estimated and a non-iterative velocity processing flow can be developed.

The processing is finalized with a rigorous analysis of the correlation between P-P and the corresponding P-S time sections. Two analysis techniques are developed for this purpose. The first technique is based on non-linear optimization of the correlation function, while the other is an approach to match data in the logarithmic time domain. Both correlation techniques produce a good visual match on both synthetic data and the Blackfoot data.

Acknowledgements

Dedication

This dissertation is dedicated to the memory of my beloved Mom.

Table of Contents

List of Tables

List of Figures

List of Symbols and Abbreviations

AMOC   Asymmetric MoveOut Correction

ACCP   Asymptotic Common Conversion Point

CCP   Common Conversion Point

CMP   Common Mid Point

DMO   Dip MoveOut correction

NMO   Normal MoveOut correction

RMS   Root Mean Square

P   Compressional wave

S   Shear wave

P-P   P-to-P seismic reflection

P-S   P-to-S conversion reflection

S-S   S-to-S seismic reflection

T_p P-wave 1-way traveltime

T_{PP} P-wave 2-way traveltime

T_s S-wave 1-way traveltime

T_{ss} S-wave 2-way traveltime

T_{ps} P-wave 1-way traveltime + S-wave 1-way traveltime

$\overline{V}_p$ P-wave average velocity in time

$\overline{V_s}$	S-wave average velocity in time
$V_{s,mig}$	effective S-wave migration velocity
V_p	P-wave RMS velocity
V_s	S-wave RMS velocity
X	source-receiver offset
X_s	horizontal distance between source and P-S conversion point
X_r	horizontal distance between receiver and P-S conversion point
Z_T	true depth
Z_p	pseudo-depth in terms of P-wave RMS velocity
Z_s	pseudo depth in terms of S-wave RMS velocity
Z_{ps}	pseudo-depth in terms of P-S time migration
α	P-wave interval velocity
β	S-wave interval velocity
γ	α/β ratio
γ_{rms}	V_p/V_s ratio
γ_{mig}	effective P-S migration V_p/V_s ratio
γ_{ps}	effective P-S mis-tie V_p/V_s ratio
g_p	P-wave velocity heterogeneity factor

g_s S-wave velocity heterogeneity factor

g_γ P-S velocity heterogeneity factor

Chapter 1   Introduction

1.1 Background

In recent years, there has been a growing interest in shear-wave exploration for hydro-carbons. Previous authors (e.g., Gregory, 1976; Tatham and Stoffa, 1976; Helbig and Mesdag, 1982; Tatham, 1982) have shown that the physical properties of rocks such as lithology, porosity, porefill, anisotropy, etc., could be inferred from combined P- and S-waves interpretation.

Although S-wave sections can be generated by S-wave sources, it has also been shown (Fertig, 1984; Tatham and Goolsbee, 1984) that in practice S-wave images generated from traditional P-wave sources often have resolution and signal-to-noise advantages over those generated by S-wave sources. In addition to difficulties with generating shear-waves directly, shear source operation is relatively inefficient, since recording of two perpendicularly polarized emissions are required for each source location (Garotta et al, 1990). Furthermore, S-S data have longer recording time than P-S data which can be an issue in some systems. In comparison, a P-wave source requires only 3-component geophones to record both P-P and P-S data, with perhaps some adjustment to recording time. In terms of processing, S-S reflection data need a solution for relatively large shot and receiver statics, while the P-S data benefit from previously determined P-wave source statics. Another problem with shear source data, as discussed by Garotta et al (1990) and Simin (1997), is that the frequen-

cy content of the S-S data is lower than that of P-S data, and hence S-S data are seriously contaminated by low-frequency, source-generated noise. Therefore, from an operational point of view (both acquisition and processing), P-S data are the preferred data set for S-wave reflection seismology studies.

To realize the potential advantages of P-S data, it is necessary to isolate P-S reflection arrivals and to account for the asymmetric travel path of these converted-waves. Although some success has been achieved in the separation of P- and S-wave events (Tatham and Goolsbee, 1984; Dankbaar, 1985), algorithms for handling the asymmetric ray path are generally limited to low relief data. For example, common conversion point (CCP) binning and P-S DMO are only partial solutions to the asymmetry problem and face some difficulty with structural data.

The traditional way of estimating static corrections is by correlating prestack traces with pilot traces created from CMP stacks. The absence of symmetric travel path in the CMP domain for P-S data, forces the pilot traces to be assembled from the asymptotic common conversion point (ACCP) curve. Unlike depth-variant binning, ACCP does not involve trace mixing and hence surface consistency is preserved (Cary, 1994). Unfortunately, ACCP is only valid for the deep part of data recorded over an horizontally layered earth with slowly varying Vp/Vs ratios.

Although P-S reflection data contain S-wave velocity information, traditional time processing does not yield direct estimation of the interval S-wave velocity. By correlating

events on both P-P and P-S sections, interval P-to-S velocity ratios (γ) can be derived. This information, together with interval P velocity, is then used for lithology detection (Garotta et al., 1985, Miller and Stewart,1990). One of the simplest ways of matching P-S to P-P sections is by visual inspection after the P-S section has been squeezed into P-P time using an estimate of Vp/Vs ratio. Using sonic logs, Lawton and Howell (1992) used a forward modeling technique to create P-P and P-S synthetic stacks to help understand the correlation between P-P and P-S data.

1.2 Dissertation objectives

The objective of this desertion is to develop a complete and consistent processing flow for converted-wave (P-S) reflection data. This new processing flow includes a solution for residual statics without NMO velocity information, missing traces interpolation, converted-wave time migration and migration velocity analysis, asymmetric P-S ray path correction, and matching of P-S to P-P sections. It is hoped that by avoiding the layered earth model assumption in the process, the flow proposed is general enough to apply to structural data sets.

1.3 Data sets used in this dissertation

Synthetic and real data sets that are used to evaluate the algorithms presented in this dissertation are described below.

1.3.1 Synthetic data sets

All the multi-component synthetic data used in this dissertation were generated by a fi-nite-difference elastic modeling program (Crase, pers. comm.) which simulates a 2-D earth 2-component (2-C) recording (vertical and radial) with a line source excitation. To avoid surface related multiples, data were generated with the absorbing surface condition option.

A 2-D P-P structural synthetic data set from Marmousi is used to evaluate the newly de-veloped statics routine discussed in Chapter 4. Surface-consistent random statics as large as 30 ms are introduced to the data.

1.3.2 Blackfoot, Alberta

A set of 2-D seismic lines was acquired by the CREWES Project over the Blackfoot field near Strathmore, Alberta. Acquisition parameters are summarized in Table 2.1. These lines included a variety of geophones (2-C 2Hz, 3-C 4.5 Hz, 3-C 10 Hz and vertical 10 Hz strings) and used a dynamite source. The processing of the vertical and the radial compo-nents of the 4.5 Hz geophone recordings is discussed in Chapter 2. This data set is also used to evaluate the new algorithms discussed in Chapters 4 to 7.

1.3.3 Pine Creek, Alberta

A 2-D 3-component (3-C) data set was acquired by Western Geophysical Company of Canada Ltd. in the spring of 1990. Acquisition parameters are summarized in Table 3.1. A vertical vibrator source was used. This data set was donated to the CREWES Project at the University of Calgary by Canadian Hunter Exploration Ltd. The processing of the vertical components of line 95-04 of the survey is discussed in Chapter 3.

Chapter 2   Conventional P-P and P-S processing

2.1 Introduction

The purpose of this chapter is to compare and contrast the state-of-the-art processing for P-P seismic data to that of P-S reflection data. The results of recent P-S processing are also used as comparison for the newly developed algorithms. Both the vertical and the radial components of 4.5 Hz Blackfoot broadband data are used to evaluate the processing flow. Although the P-S processing sequence is similar to that for P-P data, the actual algorithms for most processing steps are different and account for ray path differences. Note that P-S processing suffers from larger receiver statics due to lower shear-wave velocity near the surface, and the difficulty in determining the shear-wave replacement velocity for elevation and datum corrections. Finally, diminishing amplitude in the near-offset range for P-S data is also a problem in velocity analysis where it reduces the control on zero-offset time (T_0).

2.2 Data acquisition

A broadband 2-D 3-C survey was conducted over the Blackfoot Field in July, 1995. The field acquisition parameters are summarized in Table 2.1. The seismic line was 4 km long with receiver stations at every 20 m, and shots at every receiver station. The CMP stacking fold is as high as 200 at the middle of the survey and drops gradually to 1 at both ends of the line. To obtain more absolute energies in both the lower and the higher frequency rang-

es, 6 kg of explosive at a depth of 18 m was chosen as the source. A variety of geophones were used, but only the 4.5 Hz data are used for this dissertation. Figure 2.1 illustrates the first 4 seconds of 3-C 4.5 Hz shot record. Gain has been applied to amplify the later arrivals. Figure 2.2 is a filtered version (with band pass and gain) of Figure 2.1. Further processing has been applied to suppress the ground roll. Only a small amount of coherent signal is seen in the transverse component.

Acquisition Parameters, Blackfoot 1995

Instrument type	ARAM-24
Record length	6 seconds
Sample rate	1 ms
Pre-amp gain	18 dB
Notch filter	Out
Low cut filter	Out
Low cut slope	Out
High cut filter	240 Hz
High cut slope	70 dB / Octave
Energy source	Dynamite
Shot size	6 kg
Shot depth	18 m
Geophone array	Single 3-C and 6 phones 1-C over 20 m
Group interval	20 m
Type of geophones	OYO 30CT, 10Hz,
	Litton 1033, 3C, 10Hz,
	Mark L-28, 3C, 4.5 Hz,
	Mark L-4a, 2hz

Table 2.1. Field acquisition and recording parameters for the Blackfoot survey.
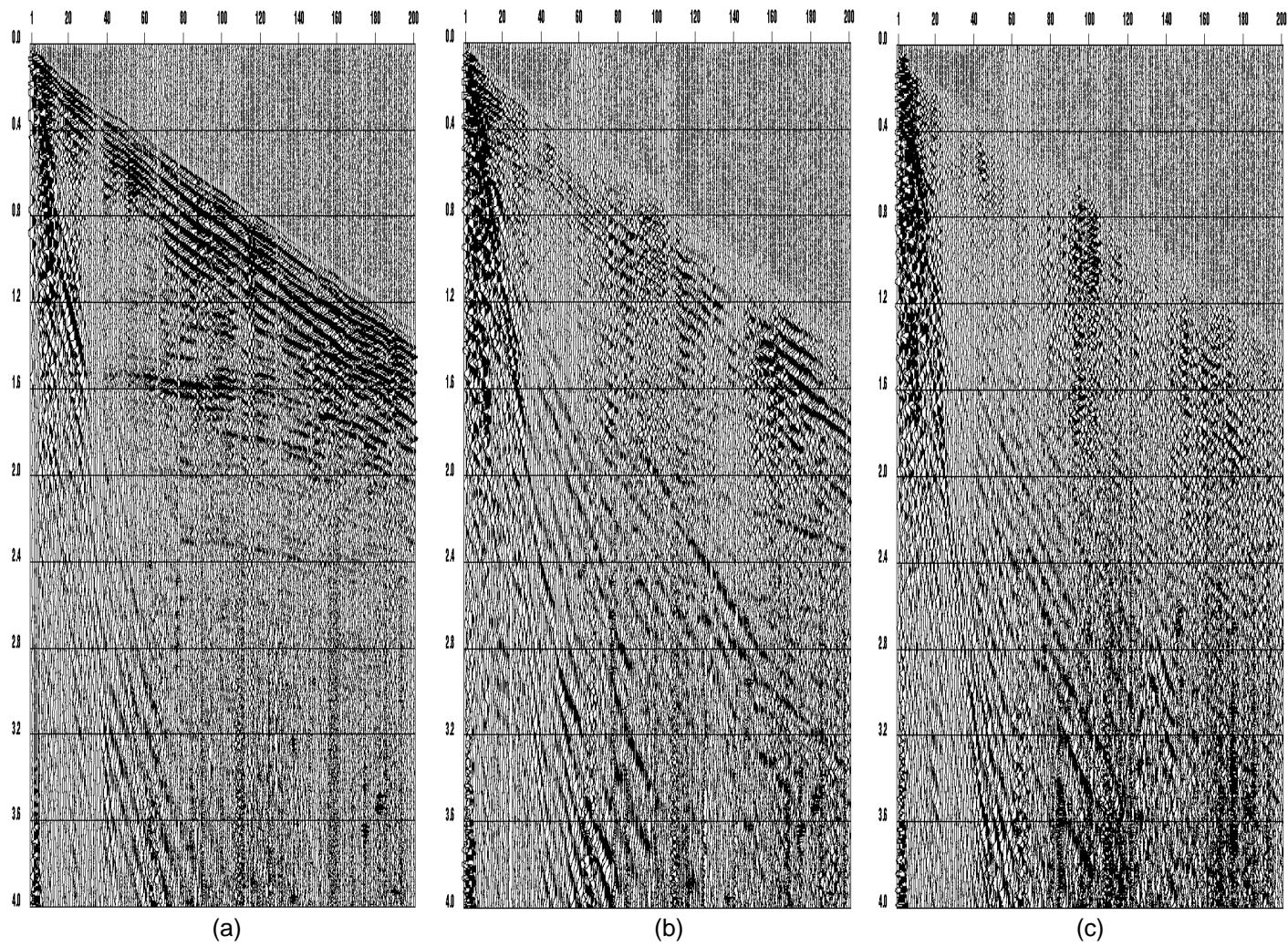
Fig. 2.1.Shot records from Blackfoot, Alberta (4.5 Hz geohones). (a) Vertical component. (b) Radial component. (c) Transverse component. Time scaling and trace balance are applied.
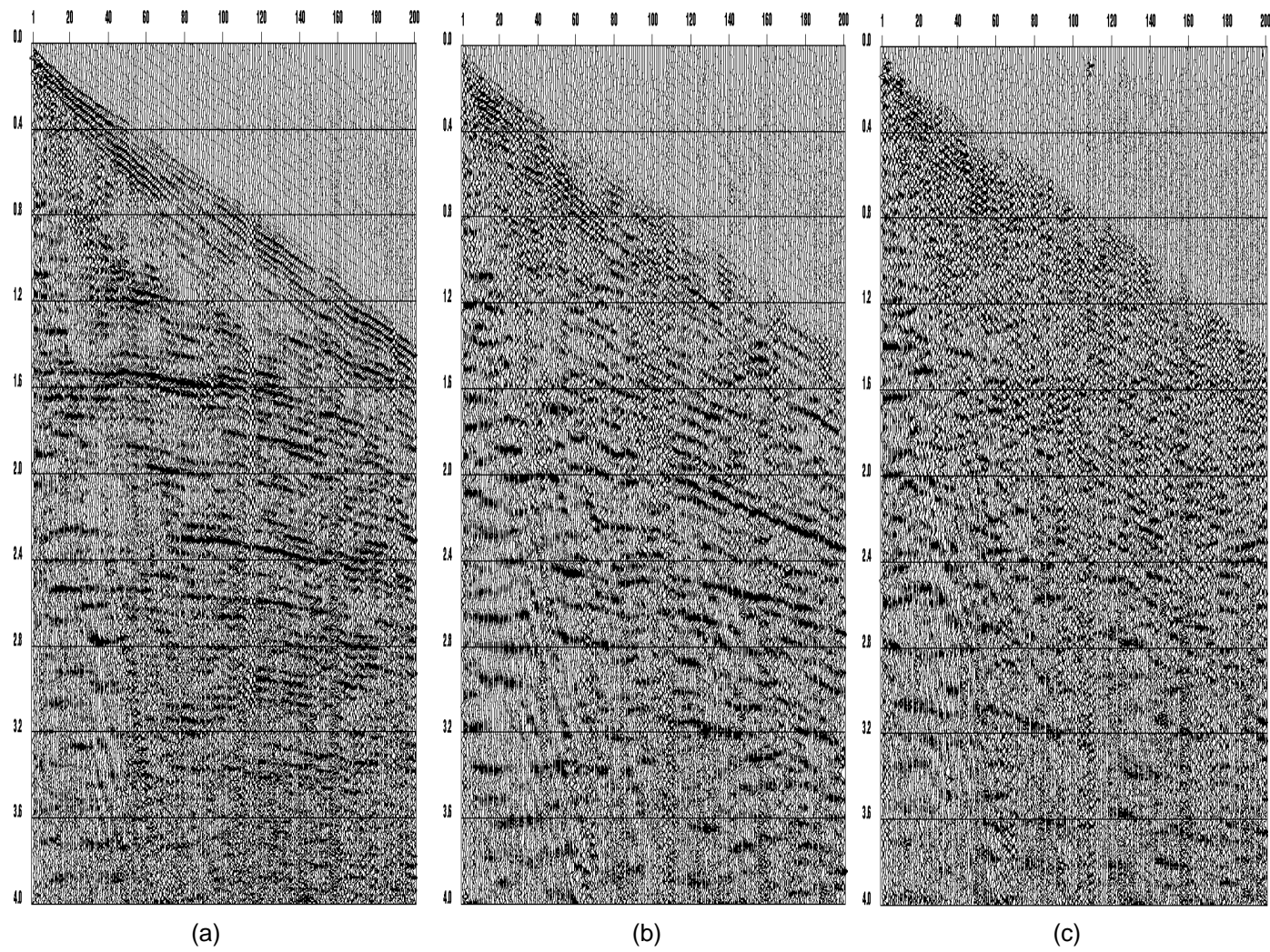
Fig. 2.2. 4.5 Hz filtered records (bandpass and gain). (a) Vertical component. (b) Radial component. (c) Transverse component.

2.3 Conventional P-P processing

Figure 2.3 presents a conventional processing flow creating a structural stack (Figure 2.4), DMO stack (Figure 2.5), and prestack time-migrated stack (Figure 2.6). The residual statics algorithm used is based on the stack power maximization approach of Ronen and Claerbout (1985). This approach requires iterations on both velocity and statics estimates. Unfortunately, as is shown in Chapter 4, when large statics are considered, cycle skipping is often introduced.

Note that the flow in Figure 2.3 requires early velocity information only for residual statics estimation. The DMO and the prestack time migration are velocity independent and are based on the algorithms from Forel and Gardner (1988), Gardner et al. (1986), Canning and Gardner (1993).

2.4 Conventional P-SV processing

Figure 2.7 presents a conventional processing flow to obtain a P-S structural stack (Figure 2.8). In general, birefringence analysis needs to be preformed to rotate the radial and the transverse components into the proper natural coordinate axes. Because of velocity anisotropy, shear-waves split into fast and slow components, and are recorded in the radial and the transverse channels potentially interfering with each other. By rotating the data into the proper axes, fast and slow components are separated. However in this data set, no no-

Demultiplex

↓

Geometry assignment

↓

Bad trace and polarity editing

↓

First break pick

↓

Refraction analysis and correction

↓

First break mute

↓

Amplitude scaling

↓

Ground roll suppression

↓

surface-consistent deconvolution

↓

Residual statics analysis and correction

Velocity analysis   DMO

NMO,mute,stack   velocity analysis   Prestack time imaging

Structural stack   NMO,mute,stack   velocity analysis

DMO stack   NMO,mute,stack

prestack time-migrated stack

Fig. 2.3. Processing flow for P-P seismic data.
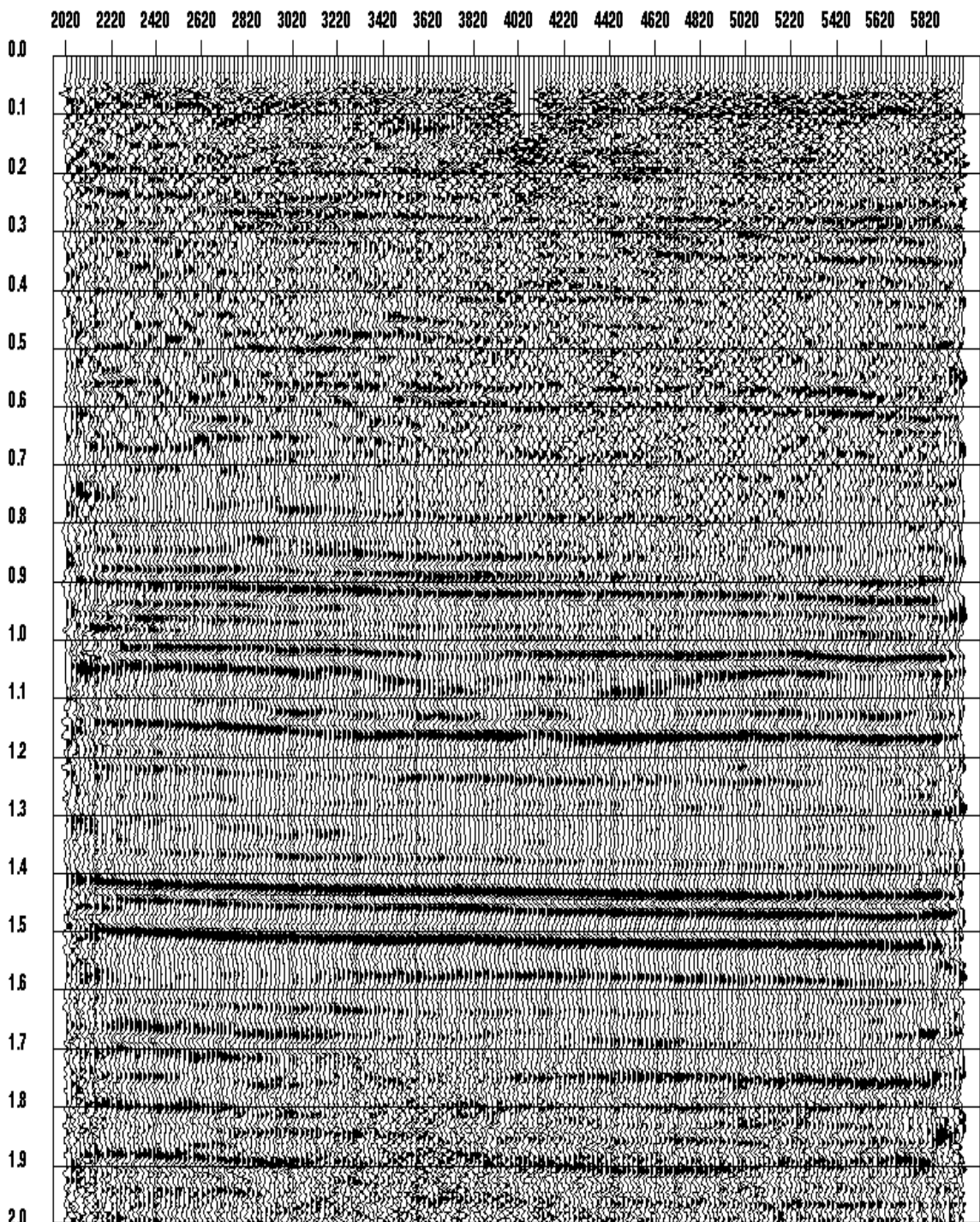
Fig. 2.4. P-P structural stack (4.5 Hz geohones) from Blackfoot, Alberta.
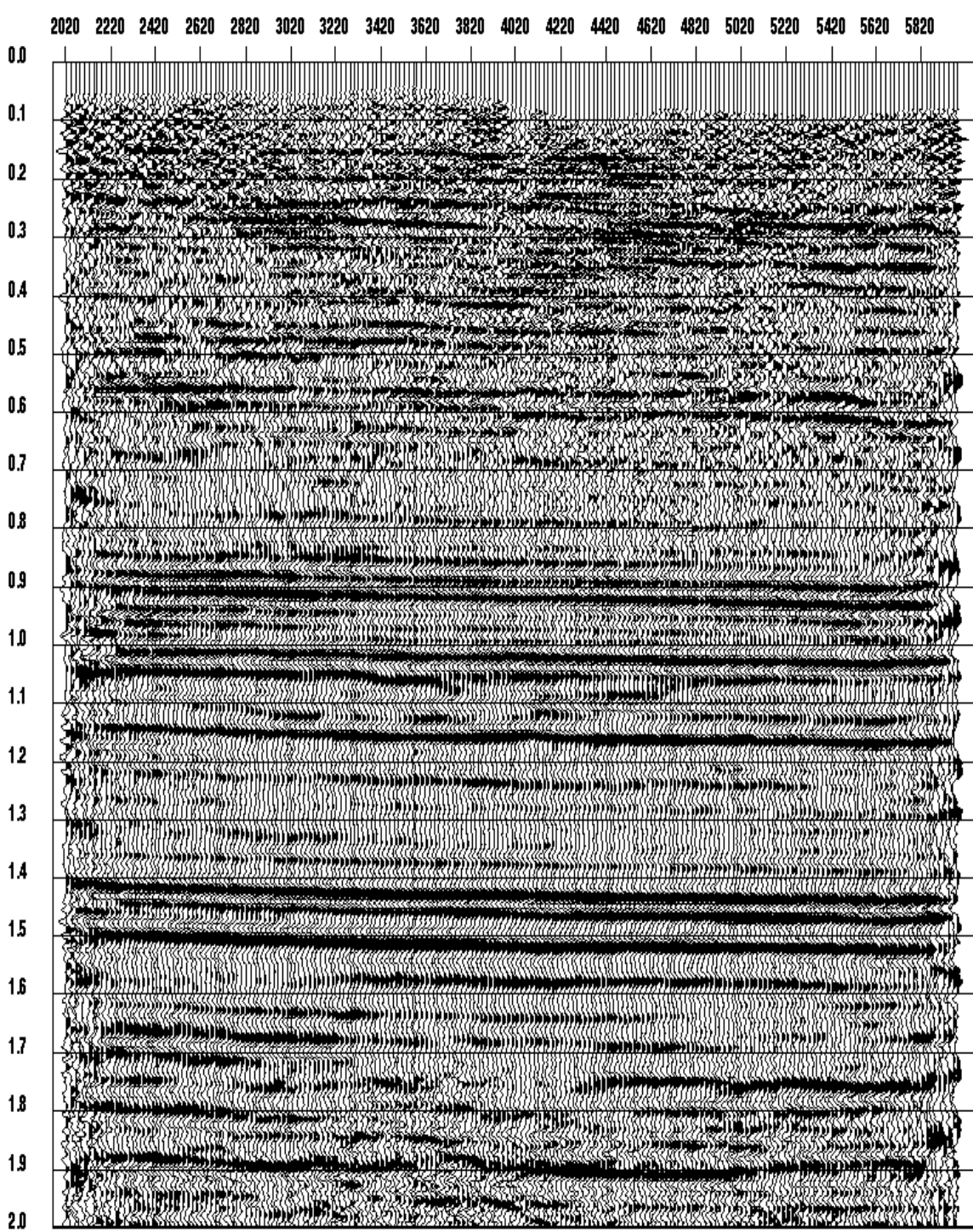
Fig. 2.5. P-P DMO stack (4.5 Hz geophones) form Blackfoot, Alberta.
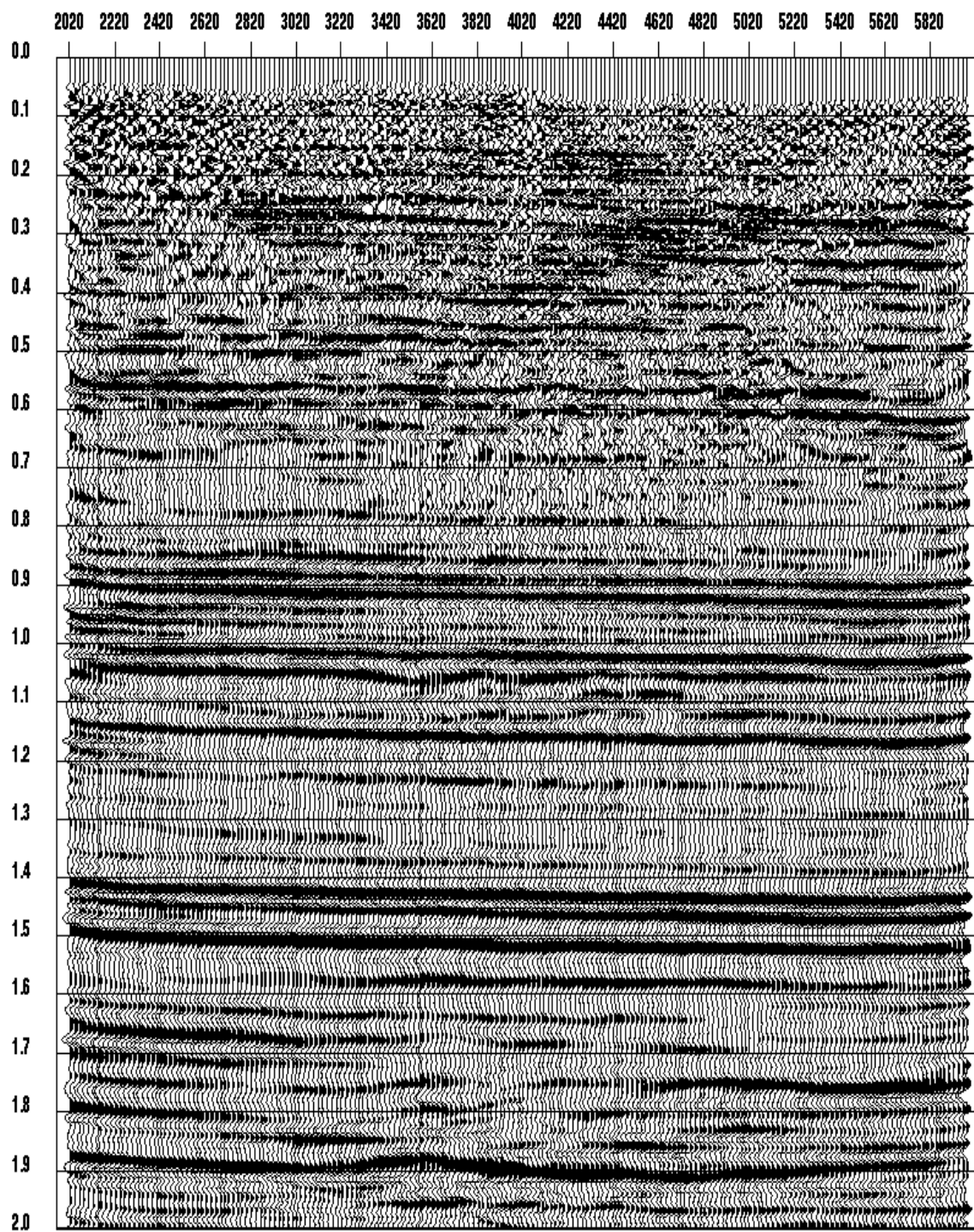
Fig. 2.6. P-P prestack time-migrated stack (4.5 Hz geohones) from Blackfoot, Alberta.

Demultiplex

Geometry assignment

Reverse polarity of trailing spread

Bad trace and polarity editing

Apply P shot statics

Apply datum corrections

First break mute

Amplitude scaling

Ground roll suppression

Surface-consistent deconvolution

Asymptotic common-conversion point (ACCP) binning (Vp/Vs=2.0)

residual receiver statics analysis and correction

Velocity analysis

NMO,mute,stack

structural stack

Fig. 2.7. Processing flow for P-S seismic data.
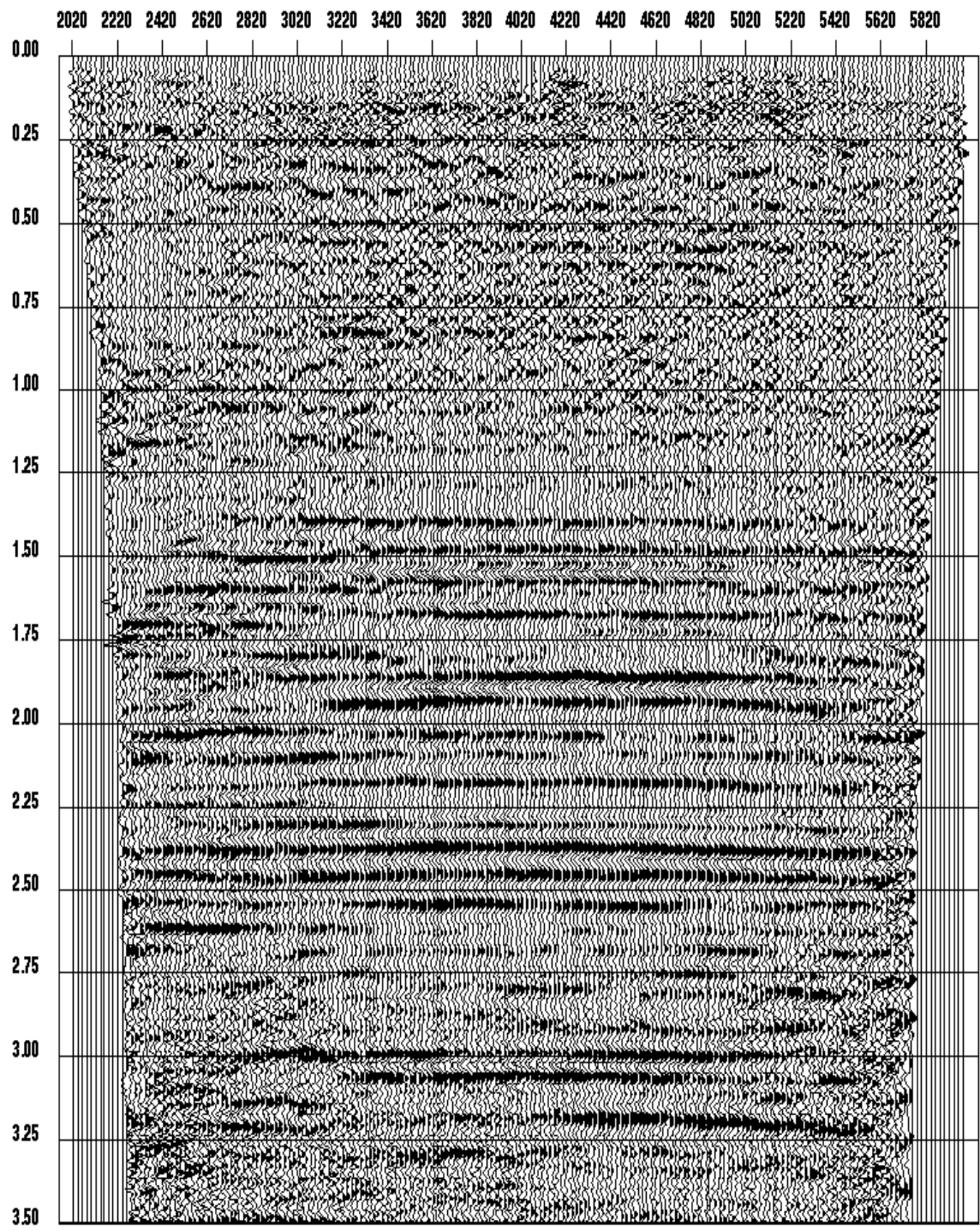
Fig. 2.8. ACCP stack (4.5 Hz geohones) from Blackfoot, Alberta.

ticeable coherent reflection energy is presented in the transverse component (Figure 2.2c). It is then believed that the velocity anisotropy is not important in this area or the recording line is coincided with one of the natural coordinate axes. Therefore, the birefringence analysis and the rotation are ignored in the flow.

2.4.1 Polarity reversal

As shown in Figure 2.9, P-wave data, recorded as vertical particle motion on the surface, have the same polarities for both positive and negative offsets. On the other hand, P-S data are largely recorded as radial particle motion. If the first motion arriving at the geophone at the positive offset is toward larger positive offsets, then, by symmetry, the first motion arriving at the geophone with negative offset will be toward larger negative offsets. The radial geophones are all planted in the same direction. As a result the radial component of geophones with opposite signed offsets, records data with reverse polarity. To stack the same event coherently across the offsets, the polarity of some of the data needs to be reversed. The choice of the offset side for the polarity reversal depends on the convention of P-P and P-S stacks, so that they both exhibit the same polarity, positive peak or negative trough, corresponding to the same reflection.
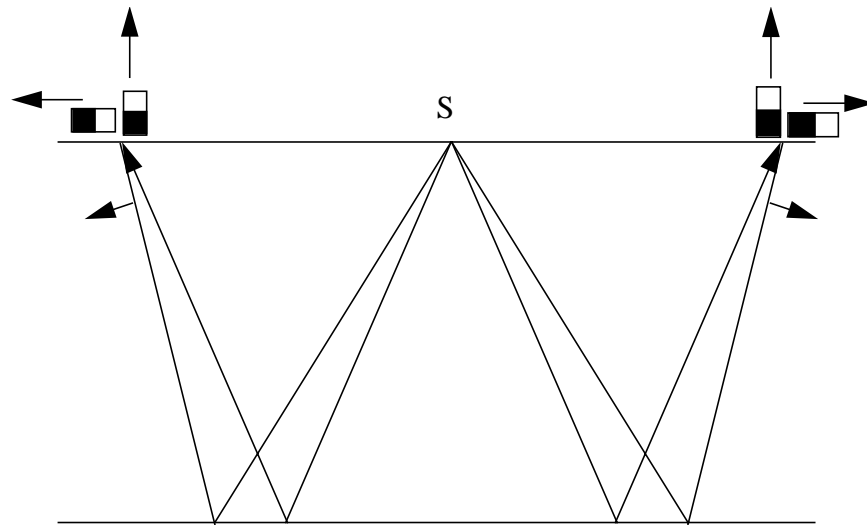
Fig. 2.9. Schematic diagram for the polarities of the particle motion recorded on the 2-C phones at different signed offsets. The vertical phones record the same polarity on both positive and negative offsets, while the radial phones, planted in the same direction, record different polarities on positive and negative offsets.

2.4.2 Refraction statics

As shown in Figure 2.10, it is believed that pure S-wave refraction arrivals found in P-S data are generated from the conversion of P-wave to S-wave soon after the source explosion (Dufour and Lawton, 1996). Unlike P-wave refraction, S-wave refraction is not a first break, and is not readily identifiable. This accentuates the problem of finding the near surface S-wave velocity model and apply proper datum corrections at the receivers.

Dufour and Lawton (1996) attempt to pick the later pure S-wave refraction arrivals to perform the shear refraction analysis. This approach heavily depends on the reliability and quality of the picks. Nevertheless, their results on the choice of S-wave replacement veloc-

ity (1200 m/s) is used to datum the receivers to 960 m, and Vp/Vs=1 is used for weathering

correction on the receiver sides in the processing of the Blackfoot data.

S   R

V_{1p}

θ_s V_{1s} θ_s

V_{2s}

$$\frac{V_{1s}}{V_{2s}} = \sin\theta_s$$
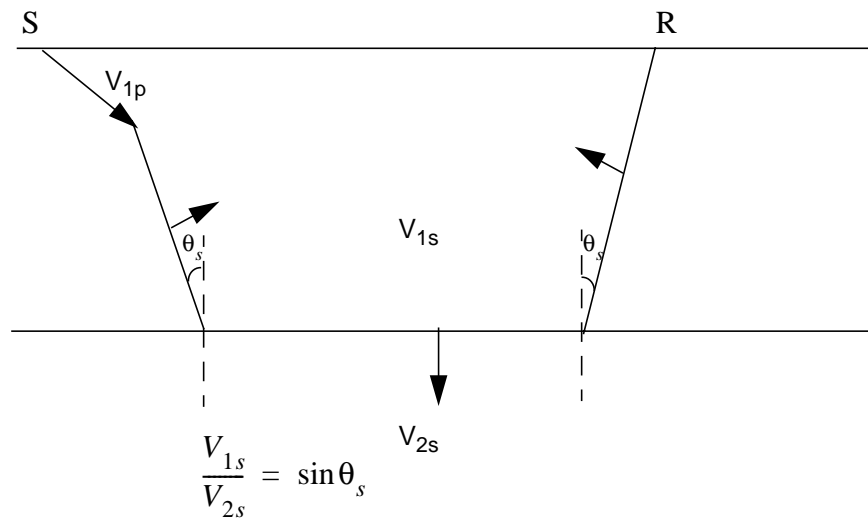
Fig. 2.10. Raypath geometry of the P-S refraction.

2.4.3 Common conversion point binning

The ray path for the converted-wave P-S mode is asymmetric, with the conversion point

situated closer to the receiver. Stacking the data with a conventional CMP bin causes large

conversion point smear even for horizontally layered earth models. To properly stack P-S

data, we need to gather the data based on a common conversion point (CCP). Unfortunate-

ly, unlike CMP binning, CCP binning is velocity dependent even for 1-D models. Several

layered earth based techniques have been developed to locate the conversion point as a function of depth or time. It is found that by sorting the P-S data into the CCP domain, the moveout curve is approximately hyperbolic. A reasonable CCP stack is obtained by normal moveout correction and stack, after traditional velocity analysis (Tessmer and Behle, 1988). For structural data sets, advanced CCP binning techniques are required. For example, conversion point binning can be done along the normal ray (P-S DMO), or along the image ray (P-S prestack time migration), or at the common depth point (P-S prestack depth migration).

However for flat data, asymptotic common conversion point (ACCP) binning, based on an average Vp/Vs for all times, is commonly used to create the structural stack. In addition to speed, ACCP also allocates complete traces to designated bins and does not destroy the surface consistency of the data (Cary, 1994), thereby simplifying the residual statics calculation. Figure 2.8 is an example of structural stack created from ACCP binning on the Blackfoot data set.

2.4.4 Residual statics

P-S residual statics requires previous P-wave static correction at the shots, and S-wave static correction at the receivers. Receiver stacks are a useful tool to examine the high frequency receiver statics, and can be used to estimate them (Cary and Eaton, 1992). Conventional P-P surface-consistent statics routines can also be applied to P-S data. In this case,

instead of analyzing data in the CMP domain, they are applied to data in the ACCP domain, and the design time window starts at deeper time (where the asymptotic common conversion point assumption is more valid).

2.4.5 Discussion

In general the quality of the near surface of the Blackfoot P-S stacked section is poor. Partly the reason is an erroneous ACCP binning of the shallow data, but also it is believed that lower velocity at the top creates severe NMO stretch so that only few near offset traces are available for stack. Furthermore, the quality problem is amplified because the near offset traces do not have strong and coherent converted-wave energy.

Chapter 3   F-x interpolation for missing traces

3.1 Introduction

In a 2-D seismic survey, it is usually desirable to sample the sub-surface uniformly by placing sources and receivers in a regular fashion. General acquisition problems disturb the sampling density and regularity to some degree. Proper binning regularizes the data to some extent and improves the quality of stack and poststack migration. However, some prestack algorithms, like DMO and migration, work directly from the acquisition geometry and require a different remedial approach.

A missing trace interpolation method based on least-squares f-x prediction filtering is proposed to improve data sampling (see Abma and Claerbout, 1995; Soubaras, 1995 for some background on the development of f-x filters). The f-x trace interpolation fills the location of the missing traces with traces predicted from neighboring information. Although the data set used in the following is a vertical component recording, it is expected that the algorithm also applies to the converted-wave data in the same manner, once the receiver statics problem is solved.

3.2 Data acquisition

The 2-D 3-C Pine Creek data set is recorded on a 240-channel instrument. It contains

411 shots with a 25 m group interval and shots at every station. The nominal fold of the

data is 40 with an end-on shooting configuration. The nearest and largest offsets on each

shot record are 150 m and 2125 m respectively (except shooting into and off the line). The

field acquisition parameters are shown in Table 3.1.

Acquisition Parameters, Pine Creek

Instrument type	Sercel SN369
Number of channels	240
Record length	5 s
Sample rate	2 ms
Pre-amp gain	42 dB
Low cut filter	Out
High cut filter	177.6 Hz
High cut slope	72 dB / Octave
Energy source	4 vibrators
Number of sweeps	8
Source pattern length	30 m
Sweep frequency	10-70 Hz
Sweep length and type	8 s (linear)
Geophone array	Single
Vibrator spacing	25 m
Group interval	25 m
CDP coverage	4000%
type of geophones	LRS L-1033, 14Hz

Table 3.1. Field acquisition and recording parameters for the Pine Creek survey.

3.3 The problem at Pine Creek

A P-P data set from Pine Creek, Alberta is used to demonstrated the effect of missing

traces on subsequent processing. Shown in Figures 3.1, 3.2, and 3.3 are NMO, DMO and
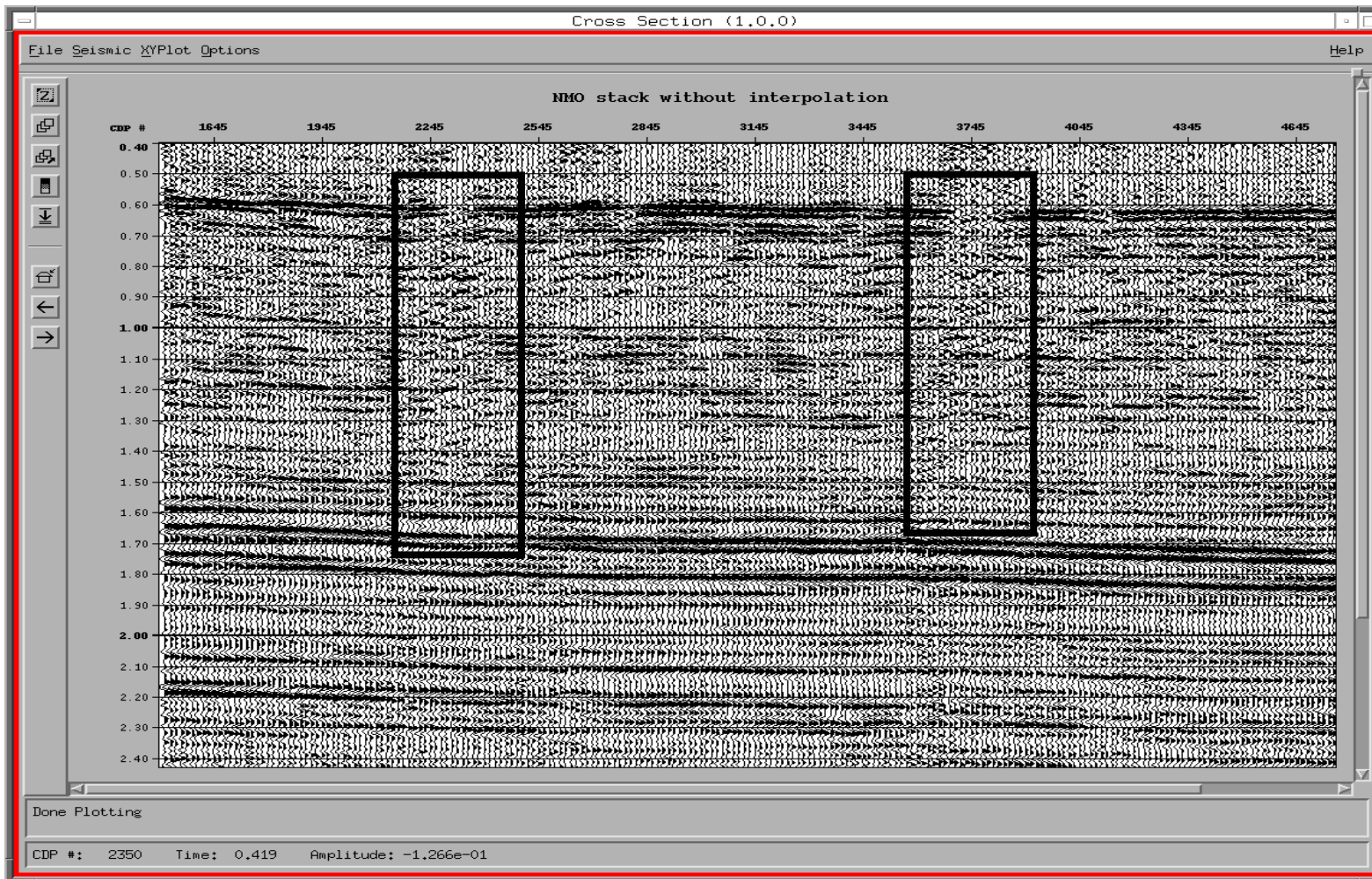
Fig. 3.1. Final structural stack without interpolation. Artifacts are observed in both boxes where there is low fold.
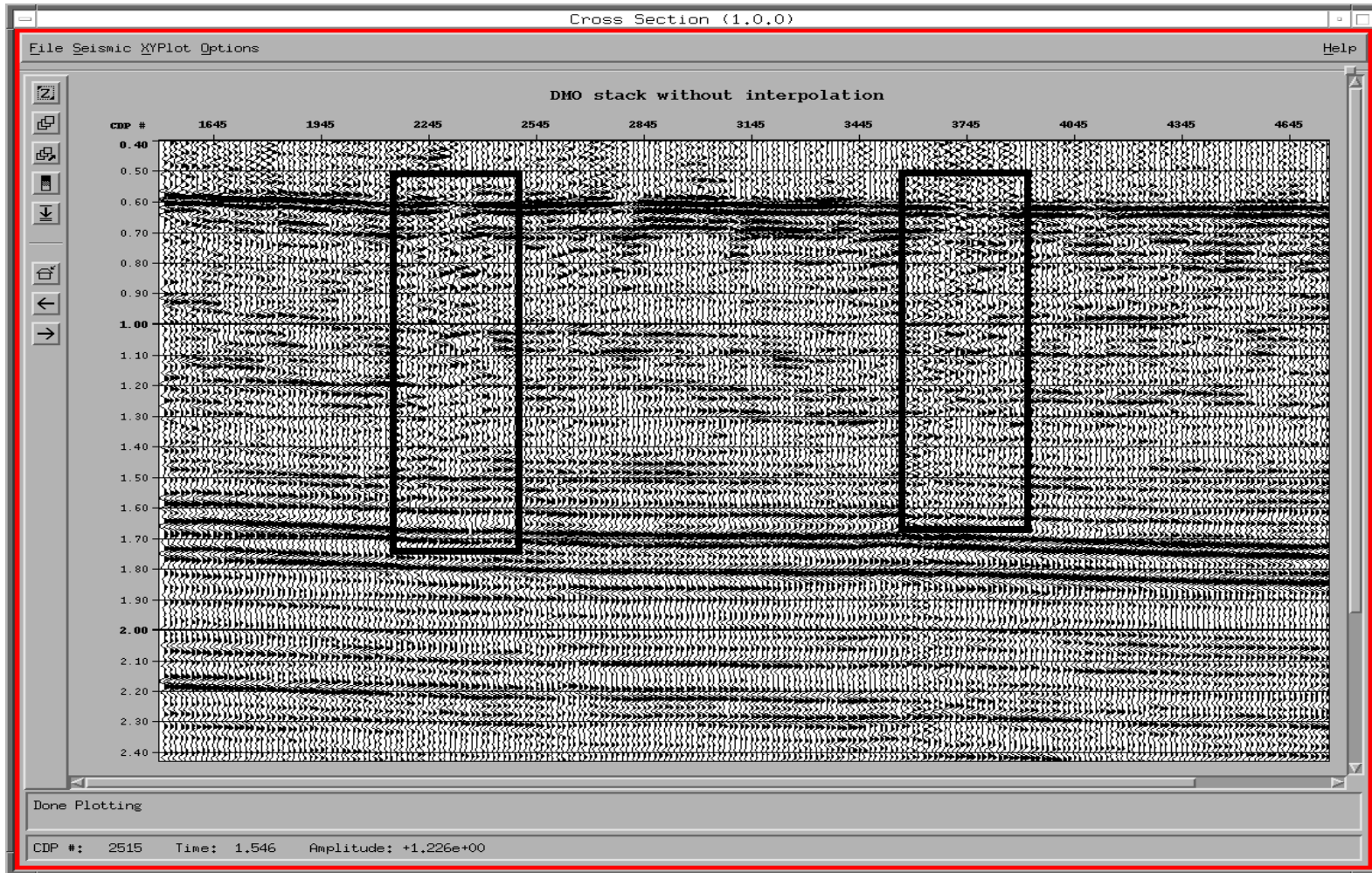
Fig. 3.2. DMO stack without interpolation. Artifacts are observed in both boxes where there is low fold.
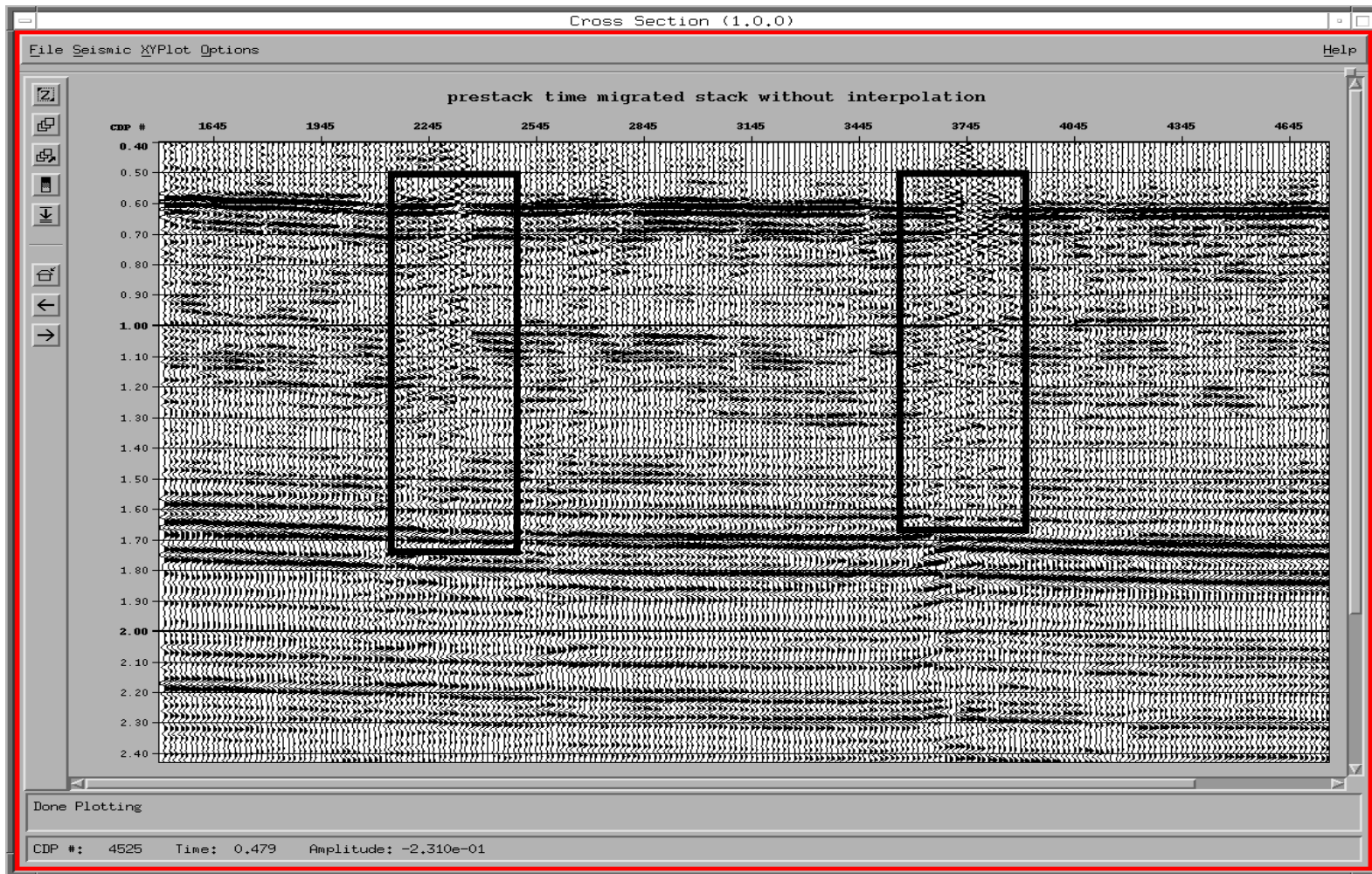
Fig. 3.3. Prestack time-migrated stack without interpolation. Artifacts are observed in both boxes where there is low fold.

prestack time-migrated stacks. Artifacts are observed at CMP locations around 2300 and 3750. By examining the prestack data in a common-offset plane (for example offset at 1165 m in Figure 3.4), it is concluded that this artifact noise is generated because of the missing traces. A CMP gather at location 3775 together with its velocity spectrum are shown in Figure 3.5 and supply a further evidence of this conclusion.

3.4 Theory

Canales (1984) has shown that linear events convolved with the same wavelet were perfectly predictable with a one-step ahead convolutional prediction filter in the f-x domain. In other words, the predicted data, at each frequency, are a linear combination of a set of complex sinusoids in the x-direction, with each sinusoid represents a single dipping event. When the linear events are corrupted by random noise, we can use the complex prediction Wiener filter theory to find a set of coefficients to estimate a least-squares approximation of the predictable part of signal (sinusoids) at each frequency. This procedure is now called f-x deconvolution and is routinely used in seismic data processing to suppress random noise. Spitz (1991) extended the idea of predictability of linear events for trace interpolation in the f-x domain. In Spitz's approach, the objective is to over-sample the input data at half of the original regular trace spacing, so that data aliasing in the x-direction is reduced. His trace interpolation scheme has two steps. First, the prediction filter coefficients are estimated for the data at half of the original trace spacing. Then given the prediction filter, the interpolated traces are solved in a least-squares sense.
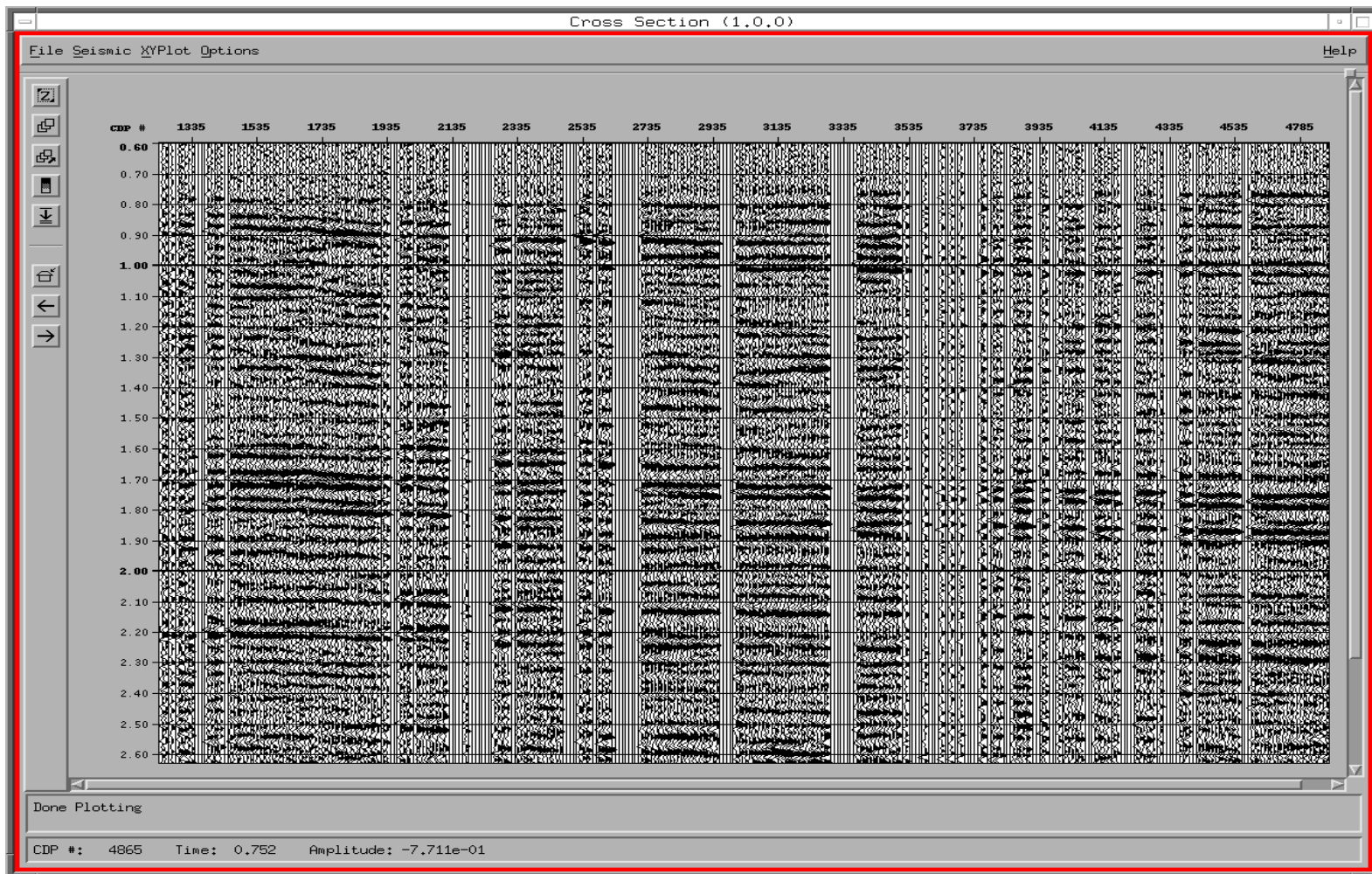
Fig. 3.4. A common-offset 1165 m section with missing trace location shown.
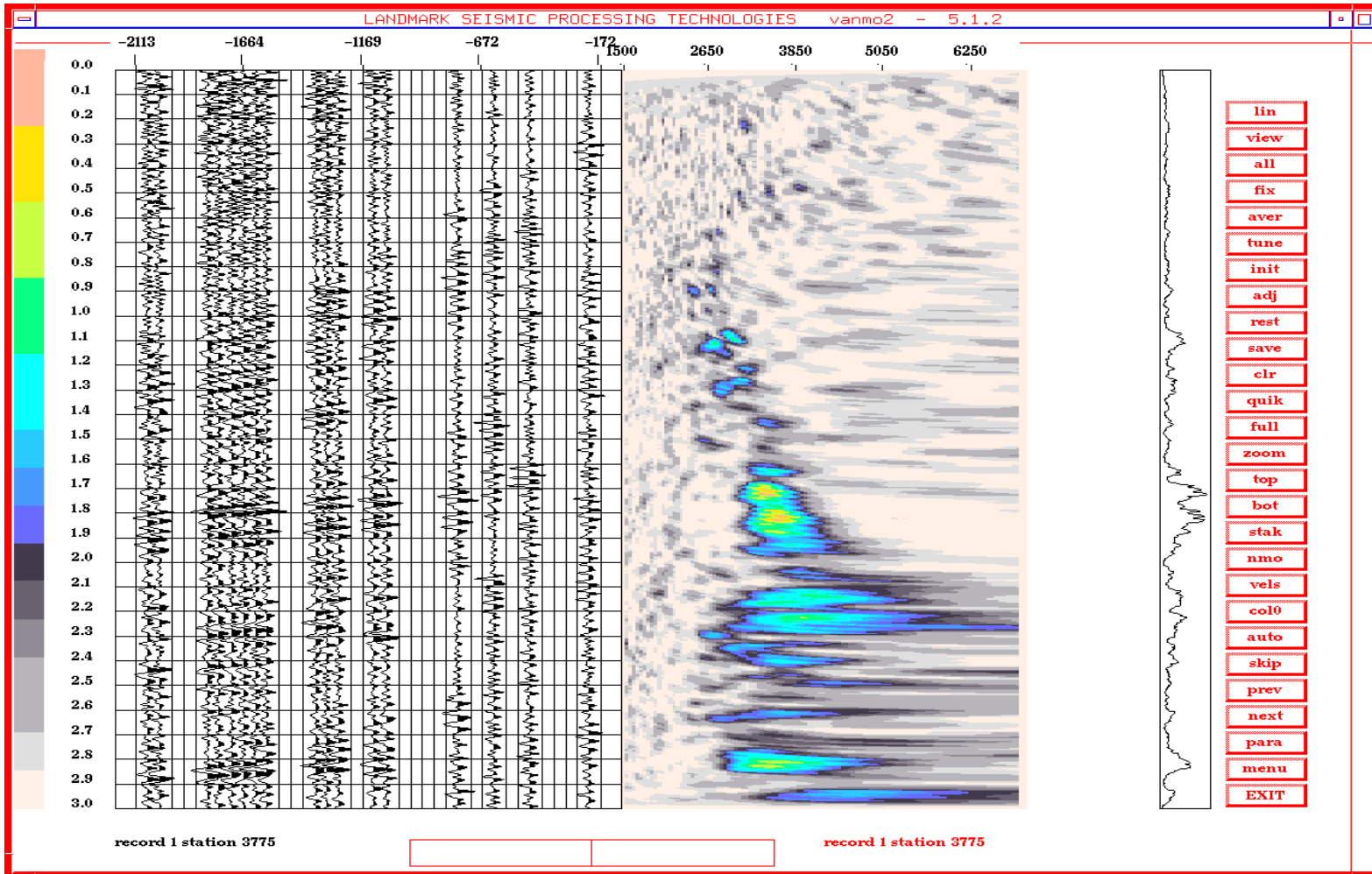
Fig. 3.5. A CMP gather at location 3775 is shown on the left, and its velocity semblance is shown on the right. Because of the missing traces, events are not easy to follow on the gather.

The missing trace interpolation in this work is a hybrid scheme of Canales' f-x deconvolution and Spitz's f-x trace interpolation. First, the data are sorted into common-offset planes, followed by the Fourier transform in time direction. For each frequency slice of a common-offset plane, the f-x prediction filter coefficients are estimated as if that frequency slice in the spatial direction is regularly spaced. It is found that if the missing traces are only a small part of the data, the prediction filter coefficients can be estimated from the data with missing traces replaced by the zeros to maintain regular spacing. Second, the missing traces for the current frequency are solved, as unknowns in a set of over-determined equations, in a least-squares sense. Unlike Spitz's f-x interpolation, we have to solve for data at random surface locations.

Prediction filtering can be written as convolution in the f-x domain. Using a matrix Notation:

$$\mathbf{FX' = Y'} \qquad\qquad (\ \mathbf{3.1}\ )$$

Here, F is a convolution matrix that contains the prediction filter coefficients at a particular frequency. Each row of F consists of the same filter coefficients shifted by one column with respected to the row above it. X' is a vector that contains the data at the corresponding frequency, and Y' is a vector consisted of predicted data, that is, a shifted version of X'. For example, for a one-step ahead prediction with a three-point f-x prediction filter as applied to a data set with 7 traces, equation (3.1) looks like:

$$
\begin{bmatrix}
f_1 & f_2 & f_3 & 0 & 0 & 0 & 0 \\
0 & f_1 & f_2 & f_3 & 0 & 0 & 0 \\
0 & 0 & f_1 & f_2 & f_3 & 0 & 0 \\
0 & 0 & 0 & f_1 & f_2 & f_3 & 0
\end{bmatrix}
\begin{bmatrix}
x_1 \\ x_2 \\ x_3 \\ x_4 \\ x_5 \\ x_6 \\ x_7
\end{bmatrix}
=
\begin{bmatrix}
y_1 \\ y_2 \\ y_3 \\ y_4
\end{bmatrix}
$$

$$
=
\begin{bmatrix}
x_4 \\ x_5 \\ x_6 \\ x_7
\end{bmatrix}
\qquad (\mathbf{3.2})
$$

Although the matrix F shown above contains only the forward prediction filters, in the actual algorithm, the matrix F contains both forward and backward prediction filters (Spitz, 1991). Because of missing traces, some of the elements in X' and Y', at the missing trace locations, are unknowns. After some re-arrangement, equation (3.1) can be re-written as:

$$
\mathbf{AX = BY} \qquad (\mathbf{3.3})
$$

where X contains all the known values of X' and Y', and Y contains all the unknown values of X' and Y' at the missing trace locations. A and B are the matrices resulting from the re-arrangement of F.

For example, if x_3 and x_5 in equation (3.2) represent the missing traces, the matrix notation of equation (3.2) can be written as a system of equations as follows:

$$f_1 x_1 + f_2 x_2 - x_4 = -f_3 x_3$$
$$f_1 x_2 + f_3 x_4 = -f_2 x_3 + x_5$$
$$f_2 x_4 - x_6 = -f_1 x_3 - f_3 x_5$$
$$f_1 x_4 + f_3 x_6 - x_7 = -f_2 x_5 \qquad (3.4)$$

The matrix form of equation (3.4) now becomes:

$$
\begin{bmatrix} f_1 & f_2 & -1 & 0 & 0 \\ 0 & f_1 & f_3 & 0 & 0 \\ 0 & 0 & f_2 & -1 & 0 \\ 0 & 0 & f_1 & f_3 & -1 \end{bmatrix}
\begin{bmatrix} x_1 \\ x_2 \\ x_4 \\ x_6 \\ x_7 \end{bmatrix}
=
\begin{bmatrix} -f_3 & 0 \\ -f_2 & 1 \\ -f_1 & -f_3 \\ 0 & -f_2 \end{bmatrix}
\begin{bmatrix} x_3 \\ x_5 \end{bmatrix} \qquad (3.5)
$$

The least-squares solution $\hat{Y}$ for the equations (3.3) or (3.5) can be written as:

$$\hat{Y} = (B^*B)^{-1}B^*AX \qquad (3.6)$$

where * denotes the conjugate transpose.

Note that equation (3.6) is solved at all signal frequencies and all common-offset planes independently.

The procedure of the f-x interpolation can be summarized by the following pseudo-code:

    sort data into common-offset planes

    for each common-offset plane

        insert zero traces at the missing trace locations to maintain regular spacing

        transform data from x-t domain into f-x domain

        for each frequency slice

        calculate prediction filter

        form equation (3.3)

        solve for missing traces using equation (3.6)

    next frequency slice

    transform data back to t-x domain

  next offset plane

3.5 Examples

  To evaluate the interpolation scheme I construct a synthetic data set shown in Figure 3.6a with 5 conflicting dips. Some traces are randomly removed to create a number of different size gaps, as shown in Figure 3.6b. The traditional f-x deconvolution is applied to the data of Figure 3.6b to fill the gaps as shown in Figure 3.7a. Figure 3.7b shows the difference plot between Figure 3.6a and 3.7a. The result of applying the least-squares f-x prediction approach to that data of Figure 3.6b is shown in Figure 3.8a. The difference between Figures 3.6a and 3.8a is shown in Figure 3.8b. Note that the non-zero values in Figure 3.8b at live trace locations are due to spectral truncation during forward and inverse Fourier transforms. From comparison of the difference plots, the new f-x interpolation gives significantly less error. The same tests are repeated for a large gap of missing traces at the crossing area, and are shown in Figures 3.9, 3.10 and 3.11. Again, the new f-x interpolation predicts the crossing events better.

  Next, the f-x interpolation is applied to the Pinecreek data. Since the f-x interpolation is based on the predictability of linear events, the natural domain to apply this technique is
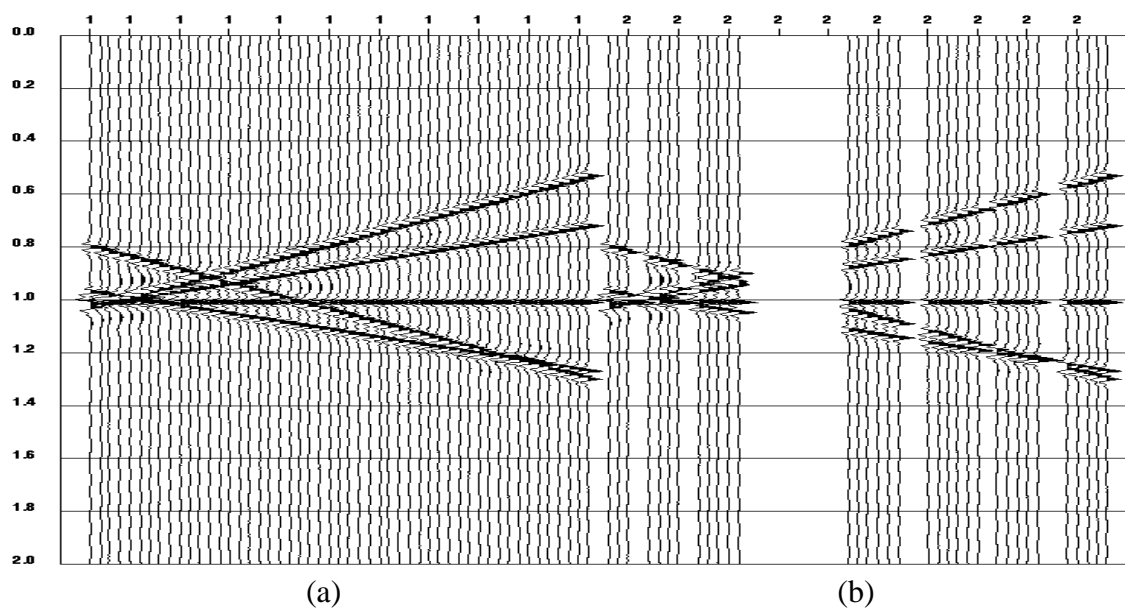
Fig. 3.6. (a) A synthetic record with 5 conflicting dips. (b) Some traces are randomly removed to create different size gaps.
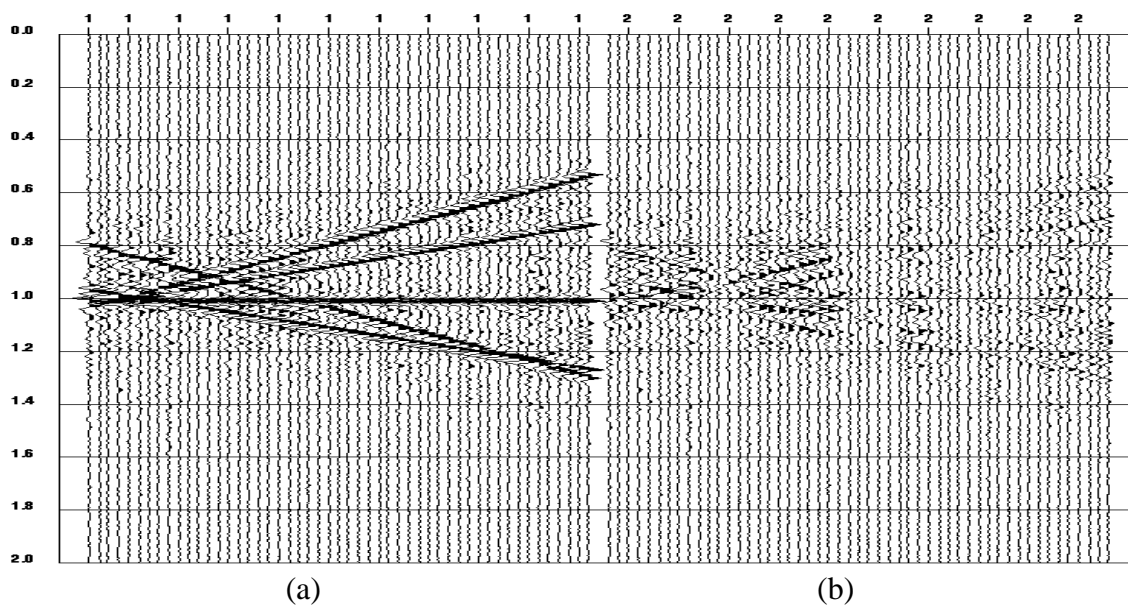
Fig. 3.7. (a) The result of applying traditional f-x deconvolution to Figure 3.6b. (b) the difference between Figures 3.6a and 3.7a.
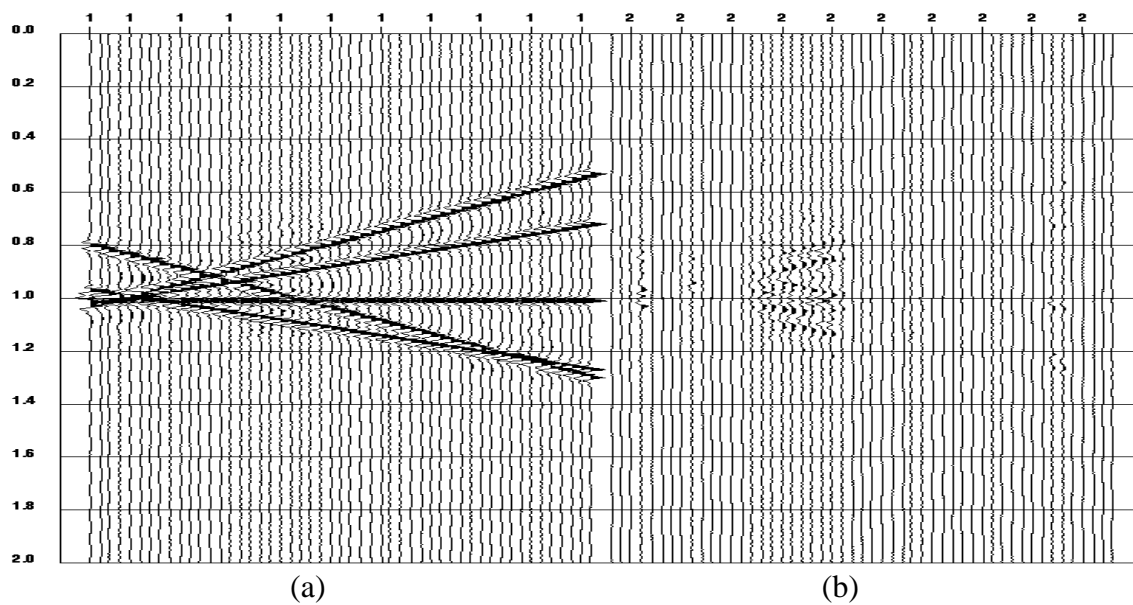
Fig. 3.8. (a) The result of applying the new least-squares f-x interpolation to Figure 3.6b. (b) the difference between Figures 3.6a and 3.8a.
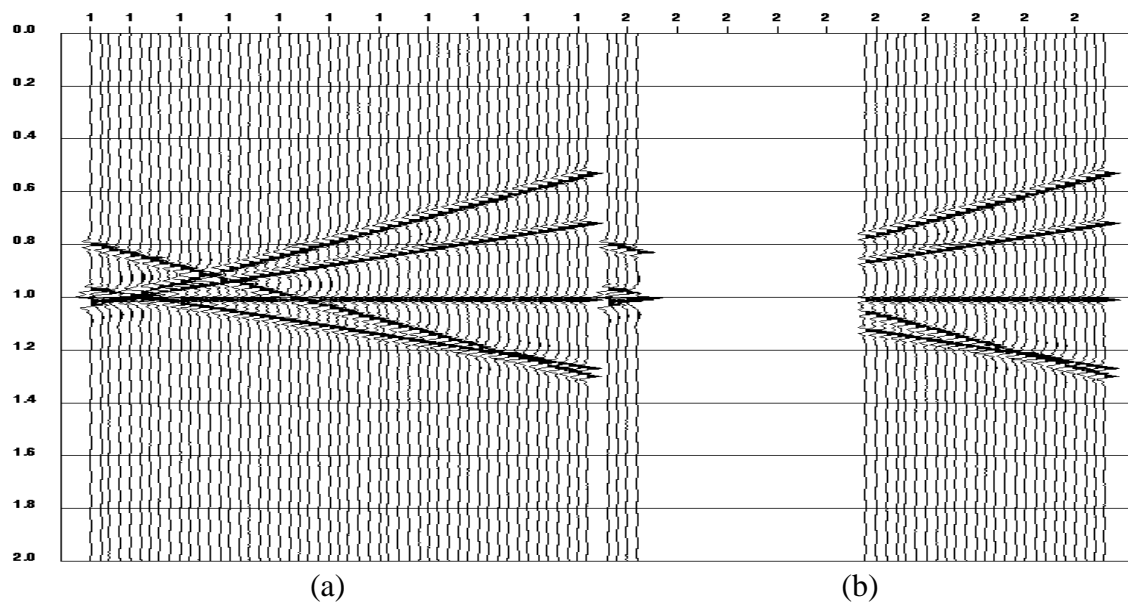
Fig. 3.9. (a) A synthetic record with 5 conflicting dips. (b) A large group of traces are removed to create a larger gaps.
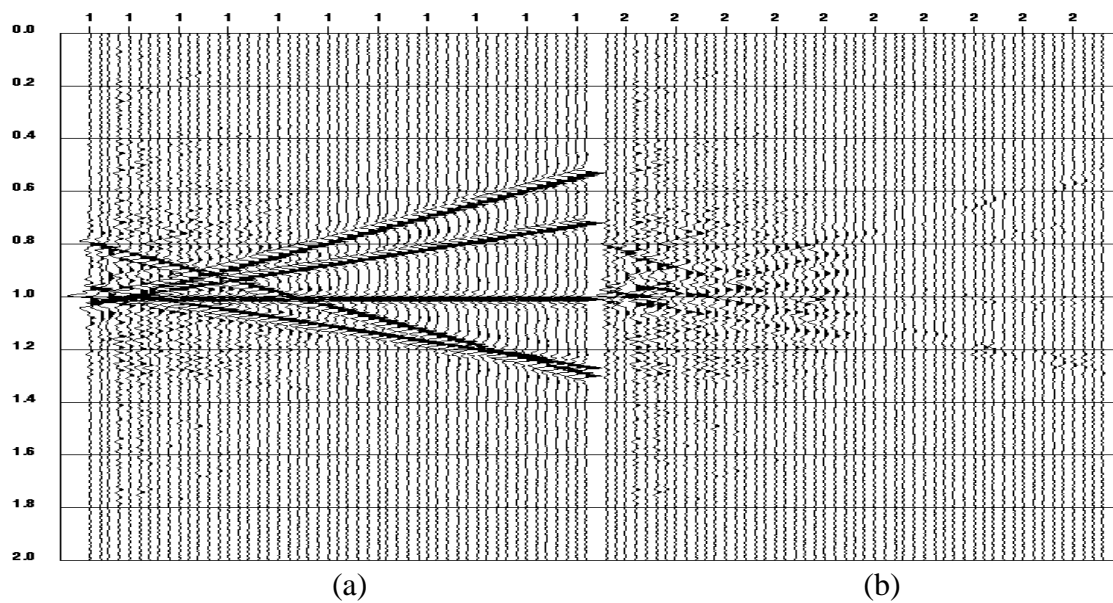
Fig. 3.10. (a) The result of applying traditional f-x deconvolution to Figure 3.9b. (b) the difference between Figures 3.9a and 3.10a.
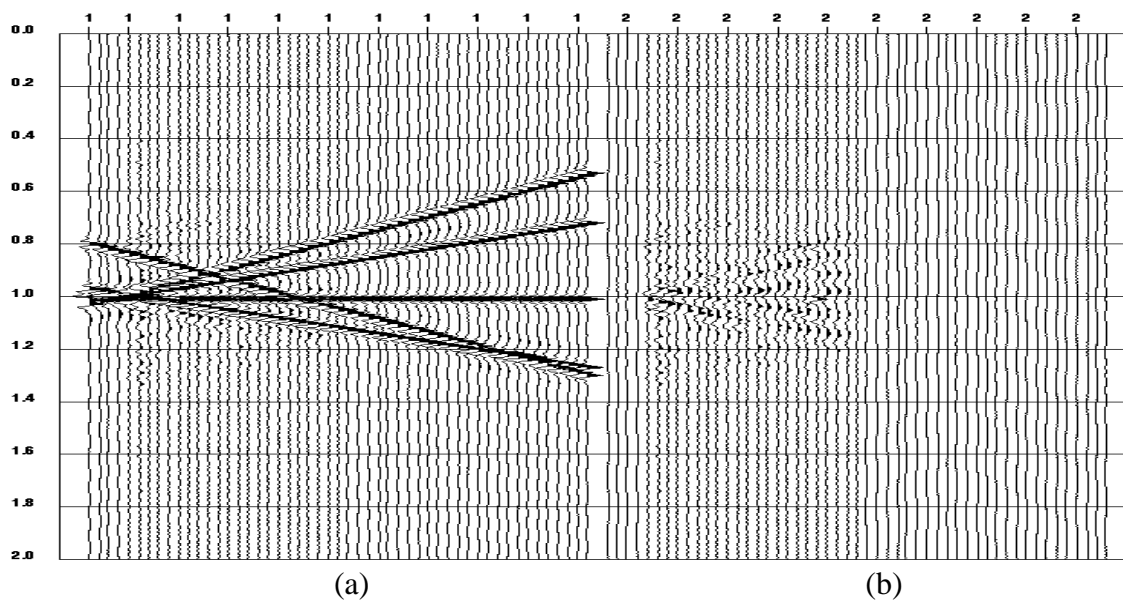
Fig. 3.11. (a) The result of applying the new least-squares f-x interpolation to Figure 3.9b. (b) the difference between Figures 3.9a and 3.11a.

common-offset planes. In common-offset planes, signals appear locally linear even without

NMO correction. Shown in Figure 3.12 is the result of applying the new technique to the

common-offset plane of Figure 3.4. After applying the interpolation to each common-offset

plane, the data are sorted back into CMPs and a semblance plot at the same location as in

Figure 3.5 is shown in Figure 3.13. The coherence of the events is improved and events are

easier to follow visually, and the velocity spectrum is more focussed. The results of the

NMO stack, DMO stack and prestack time-migrated stack are shown in Figures 3.14, 3.15

and 3.16. Artifacts of the missing traces are now suppressed, and cleaner images are ob-

tained.

3.6 Discussion

The methodology proposed here for missing trace interpolation is very similar to that of

Spitz (1991). In Spitz's approach, the operator is estimated from the data at half of the cur-

rent frequency, while in missing trace interpolation, like in normal f-x deconvolution, the

operator is estimated at the current frequency and is subjected to contamination by the

missing traces. The operators are slightly improved (not shown in this dissertation) by re-

estimation after the missing traces are filled with the current interpolation. It is believed that

the error introduced by the contaminated operator is minimized during the second least-

squares process to obtain the missing traces, and a single iteration is sufficient.

The advantage of this technique is that no a priori velocity information or the range of
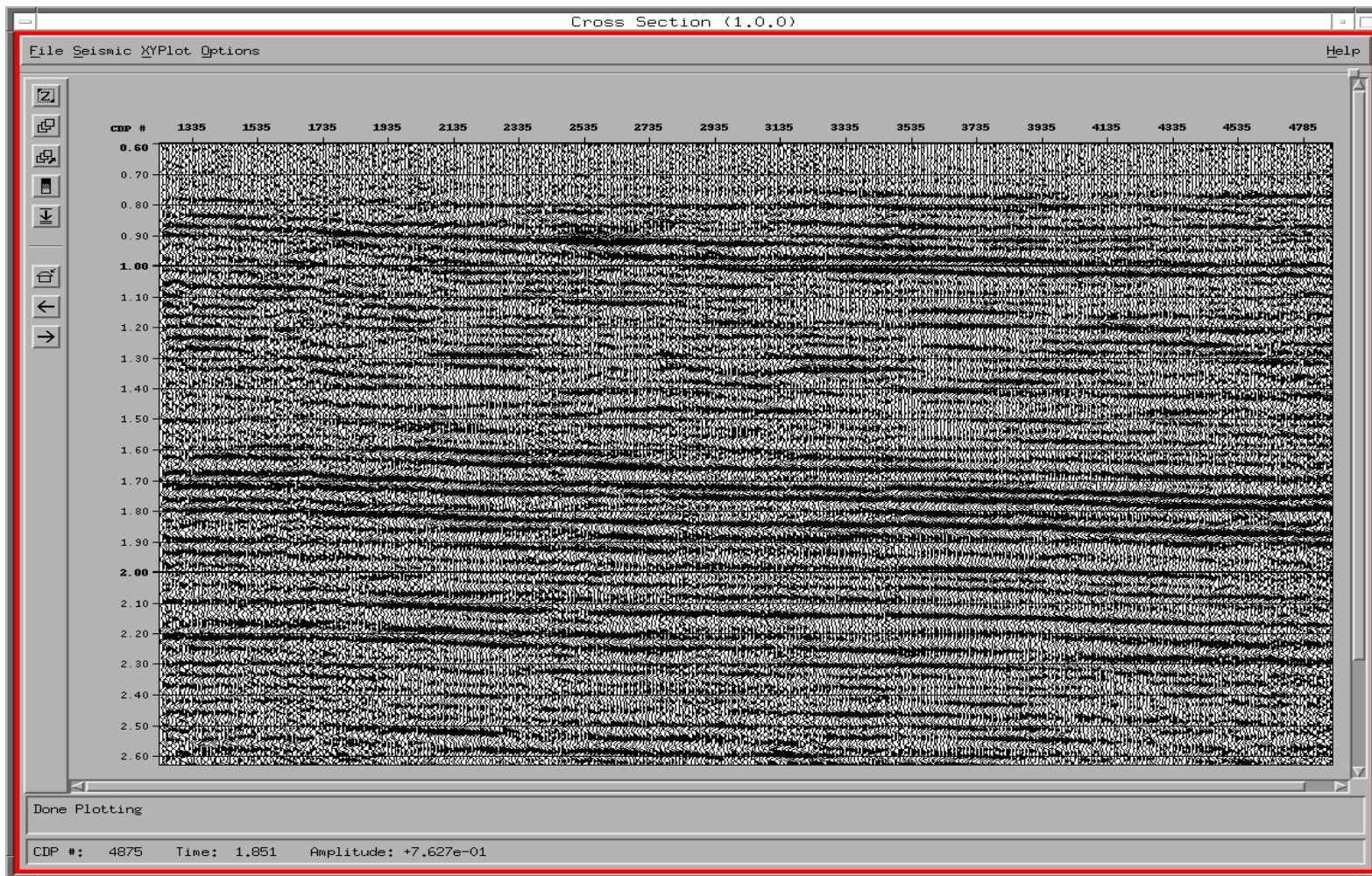
Fig. 3.12. A common-offset 1165 m section with missing traces filled by the least-squares prediction.
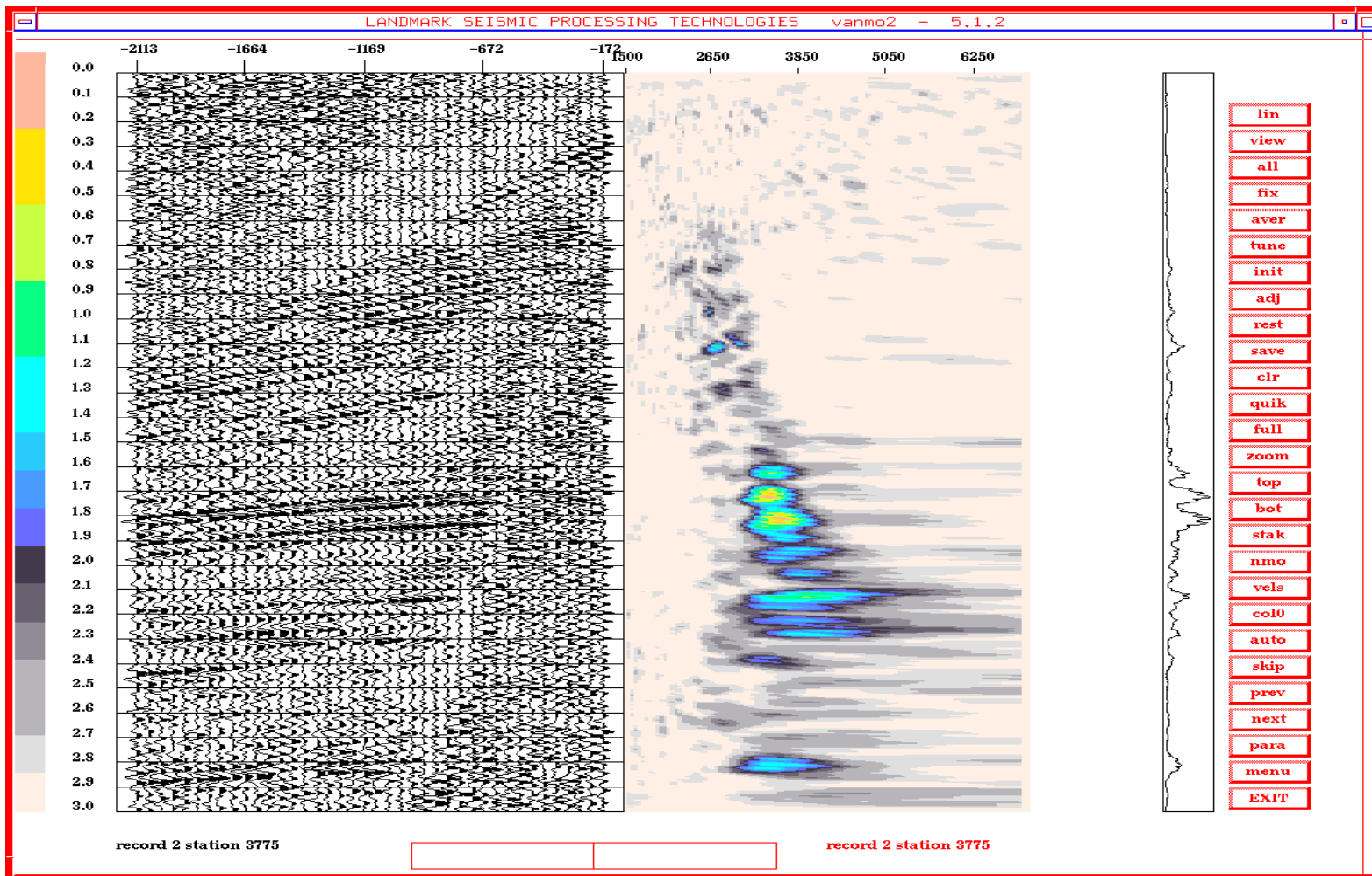
Fig. 3.13. A CMP gather and its velocity semblance after missing trace interpolation. The cmp gather is at the same location as in Figure 3.5. After interpolation, events are much easier to follow.
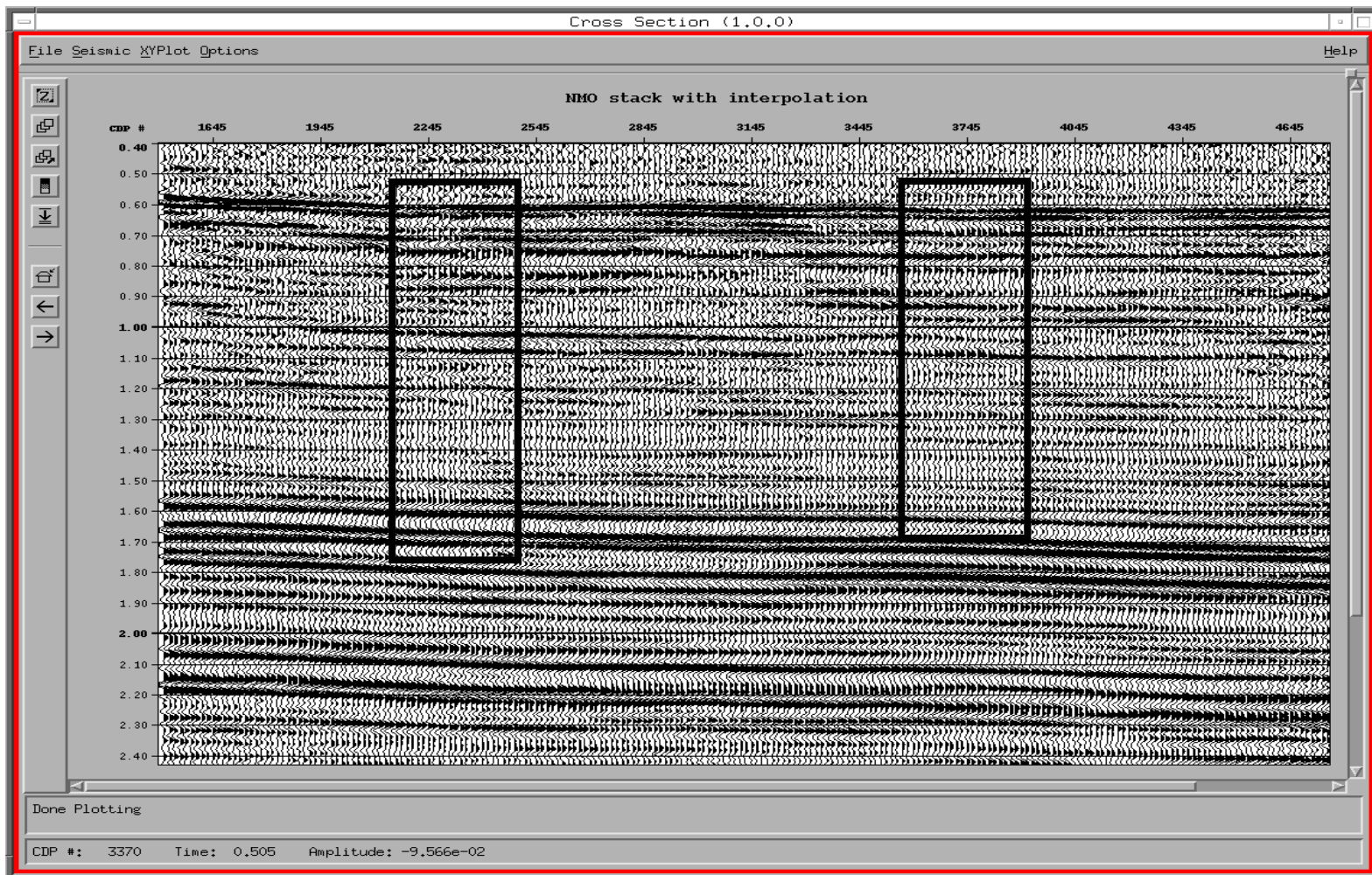
Fig. 3.14. Structural stack with the least-squares f-x interpolation. Improvement is seen when comparing this to the same section without prestack f-x interpolation in Figure 3.1.
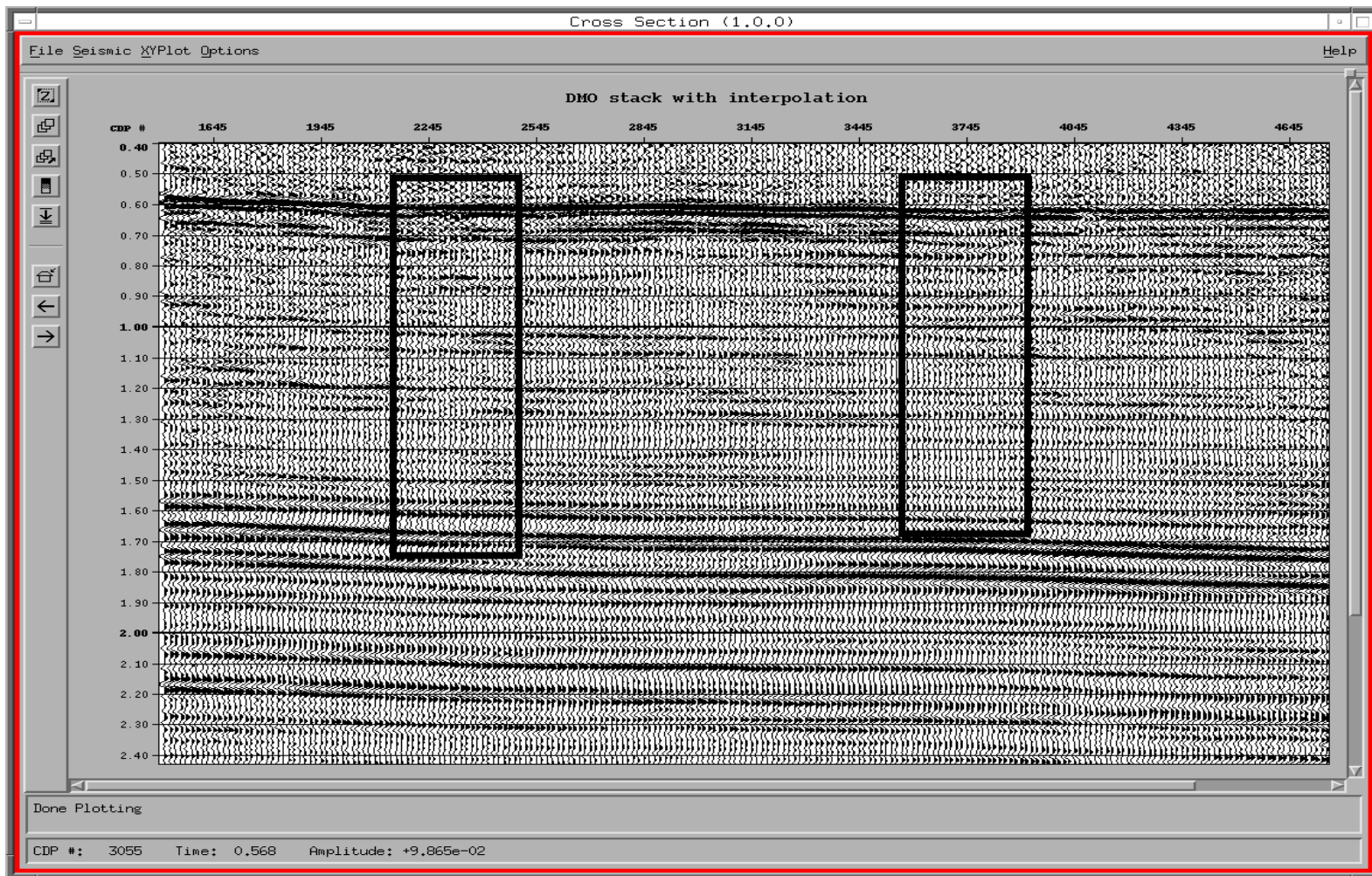
Fig. 3.15. DMO stack with the least-squares f-x interpolation. Improvement is seen when comparing this to the same section without prestack f-x interpolation in Figure 3.2.
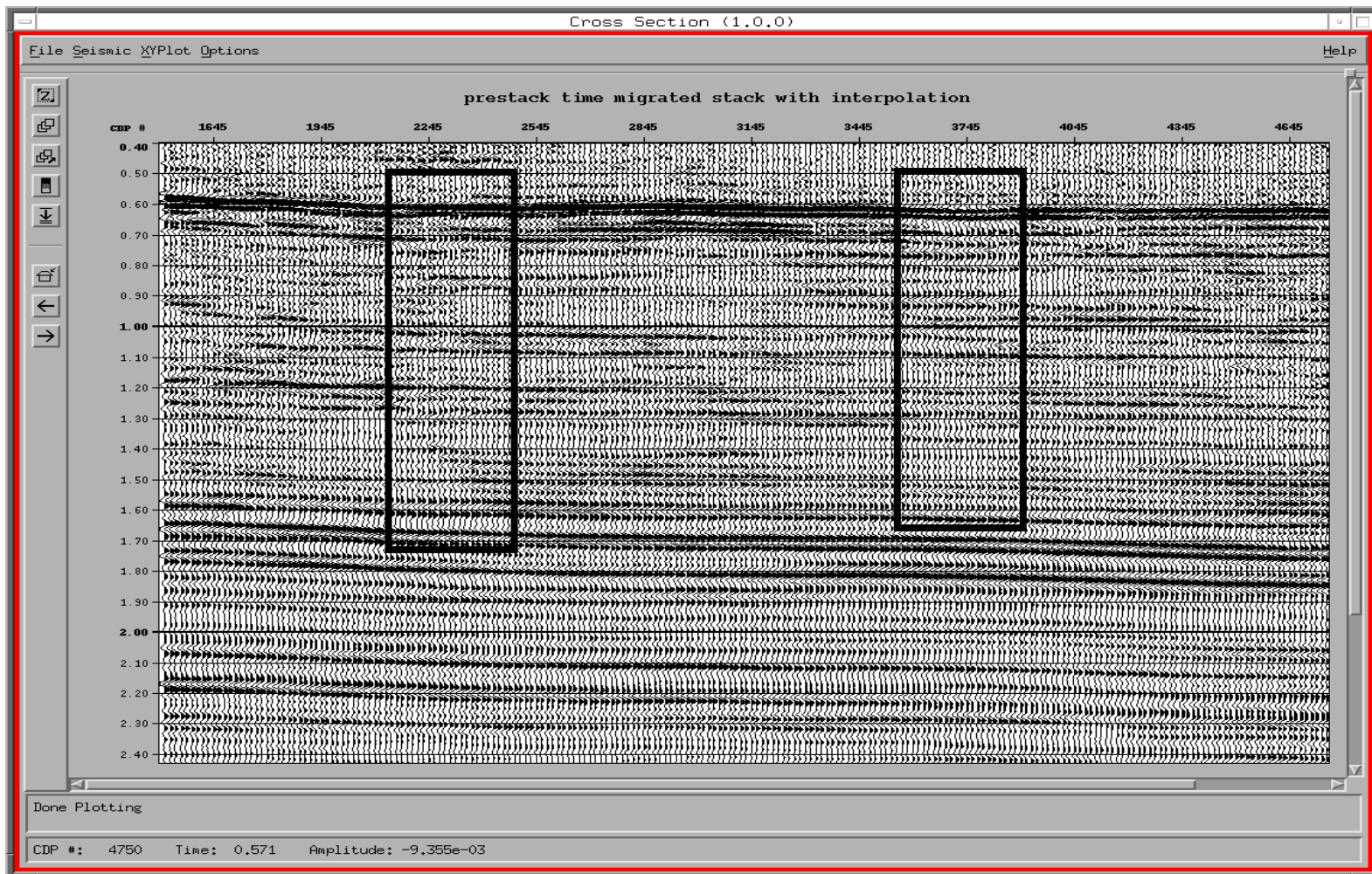
Fig. 3.16. Prestack time-migrated stack with the least-squares f-x interpolation. Improvement is seen when comparing this to the same section without prestack f-x interpolation in Figure 3.3.

dips is required for the interpolation. Unfortunately the proposed f-x interpolation is applied in the common-offset domain, and in the present it does not apply to 3-D data.

Chapter 4   Statics without a priori velocity information

4.1 Introduction

Some modern surface-consistent residual statics algorithms rely on maximizing the power of a CMP stack. However, errors in the estimated statics are strongly correlated to the NMO velocity error. Ronen and Claerbout (1985) said, "statics estimation is effectively a velocity analysis of the near-surface. Ideally, statics and velocity analysis would be done together ". In practice, the velocity and the statics are solved iteratively. This iterative procedure works well provided that the first velocity estimation is reasonable.

In a complex structural region, reasonable velocity estimation in the presence of large statics is not possible. In general, the assumption of hyperbolic moveout in the CMP domain is violated and hence, the maximum stack power may not reflect the proper statics. The problem is even worse for converted-wave data where S-wave receiver statics are solved in the ACCP domain. Note that ACCP binning requires an estimate of the average Vp/Vs ratio, and that even for 1-D earth models this binning is only an approximation.

There are some other problems with residual statics, for example, when long wavelength statics and structural variations mixed together. However, in this chapter I just focus on the velocity issue and an alternative method of solving statics without a priori velocity information is proposed. This new approach operates in the common-offset domain and does not require a priori NMO velocity information or the assumption of hyperbolic moveout.

Recently, some other approaches in separating velocity and statics estimation are developed, and they can be found in Taner and Berkhout (1997, 1998), Li and Bancroft (1997).

4.2 Theory

The basic requirement of the new statics routine is that reflection events without statics contamination, in the common-offset plane are smooth. When statics are present, the image in each common-offset plane exhibits trace-to-trace jitter, and that can be considered as random error superimposed on the smooth events. Using linear prediction iteratively in the f-x domain for each offset (Canales, 1984), the smoothness of the observed events is improved by virtue of the fact that the f-x prediction filter is estimated by a least-squares approach. The smoothed common-offset plane, that is, a common-offset gather where every data trace is replaced by a trace predicted from neighboring information, is served as model. Once the models are created for all offset-planes, they are correlated with the original traces to find static shifts for each trace in the data. These static shifts are then decomposed into shot and receiver components in a surface-consistent manner. The statics are applied to the data, new models are predicted and subsequently new statics are estimated. Iterations continue until no significant change to statics estimate is detected.

4.3 Synthetic test

To demonstrate the new statics application, the Marmousi model data set is used. To

start, brute velocity functions at 5 CMP locations were picked from the statics-free data. For comparative NMO and stack, these velocity functions are used for all subsequent tests. The brute stack of the statics-free data is shown in Figure 4.1. Next, random, but surface-consistent shot and receiver statics are applied to the prestack data. The maximum shot and receiver statics are 30 ms each. These data are stacked and the result is shown in Figure 4.2. Figure 4.3 is the stack after applying the statics derived from Ronen and Claerbout's algorithm. Both stacks are created with the same brute velocity functions previously picked from statics-free data. Because of the size of the statics, cycle skipping occurs everywhere, especially at both ends of the line. In the middle of the line, the structure is so complex that the hyperbolic assumption is violated, and the statics solution fails. The Ronen and Claerbout algorithm is modified to allow summing of three adjacent CMPs to build a pilot trace. The result of the stack is shown in Figure 4.4. The quality of the stack is improved, especially on the right hand side. By summing 3 CMPs together, the quality of the pilot trace is improved when the dips are gentle. However the result is still very poor compared to Figure 4.1, indicating the calculated statics are still poor.

Using the new velocity independent f-x approach, the statics were re-calculated from the statics contaminated model data. Figure 4.5 shows the stack obtained after correction of the f-x statics, and NMO correction with the same brute velocity functions. The quality of the stack is improved, even in the middle of the structure where the hyperbolic assumption breaks down.

A comparative view of the effect of the statics, with different statics solutions, is ob-
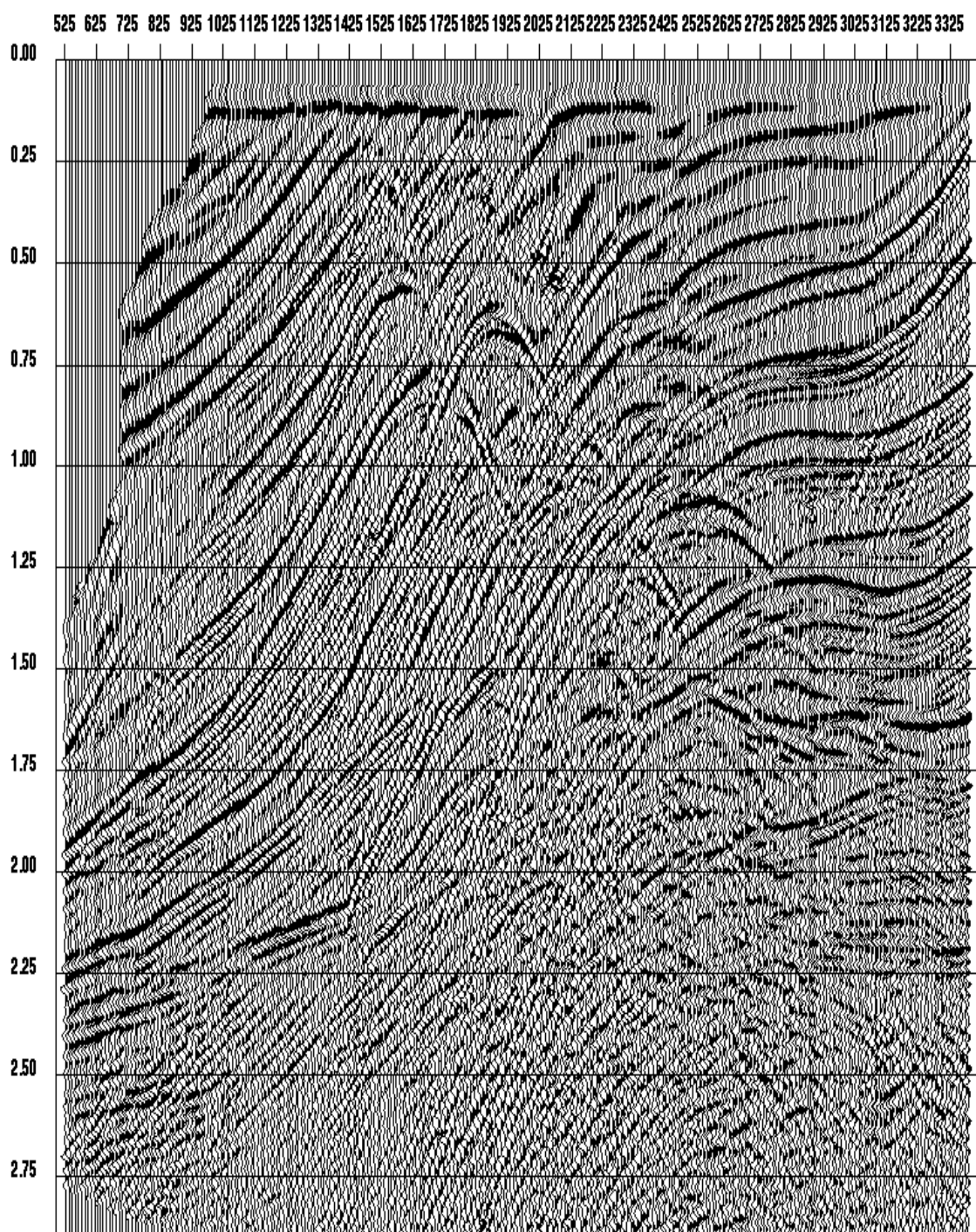
Fig. 4.1. The stack of the statics-free Marmousi data.
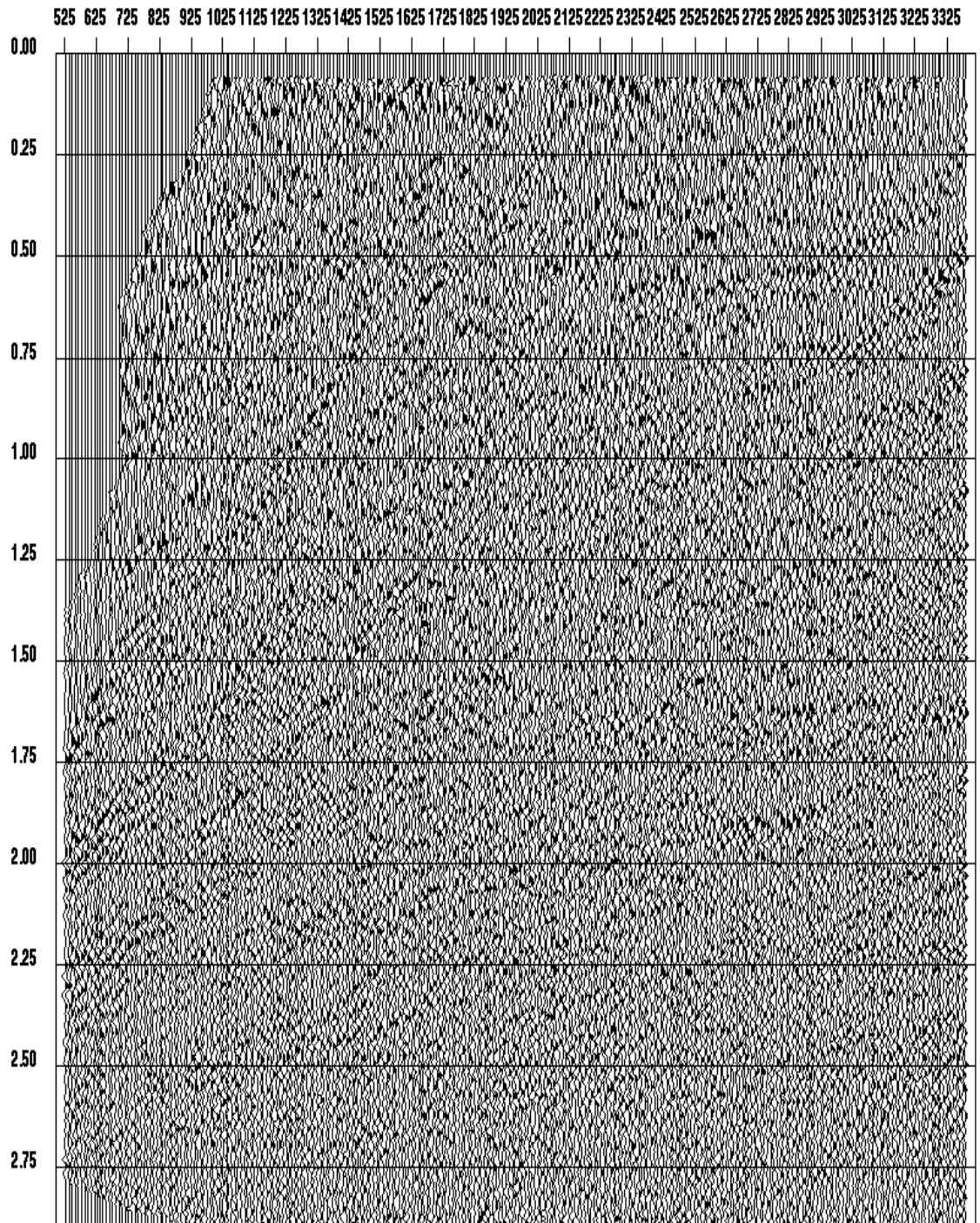
Fig. 4.2. The stack of the Marmousi data after introducing maximum 30 ms random statics for both shot and receiver.
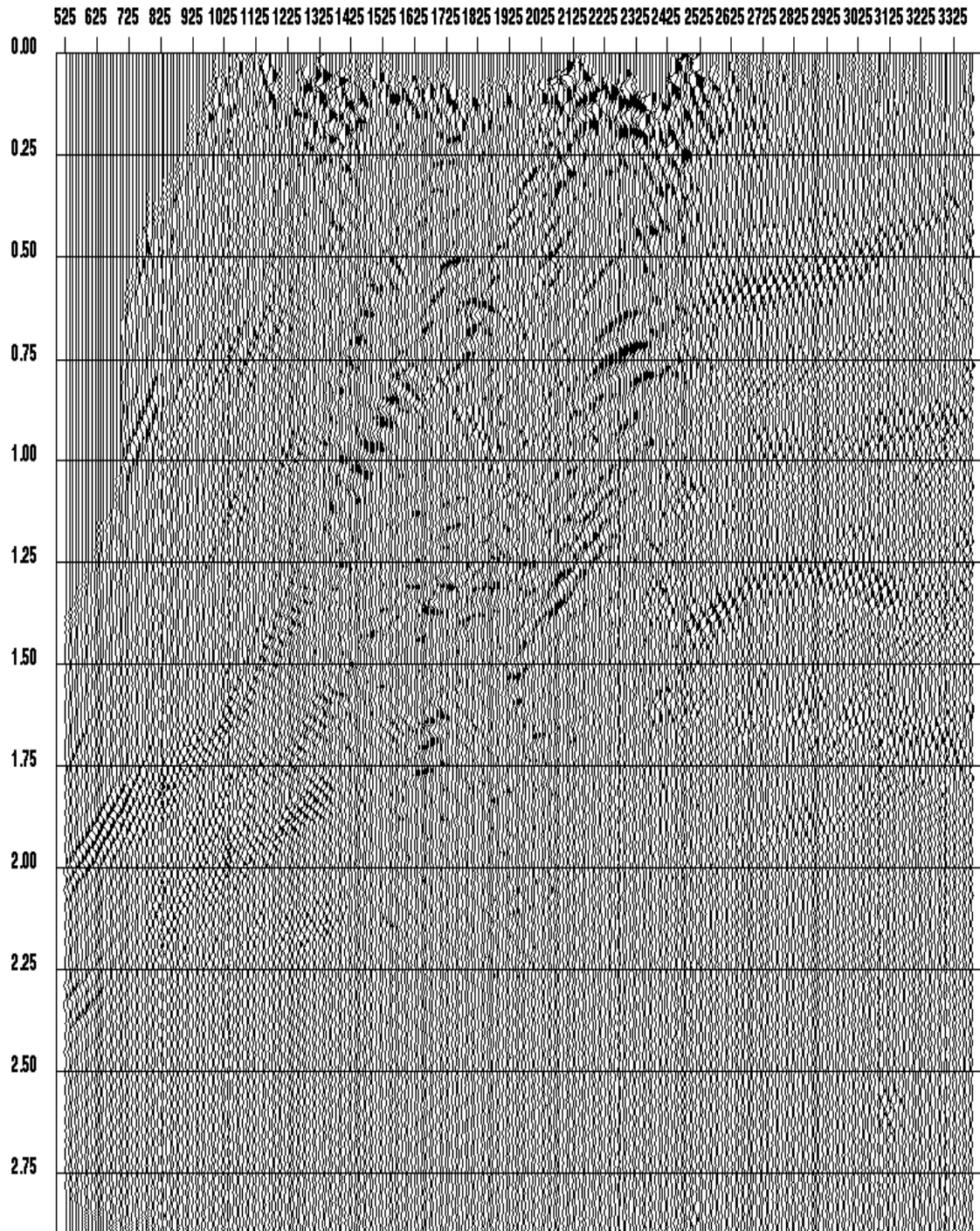
Fig. 4.3. The stack of the Marmousi data after applying the Ronen and Claerbout's statics. Because of the size of statics, cycle skipping occurs everywhere especially at both ends. The structure in the middle is not improved by the statics.
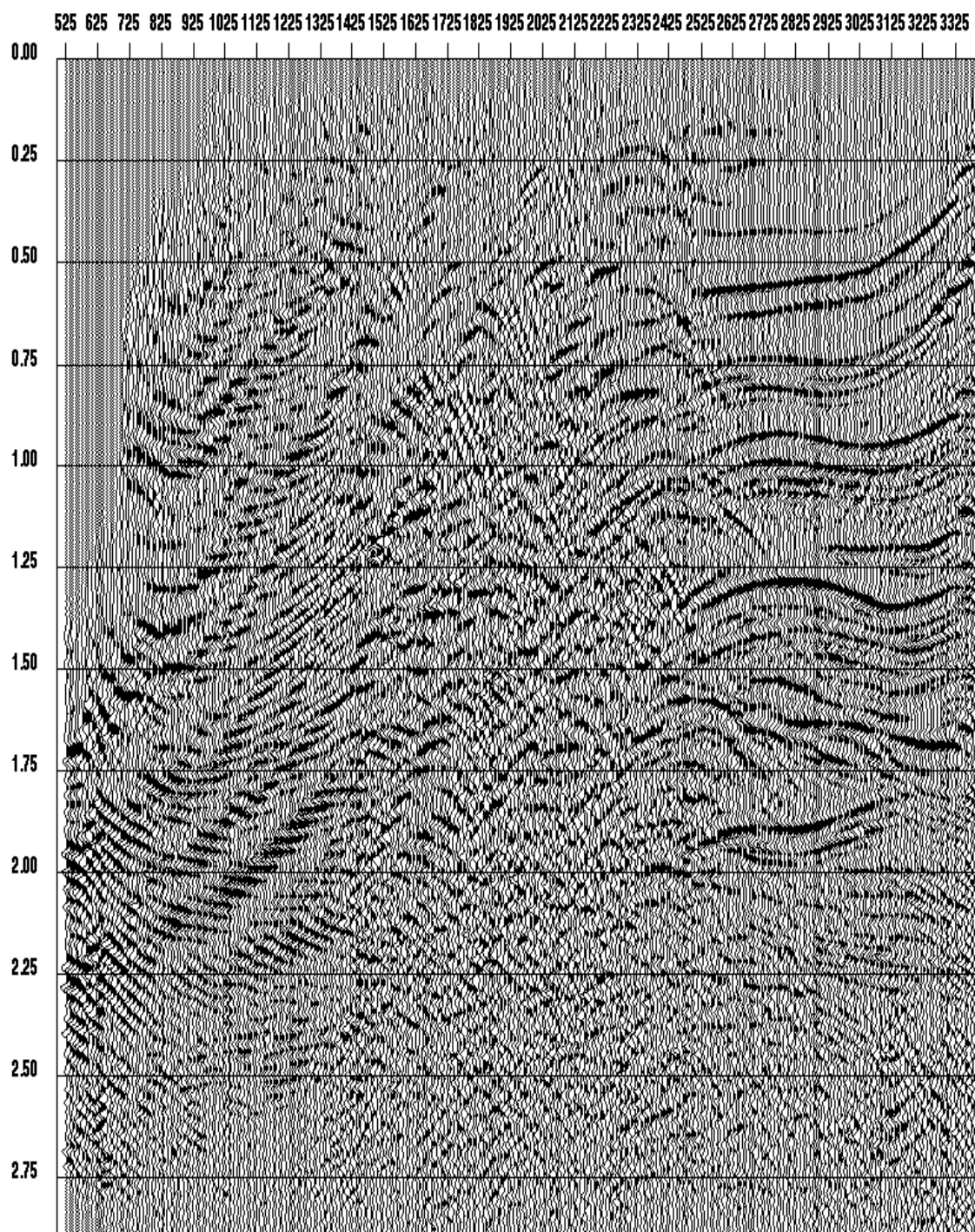
Fig. 4.4. The stack of the Marmousi data after applying the modified version of Ronen and Claer-
bout's statics. 3 CMPs are summed vertically to build the pilot trace. The effect of cycle skipping is
lessened especially on the right hand side of the data where the dips are gentle.
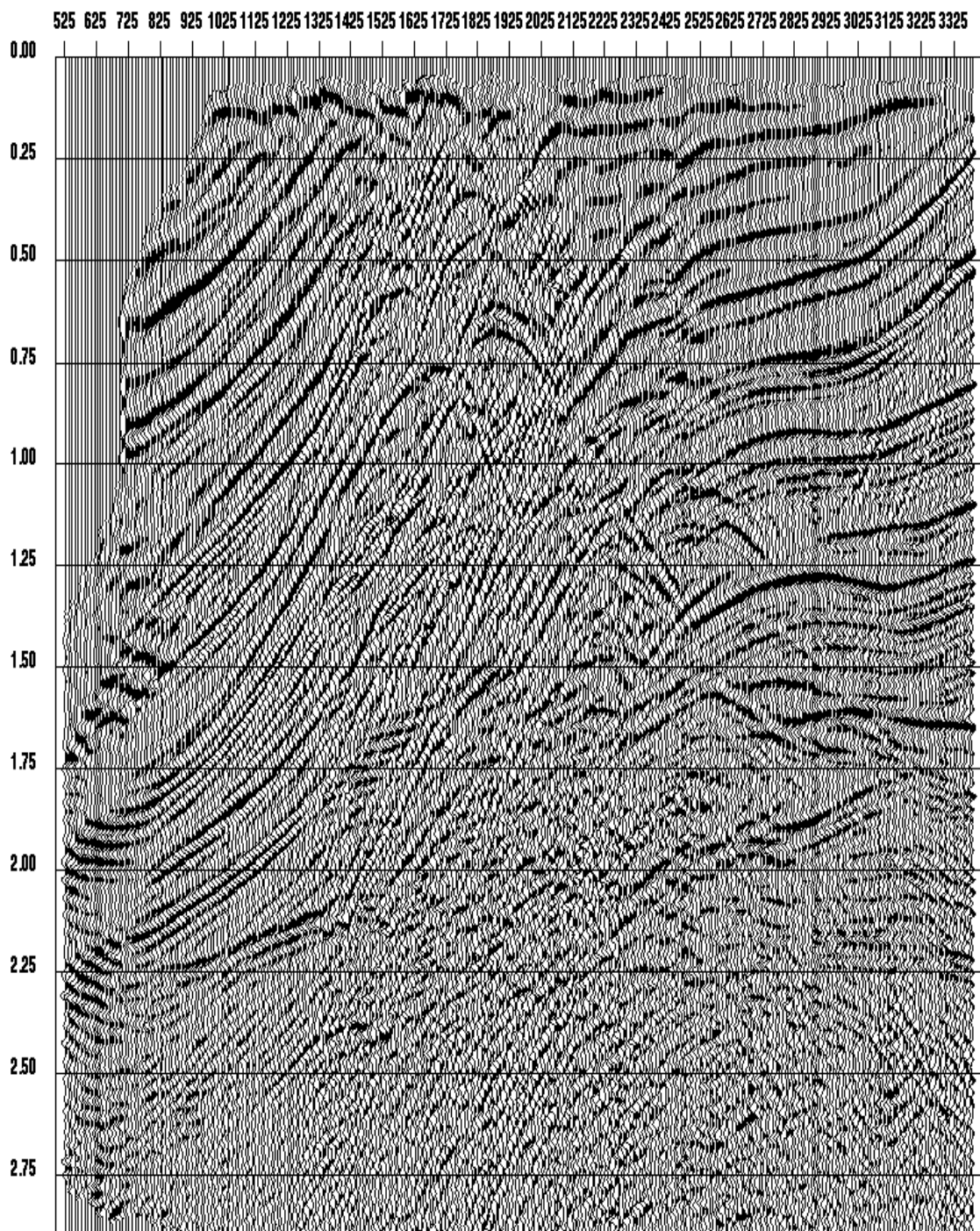
Fig. 4.5. The stack of the Marmousi data after applying the f-x statics. The complex structure starts showing up.

tained by inspecting selected CMP gathers along with their associated velocity spectra. Figure 4.6 shows a CMP gather and its velocity spectrum for statics-free data, at CMP station 2225. Figure 4.7 is the same after the statics are introduced. It is clear that the reference velocity function is very difficult to identify. Figure 4.8 is the velocity spectrum after applying the Ronen and Claerbout statics. The statics solution effectively tries to satisfy the given velocity function and forces the reflections to obey hyperbolic moveout, even though the original CMP data does not. Figure 4.9 is the velocity spectrum with the new velocity independent f-x statics applied. The similarity between Figures Figure 4.6 and Figure 4.9 indicates the statics solution is good, and that the velocity function can now be picked as reliably as when the data had no static shift.

Since the velocity can be picked relatively accurately, we may follow the f-x statics solution with a Ronen and Claerbout statics algorithm to improve the quality of the stack. The CMP gather at station 2225 and its velocity spectrum after correction with f-x followed by Ronen and Claerbout statics is shown in Figure 4.10. Finally, Figure 4.11 displays the resulting stack.

4.4 Blackfoot example

In this section, the new f-x based statics calculation is applied to a subset of a broad-band 3-C 2-D seismic experiment conducted at the Blackfoot Field in July 1995. The vertical component data (4.5 Hz geophones) are first processed in the traditional way to obtain P-
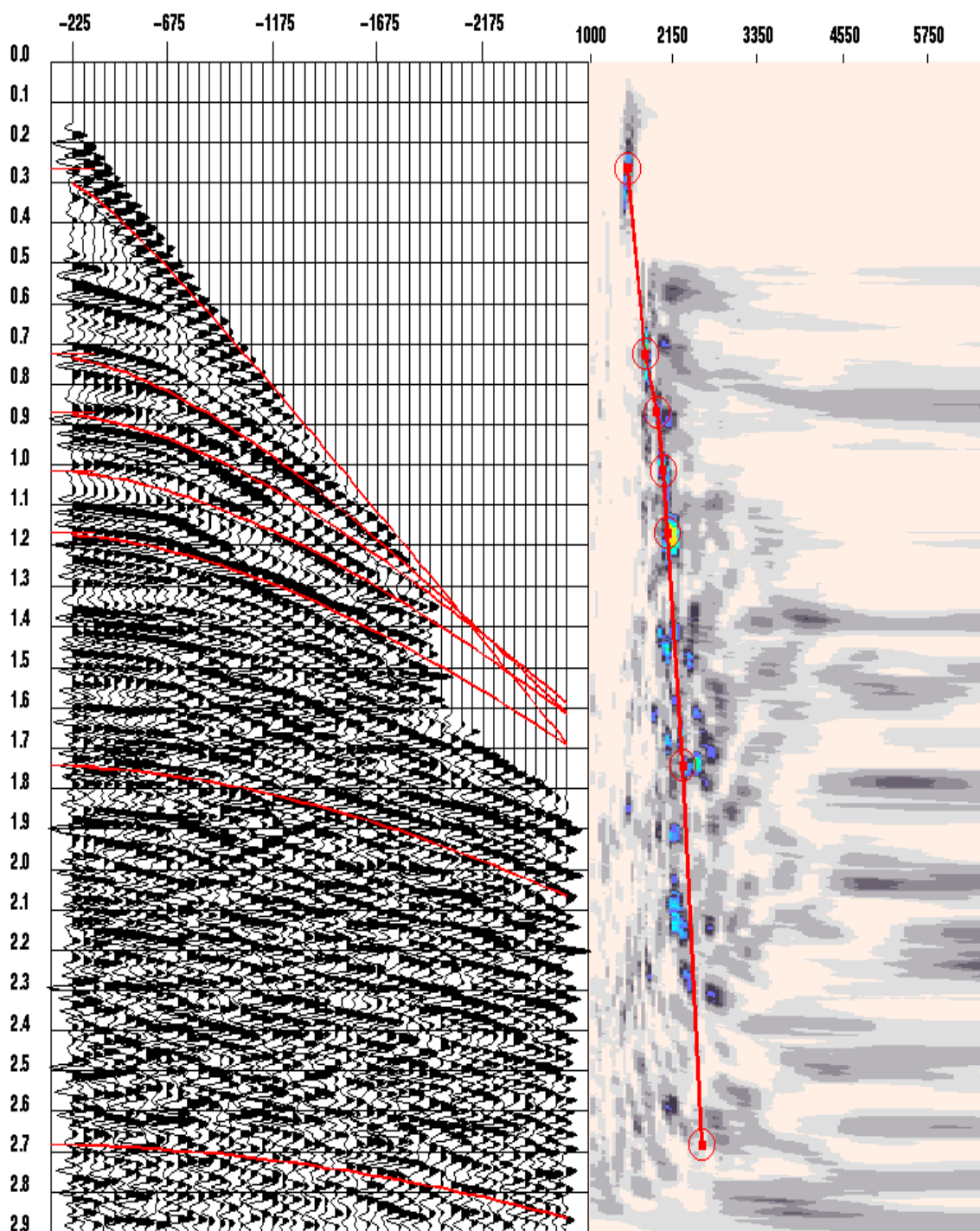
Fig. 4.6. The velocity semblance of the statics-free data at station 2225. A brute velocity function is picked as a reference for the test.
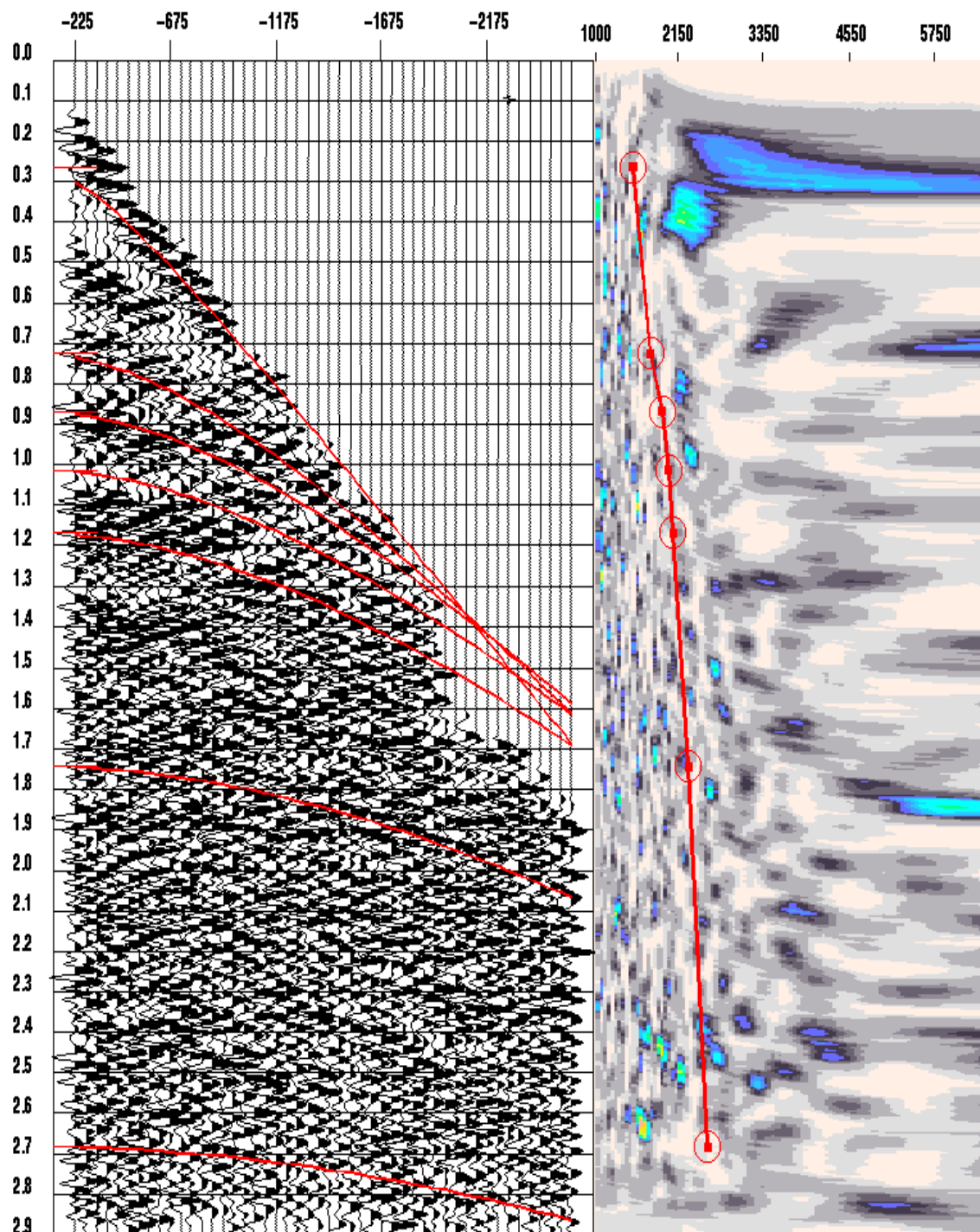
Fig. 4.7. The velocity semblance after random statics applied. The reference velocity function is difficult to identify.
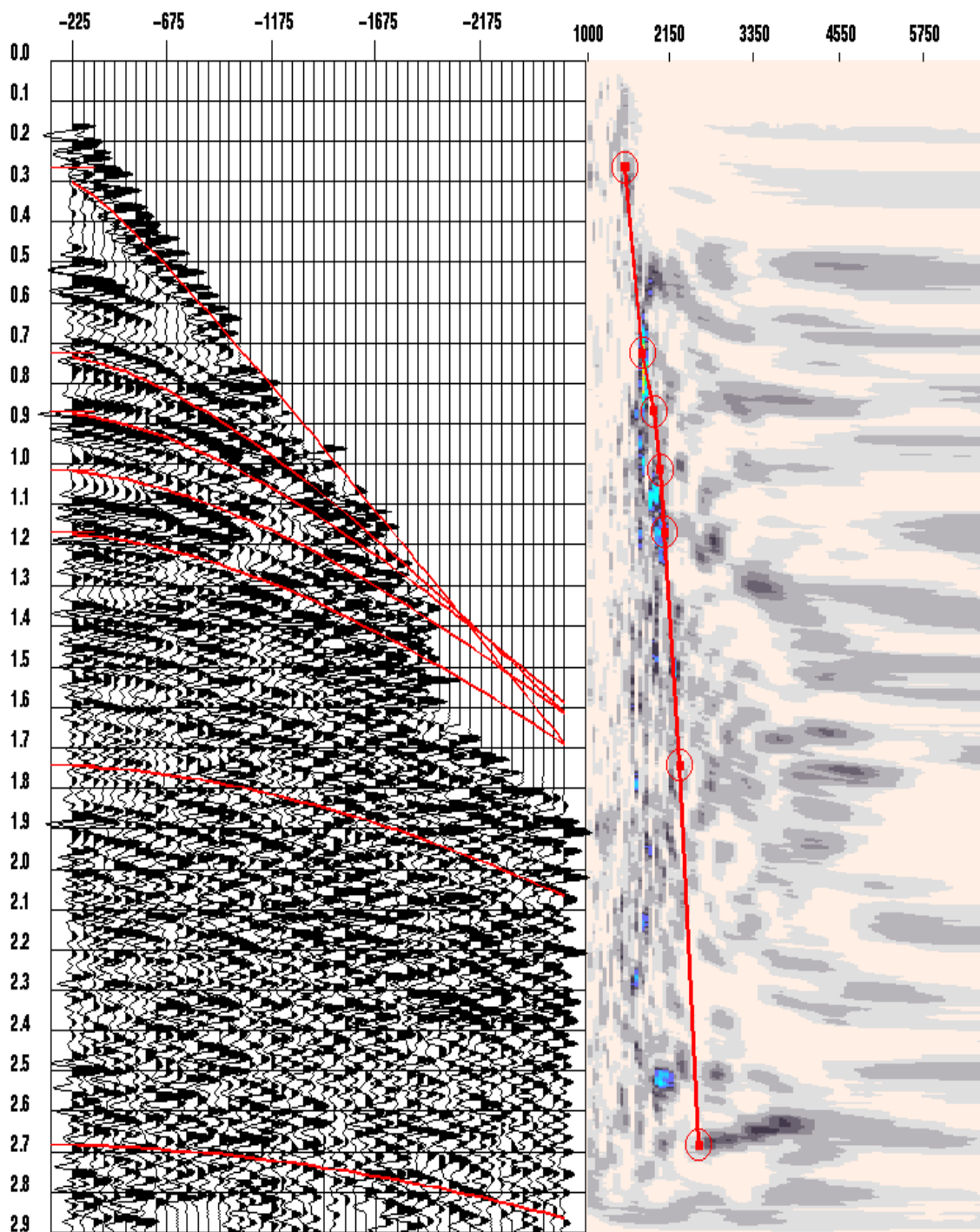
Fig. 4.8. The velocity semblance after applying the Ronen and Claerbout's statics. Cycle skipping is seen within the CMP gather.
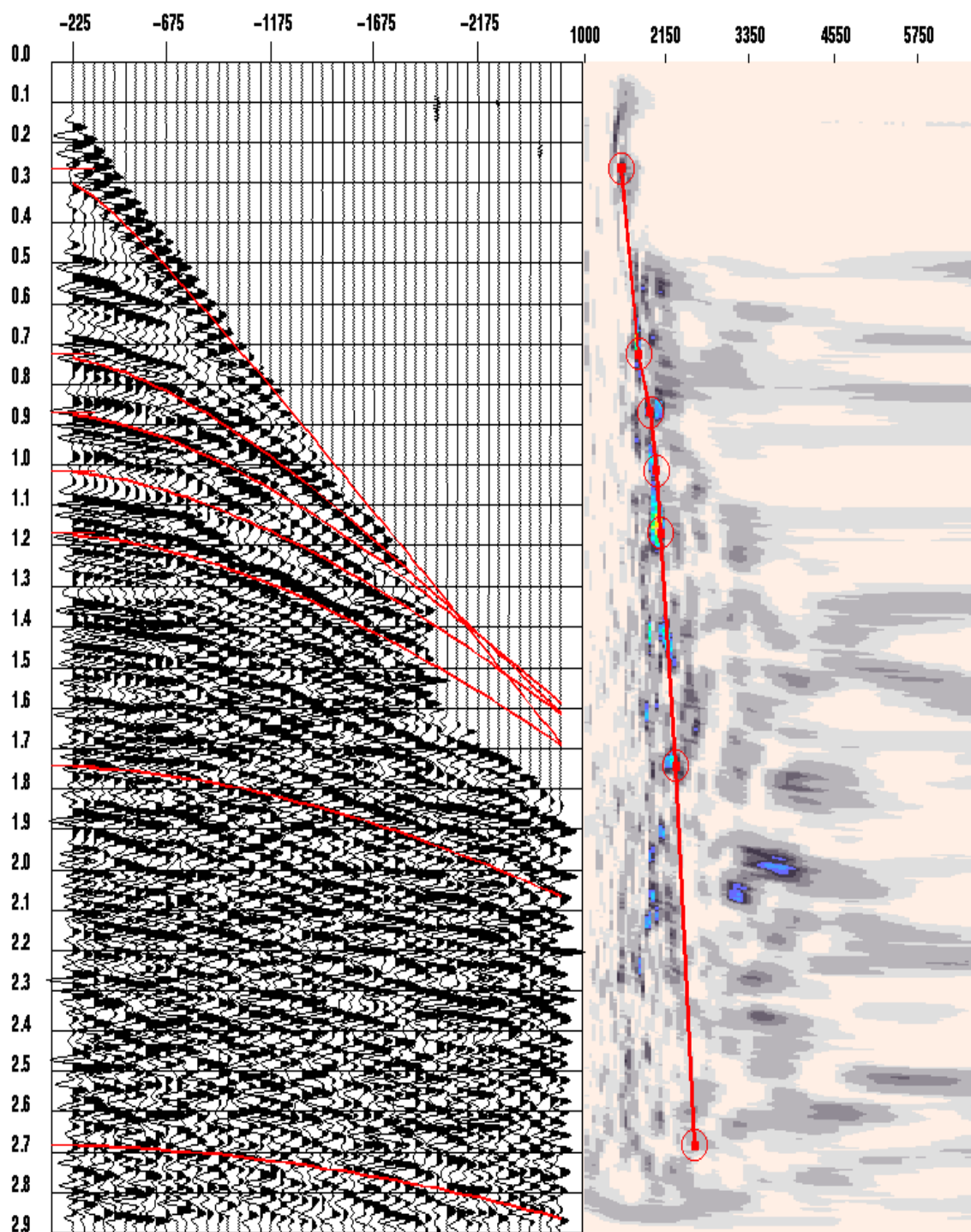
Fig. 4.9. The velocity semblance after applying the f-x statics. The semblance reveals a similar velocity function to the reference.
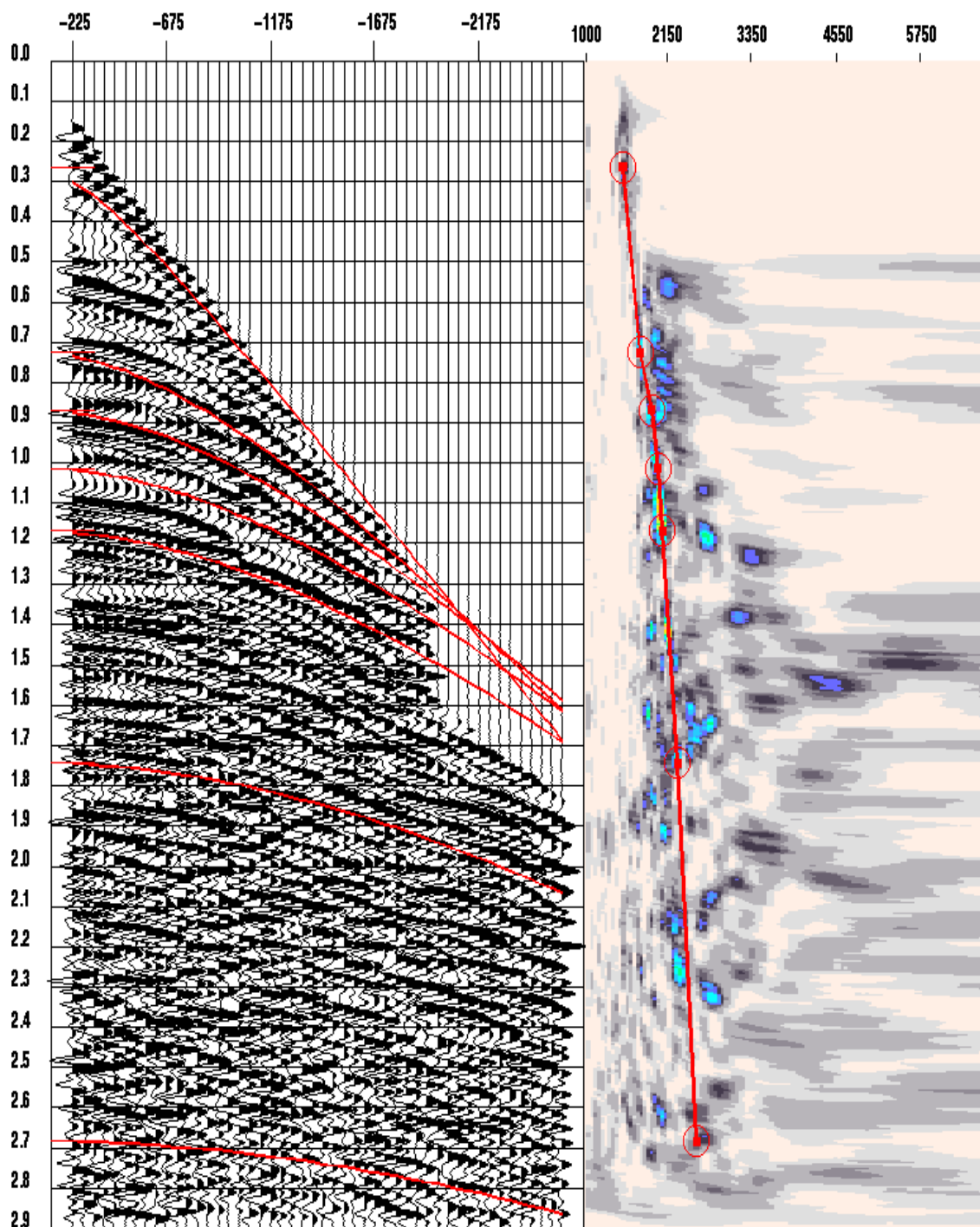
Fig. 4.10. The velocity semblance after f-x statics and the modified Ronen-Claerbout statics.
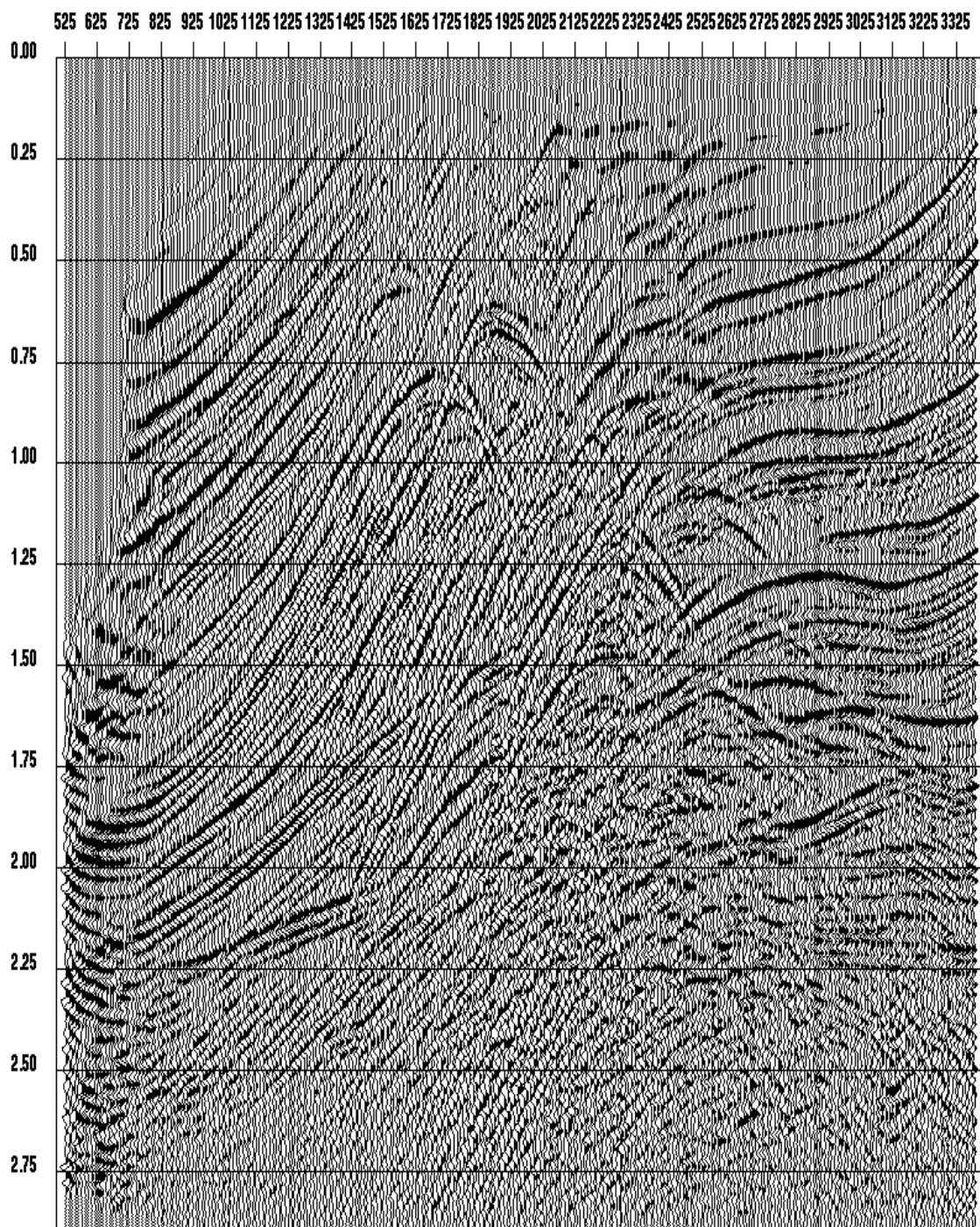
Fig. 4.11. The stack of the Marmousi data after applying the f-x statics and the modified Ronen-Claerbout's statics. The diffraction patterns in the middle of the line now show clearly.

wave refraction statics and P-wave residual statics (Ronen-Claerbout residual statics calculation). The processing flow for the vertical component is shown in Figure 2.3. The radial component data (4.5 Hz geophones) are then processed in a receiver-consistent manner. The data set is first datumed to 960 m with a P-wave replacement velocity of 3000 m/s at the shot and an S-wave replacement velocity of 1200 m/s at the receiver. As well, P-wave refraction statics and P-wave residual statics for both shots and receivers are applied (i.e., Vp/Vs=1 is assumed). Any un-corrected part of S-wave statics is treated during the S-wave residual statics calculation.

To avoid cycle skipping due to large statics, I need to work in a lower frequency band. Unfortunately, the lower frequency signal is largely contaminated by the ground roll. To solve this problem, I suppressed the ground roll in the receiver-domain and limited the statics calculation to offsets larger than 1000 metres. A local slant stack procedure is also applied in the receiver-domain to improve the signal-to-noise ratio. The data set is then processed with gather-oriented minimum phase deconvolution for all receivers followed by gather-oriented zero-phase deconvolution (to maintain the receiver-consistent phase) for all shots. The processed results are then analyzed with the f-x statics calculation.

For comparison purposes, Figures 4.12, 4.13 and 4.14 display the ACCP stack without residual receiver statics, with conventional residual receiver statics, and with f-x statics, respectively. Both static routines improve the quality of the stack. In fact, the conventional statics gives an apparently crisper stack than the f-x statics, especially in the time window 2.25 s to 2.75 s. Figure 4.15 displays the f-x and the conventional statics. The first trace
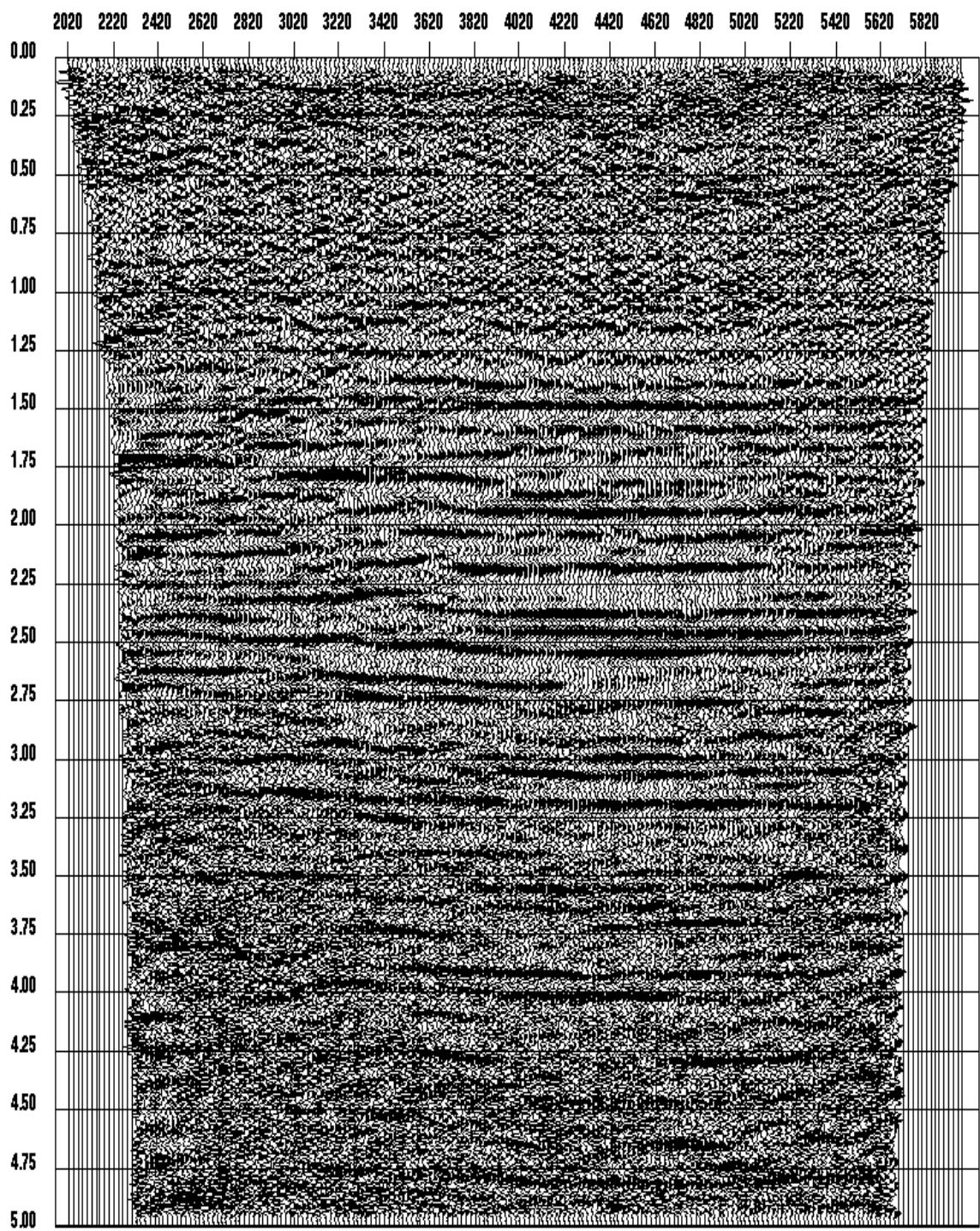
Fig. 4.12. ACCP stack without residual receiver statics applied.
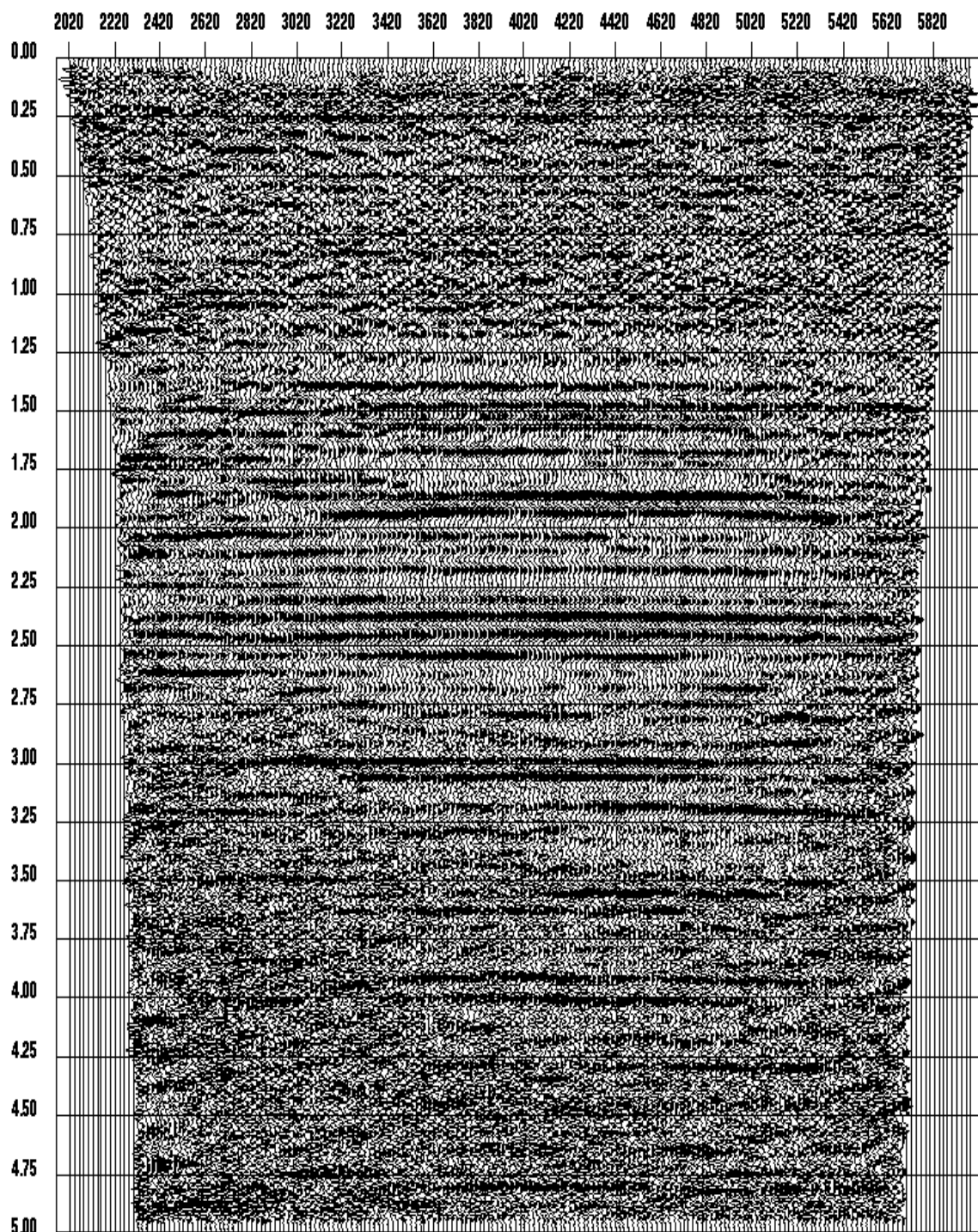
Fig. 4.13. ACCP stack with conventional residual receiver statics. The quality of the stack is considerably improved.
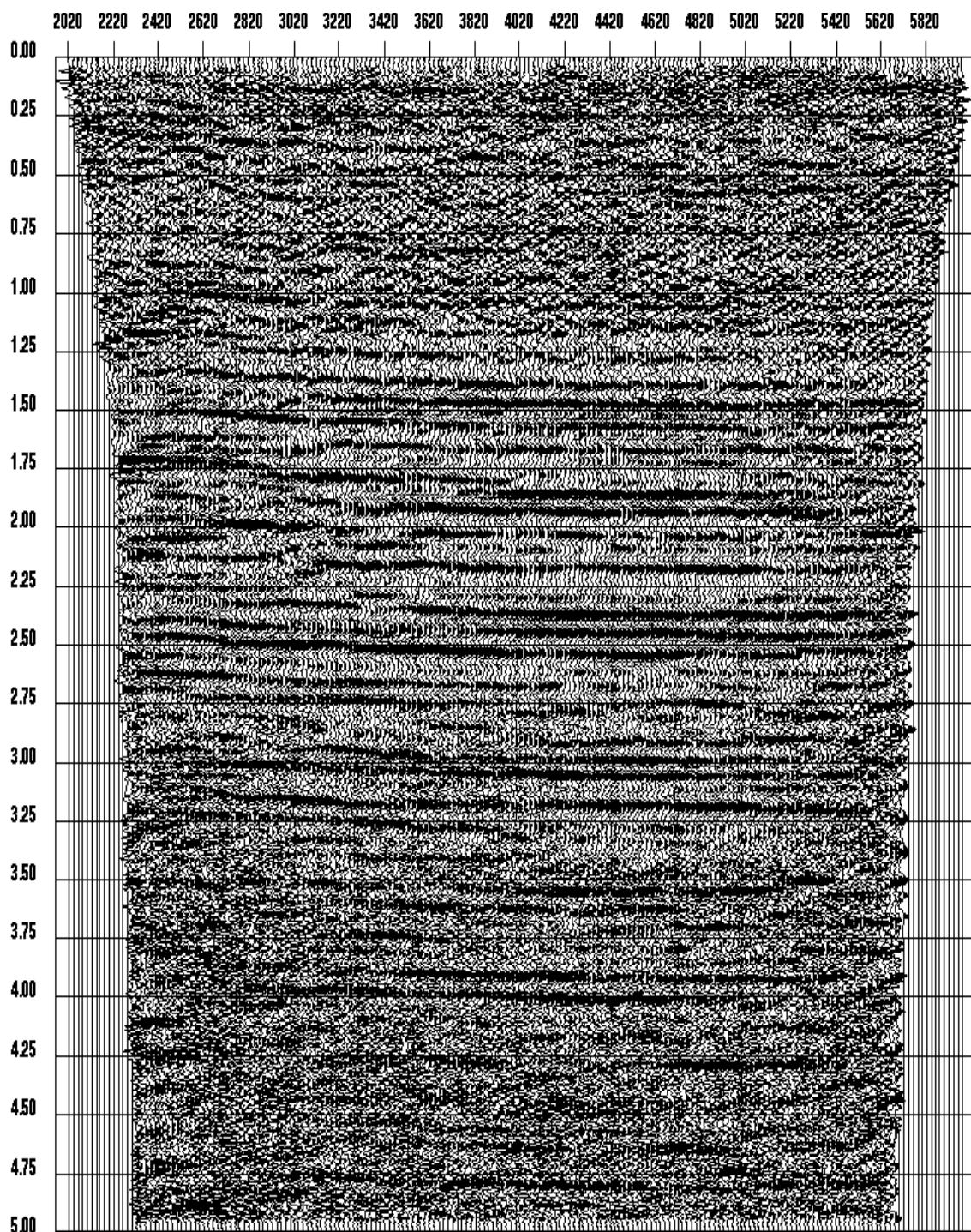
Fig. 4.14. ACCP stack with f-x residual statics. The quality of the stack is better than the stack without residual receiver statics, but not as high as that of the stack with conventional residual receiver statics.
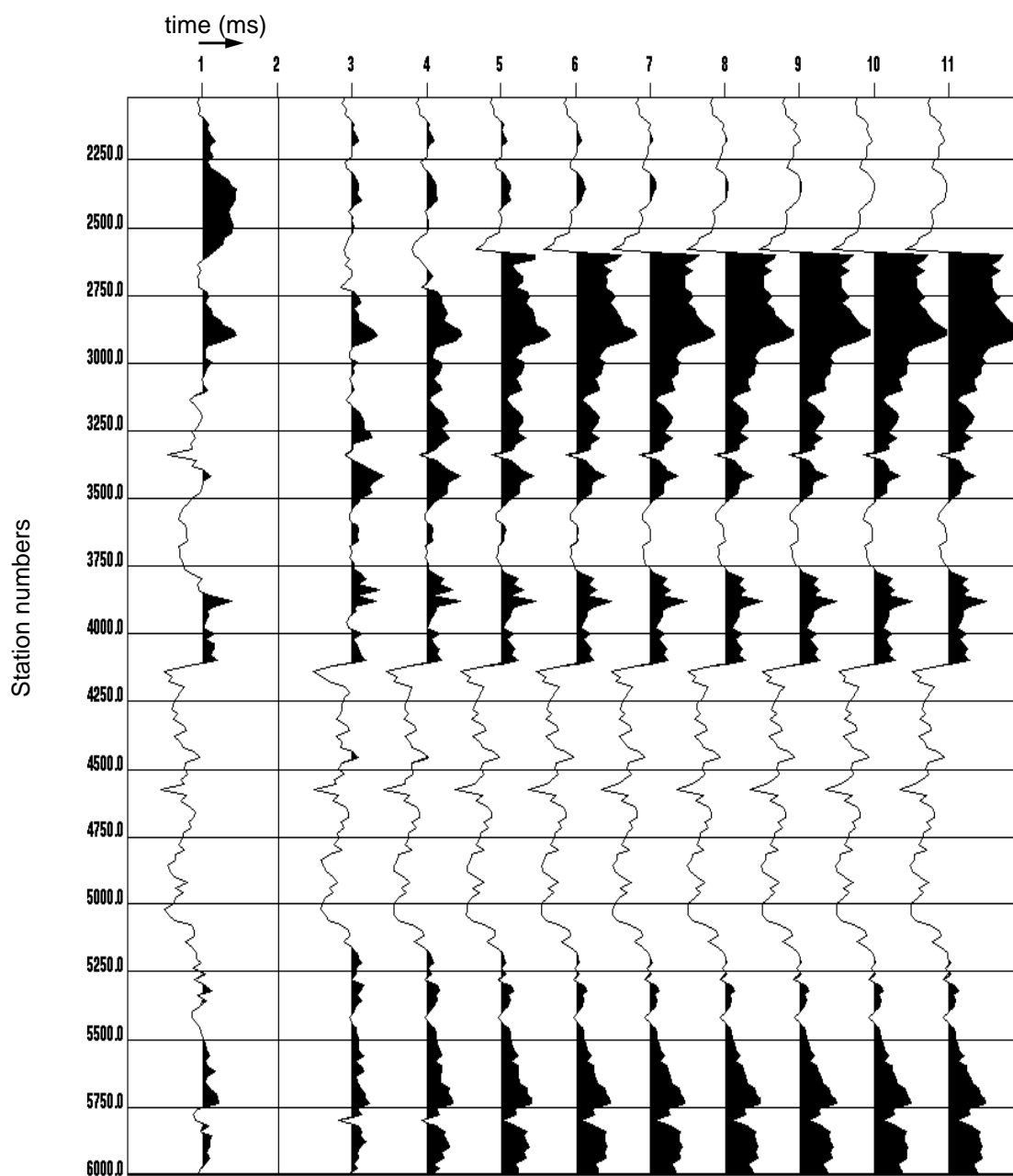
Fig. 4.15. Comparison of the results of f-x statics and the Ronen and Claerbout statics. The maximum size of statics is around 20 ms. Application of f-x statics is shown in the first trace. The first nine iterations of the Ronen and Claerbout statics are shown in the next nine traces. Both algorithms show similar results from receiver stations between 2700 to 6000. Starting from the third iteration of the Ronen and Claerbout algorithm, a D.C. bias of the statics around receiver station 2600 is built-up, and eventually it develops into a cycle-skip.

shown in the figure is the f-x statics solution, while the next nine traces represent the solution for nine subsequent iterations of conventional statics. By comparing the f-x statics and the last iteration of the conventional statics, it is observed that they both show similar short wavelength results from stations 2700 to 6000. It is also observed that, in the conventional statics, a constant negative shift is superimposed on stations 2020 to 2600, and a positive shift is superimposed on stations 2600 to 3500, creating a break in statics at station 2600. This suggests that a cycle skip is occurred in the conventional statics solution. A similar pattern of a statics break is also seen at station 4100 for both the f-x and the conventional statics. This statics break, however, is smaller in magnitude and is not likely to create a leg jump.

Some common-offset planes before and after application of conventional and f-x residual receiver statics are shown in Figure 4.16 to Figure 4.21. Figures 4.16 and 4.17 are a comparison of the results at an offset of 2270 m. Since this offset only includes stations 4300 to 6000, the results are very similar. The next two figures (Figures 4.18 and 4.19) are at an offset of -1530 m and include stations 2020 to 4480. Here, the f-x based statics estimation approach produces smoother result than the conventional statics estimation. A discontinuity in reflection events occurs at station 2600 in the conventional statics result. Figures 4.20 and 4.21 display an offset panel of -2130 m with stations ranging from 2040 to 3880. The statics break at station 2600 is obvious in Figure 4.20 while it is clearly missing in Figure 4.21 which shows the same offset corrected with f-x based statics estimates.

The next comparison involves statics application in the shot record domain. Figure 4.22
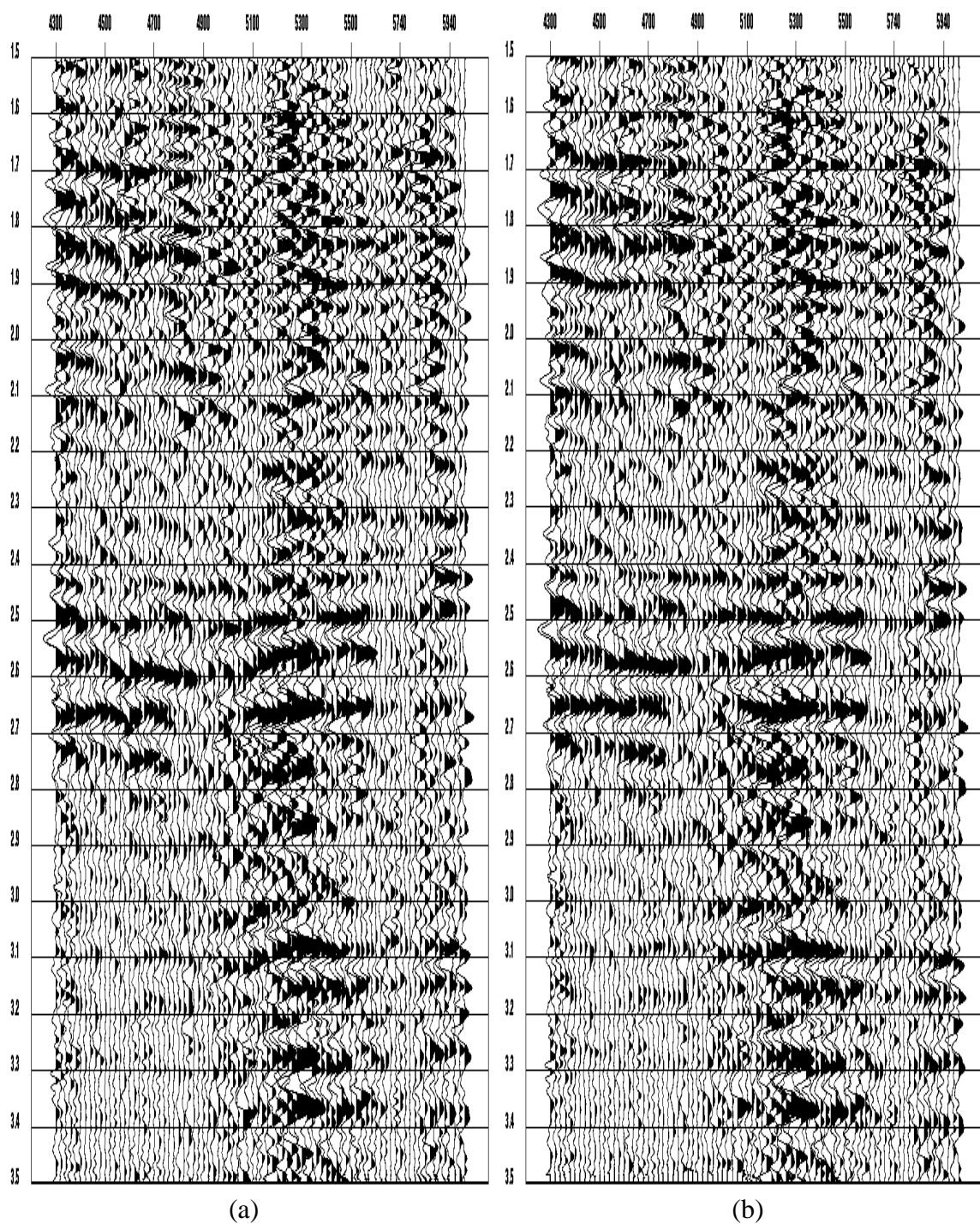
Fig. 4.16. A common-offset plane at 2270 m. (a) Without residual receiver statics. (b) With conventional residual receiver statics.
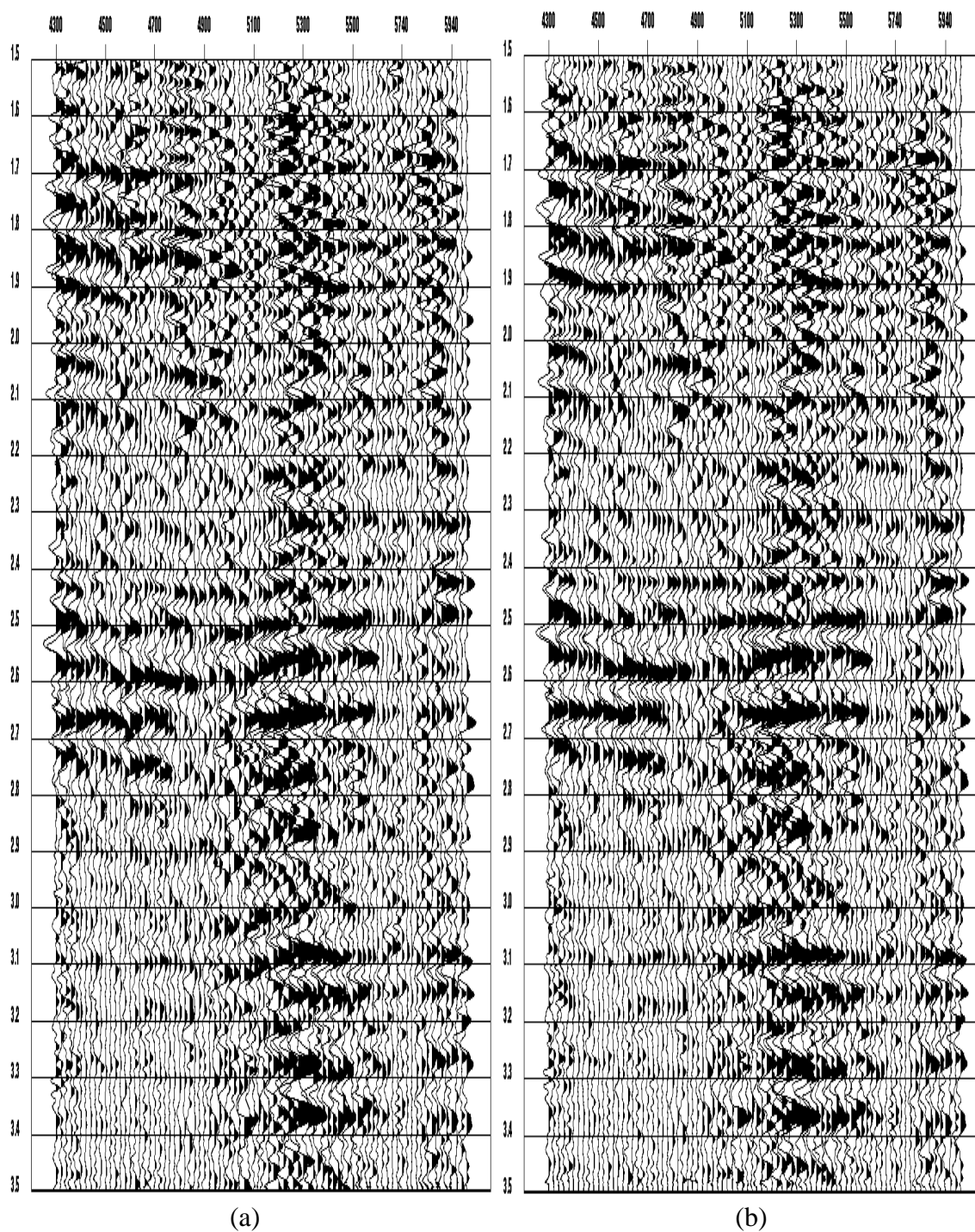
Fig. 4.17. A common-offset plane at 2270 m. (a) Without residual receiver statics. (b) With f-x residual receiver statics.
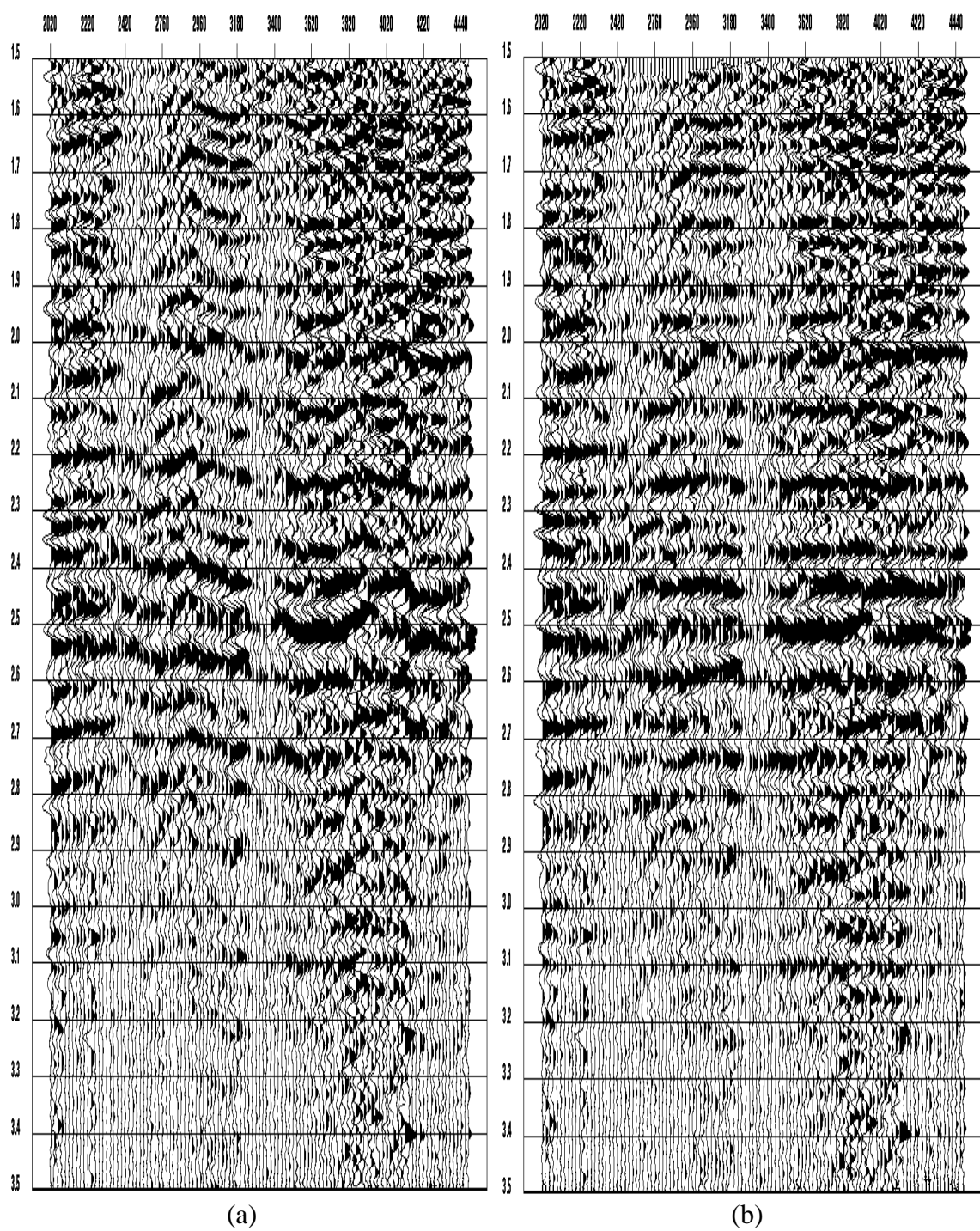
Fig. 4.18. A common-offset plane at -1530 m. (a) Without residual receiver statics. (b) With conventional residual receiver statics.
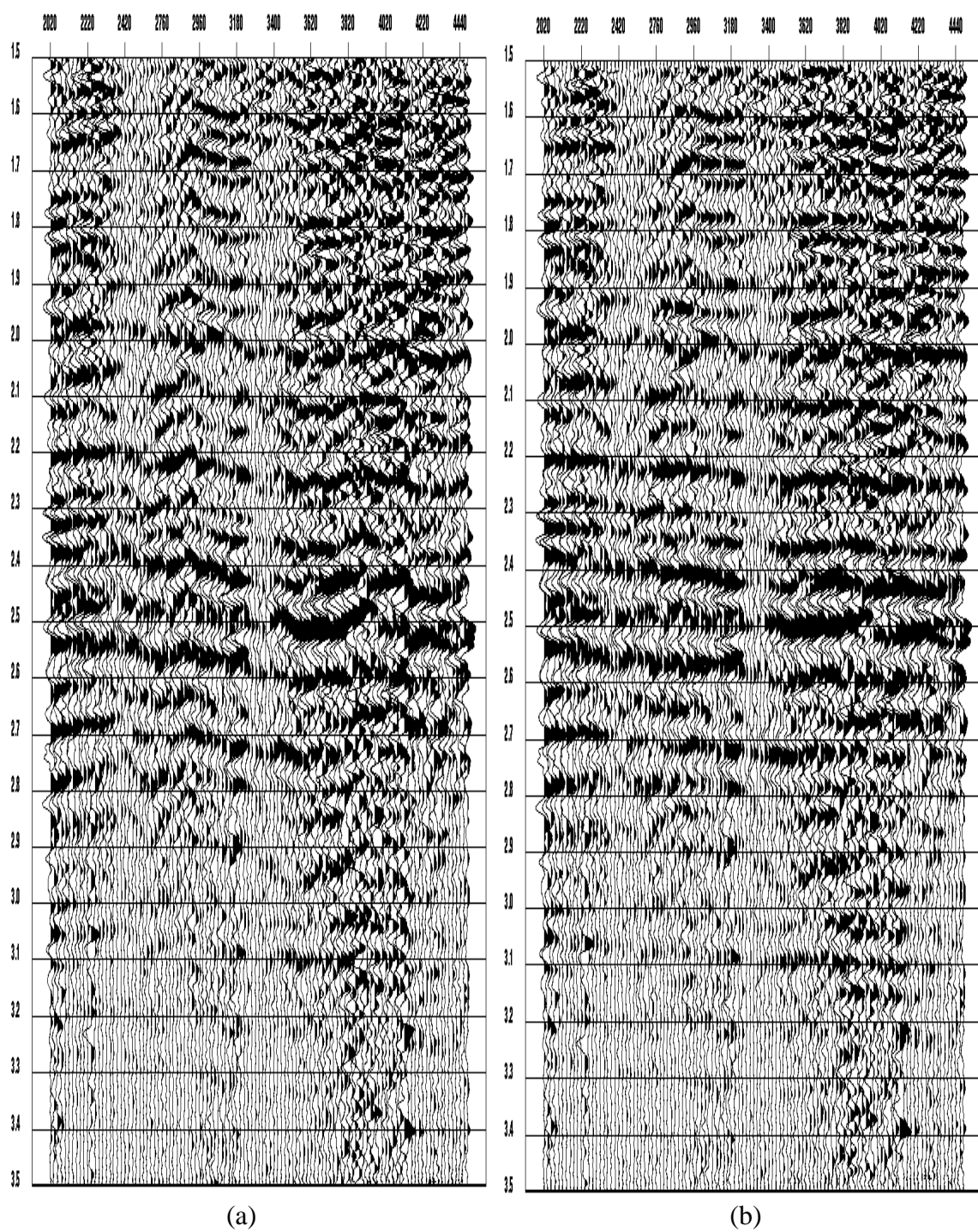
Fig. 4.19. A common-offset plane at -1530 m. (a) Without residual receiver statics. (b) With f-x residual receiver statics.
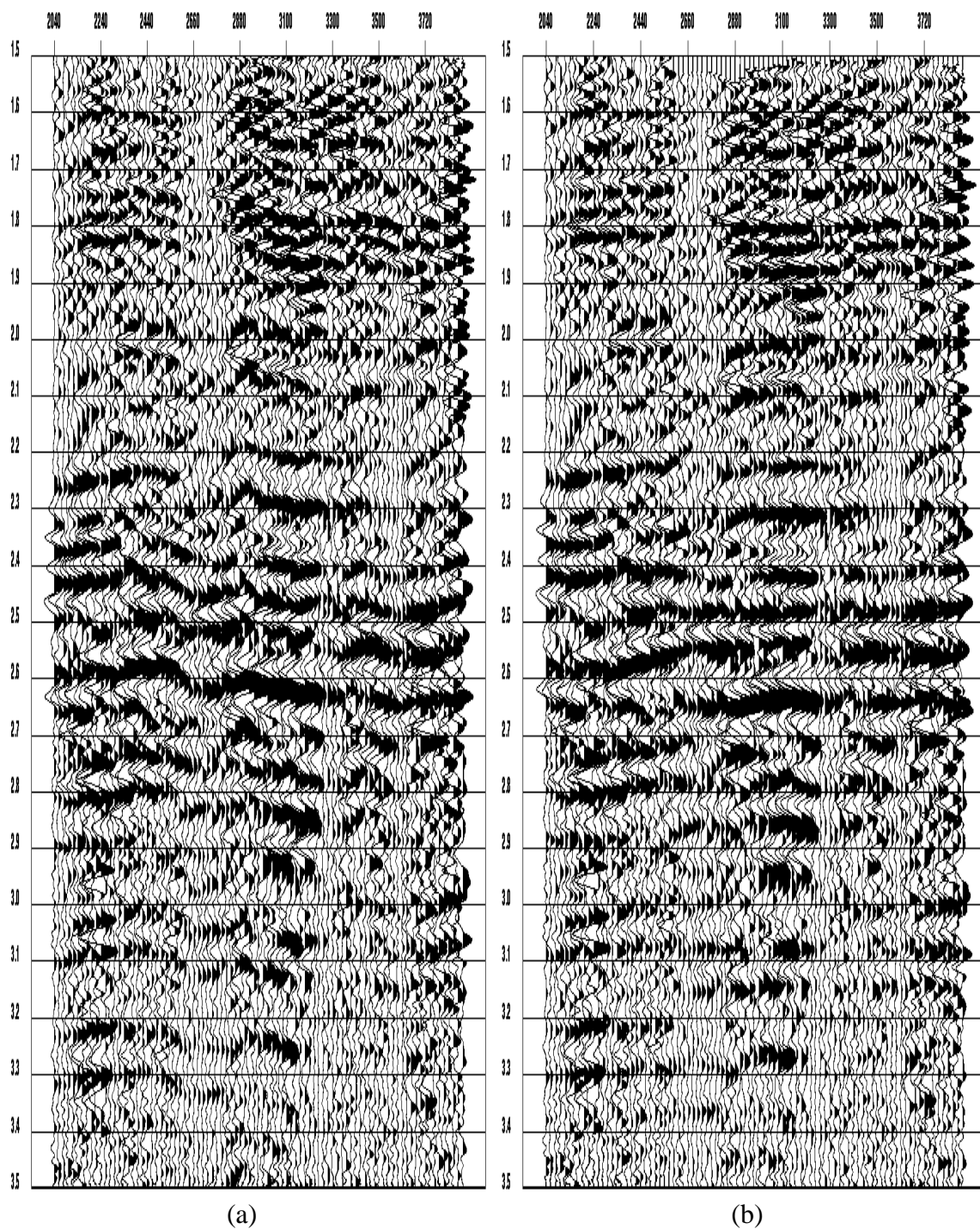
Fig. 4.20. A common-offset plane at -2130 m. (a) Without residual receiver statics. (b) With conventional residual receiver statics.
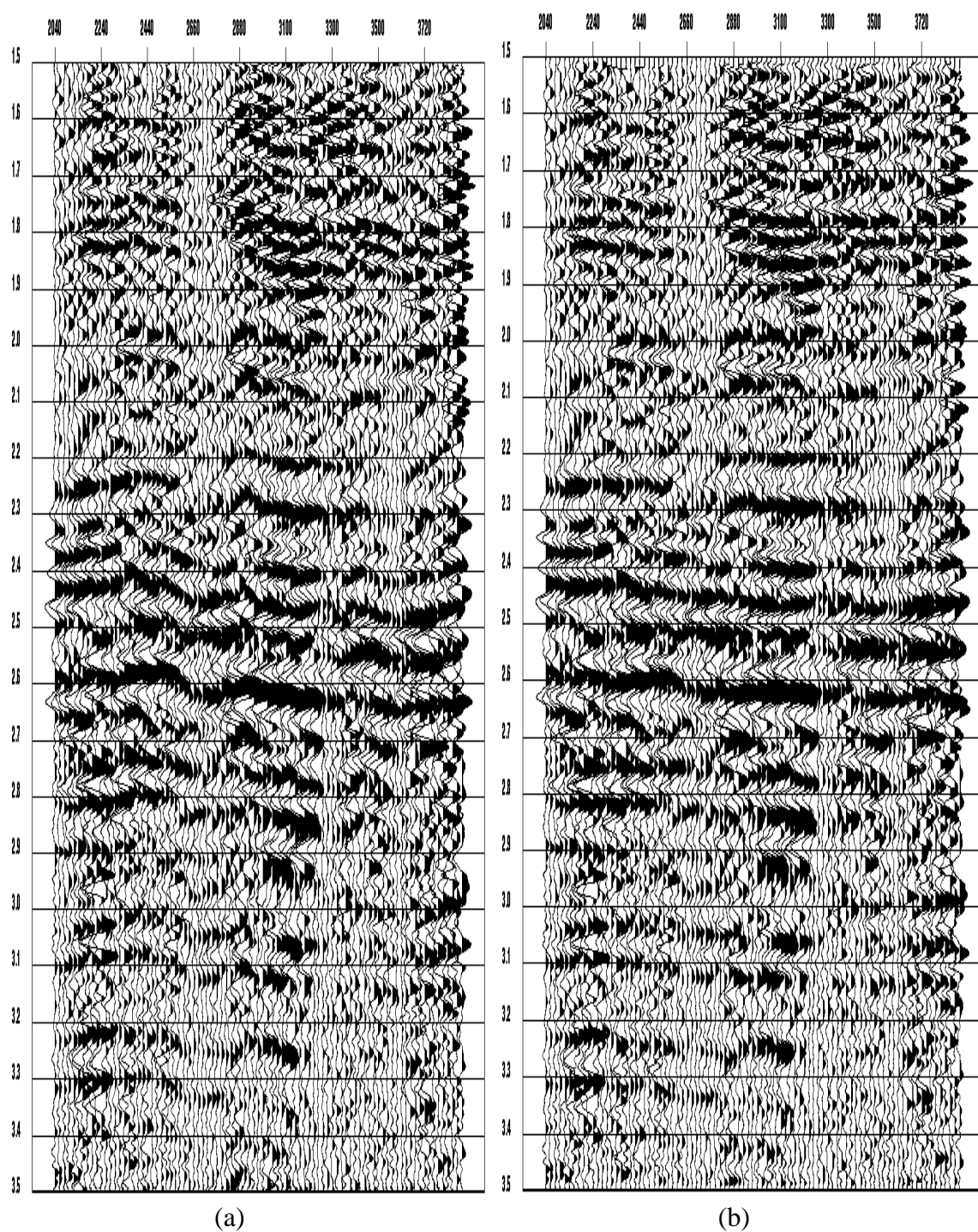
Fig. 4.21. A common-offset plane at -2130 m. (a) Without residual receiver statics. (b) With f-x residual receiver statics.
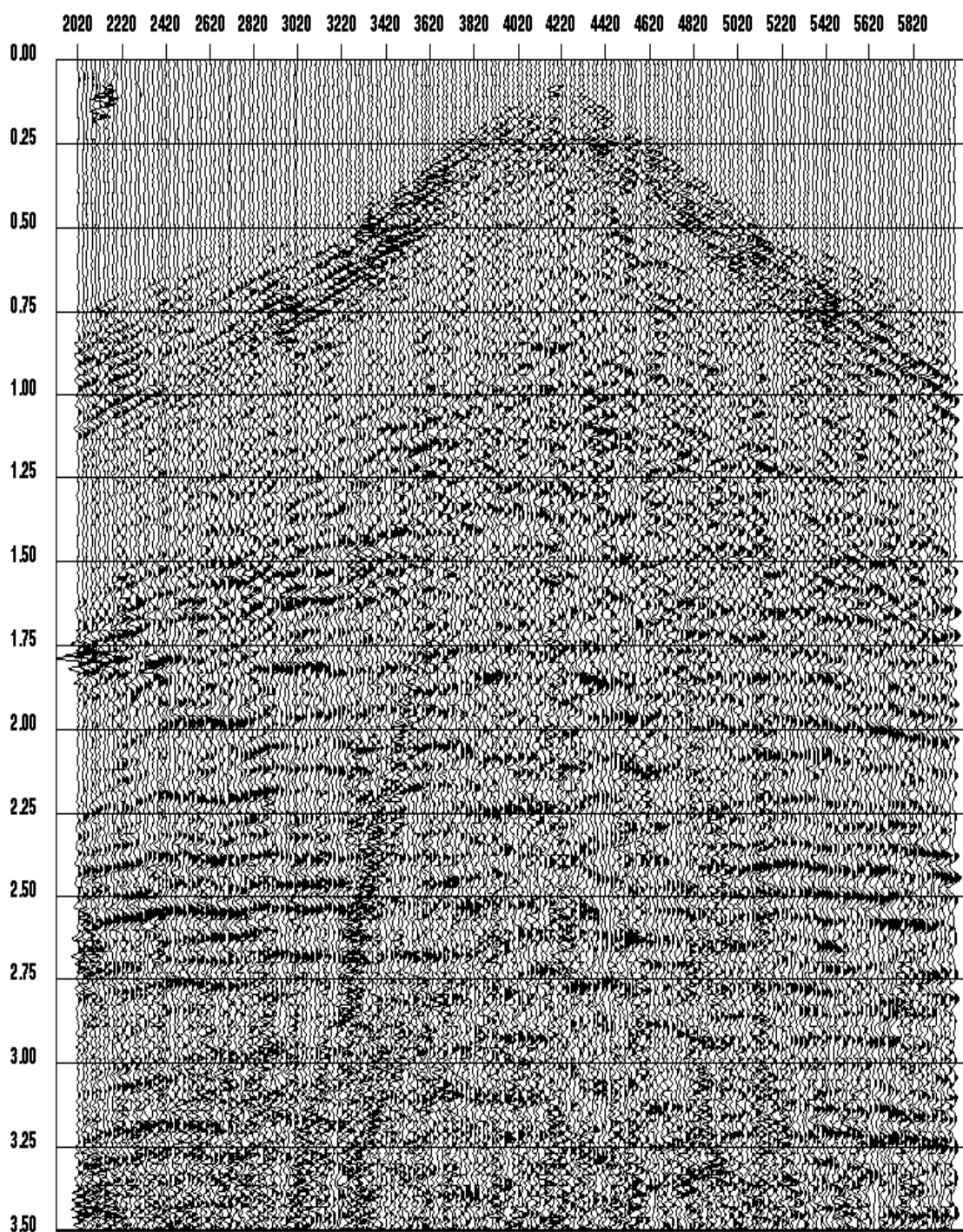
Fig. 4.22. Shot record at 4180 without residual receiver statics applied.

displays a shot record at station 4180 without residual receiver statics applied. Figures 4.23 and 4.24 are the same shot record after the application of conventional and f-x statics respectively. Both statics improve the smoothness of the reflections, except for a discontinuity at station 2600 in the conventional statics result. The next three figures (Figures 4.25 to 4.27) show the same comparison for a shot at station 5120, where the same observations hold.

The final definitive observation stage is the receiver stack domain. Figure 4.28 displays the receiver stack without residual receiver statics application. Figure 4.29 shows receiver stack with the conventional statics applied. From this figure it is concluded that statics are generally properly resolved except at the vicinity of station 2600. Note that although the raw receiver stack is wavy around station 2600, no discontinuity is seen there. Figure 4.30 shows a receiver stack with f-x statics applied. It is observed that the coherency of events is improved, without a discontinuity at station 2600.

4.5 Discussion

From the previous examples one can see that the reflector smoothness condition is powerful enough to allow a robust statics estimation procedure. Since this procedure operates in the common-offset domain, no prior NMO velocity information is required and hence the approach is deemed suitable for the studies of converted P-S mode data. Note that although an ACCP stack is displayed in Figure 4.14, the associated statics are totally inde-
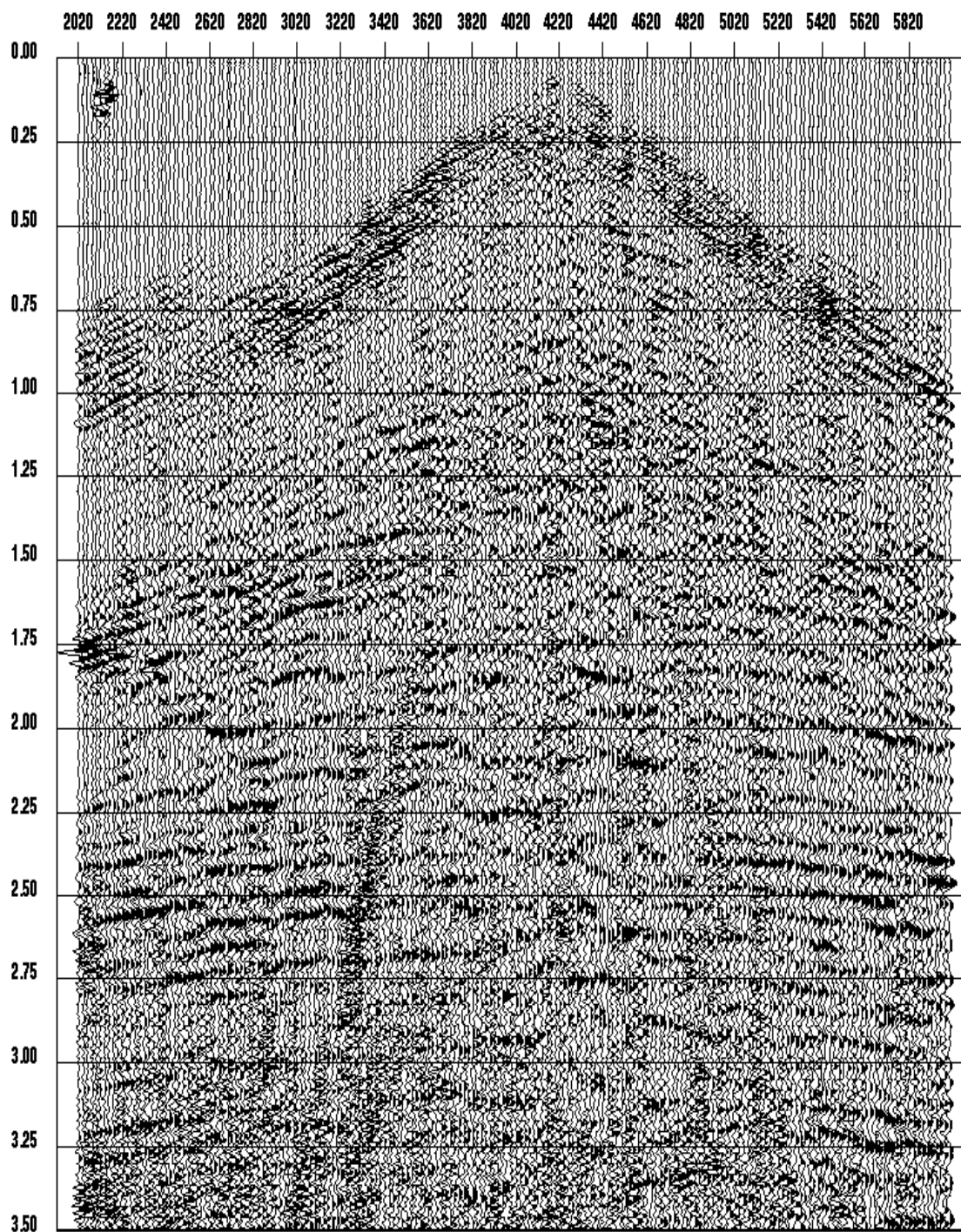
Fig. 4.23. Shot record at 4180 with conventional residual receiver statics applied.
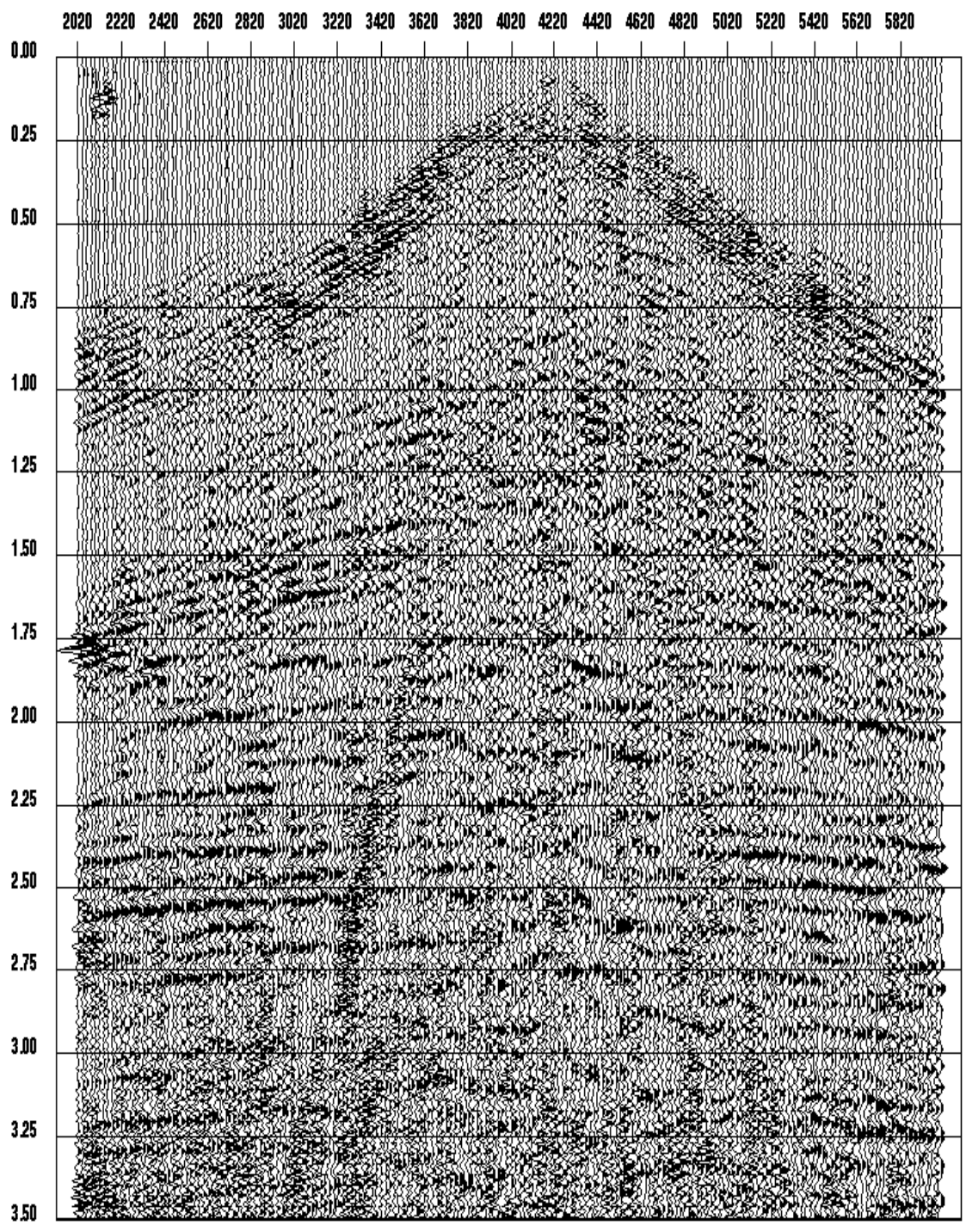
Fig. 4.24. Shot record at 4180 with f-x residual receiver statics applied.
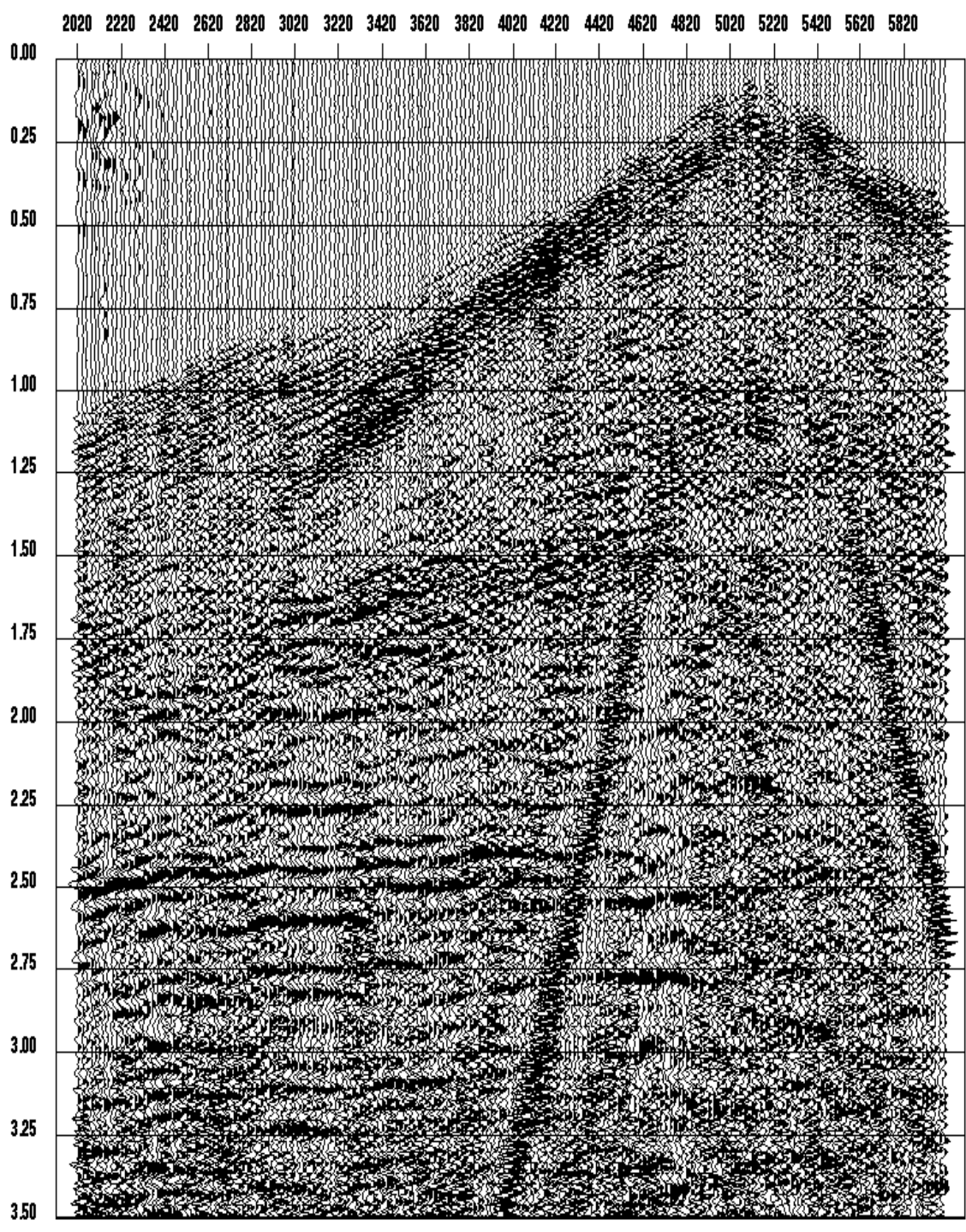
Fig. 4.25. Shot record at 5120 without residual receiver statics applied.
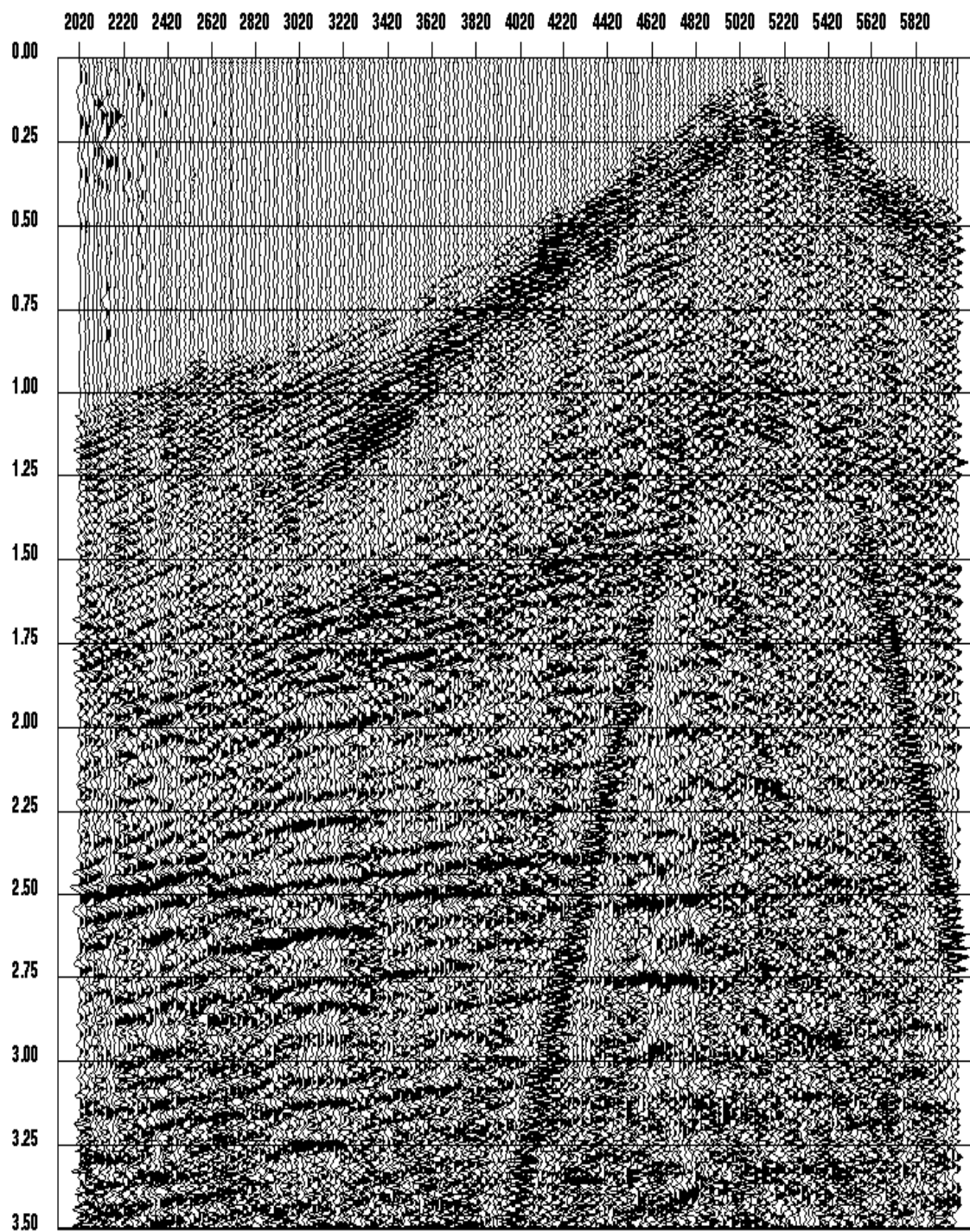
Fig. 4.26. Shot record at 5120 with conventional residual receiver statics applied.
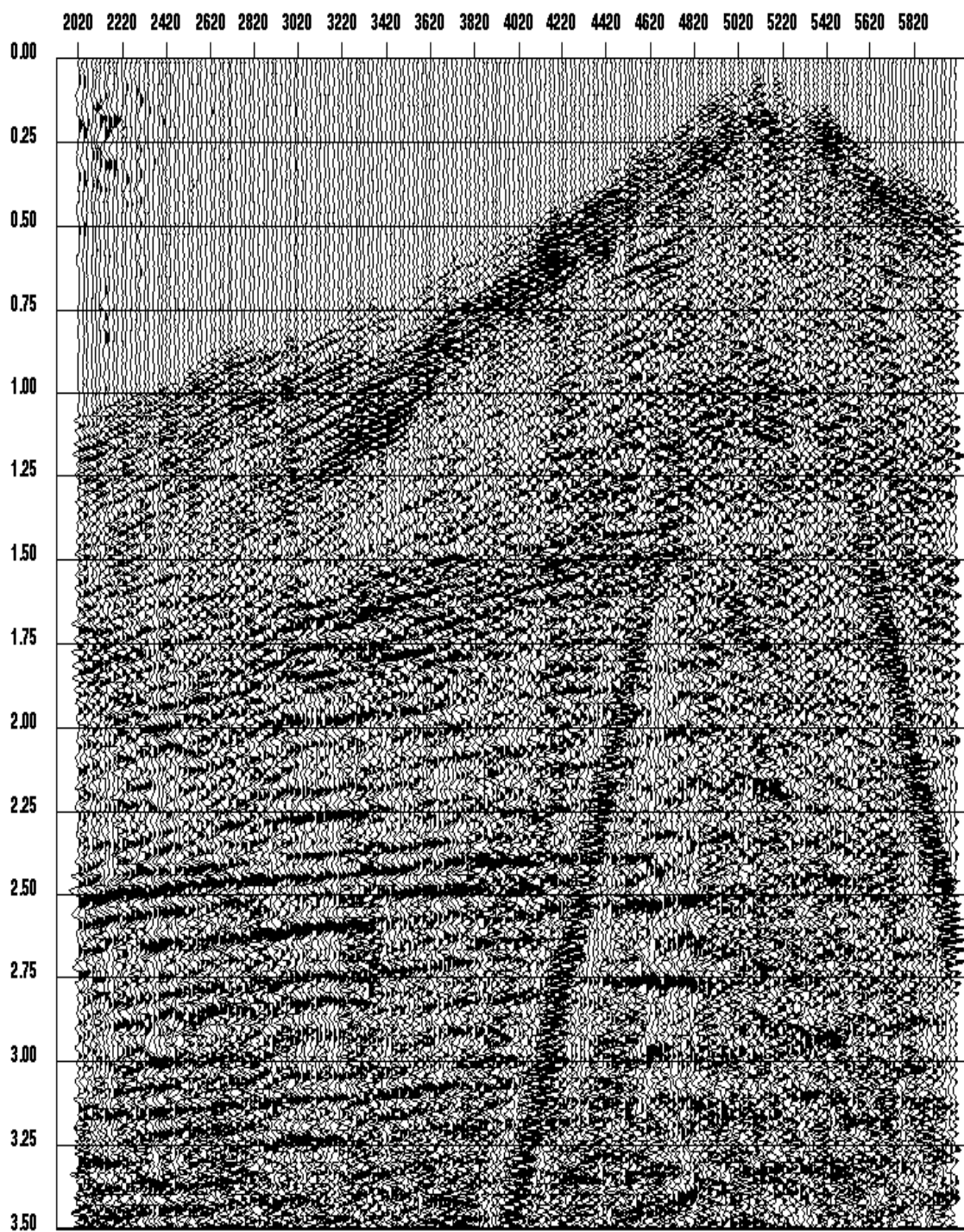
Fig. 4.27. Shot record at 5120 with f-x residual receiver statics applied.
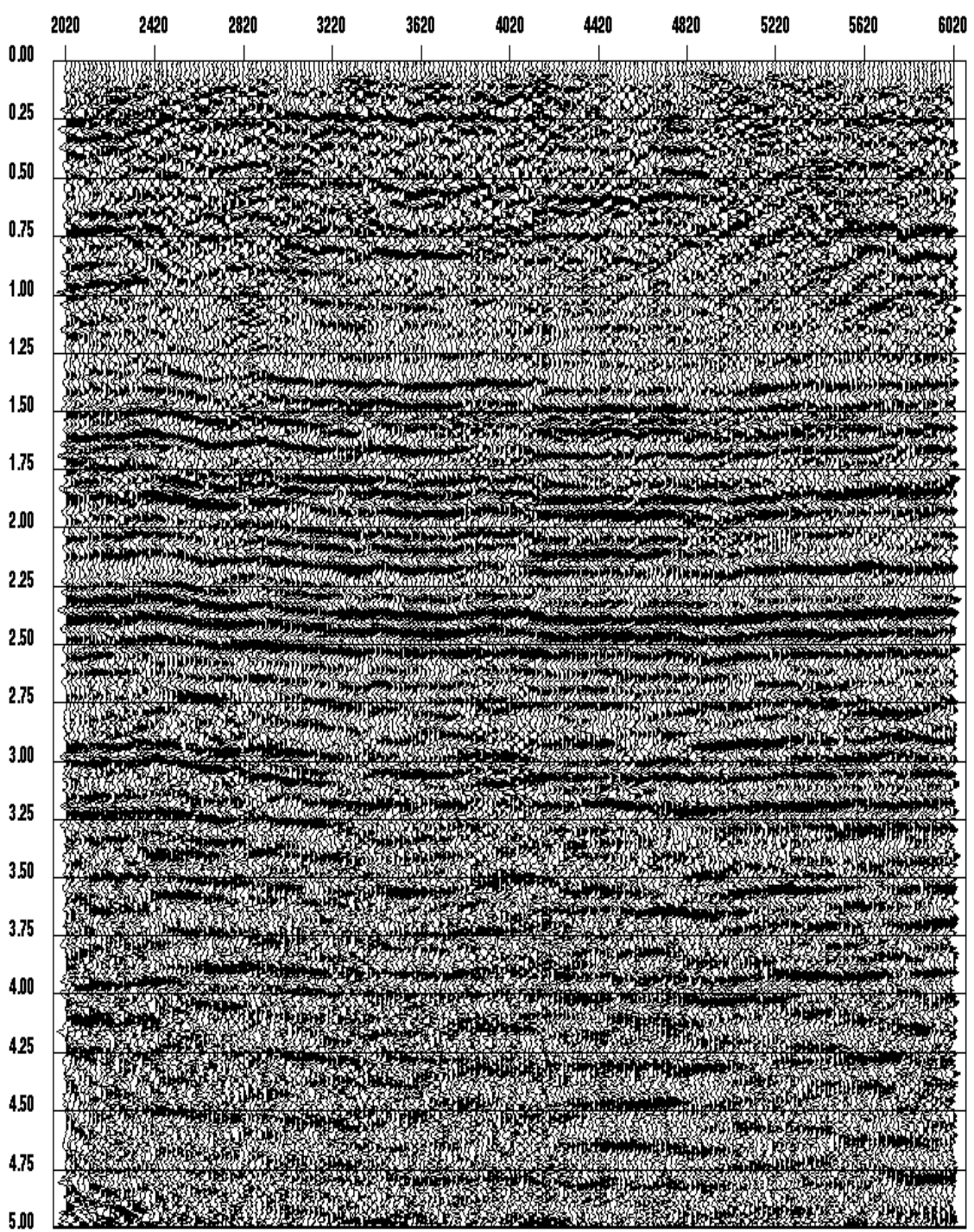
Fig. 4.28. Receiver stack without residual receiver statics.
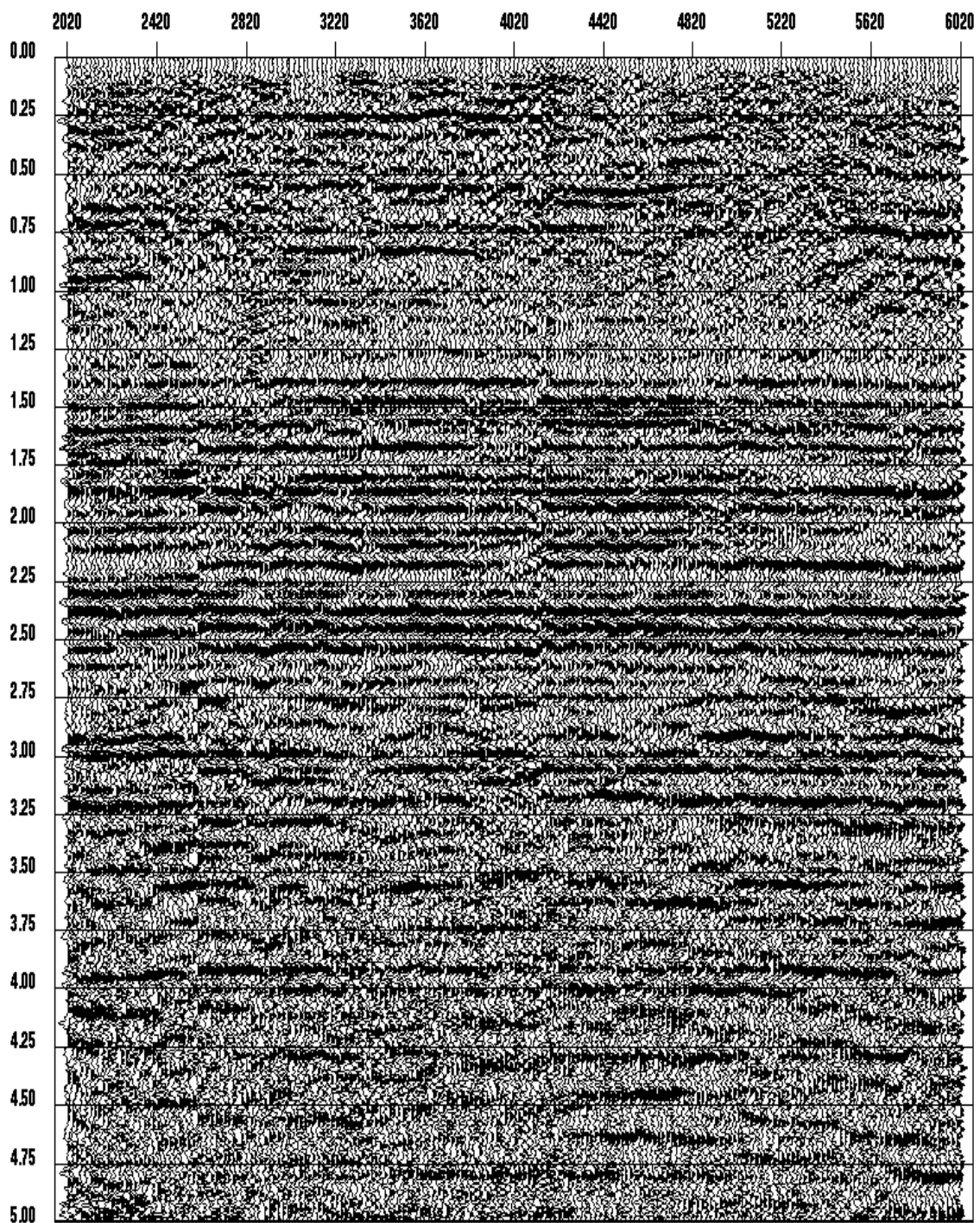
Fig. 4.29. Receiver stack with residual statics based on the Ronen and Claerbout algorithm. Cycle skipping is clearly seen at station 2600.
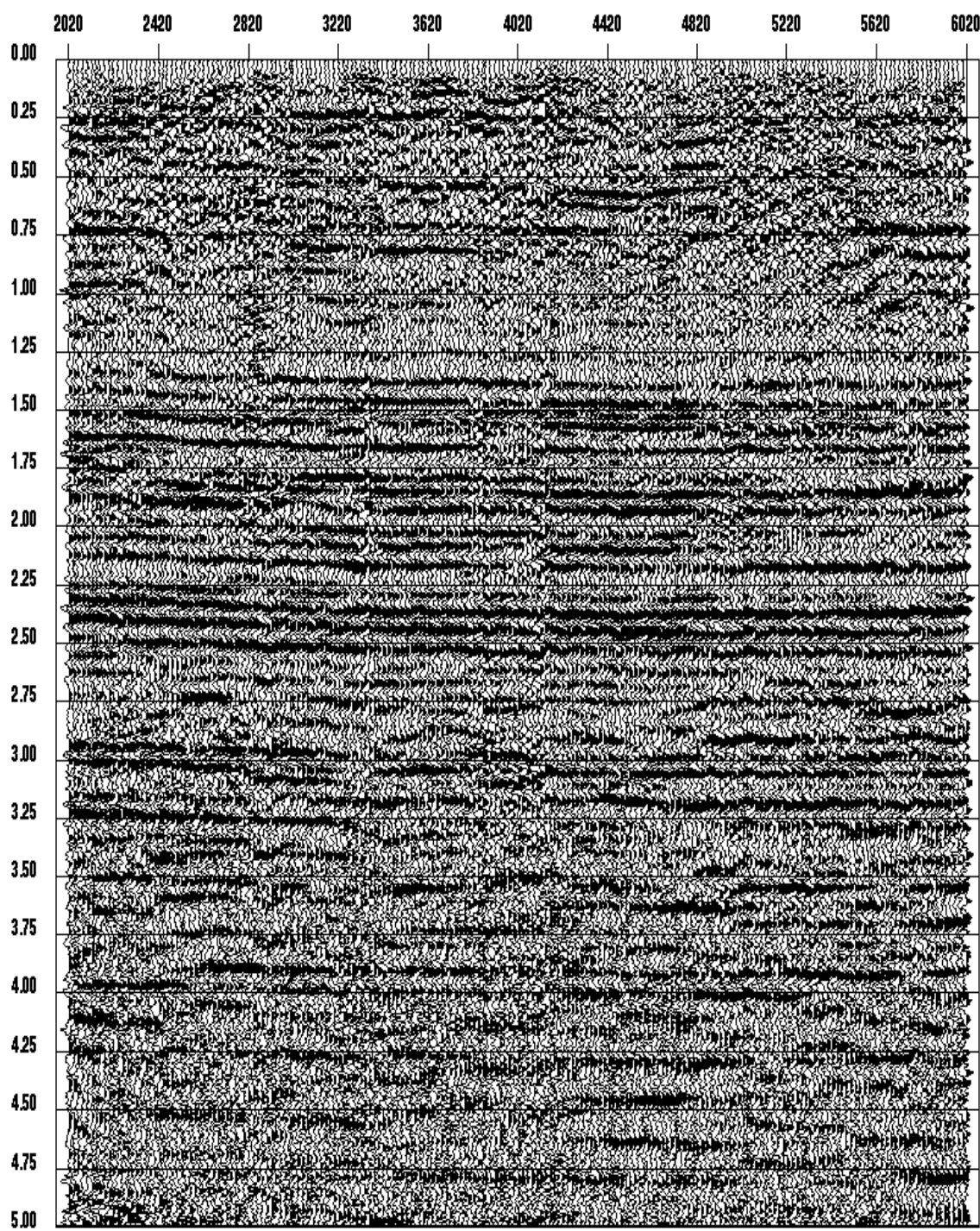
Fig. 4.30. Receiver stack with residual receiver statics based on f-x statics.

pendent of ACCP binning. Conventional statics routine introduce a discontinuity while the f-x procedure gives a more plausible and smoother section.

Unfortunately, the method in its current form is not applicable to 3-D data, especially in land 3-D. In the 2-D survey, the data are normally acquired quite regularly, and a common-offset plane is easily gathered. However, irregular shooting may make common-offset planes binning difficult.

Chapter 5   P-S time migration and migration velocity analysis

5.1 Introduction

Stacking velocity analysis is a powerful and popular tool in processing P-P data. Tessmer and Behle (1988) extended Taner and Koehler's approach (1969) and derived a series expansion for the P-S traveltime in a horizontally layered medium. Their conclusion is that a conventional stacking velocity procedure can be applied to determine P-S stacking velocities, provided these data have a limited offset range and are sorted into CCP (common conversion point) gathers. Since CCP gathering requires prior knowledge of α / β ratios, this approach encounters obvious difficulties.

In a subsequent work, assuming a constant velocity environment, Harrison (1992) proposed P-S DMO as a possible asymmetric travel-path binning solution. This method is elegant but has limited applicability for complex structures. As well, it is expensive and requires an iterative velocity analysis procedure. For improving the interpretability of converted-wave data, prestack time migration processing of P-S data seems the next logical step.

Over the past two decades, migration velocity analysis (MVA) both in time and depth domains has been successfully applied to P-wave reflection data (Gardner et al, 1974, Taner, 1979, Reshef, 1992). In this chapter, a P-S time migration velocity analysis technique is introduced and investigated. It is found that the effort involved in calculating RMS migra-

tion velocities for P-S and P-P data are similar, with no special effort required to account for the asymmetric ray path.

Once the migration velocity is found at selected locations, the estimated velocity field is used to migrate the whole data volume to form migrated gathers. The final image is then obtained by stacking the migrated gathers.

The theory developed suggests that P-S MVA and subsequent P-S time migration are generally less valid than similar algorithms applicable strictly to P-P reflection data. In particular, the applicability of the exploding reflector model to P-S time migration is questionable. One result of this is that the effective estimated S-wave migration velocity field generally does not match the velocity field estimated from an S-S reflection data set. From these results, it seems that depth migration is the proper solution to P-S processing. Unfortunately, at this time the industry is generally more accustomed to the interpretation of time sections. But this may well change in the future.

Finally, the examples discussed in this chapter use a 2-D synthetic data created by finite difference elastic modeling, as well as the Blackfoot data set described previously.

5.2 Theory

The following discussion is divided into two parts. In the first part, the RMS velocity Vp/Vs ratio (γ_{rms}), is defined in a manner allowing comparison to the ratio γ of the P and

S interval velocities (α and β respectively), where $\gamma = \alpha/\beta$. In the second part, the P-S traveltime relationship is derived. It is shown that migration velocity analysis involves a two-parameter search. These parameters are related to the P- and S- wave RMS velocity ratio and velocity heterogeneity factors. Subsequent introduction of a single parameter approximation γ_{mig} simplifies the migration velocity analysis to a single parameter search.

5.2.1 γ_{rms} (RMS Vp/Vs ratio) and vertical traveltime

We define a layered earth model with layer thicknesses Δz_i, and P- and S-wave interval velocities of the ith uniform layer, α_i and β_i respectively. V_{pn} and V_{sn} are defined as P- and S-wave RMS velocities from the surface down to the bottom of the nth layer:

$$
\begin{aligned}
V_{pn}^{2} &= \frac{\sum_{i=1}^{n} \alpha_i^2 \Delta t_i}{\sum_{i=1}^{n} \Delta t_i} \\[2ex]
&= \frac{\sum_{i=1}^{n} \alpha_i \Delta z_i}{\sum_{i=1}^{n} \Delta t_i} \\[2ex]
&= \frac{\sum_{i=1}^{n} \alpha_i \Delta z_i}{T_{pn}}
\end{aligned}
\tag{5.1}
$$

where $\Delta t_i = \dfrac{\Delta z_i}{\alpha_i}$;

$$T_{pn} = \sum_{i=1}^{n} \Delta t_i \text{ is the one-way P-wave normal ray traveltime to the bottom of the } n^{\text{th}}$$

layer.

Similarly:

$$V_{sn}^{2} = \frac{\displaystyle\sum_{i=1}^{n} \beta_i \Delta z_i}{T_{sn}} \tag{5.2}$$

where T_{sn} is the one-way S-wave normal ray traveltime to the bottom of the nth layer.

For subsequent notation ease, we will omit the subscript 'n' from following equations, with the implicit understanding that the interface 'n' is defined from the summation limits, and is the same for both P and S raypaths.

Define γ_{rms} as: $\gamma_{rms} = V_p / V_s$

therefore,

$$\gamma^2_{rms} = \frac{V_p^2}{V_s^2}$$

$$= \frac{T_s \sum_{i=1}^{n} \alpha_i \Delta z_i}{T_p \sum_{i=1}^{n} \beta_i \Delta z_i} \qquad (\mathbf{5.3})$$

Also, equation (5.1) can be re-written as:

$$V_p^2 T_p = \sum_{i=1}^{n} \alpha_i \Delta z_i$$

$$V_p Z_p = \sum_{i=1}^{n} \alpha_i \Delta z_i$$

$$V_p = \frac{\sum_{i=1}^{n} \alpha_i \Delta z_i}{Z_p} \qquad (\mathbf{5.4})$$

where Z_p has been defined as: $Z_p = V_p T_p$.

Note that Z_p is a pseudo-depth, and only under very special circumstances (such as a constant velocity medium) will it equal true depth.

Similarly, equation (5.2) can be rewritten as:

$$V_s = \frac{\sum_{i=1}^{n} \beta_i \Delta z_i}{Z_s} \qquad (\mathbf{5.5})$$

with $Z_s = V_s T_s$.

Again, Z_s is a pseudo-depth and may not equal Z_p.

Therefore:

$$\gamma_{rms} = \frac{Z_s \sum_{i=1}^{n} \alpha_i \Delta z_i}{Z_p \sum_{i=1}^{n} \beta_i \Delta z_i} \qquad (5.6)$$

If $Z_p = Z_s$, then the above equation becomes

$$\gamma_{rms} = \frac{\sum_{i=1}^{n} \alpha_i \Delta z_i}{\sum_{i=1}^{n} \beta_i \Delta z_i} \qquad (5.7)$$

Substituting equation (5.7) into equation (5.3),

$$\gamma_{rms}^2 = \frac{T_s}{T_p}\gamma_{rms}$$

$$\gamma_{rms} = \frac{T_s}{T_p} \qquad (5.8)$$

Now define $T_{ps}=T_p+T_s$ as two-way P-S traveltime (i.e., one-way P-wave traveltime from the surface to a given flat reflector plus one-way S-wave traveltime from the same reflector back to the surface), $T_{pp}=T_p+T_p$ as two-way P-wave traveltime and $T_{ss}=T_s+T_s$ as two-way S-wave. After some re-arrangement, equation (5.8) becomes,

$$\frac{T_{ps}}{T_{pp}} = \frac{1 + \gamma_{rms}}{2} \qquad (5.9)$$

Note that equation (5.9) can be used to estimate γ_{rms}, provided that $Z_p = Z_s$. The quality of this assumption motivates the following discussion.

5.2.2 Heterogeneity factors, true and pseudo depth

The average P-wave velocity in time, $\overline{V}_p$, is defined as,

$$\overline{V}_p = \frac{\sum\limits_{i=1}^{n} \alpha_i \Delta t_i}{\sum\limits_{i=1}^{n} \Delta t_i}$$

$$\overline{V}_p T_p = \sum\limits_{i=1}^{n} \alpha_i \Delta t_i$$

$$\overline{V}_p T_p = \sum\limits_{i=1}^{n} \Delta z_i$$

$$\overline{V}_p T_p = Z_T \qquad (5.10)$$

with $Z_T = \sum\limits_{i=1}^{n} \Delta z_i$, the true depth to the bottom of the nth layer.

Al-Chalabi (1974) shows that for a 1-D layered earth,

$$\frac{V_p}{\overline{V}_p} = (1 + g_p)^{1/2} \qquad (5.11)$$

where g_p is a measure of the P-wave velocity heterogeneity:

$$g_p = \frac{1}{Z_T^2} \sum_{k=1}^{n-1} \Delta z_k \sum_{j=k+1}^{n} \Delta z_j \frac{(\alpha_k - \alpha_j)^2}{\alpha_k \alpha_j} \qquad (5.12)$$

Similarly,

$$\frac{V_s}{\bar{V}_s} = (1 + g_s)^{1/2} \qquad (5.13)$$

where $g_s = \dfrac{1}{Z_T^2} \displaystyle\sum_{k=1}^{n-1} \Delta z_k \sum_{j=k+1}^{n} \Delta z_j \dfrac{(\beta_k - \beta_j)^2}{\beta_k \beta_j}$

Therefore

$$V_p = \bar{V}_p (1 + g_p)^{1/2} \qquad (5.14)$$

$$V_s = \bar{V}_s (1 + g_s)^{1/2} \qquad (5.15)$$

The heterogeneity quantities, g_p and g_s, can be positive or zero, and are equal to zero only when all of the layers have the same velocity. Their values are independent of the order of layering to the current layer. Therefore, we have $V_p \geq \bar{V}_p$ and $V_s \geq \bar{V}_s$.

Multiply both sides of equation (5.14) by T_p,

$$V_p T_p = \bar{V}_p T_p (1 + g_p)^{1/2}$$
$$Z_p = Z_T (1 + g_p)^{1/2} \qquad (5.16)$$

Similarly,

$$Z_s = Z_T (1 + g_s)^{1/2} \qquad\qquad (\textbf{5.17})$$

Therefore we also have $Z_p \geq Z_T$ and $Z_s \geq Z_T$. The equality for each holds when g_p, or g_s is zero respectively.

Also, if $g_p \neq g_s$, then $Z_p \neq Z_s$. For example, assume that in the near surface, the only heterogeneity factor is due to the water table. The P-wave velocity above the top of the water table is different from below the water table. In this case $Z_p > Z_T$, because g_p is not zero. Conversely, S-wave velocity is largely unaffected by water saturation, therefore g_s is close to zero, and it is expected that $Z_s \approx Z_T$. Hence, in this situation we have $Z_p > Z_s$.

One of the advantages of using the RMS velocity to process P-P reflection data is that if the algorithm is applicable to one uniform layer, the same algorithm can be generalized to the multi-layer case. This advantage may not be true for P-S converted-wave data since in general $Z_p \neq Z_s$ for the multi-layer case.

5.2.3 Relating P-P to P-S time for non-zero heterogeneity factors

Substitute equations (5.15) and (5.16) into equation (5.6),

$$\gamma_{rms} = \frac{(1 + g_s)^{1/2} \sum_{i=1}^{n} \alpha_i \Delta z_i}{(1 + g_p)^{1/2} \sum_{i=1}^{n} \beta_i \Delta z_i}$$

$$\frac{\sum_{i=1}^{n} \alpha_i \Delta z_i}{\sum_{i=1}^{n} \beta_i \Delta z_i} = \gamma_{rms} \sqrt{\frac{1 + g_p}{1 + g_s}}$$

$$\frac{\sum_{i=1}^{n} \alpha_i \Delta z_i}{\sum_{i=1}^{n} \beta_i \Delta z_i} = \gamma_{rms} g_\gamma \qquad (5.18)$$

where $g_\gamma = \sqrt{\dfrac{1 + g_p}{1 + g_s}}$.

Note that: $g_\gamma = 1$ if and only if $g_p = g_s$.

From equations (5.11), (5.12) and (5.13), if α_i / β_i are the same for all i, then we have

$g_p = g_s$. Substitute equation (5.18) into equation (5.3),

$$\gamma_{rms}^2 = \frac{T_s}{T_p} \gamma_{rms} g_\gamma$$

$$\frac{T_s}{T_p} = \frac{\gamma_{rms}}{g_\gamma} \qquad (5.19)$$

and equation (5.9) becomes

$$\frac{T_{ps}}{T_{pp}} = \frac{T_p + T_s}{T_p + T_p}$$

$$= \frac{1 + \dfrac{\gamma_{rms}}{g_\gamma}}{2} \qquad\qquad (\textbf{5.20})$$

From equations (5.19) and (5.20), we have:

$$\frac{T_{ps}}{T_{ss}} = \frac{T_{ps}}{2T_s}$$

$$= \frac{T_{ps}}{2T_p \dfrac{\gamma_{rms}}{g_\gamma}}$$

$$= \frac{T_{ps}}{T_{pp}} \Big/ \frac{\gamma_{rms}}{g_\gamma}$$

$$= \frac{1 + \dfrac{\gamma_{rms}}{g_\gamma}}{2} \Big/ \frac{\gamma_{rms}}{g_\gamma} \qquad\qquad (\textbf{5.21})$$

The last two equations show that if $g_\gamma \neq 1$, T_{ps}/T_{pp} and T_{ps}/T_{ss} are not a function of γ_{rms} alone and therefore, knowing γ_{rms} is not sufficient to tie P-S to P-P or P-S to S-S stacked sections.

Note that the heterogeneity factor defined in equations (5.11) or (5.12) is measured along the vertical raypath. If the heterogeneity factor is measured along the actual path the ray travelled in a layered medium, then due to Snell's law, the factor decreases as the angle of incidence increases. In a limiting case, since the ray spends most of the time in the high-est velocity zone, the factor becomes zero as the angle of incidence approaches to 90 de-

grees. As a result, g_γ measured along the P-S raypth approaches to one as the offset between source and receiver becomes infinity.

5.2.4 P-S traveltime

Figure 5.1a shows a P-S ray path diagram for a depth dependent interval velocity model. The down-going P-wave and up-going S wave are shown again in Figures 5.1b and 5.1c, respectively. Taner and Koehler (1969) use a series expansion to the second power of offset to show that the traveltime of a Snell's law ray in horizontally layered medium can be approximated by a traveltime along a straight ray with the corresponding RMS velocity and offset. With that approximation, the traveltime in Figures 5.1b and 5.1c is practically equal to that described by the straight ray diagrams of Figures 5.1d and 5.1e. From equations (5.10), (5.15) and (5.16), utilization of the RMS velocity pair Vp and Vs in a migration process will result in an inconsistent conversion point pseudo-depth estimation if $g_\gamma \neq 1$, as shown in Figure 5.1f.

Referring to Figure 5.1f and equations (5.20) and (5.21), the double-square-root equation for P-S traveltime can be written as,
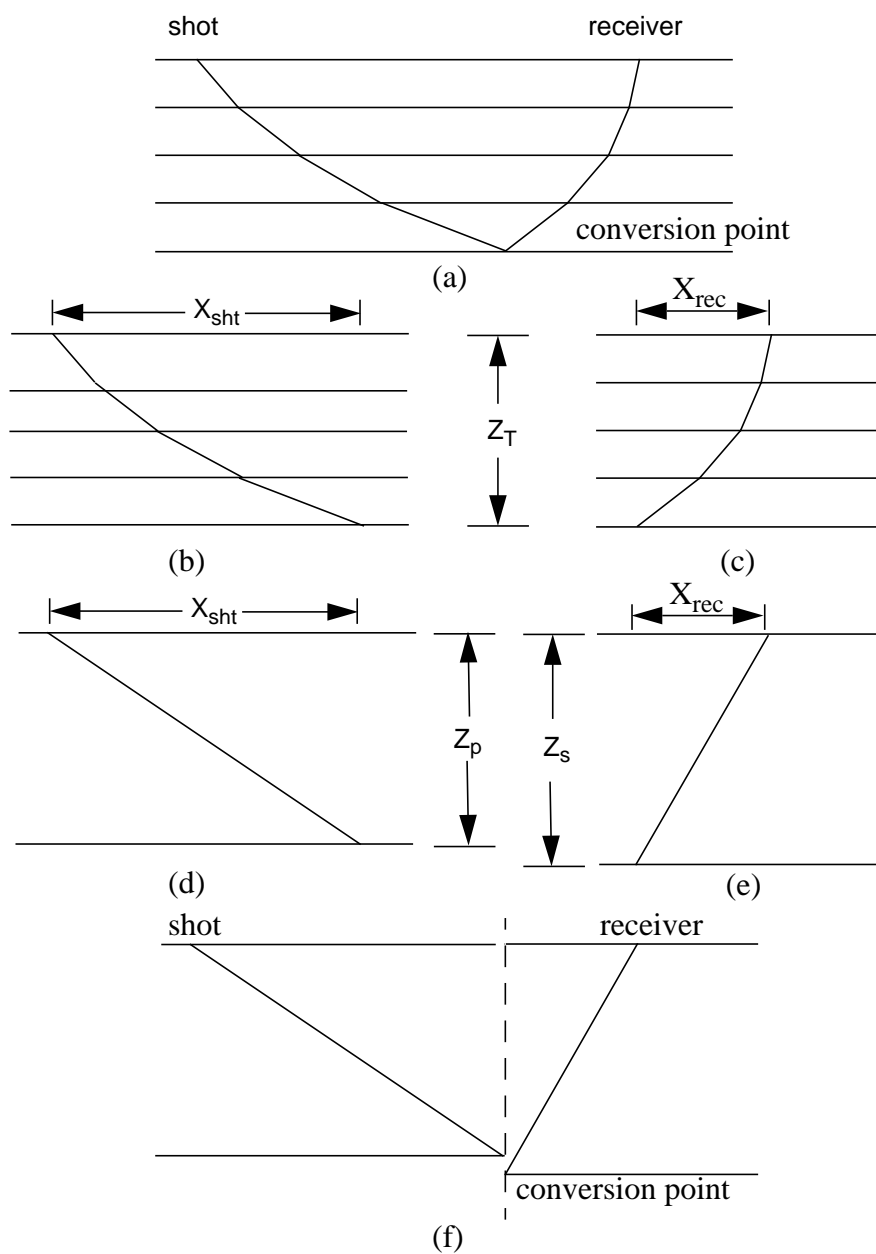
Fig. 5.1. a) P-S raypath model with interval velocity field. b) Down-going P-wave travel (interval velocity field). c) Up-going S-wave travel (interval velocity field). d) Down-going P-wave travel (RMS velocity field). e) Up-going S-wave travel (RMS velocity field). f) P-S raypath model with RMS velocity field. Note that a) and f) are equivalent in terms of the traveltimes and offset.

$$T_{ps}(X_i) = \sqrt{\frac{Z_p^2}{V_p^2} + \frac{X_{sht}^2}{V_p^2}} + \sqrt{\frac{Z_s^2}{V_s^2} + \frac{X_{rec}^2}{V_s^2}}$$

$$= \sqrt{\frac{T_{pp}^2}{4} + \frac{X_{sht}^2}{V_p^2}} + \sqrt{\frac{T_{ss}^2}{4} + \frac{X_{rec}^2}{V_s^2}}$$

$$= \sqrt{\frac{T_{ps}^2}{\left(1 + \dfrac{\gamma_{rms}}{g_\gamma}\right)^2} + \frac{X_{sht}^2}{V_p^2}} + \sqrt{\frac{\left(\dfrac{\gamma_{rms}}{g_\gamma}T_{ps}\right)^2}{\left(1 + \dfrac{\gamma_{rms}}{g_\gamma}\right)^2} + \frac{X_{rec}^2}{\left(\dfrac{V_p}{\gamma_{rms}}\right)^2}} \qquad (\textbf{5.22})$$

where X_i is the surface location of the conversion point,

X_{sht} is the horizontal distance between the source and the conversion point and

X_{rec} is the horizontal distance between the conversion point and the receiver.

Note that equation (5.22) contains two unknowns, γ_{rms} and g_γ. Therefore, time migration

velocity analysis requires an expensive two-dimensional search for both γ_{rms} and g_γ. To

simplify the migration velocity analysis and the migration, equation (5.22) is approximated

by the following equation with one unknown parameter:

$$T_{ps}(X_i) \approx \sqrt{\frac{T_{ps}^2}{(1 + \gamma_{mig})^2} + \frac{X_{sht}^2}{V_p^2}} + \sqrt{\frac{(\gamma_{mig}T_{ps})^2}{(1 + \gamma_{mig})^2} + \frac{X_{rec}^2}{V_{s,mig}^2}} \qquad (\textbf{5.23})$$

with

$$V_{s,mig} = \frac{V_p}{\gamma_{mig}} \qquad (\textbf{5.24})$$

The unknown parameter γ_{mig} is an effective P-S migration parameter. It is adjusted such that the traveltime described by equation (5.23) best matches the true traveltime curve in a least-squares sense within the observed offset range. By inspecting equations (5.22) and (5.23), one concludes that γ_{mig} lies between γ_{rms}/g_γ and γ_{rms}. In fact, γ_{rms}/g_γ is a small offset approximation to γ_{mig}, while γ_{rms} is a large offset approximation to γ_{mig}. In other words, g_γ affects γ_{mig} more at the near offset than the far offset. When g_γ is equal to 1, γ_{mig} and γ_{rms} will be the same.

Assuming V_p is known, the above equations (5.23) and (5.24) can be used for velocity analysis by migrating the P-S data with different γ_{mig} values and forming image gathers at the selected surface locations. The desired γ_{mig} value at the current P-S time is the one which best flattens the corresponding event on the analyzed image gather. Note that in general, γ_{mig} can not be used to relate P and S-wave velocity. Equation (5.20) suggests that if we can tie an event time on P-S and P-P stacks (or time-migrated stacks), then we can deduce $\dfrac{\gamma_{rms}}{g_\gamma}$. Further utilizing equation (5.22) enables us to estimate γ_{rms}, which can be used to obtain S-wave RMS velocity from P-wave velocity for the same event.

Note that V_p in equation (5.23) is measured at time $2/(1 + \gamma_{mig}) T_{ps}$ rather than at T_{pp}. In other words, equation (5.20) is approximated by,

$$\frac{T_{ps}}{T_{pp}} \approx \frac{1 + \gamma_{mig}}{2} \qquad\qquad (5.25)$$

Therefore, the P-wave velocity used to migrate a P-S reflection at T_{ps} may not be the same as the P-wave velocity corresponding to the P-P reflection for the same event at T_{pp}. In fact, the V_p used in equation (5.23) is an interpolated velocity value at time $2/(1 + \gamma_{mig}) T_{ps}$.

5.3 P-S Migration velocity analysis (MVA)

Based on a Kirchhoff-like migration, the procedure of MVA is summarized as follows:

- for all selected γ_{mig}

    - for all input traces that contribute to the surface location X_i of the analyzed migrated gather

        - for all T_{ps} times

            calculate:

            $$T_{pp} \approx \frac{2 T_{ps}}{1 + \gamma_{mig}} \quad \text{(from 5.25)}$$

            $$V_{s, mig}(T_{ps}) = \frac{V_p(T_{pp})}{\gamma_{mig}(T_{ps})} \quad \text{(from 5.24)}$$

            $$X_{sht} = X_i - \overline{X_{sht}}$$

$$X_{rec} = X_i - \overline{X_{rec}}$$

$$t \approx \sqrt{\frac{T_{ps}^2}{(1 + \gamma_{mig})^2} + \frac{X_{sht}^2}{V_p^2}} + \sqrt{\frac{(\gamma_{mig} T_{ps})^2}{(1 + \gamma_{mig})^2} + \frac{X_{rec}^2}{V_{s,mig}^2}} \quad \text{(from 5.23)}$$

$$\text{DATA\_OUT}(T_{ps}, X_{sht}) = \text{DATA\_OUT}(T_{ps}, X_{sht}) + \text{DATA\_IN}(t, \overline{X_{sht}}, \overline{X_{rec}})$$

$\overline{X_{sht}}$ = shot location of the current trace

$\overline{X_{rec}}$ = receiver location of the current trace

- finish all T_{ps}

- finish all traces

- finish all γ_{mig}

Here, DATA_OUT contains the migrated gathers, and DATA_IN contains the input traces.

Note that, in other to speed up the migration velocity analysis, only the kinematic part of Kirchhoff equation is used.

After the migrated gathers are formed at the selected surface location for a range of γ_{mig} values, γ_{mig} as a function of T_{ps} time is picked based on the flatness of each event. Note that if γ_{mig} is too high, the event curves upwards as the distance from the shot to the analyzed surface location increases. If γ_{mig} is too low, the event curves downwards. Furthermore, the event shifts to the larger shot to analyzed surface location distance as the dip of the event increases.

5.4 P-S prestack time migration

Although most migration velocity estimation procedures use a Kirchhoff like approach with trace-by-trace operation, the final migration of 2-D data is found to be more economical in terms of I/O when performed with common shot migration. Common shot migration uses the imaging condition which states that reflection has occurred when the down and up-going waves coincide. The up-going waves at some depth level are obtained by downward continuation of the receivers within a shot gather. The corresponding down-going waves are represented by an amplitude term (characterizing geometrical spreading) delayed by the straight ray traveltime from the shot location to each of the receiver projections at the same depth level. The image at each depth is produced by correlating the up and the down going waves and finding the reflection response at time zero (Claerbout, 1985).

Rewriting equation (5.23) in terms of a pseudo-depth we replace T_{ps} with a single common P-S pseudo-depth Z_{ps}:

$$ Z_{ps} = \frac{V_p T_{ps}}{1 + \gamma_{mig}} \qquad (\textbf{5.26}) $$

Please note that Z_{ps} resides between Z_p and Z_s.

Multiply both sides of equation (5.26) $\dfrac{\gamma_{mig}}{V_p}$, we obtain

$$\frac{\gamma_{mig}T_{ps}}{1 + \gamma_{mig}} = \frac{\gamma_{mig}Z_{ps}}{V_p}$$

$$= \frac{Z_{ps}}{V_{s,\,mig}} \qquad (\,5.27\,)$$

Substitute equations (5.26) and (5.27) into equation (5.23) to get:

$$T_{ps}(X) \approx \sqrt{\frac{Z_{ps}^2}{V_p^2} + \frac{X_{sht}^2}{V_p^2}} + \sqrt{\frac{Z_{ps}^2}{V_{s,\,mig}^2} + \frac{X_{rec}^2}{V_{s,\,mig}^2}} \qquad (\,5.28\,)$$

From equation (5.28) we see that the up-going waves in the RMS approximation (second square root) can be considered to propagate with the velocity $V_{s,\,mig}$, while the down-going waves propagate with the velocity V_p. This leads to a shot-domain P-S migration summarized by the following pseudo-code:

- for each shot S

    - for each T_{ps}

    calculate:

    - $Z_{ps} = \dfrac{V_p T_{ps}}{1 + \gamma_{mig}}$ (from 5.27)

    - using straight rays with V_p, calculate traveltime t_{sr}, from current shot location to

        receiver projection locations X_{rec} at depth Z_{ps}.

    - use distance weights and the calculated traveltime t_{sr} to construct 'effective'

        down-going waves: $D_{z_{ps}}(T, X_{rec}) = V_p t_{sr} \delta(T - t_{sr}, X_{rec})$

- using a phase-shift operator with velocity $V_{s,mig}$, downward continue receivers from the surface to Z_{ps} and obtain upgoing waves $U_{z_{ps}} (T, X_{rec})$ at current level:

$$U_{z_{ps}} (\omega, k_x) = U_0 (\omega, k_x) e^{iz_{ps}\sqrt{\frac{\omega^2}{V_{s,mig}^2} - k_x^2}}$$

  where U_0 is the recorded wavefield at the surface.

- correlate up and down-going waves at zero-lag to obtain reflection response at the current Z_{ps} level, at all locations X_{rec}.

- finish all T_{ps}

- finish all shots

- sort migrated shots to common surface location gathers and stack.

Wang (1997) shows that equation (5.28) can also be implemented based on the equivalent offset migration algorithm.

5.5 Lateral conversion point shift in P-S time migration

Schneider (1978) described zero-offset (P-P) time migration as a set of summations along hyperbolic diffraction curves followed by the placement of the sums at the diffraction apices. The locations of the apices represent the diffraction point locations. In a similar manner, we can consider P-S prestack time migration as summations along the traveltime curves described by equation (5.28) and placing the sums at the apices of the curves.

Hubral (1977) used the shortest traveltime raypath concept or image ray principal to re-

late the locations of the diffraction apices in the time-migrated section to the actual loca-
tions in the earth. He has shown that, kinematically, time-migrated sections are composed
of image ray information. That is, time-migrated event positioning is described by rays that
emanate normal to the surface and obey Snell's law along their travel-path. From the
Snell's law constraint, one can see that if γ values throughout the velocity model are not
constant, or the model is not horizontal layered, the S-wave image ray and P-wave image
ray that coincide at some subsurface point must emanate from different surface locations.

To visualize the situation, consider a model (Figure 5.2) consisting of a ball underlying
a dipping interface. The P- and the S-wave velocities above and below the interface are giv-
en by α_1, β_1 and α_2, β_2, respectively with $\dfrac{\alpha_1}{\beta_1} < \dfrac{\alpha_2}{\beta_2}$. It is obvious that the ball is imaged
at different surface locations depending on P-wave or S-wave data are used in the imaging
process.

It is because the locations of P- and S- image rays at the surface are different, therefore,
the apex of the true P-S traveltime curve for the ball in the model located at an non-zero-
offset. This causes another approximation for using the traveltime curve described by equa-
tion 5.29, for the P-S prestack time migration, which has an apex located at a zero-offset.
As a result of the P-S migration, it is believed, the ball is imaged at a lateral position some-
where between P-P and S-S migrated images.

With the above statements in mind, it is understood that matching P-P and P-S time-mi-

grated data requires both time and space corrections. However, it is assumed that the required spatial corrections are small enough for relatively simple earth models and can be ignored.
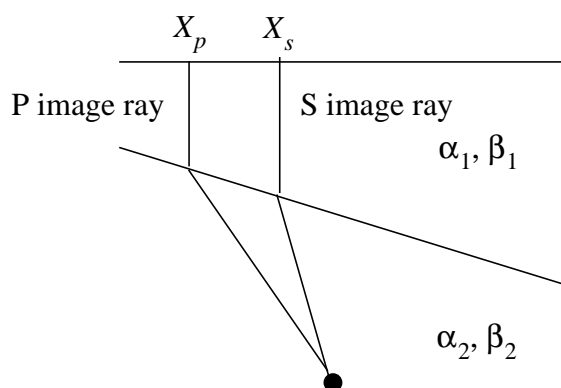
Fig. 5.2. A ball below a dipping layer with $\dfrac{\alpha_1}{\beta_1} < \dfrac{\alpha_2}{\beta_2}$. Hubral (1977) shows that the shortest time ray-path connecting the point diffractor and the surface corresponds to the image ray path. Both P and S image raypaths are shown for P-P and S-S models. The shortest path (up- and-down going ray-path) for P-S model is down-going P image ray-and-up-going S image raypath.

5.6 Synthetic examples

In order to test if the P-S prestack time migration based on the double-square-root equation for a single pseudo-depth (Z_{ps}) model is applicable to structural data, a set of 2-C 2-D prestack gathers is created using a finite-difference elastic modeling program. The model shown in Figure 5.3 consists of a syncline, a dipping layer and an anticline. A uniform explosive point source is simulated at each shot location with both vertical and radial components are recorded at the receiver stations. Each split spread record has 59 receivers, and with 50 meters group spacing. The maximum offset is 1450 metres. Shots are at every sta-
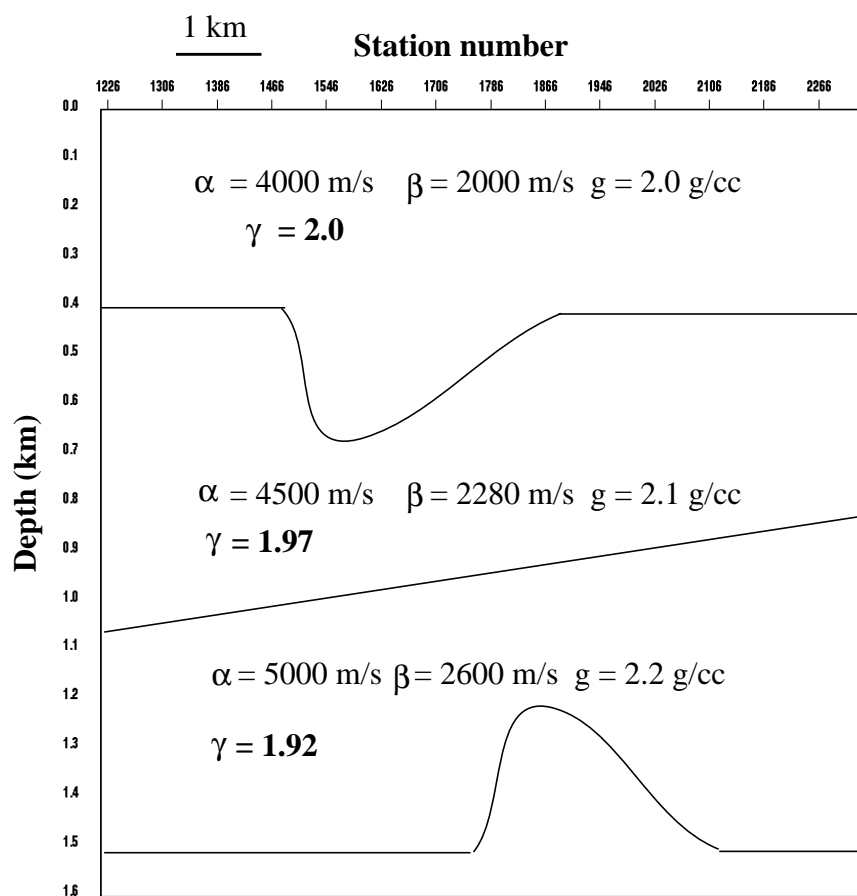
Fig. 5.3. A velocity-density model for the synthetic data set.

tion. 2-C shot record at station 1728 is shown in Figure 5.4. The vertical component is shown on the left, while the radial component is shown on the right. Polarity reversal has been applied to the radial component. The vertical component data are first processed and create different stacks. Figures 5.5, 5.6 and 5.7 are P-wave structural stack, DMO stack and prestack migrated stack. The P-wave migration velocities shown in Table 5.1 are used to preform the P-S migration velocity analysis with different γ_{mig}. Shown in Figure 5.8 are the image gathers at station 1683. Figure 5.8a shows the trial γ_{mig} is too low for all three events. Figure 5.8c shows the trial γ_{mig} is too high for all three events. Figure 5.8b shows the proper γ_{mig} with exception of slightly lower for the first event. A constant γ_{mig} of 1.95 is chosen to migrate all the shots and stack all the common surface location image gathers to produce the final migrated P-S stack in P-S and P-P times (Figures 5.9 and 5.10). The conversion of P-S into P-P times is based on equation (5.25) with $\gamma_{mig} = 1.95$. It is noted that the P-S migrated stack section in P-P times is practically the same as the P-P migrated stack section shown in Figure 5.7, in terms of the two-way times. Since the γ_{mig} is relatively constant in the synthetic model, it is expected that $g_\gamma \approx 1$ (at station 1306, g_γ at the bottom of the third layer is around 0.999), therefore the conversion of the P-S times into P-P times using equation 5.26 is adequate. In the next synthetic model, the S-velocity model is modified such that the g_p and g_s are sufficiently different for the third layer, so that the tie between the P-P and P-S migrated stacks is not good for the third layer.

The new velocity model is shown in Figure 5.11. 2-C shot record at station 1728 is
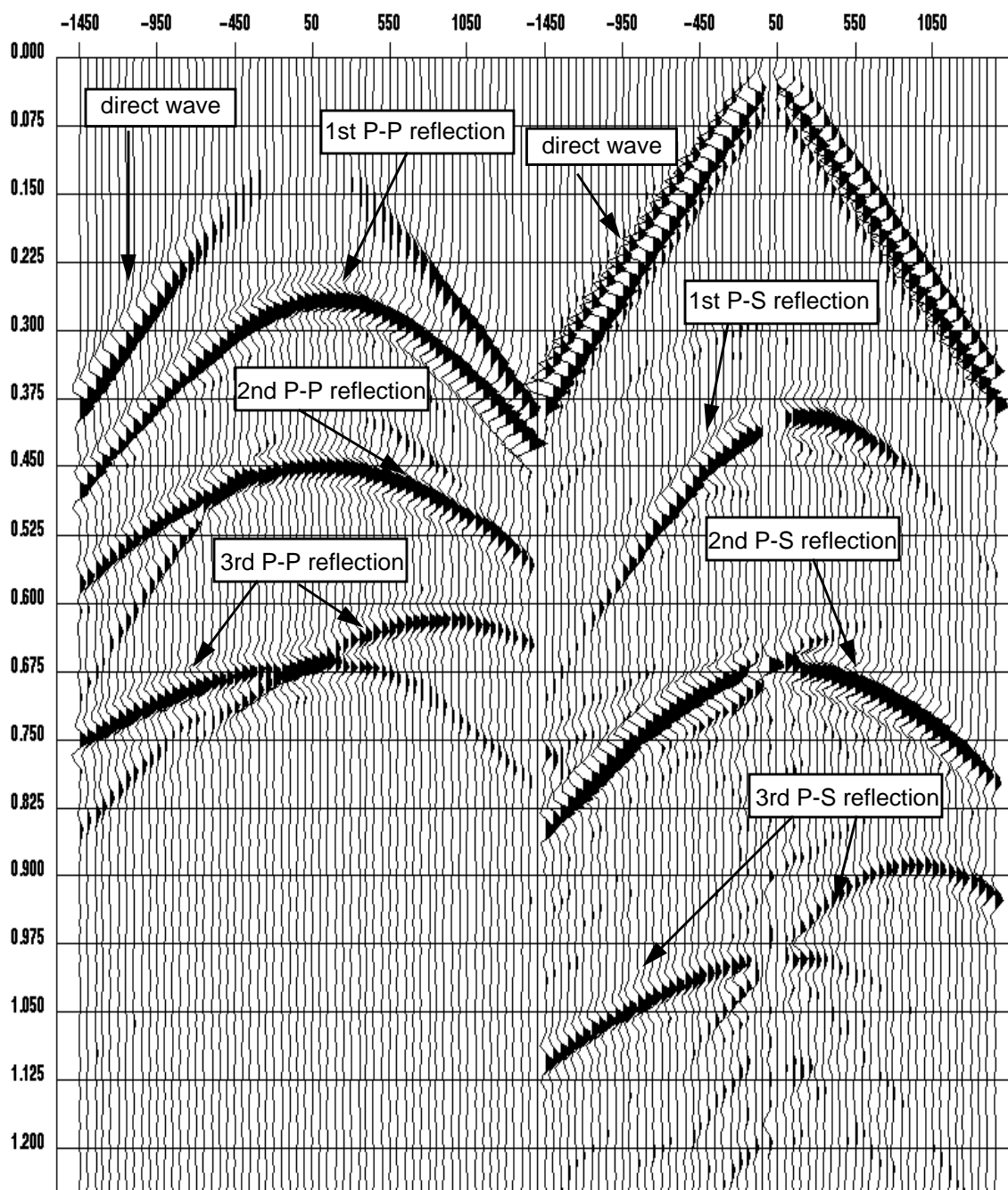
Fig. 5.4. Two-component synthetic shot records at station 1728. The first record is vertical component and the second record is radial component. Polarity reversal for the radial component has been applied. Offsets are shown at the top of the records.
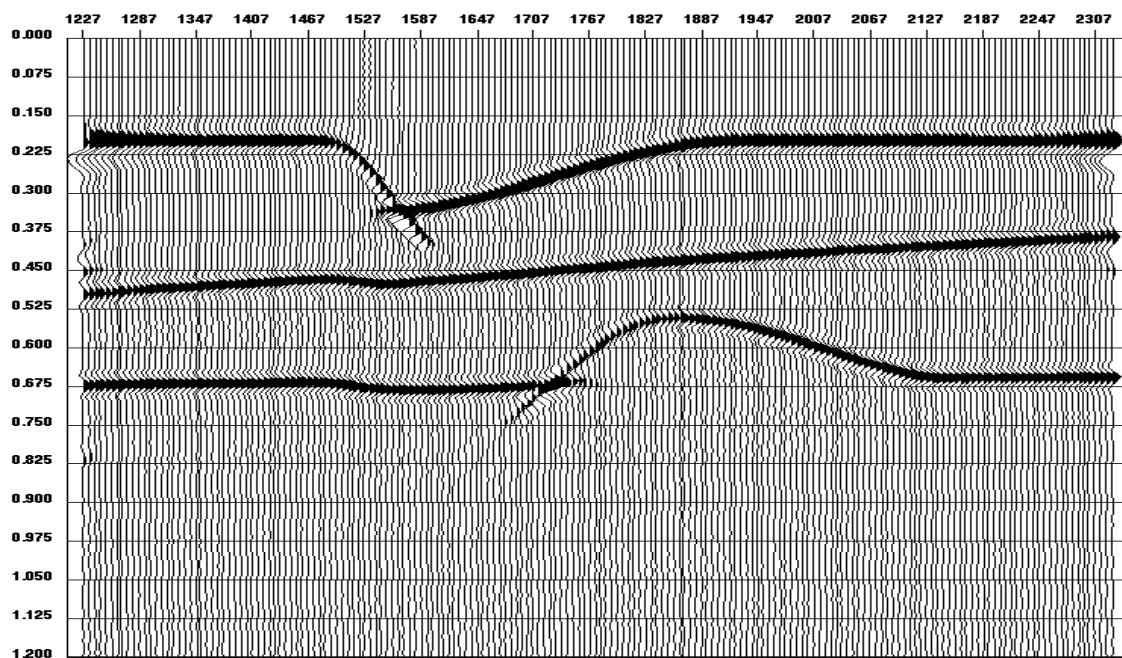
Fig. 5.5. P-P structural stack.
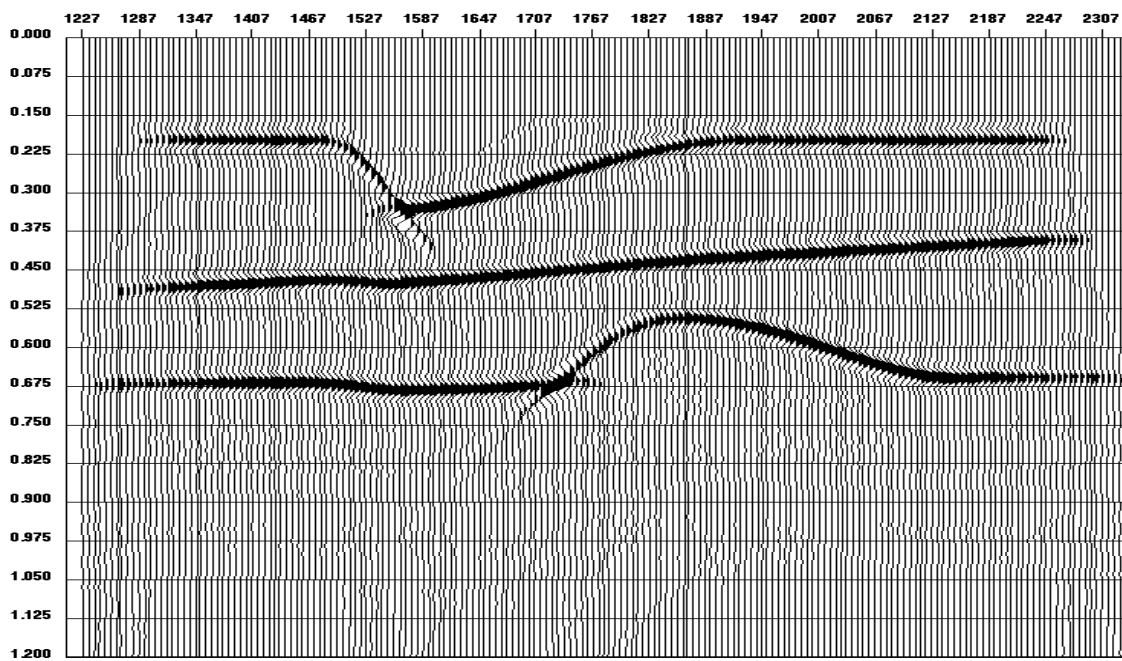
Fig. 5.6. P-P DMO stack.
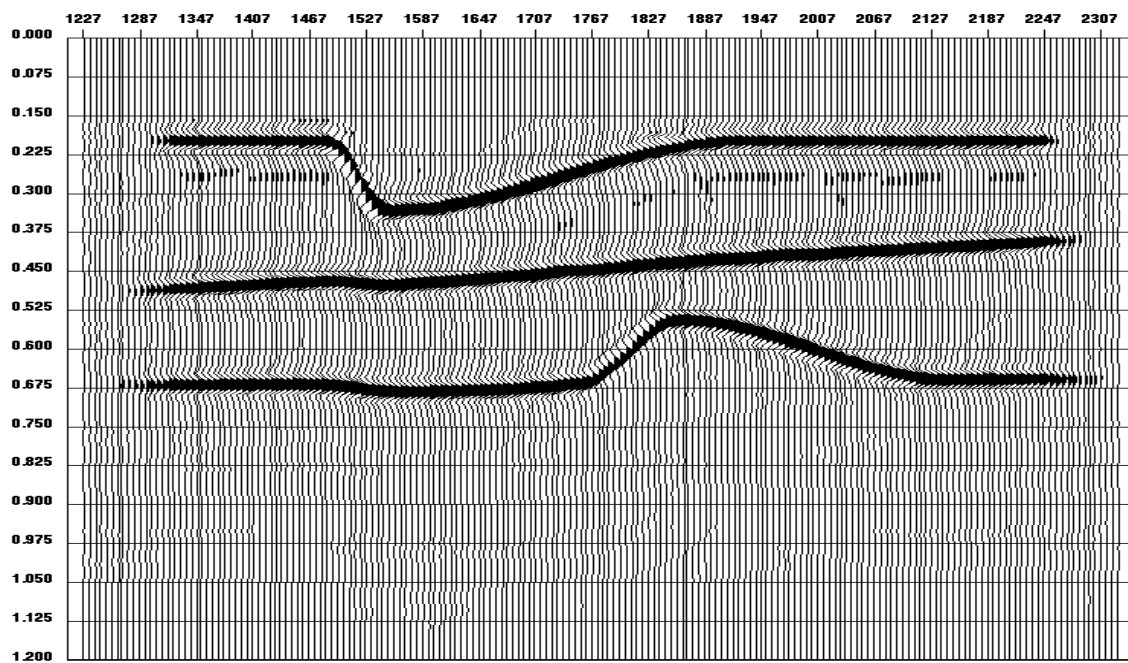
Fig. 5.7. P-P prestack migrated stack.

108

station	time (s)	velocity (m/s)	station	time (s)	velocity (m/s)	station	time (s)	velocity (m/s)
1284	0.208	4007.56	1314	0.208	4007.56	1344	0.200	4020.15
	0.488	4397.98		0.488	4397.98		0.480	4612.09
	0.664	4599.50		0.672	4637.28		0.672	4700.25
1374	0.216	4020.15	1404	0.200	4007.56	1434	0.200	4007.56
	0.480	4372.80		0.472	4467.25		0.472	4479.85
	0.672	4624.69		0.672	4643.58		0.664	4599.50
1464	0.208	4020.15	1494	0.216	4007.56	1524	0.288	4020.15
	0.472	4347.61		0.464	4360.20		0.472	4473.55
	0.672	4492.44		0.672	4416.88		0.680	4712.85
1554	0.336	4007.56	1584	0.328	4013.85	1614	0.312	4013.85
	0.480	4454.66		0.472	4259.45		0.472	4335.01
	0.680	4756.93		0.680	4656.17		0.680	4624.69
1644	0.312	4032.75	1674	0.296	4032.75	1704	0.280	4013.85
	0.464	4322.42		0.464	4303.53		0.456	4360.20
	0.680	4574.31		0.680	4574.31		0.672	4719.14
1734	0.264	4013.85	1764	0.256	4020.15	1794	0.232	4020.15
	0.448	4215.37		0.440	4397.98		0.440	4423.17
	0.672	4511.33		0.664	4240.55		0.624	4460.96
1824	0.224	4020.15	1854	0.224	4020.15	1884	0.208	4020.15
	0.432	4353.90		0.432	4372.80		0.424	4360.20
	0.568	4511.33		0.536	4555.42		0.536	4580.60
1914	0.200	4020.15	1944	0.200	4013.85	1974	0.200	4020.15
	0.424	4372.80		0.416	4360.20		0.416	4297.23
	0.544	4593.20		0.568	4586.90		0.584	4517.63
2004	0.200	4013.85	2034	0.200	4013.85	2064	0.208	4007.56
	0.416	4473.55		0.416	4416.88		0.408	4397.98
	0.608	4599.50		0.624	4612.09		0.640	4637.28
2094	0.200	4020.15	2124	0.200	4032.75	2154	0.200	4020.15
	0.408	4442.07		0.400	4423.17		0.400	4429.47
	0.648	4612.09		0.656	4668.77		0.656	4706.55
2184	0.200	4007.56	2214	0.192	4013.85	2244	0.200	4013.85
	0.400	4442.07		0.392	4435.77		0.392	4429.47
	0.656	4675.06		0.656	4693.95		0.656	4706.55

Table 5.1. P-wave migration velocities for Figure 5.7.
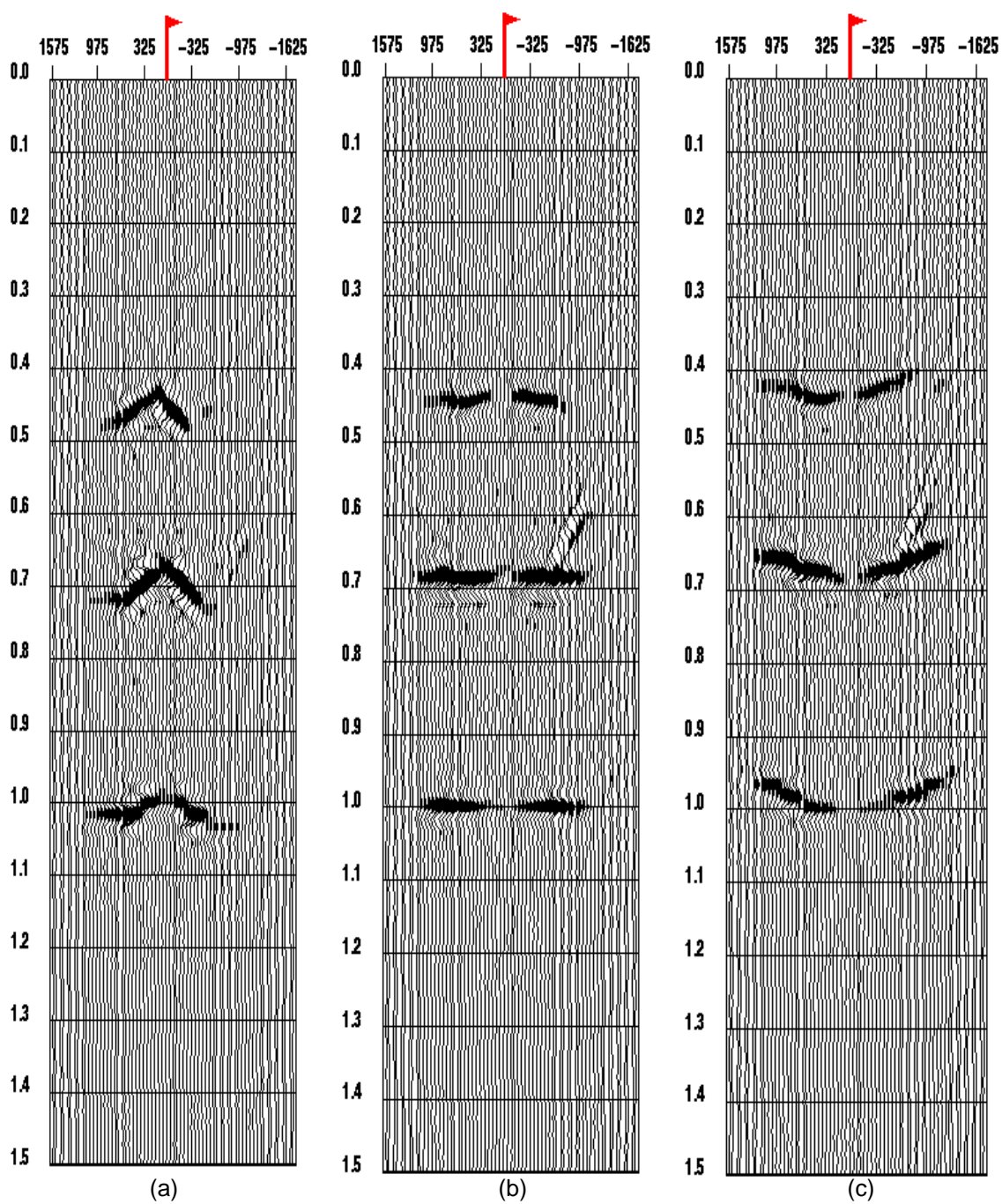
Fig. 5.8. MVA at station 1683 with 3 different γ_{mig}. (a) with low $\gamma_{mig} = 1.35$, all events appear curving downwards. (b) with proper $\gamma_{mig} = 1.95$, bottom 2 events are flat, slightly lower for the first event. (c) with high $\gamma_{mig} = 2.5$, all events appear curving upwards.
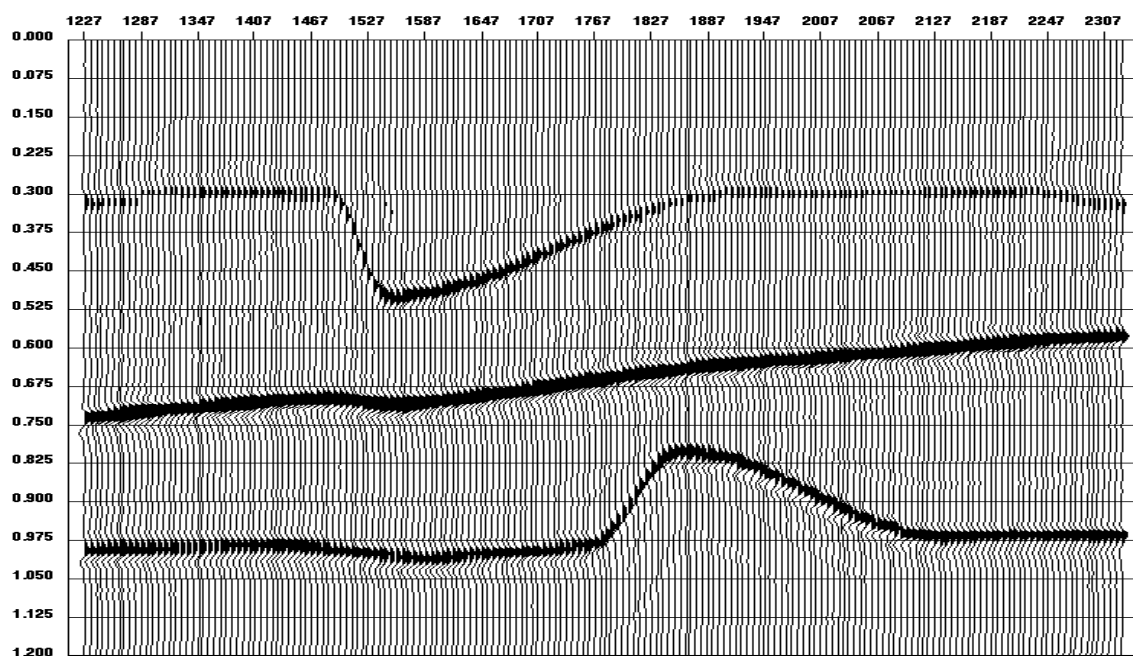
Fig. 5.9. P-S prestack migrated stack.
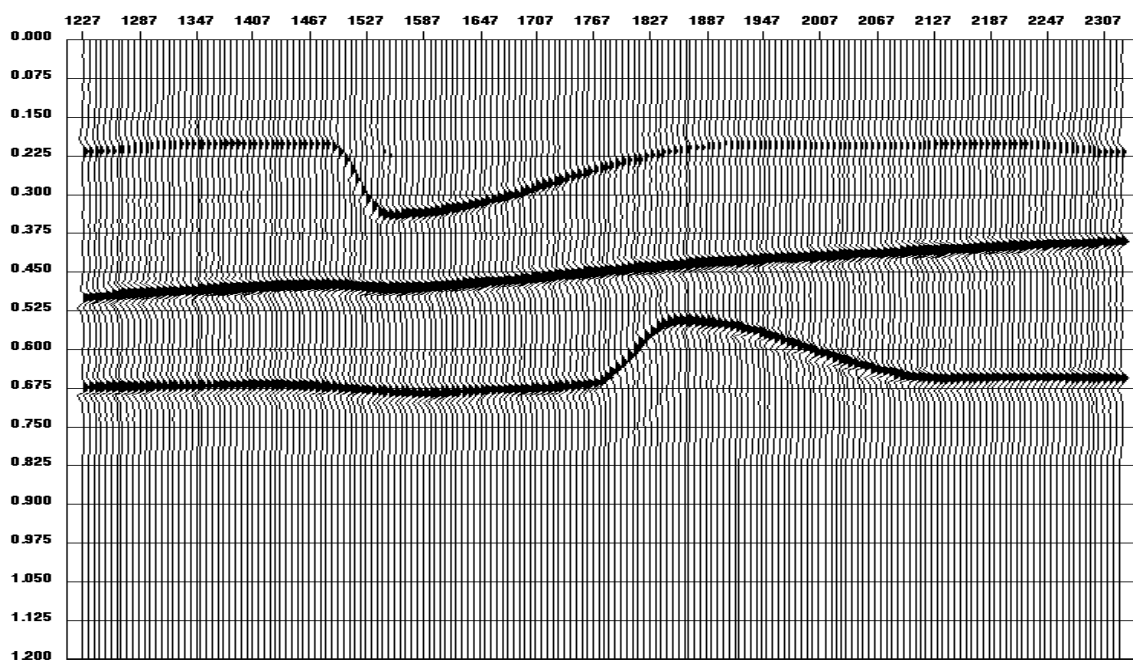
Fig. 5.10. P-S prestack migrated stack converted to P-P times.
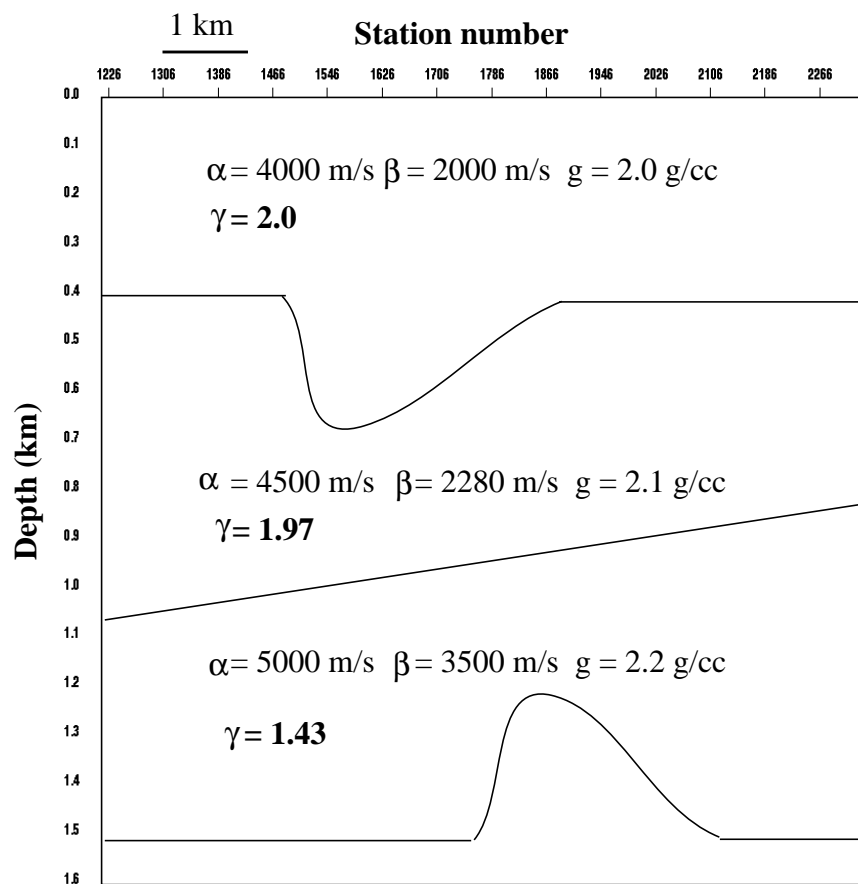
Fig. 5.11. The new velocity-density model. It is same as in Figure 5.3, except the β value for the third layer.

shown in Figure 5.12. The kinematic of the P-P reflections are the same as in Figure 5.4. Due to an increased in S-wave velocity in the third layer, the P-S reflection for that layer arrives earlier than in Figure 5.4. The MVA shown in Figure 5.13 suggests that the γ_{mig} for the third layer is roughly 1.65. Therefore γ_{mig} of 1.95 is used to migrate the top two layers and γ_{mig} of 1.65 is used to migrate the bottom layer. The P-S migrated stacks in P-S and P-P times are shown in Figure 5.14 and Figure 5.15 respectively. (Note that the strong amplitude in the second event is due to an increased in S-wave velocity contrast.) As expected only the first two layers are tied with the P-P prestack migrated stack in Figure 5.7 and the third layer is inaccurate (at station 1306, g_γ at the bottom of the third layer is around 0.978). However, it is surprising that no noticeable difference in lateral position of the third layer is observed between the P-P and P-S migrated stacks. It may be because of the low seismic bandwidth and the large trace spacing (25 m).

5.7 Real example

The P-S MVA and the P-S prestack migration discussed in this chapter are applied to the 4.5 Hz Blackfoot data set. The migration velocity panels at station 4310 are shown in Figure 5.16 with γ_{mig} ranges from 1.8 to 2.2. Figure 5.17 is an example of before and after the P-S migration for the shot at station 1250. The result of the P-S migrated stack is shown in Figure 5.18.
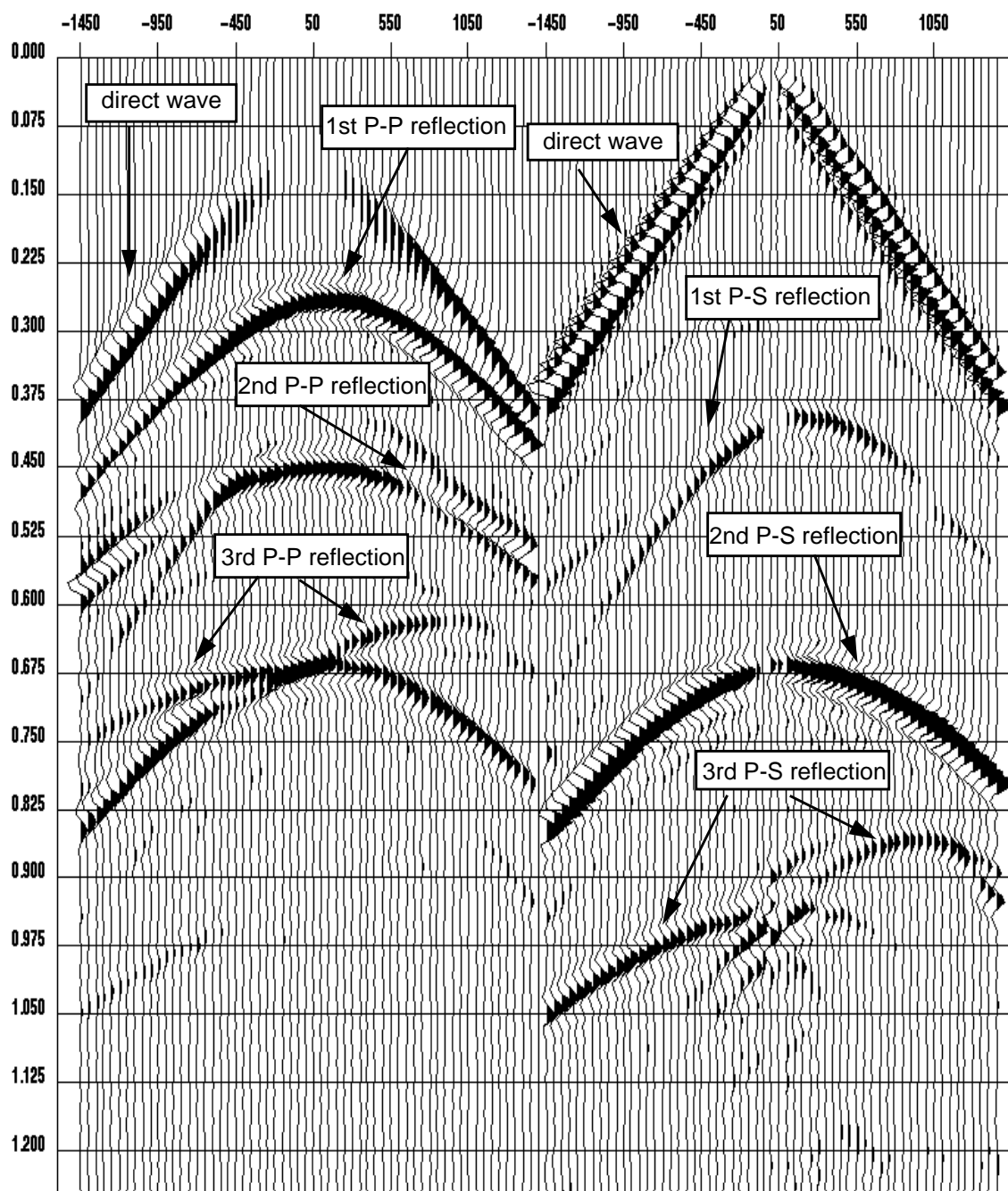
Fig. 5.12. Two components shot records of the new model at station 1728. The vertical component is shown at the left and the radial component is shown at the right. The kinetmatic of P-P reflections are same as in Figure 5.4
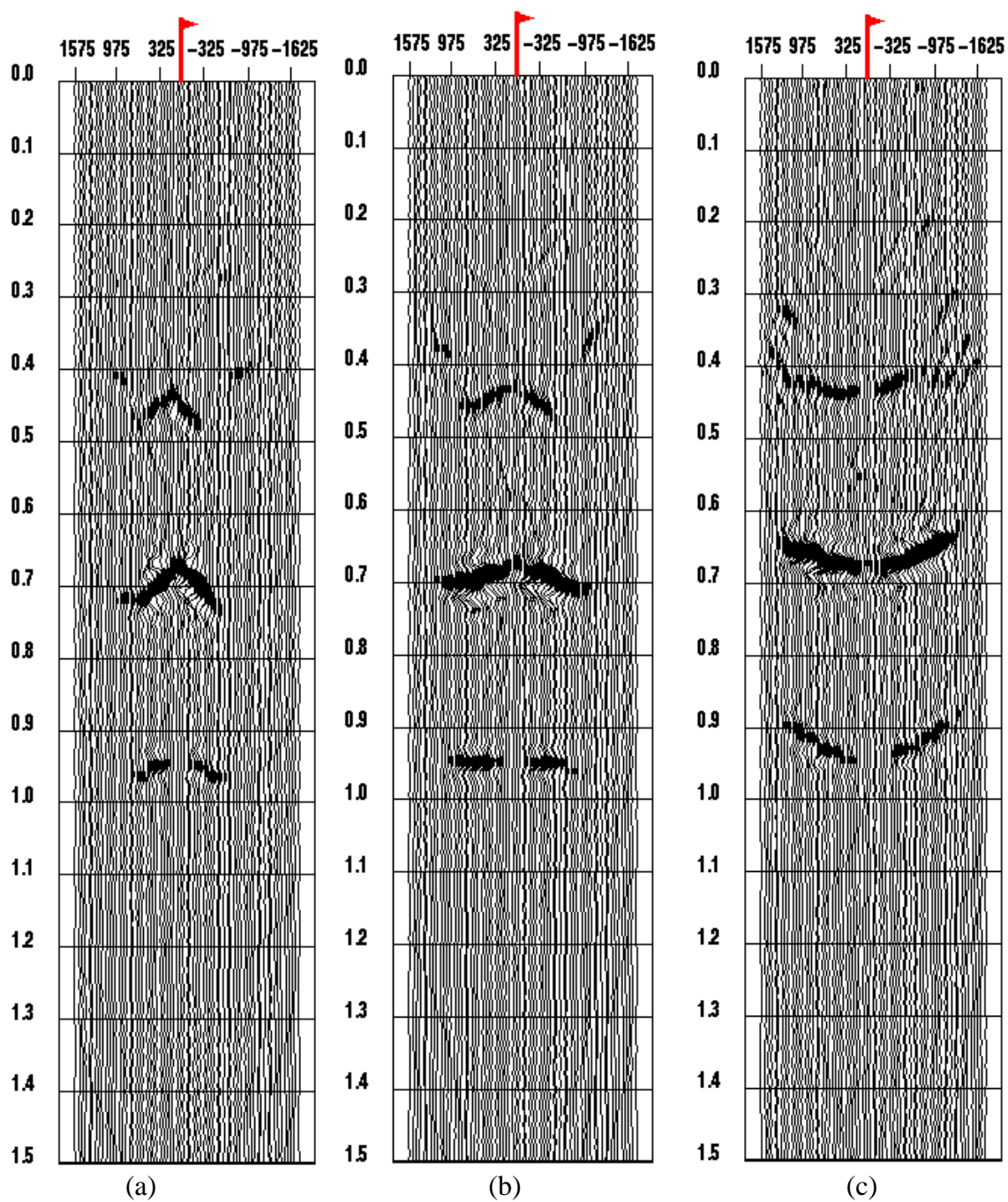
Fig. 5.13. MVA for the third layer at station 1683 with 3 different γ_{mig}. (a) with low $\gamma_{mig} = 1.35$, the third event appears curving downwards. (b) with proper $\gamma_{mig} = 1.65$, the event is flat. (c) with high $\gamma_{mig} = 2.5$, the event appears curving upwards.

116
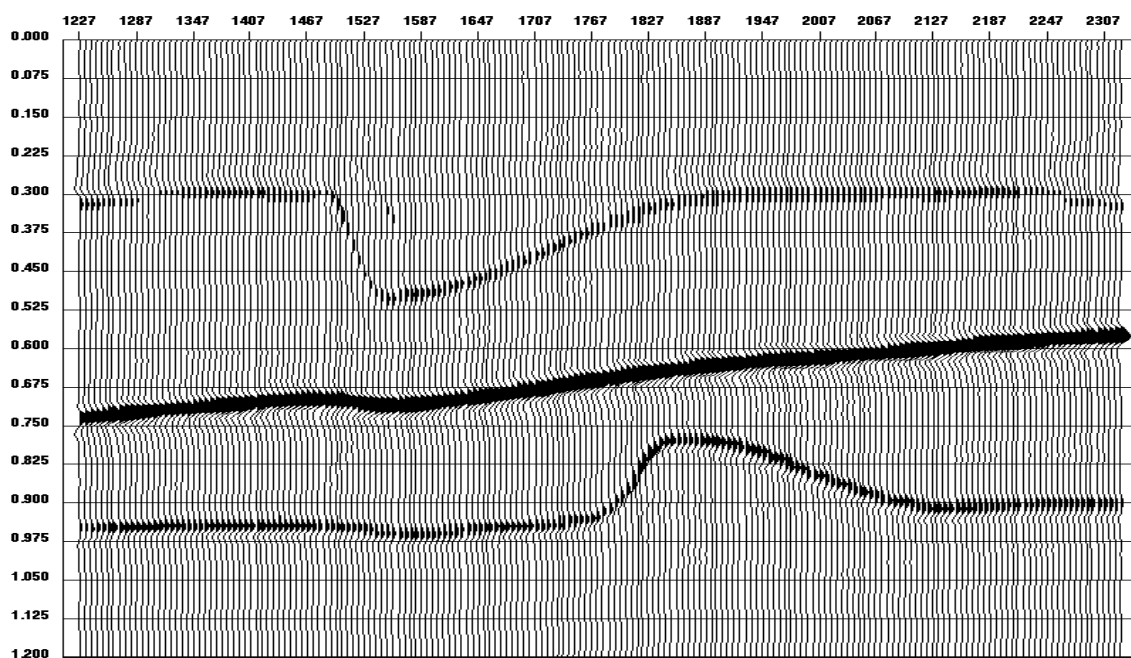
Fig. 5.14. The P-S prestack migrated stack of the new model in P-S times.
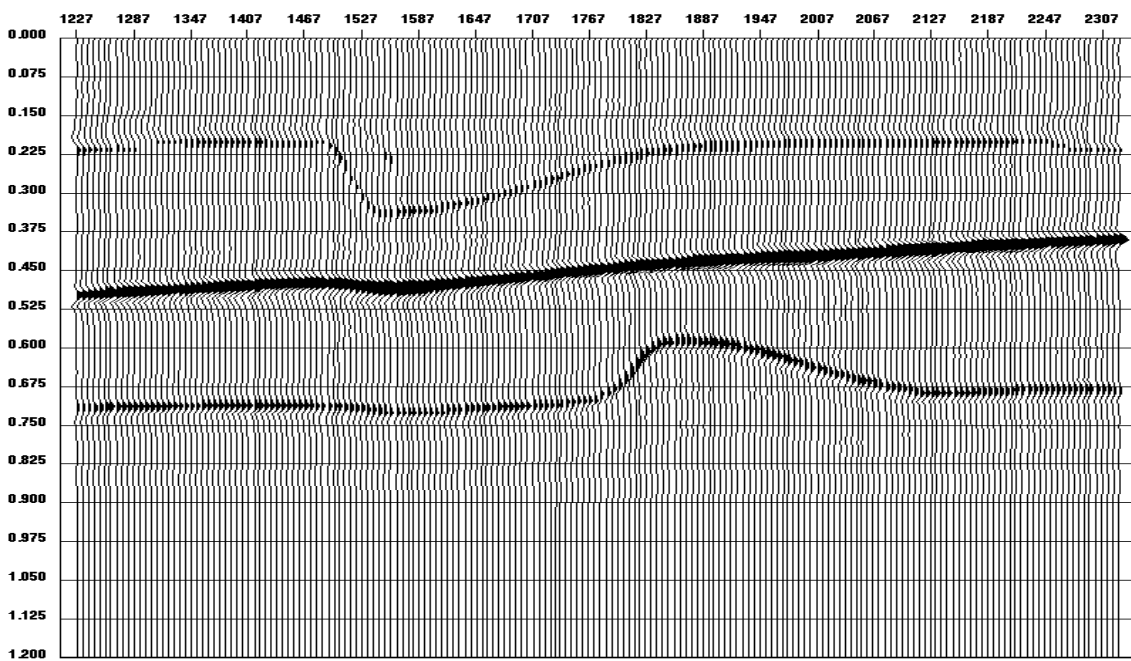
Fig. 5.15. The P-S prestack migrated stack of the new model in P-P times.
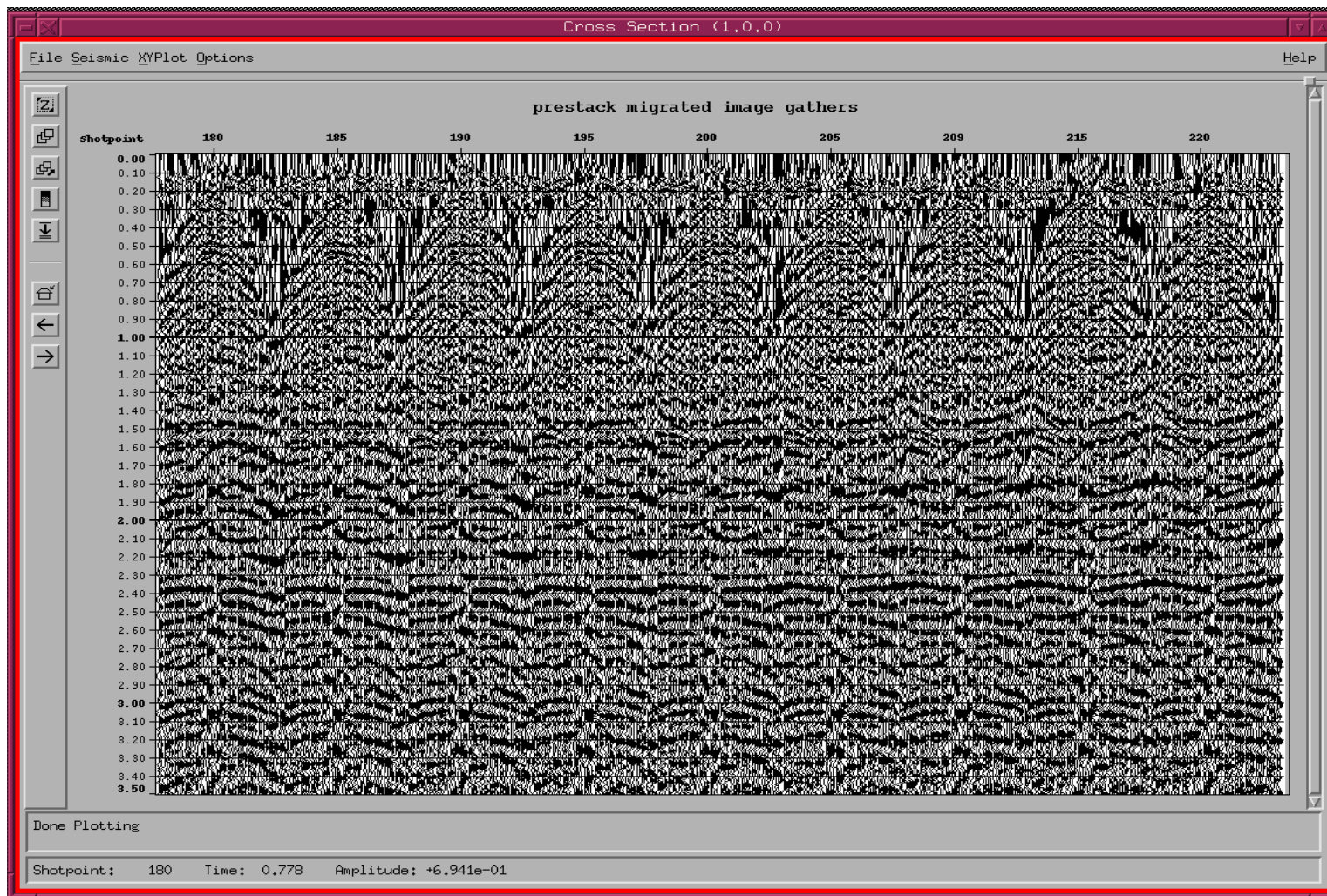
Fig. 5.16. The MVA of the Blackfoot data at station 4310. $\gamma_{mig} \times 100$ are shown at the top of each image gather.
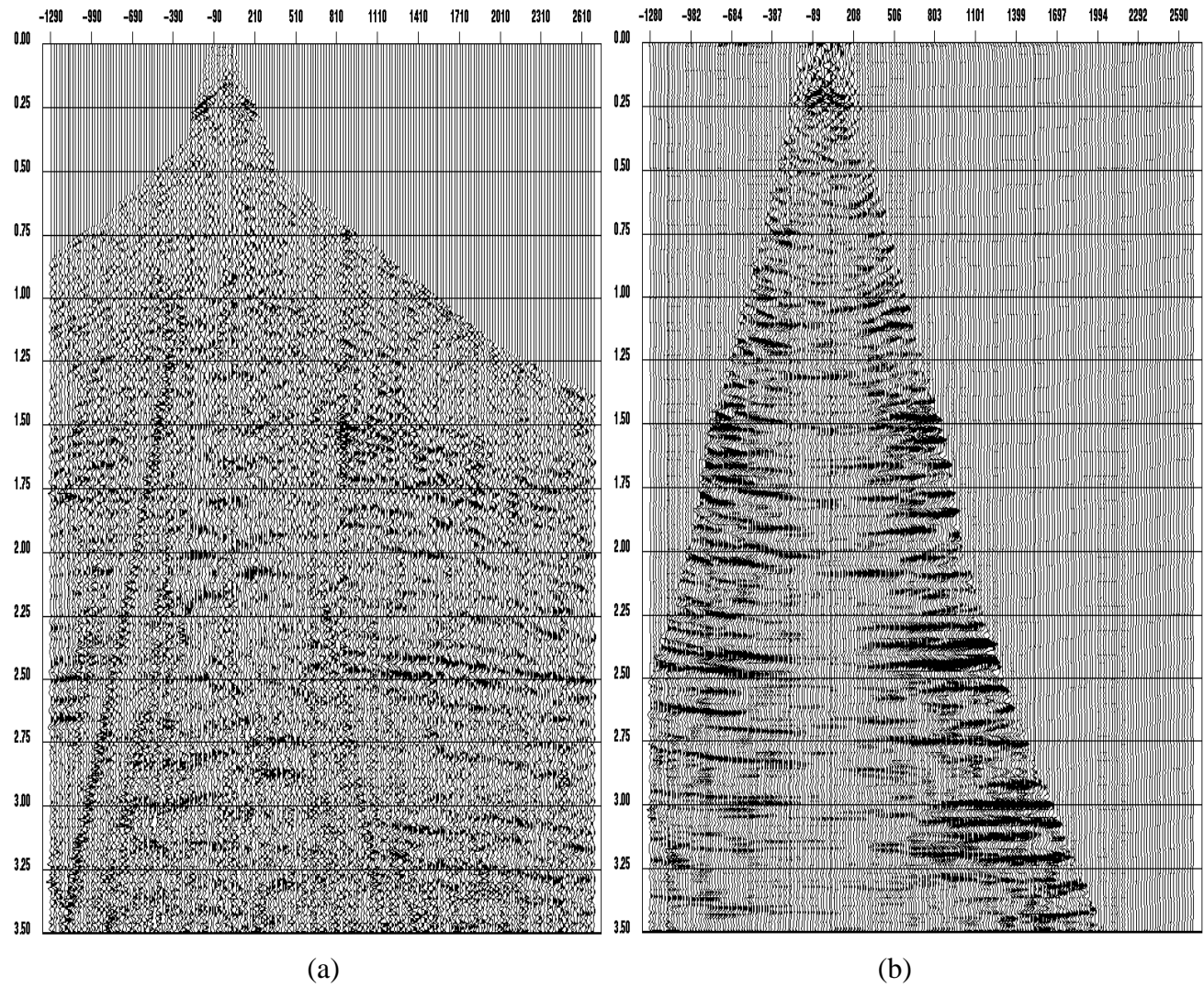
Fig. 5.17. P-S prestack migrated shot gather at station 1250. (a) Before migration. (b) After migration.
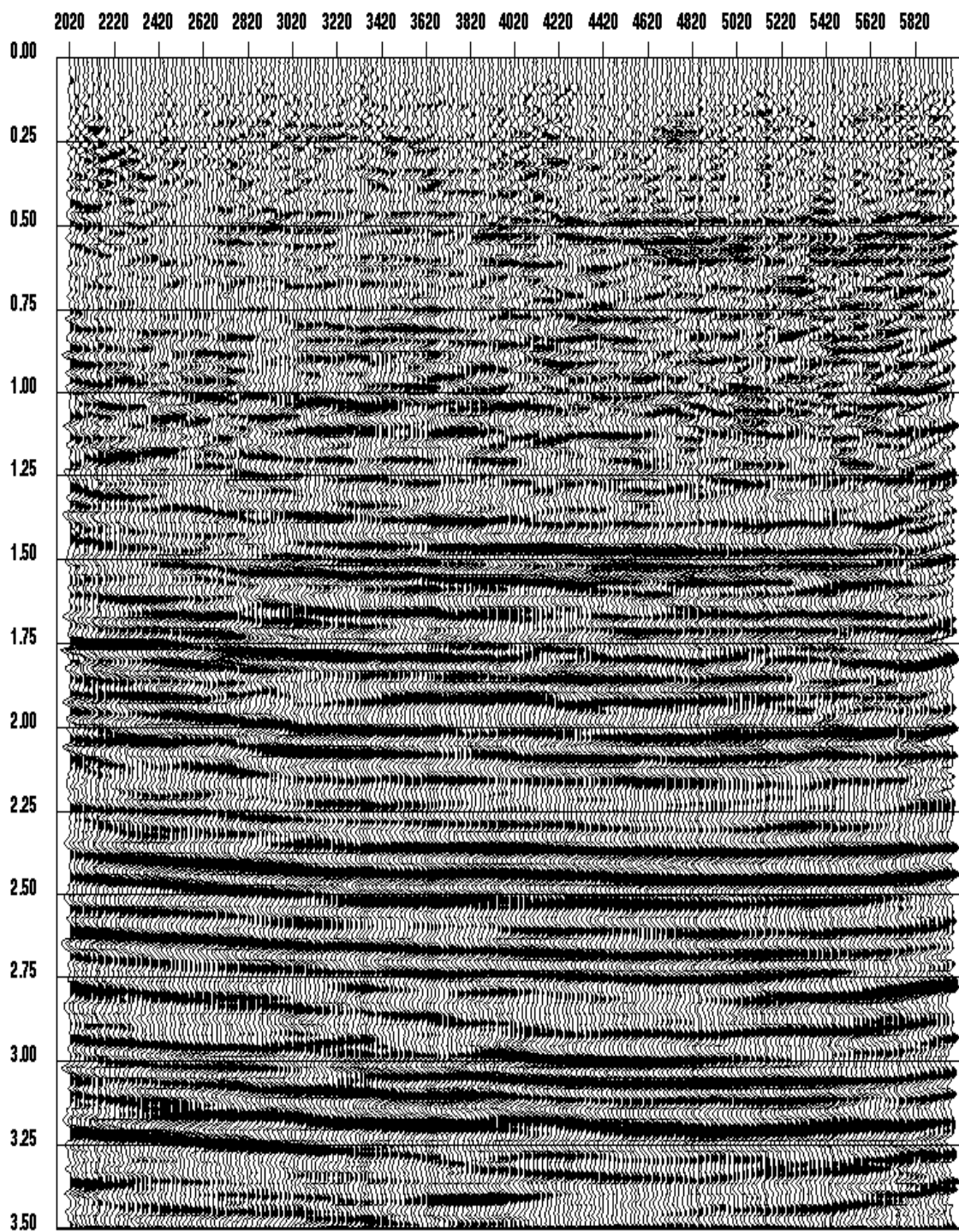
Fig. 5.18. P-S prestack time migrated stack.

5.8 Discussion

In this chapter, it is shown in the synthetic example that the prestack time migration based on the double-square-root equation for a single pseudo-depth (Z_{ps}) model is applicable to dipping layers when the P-and-S RMS velocity model is laterally smooth. Also, it is shown in theory that the P-S time migration has more approximations than in P-P time migration. First, the P-S moveout curve within a migrated gather flattened by a single parameter γ_{mig} is not as good as P-P moveout curve. However, the unflattened portion of the moveout curve can be muted away before they stack together. Second, the lateral location of the events on P-S may not relate to the image ray location, however, the difference may be small. Third, the processing parameter γ_{mig} obtained from P-S migration does not directly reflect any physical properties, and cannot be used to convert P-S time into P-P time.

Even though the results of applying P-S time migration to both real and synthetic data are encouraging and it may be possible to use P- and S- image rays to converted P-S time-migrated events into depth, the potential problem described in this chapter can be existed for some data with complex P- and S- velocity fields. In that case, P-S prestack depth migration is needed to solve the imaging problem.

Chapter 6   P-S to P-P transformation

6.1 Introduction

One of the major reasons for the difficulty in processing P-S data is the asymmetry of the P-S ray paths. In P-P processing, because the ray path is symmetric with respect to the shot direction, the data can be efficiently processed and stacked in the CMP domain, even in the present of dips. However, in the P-S case, the conversion point for P-S reflections has a large shift relative to the CMP location, even for flat earth models. Because of this conversion point dispersal, processing algorithms are more complicated, and also, velocity information is required at a much earlier stage (CCP binning).

We propose to solve some of these problems by transforming P-S prestack data to a symmetric ray path geometry in pseudo P-P time-and-space. This will reposition the P-S data (with their asymmetric ray paths and gathers) to look like symmetric P-P data (Figure 6.1). After transformation, we can then use many of the efficient and non-iterative P-P processes such as CMP binning, DMO and prestack time migration, and importantly, can solve for the S-wave receiver statics.

Although γ_{mig} is required for this transformation, it can be obtained by migration velocity analysis at selected locations, as described in the previous chapter. Velocities obtained earlier from P-P processing can be used to process the pseudo P-P data. Alternatively, any

reasonable γ_{mig} function can be used for the transformation. However, velocity analysis on

the pseudo P-P data may be required at a later stage.

I call this new transformation technique Asymmetric MoveOut Correction (AMOC).
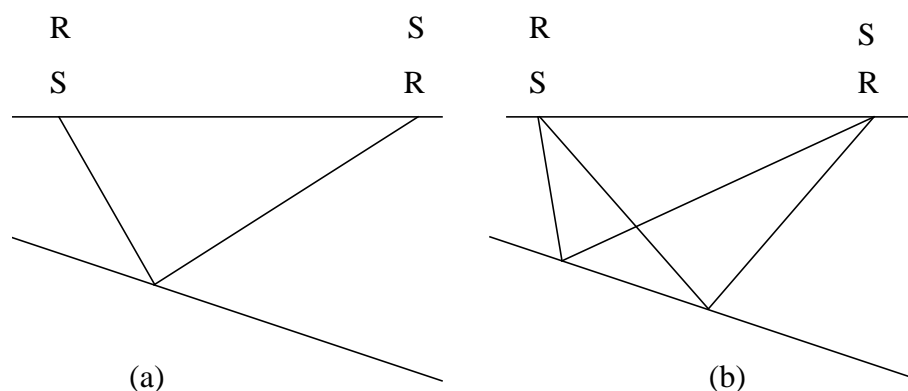
Fig. 6.1. (a) By exchanging source (S) and receiver (R) positions, the ray paths remain the same for P-P or S-S reflections, therefore the traveltime is symmetric with respect to the source-receiver mid-point. (b) By exchanging source (S) and receiver (R) positions, the P-S reflections follow different paths, with the conversions positioned away from the shot (S). In the presence of dip, the traveltimes are different and the symmetry breaks down with respect to the source-receiver mid-point.

6.2 Theory of AMOC

The AMOC method starts with downward continuation of the received wavefield, for a

given shot record down to a depth level, using the S-wave velocity (β). The P-wave trav-

eltime from the shot to the depth location is then calculated. The time samples of the down-

ward continuation wavefield that correspond to the calculated traveltime are then upward

continued back to the receiver locations with the P-wave velocity (α)(see Figure. 6.2). This

procedure is repeated for all depth increments and the output of the transformation is the

summation of all the upward continuations of the P-wavefield. In detail: let S(x,z=0,t) de-

note the recorded P-S shot gather at the Earth's surface, then the corresponding pseudo P-

P shot gather, P(x,z=0,t) is given by

$$ P(x, 0, t) \; = \; \sum_{z} U_z^{\alpha} \Big[\Big(D_z^{\beta} \, [S(x, 0, t)] \Big) \delta \Big(t - t_d^{\alpha}(x, z) \Big) \Big] \qquad (\textbf{6.1}) $$

where U_z^{α} is the upward continuation operator from depth z to the surface with the α

velocity,

D_z^{β} is the downward continuation operator from the surface to depth z with the

β velocity,

t_d^{α} is the P-wave traveltime from the shot to the depth points (x,z),

δ is the Dirac delta function.
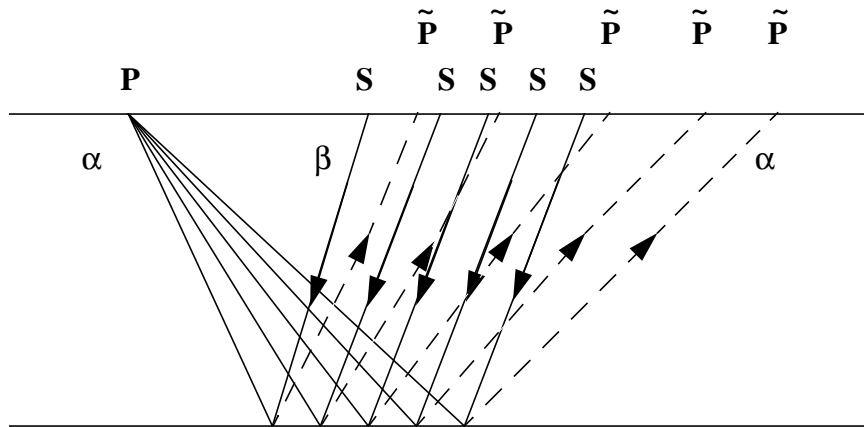
Fig. 6.2. The AMOC can be visualized as the receivers being downward continued with S velocity (β) to a certain depth, followed by upward continuation to the surface with P velocity (α).

We note that during the process, the amplitudes of the P-S reflections are mapped from P-S time-and-space positions into the P-P symmetric configuration. If the pseudo P-P shot is migrated with the P-wave velocity, the amplitude of the migrated shot image is simply the P-S reflectivity that could also be obtained from P-S migration of the same P-S shot. After the transformation, note that the pseudo P-P shot gather has greater lateral offset than the original P-S data (Figure 6.2), which is due to the fact that the receiver to conversion point offset is smaller for S-wave travel than for P-wave travel (from Snell's law). The AMOC procedure can be modified to apply in the common receivers, which results in lessening the offsets. An advantage to doing AMOC in this order is that in the common receiver-domain, the known P-wave shot statics can be applied first, thus removing the smearing problem of the statics in the AMOC process. The residual receiver statics can then be solved in the CMP domain, as usual, after NMO correction and stretching back into P-S times. The disadvantage to performing AMOC in this order is that in practice, the shot spacing will often be larger than the receiver spacing, making aliasing a larger problem in the wavefield continuation.

If both P- and S- velocities have small lateral variation and the γ_{mig} values vary smoothly, then P-S time migration is applicable, and we can use straight ray path approximations to speed up the AMOC process. The S velocity required for the AMOC can be obtained from the time migration velocity analysis technique described from the previous chapter (i.e., $V_{s,mig}$). In this case, the depth increment becomes the P-S pseudo-depth increment, and the traveltime, t_d^α, in equation (6.1), is calculated using the straight ray-path approxi-

mation. After the transformation, the zero-offset events are located at the P-S pseudo-depth, rather than the P pseudo-depth. Nevertheless, symmetry of the moveout curves in the CMP domain is achieved.

From equations (5.20) and (5.26), the pseudo P-wave two-way zero-offset time is:

$$\tilde{T}_{pp} = \frac{2Z_{ps}}{V_p}$$

$$= T_{pp} \frac{\left(1 + \frac{\gamma_{rms}}{g_\gamma}\right)}{(1 + \gamma_{mig})}$$

$$= T_{pp}\left(\frac{1 + \gamma_{ps}}{1 + \gamma_{mig}}\right) \qquad (6.2)$$

where:

$$\gamma_{ps} = \frac{\gamma_{rms}}{g_\gamma} \qquad (6.3)$$

Therefore, in general, the two-way P-wave vertical traveltime in the pseudo P-P data may be different from that in the true P-P data. However, if this pseudo P-P zero-offset time is converted into P-S time using γ_{mig}, then

$$\tilde{T}_{pp}\left(\frac{1 + \gamma_{mig}}{2}\right) = T_{pp}\left(\frac{1 + \gamma_{ps}}{1 + \gamma_{mig}}\right)\left(\frac{1 + \gamma_{mig}}{2}\right)$$

$$= T_{pp}\left(\frac{1 + \gamma_{ps}}{2}\right)$$

$$= T_{ps} \qquad (6.4)$$

In other words, the zero-offset P-S time can be found by vertically stretching the pseudo P-

P stack data using the same γ_{mig} as for the transformation. This property will be demonstrated in the following examples.

6.3 Synthetic example

Figure 6.3 is the velocity-density model for the synthetic data. A total of 200 split-spread shots are generated with finite difference numerical modeling package. Each record contains 131 channels (including zero-offset) on one side, and 100 channels on the other side. The station interval is 25 m and every station is shot. Figures 6.4 and 6.5 are vertical and radial components respectively of a shot at station 1200. Only 201 channels are shown. Scaling has been applied on both records and polarity reversal has been applied on the radial component. Figures 6.6 and 6.7 are P-P and P-S CMP gathers respectively, at station 1200 respectively. Note that the second layer reflection on the P-P CMP gather is symmetric with respect to the offset, but is not in the P-S CMP gather. Figures 6.8 and 6.9 are the P-P DMO stack and P-P prestack time-migrated stack (Gardner et al., 1986; Canning, 1993). Figure 6.10 is the ACCP stack gathered using a Vp/Vs ratio of 2.

Ideally, in the new AMOC flow, the γ_{mig} function obtained from the P-S migration velocity analysis is required for the transformation of P-S data into pseudo P-P. However, this step may be time consuming. Instead, we will show results of using different approximations of γ_{mig} values.
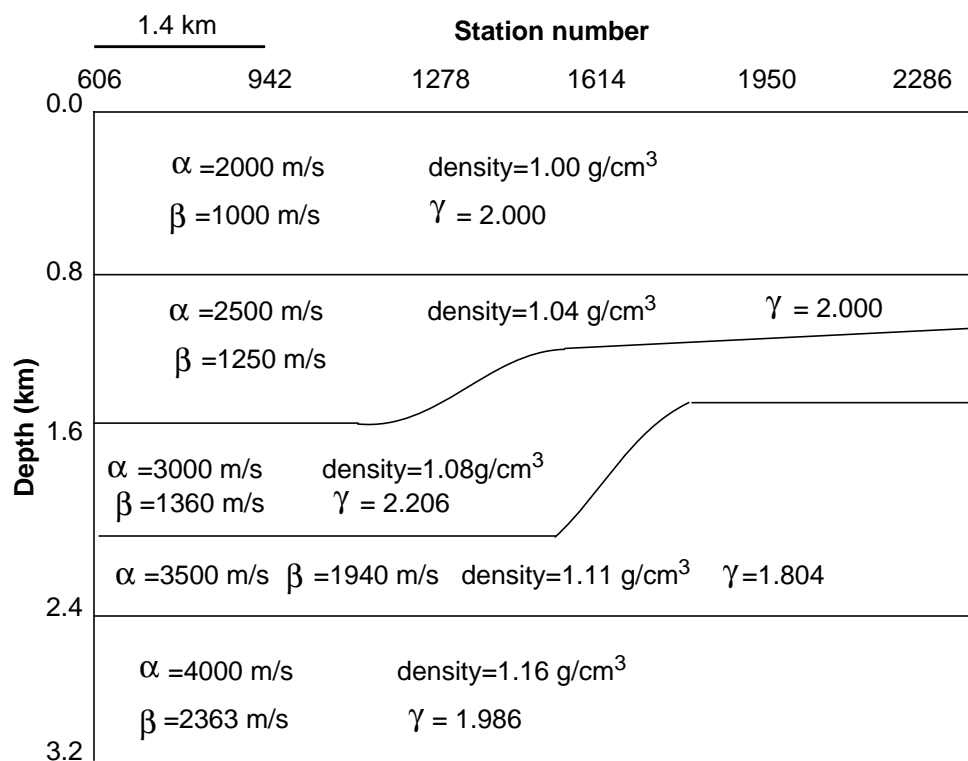
Fig. 6.3. Velocity-density depth model for the numerical synthetic example.
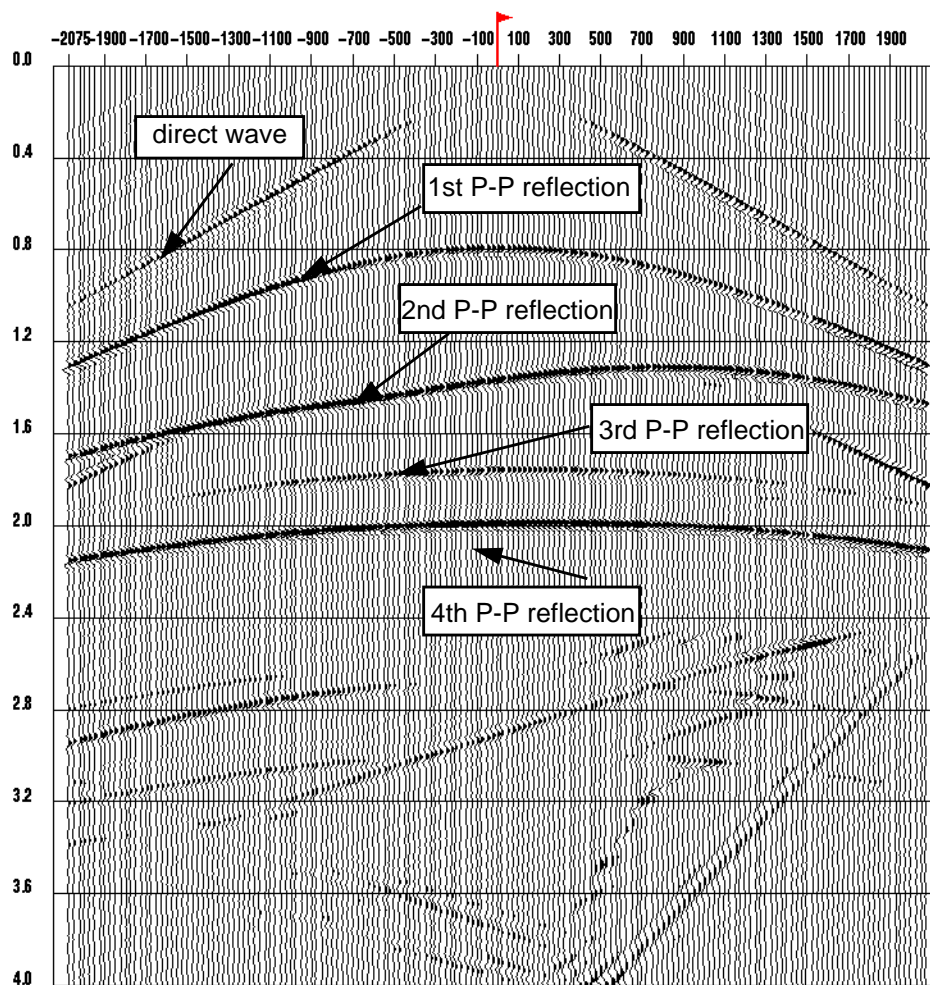
Fig. 6.4. Vertical component of a shot record at station 1200. The 4 primary P-P reflections are at 0.8 s, 1.3 s, 1.8 s and 2 s of zero-offset times respectively. Scaling has been applied to the record.
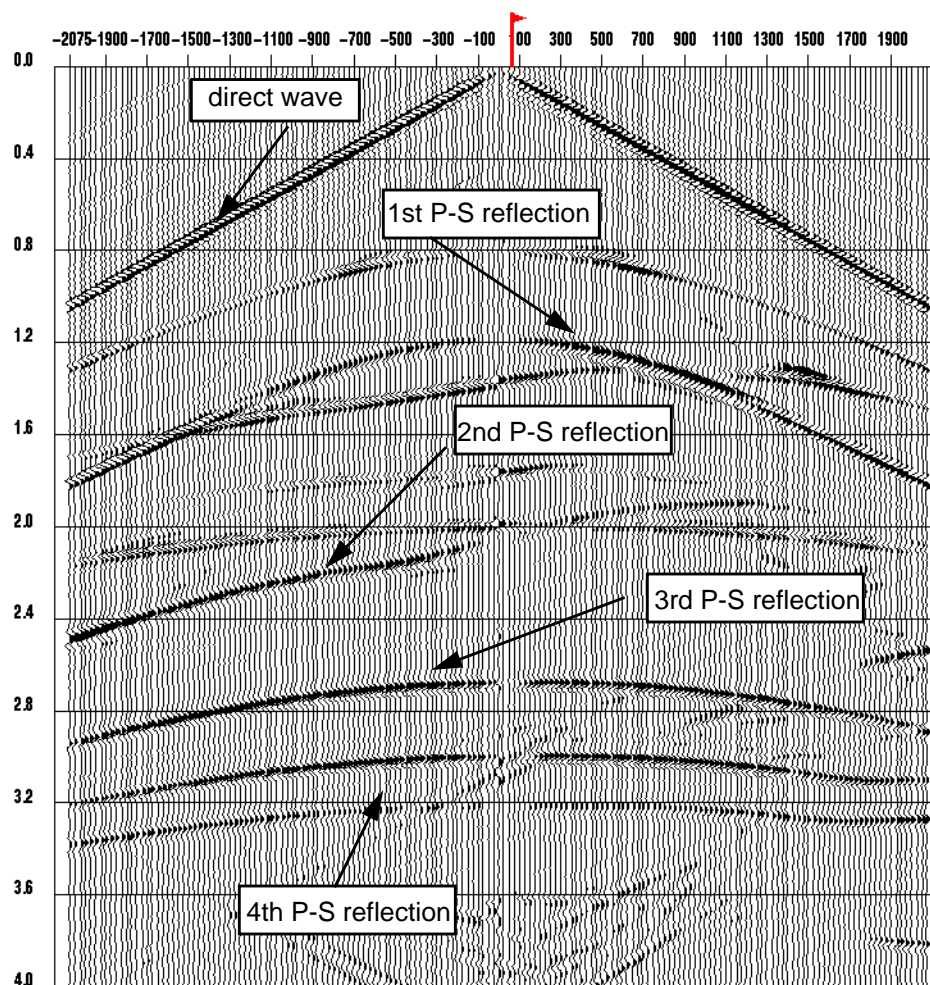
Fig. 6.5. Radial component of a shot record at station 1200. The 4 primary P-S reflections are at 1.2 s, 2.0 s, 2.7 s and 3 s of zero-offset times respectively. Scaling and polarity reversal have been applied to the record.
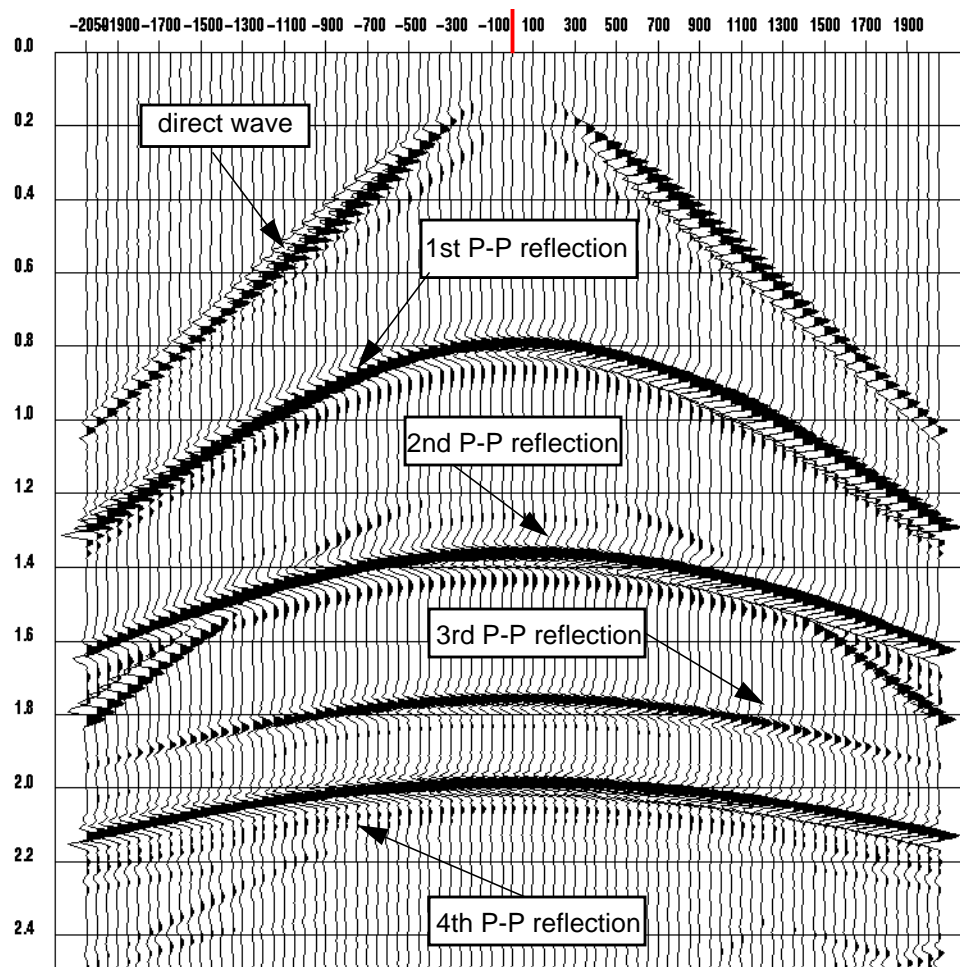
Fig. 6.6. A P-P CMP gather at station 1200. Note that the event at 1.35 seconds is symmetric with respect to the offset.
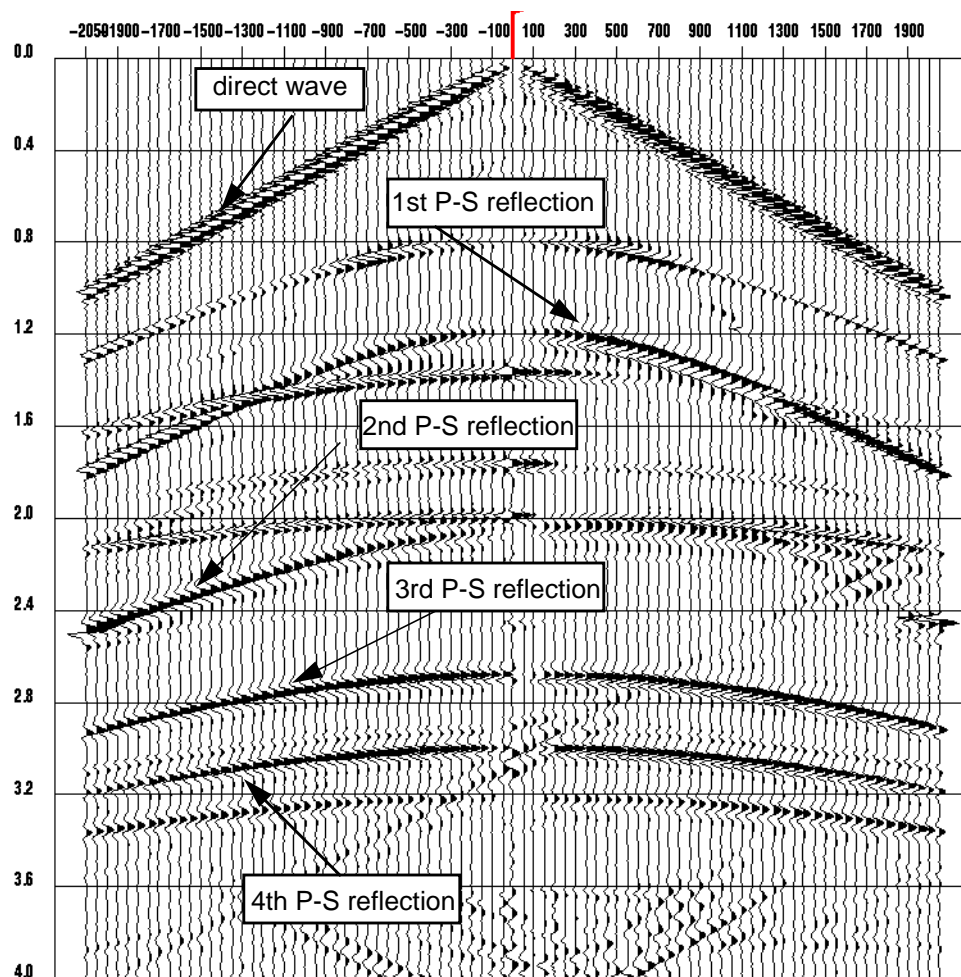
Fig. 6.7. A P-S CMP gather at station 1200. Note that the event at 2 seconds is asymmetric with respect to the offset.
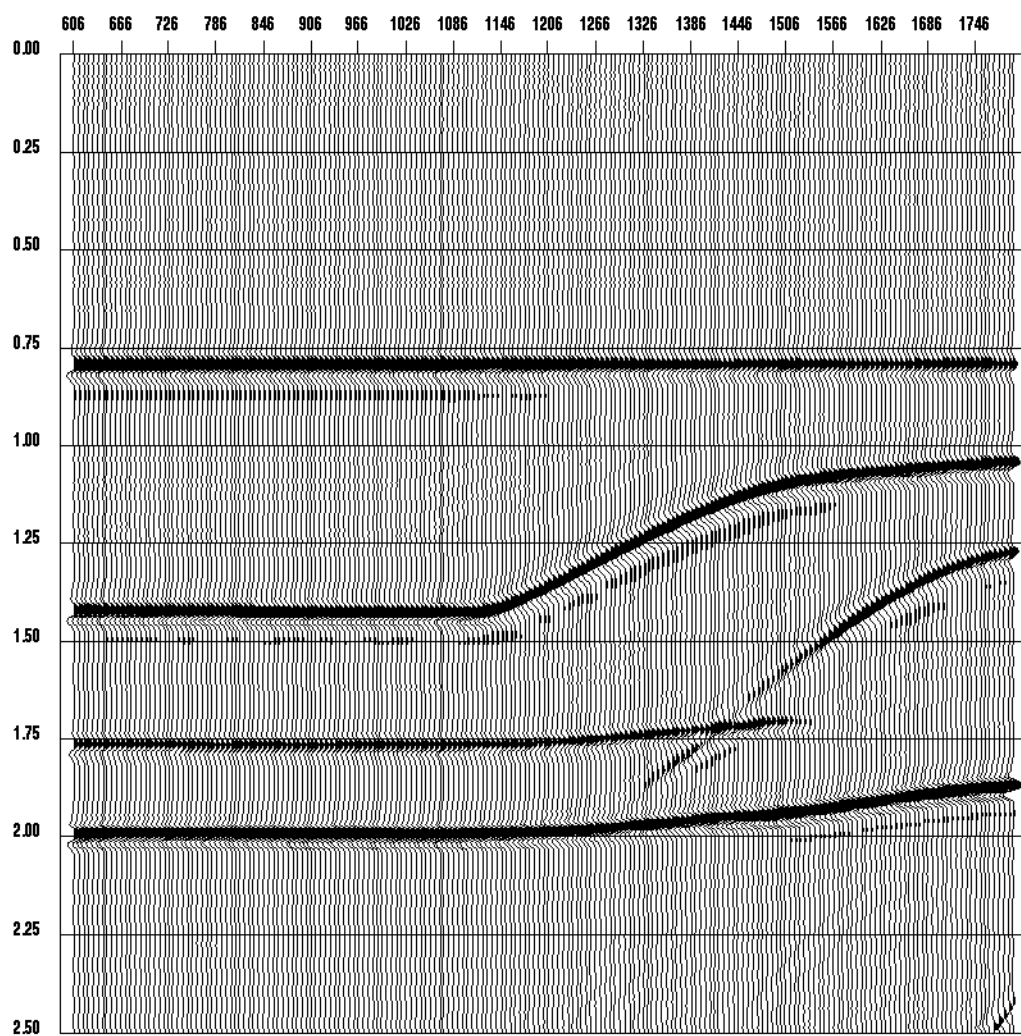
Fig. 6.8. P-P DMO stack.
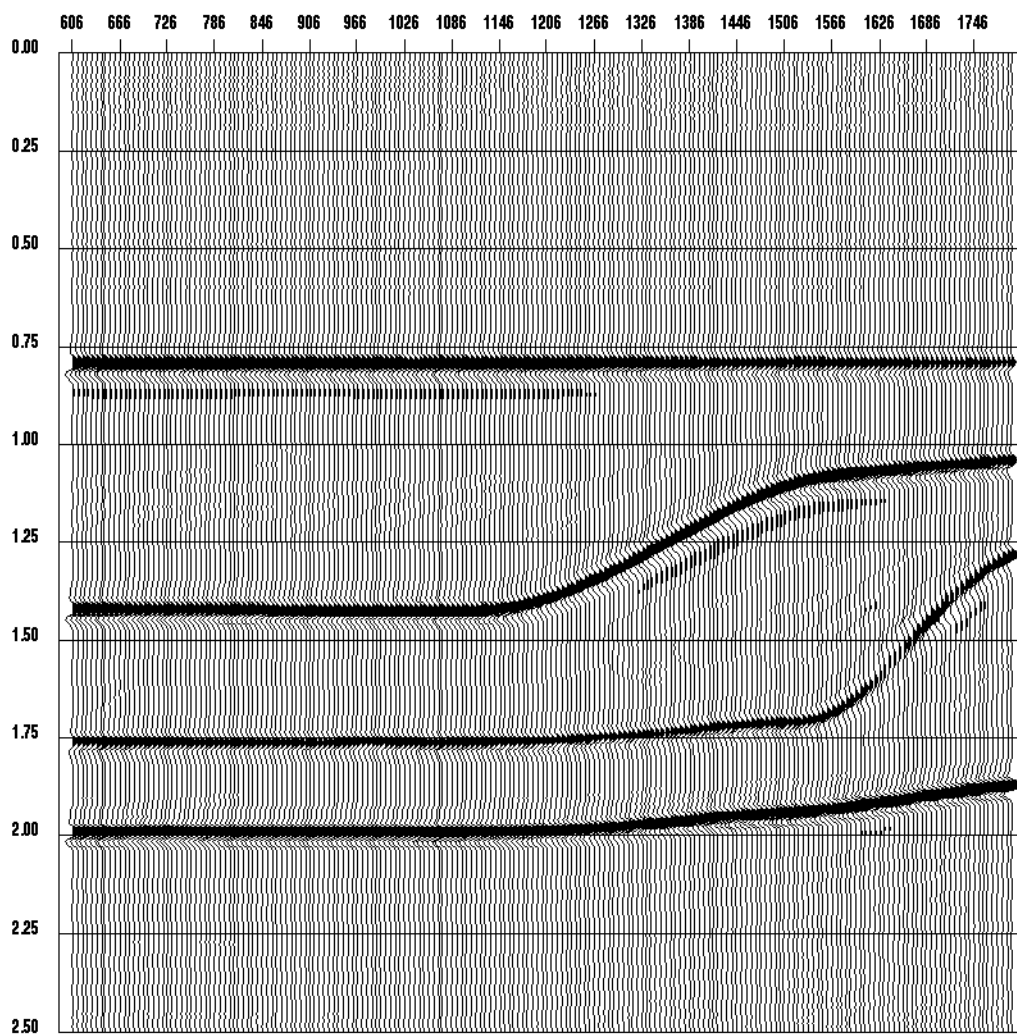
Fig. 6.9. P-P prestack time-migrated stack.
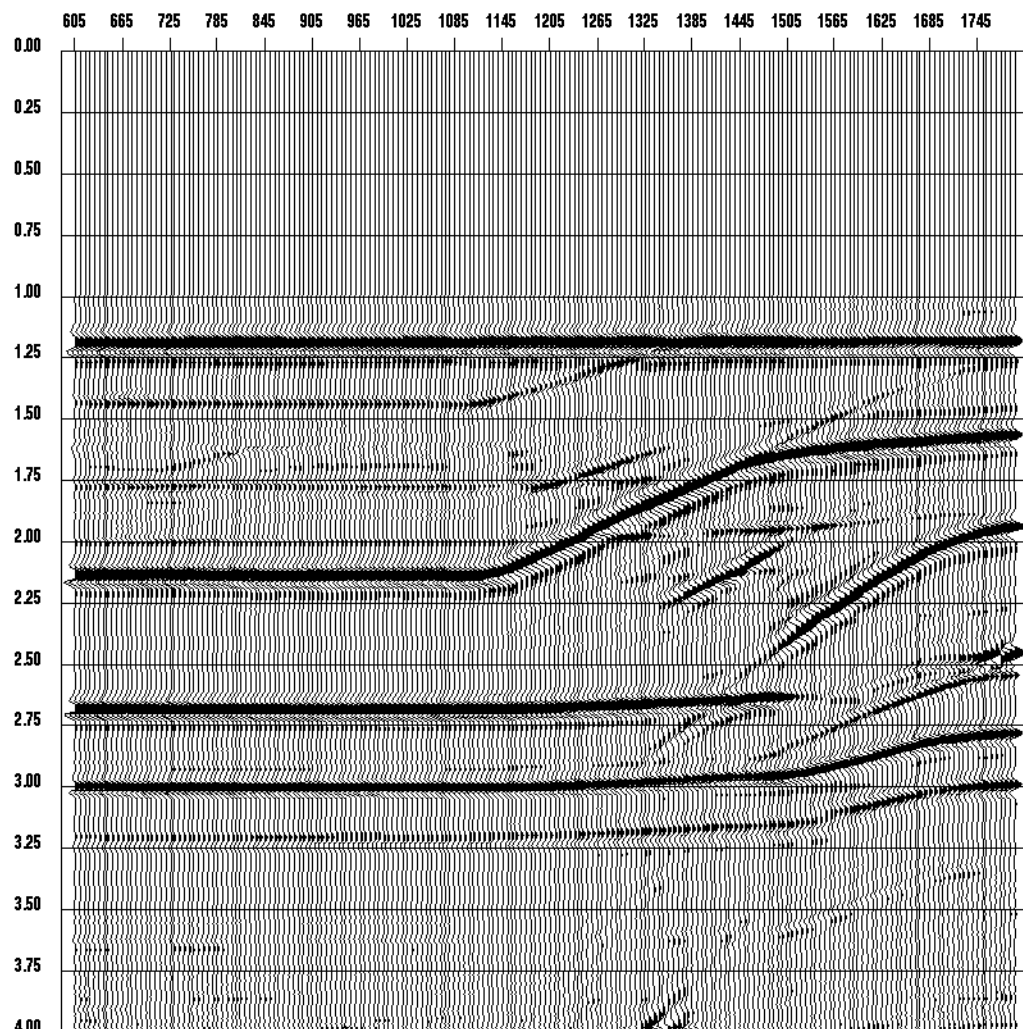
Fig. 6.10. Asymptotic common conversion point (ACCP) stack of P-S data with Vp/Vs=2.0.

First, a constant and slightly erroneous γ_{mig} of 1.8 is used for the transformation of the P-S shot gather into a pseudo P-P shot gather. This is followed by DMO and stack. The pseudo P-P DMO stack is shown in Figure 6.11. The stack does not match the P-P DMO stack (Figure 6.8), in terms of the zero-offset times. However, after stretching the pseudo-section back to P-S time with the same γ_{mig} used for the transformation, the resultant section (Figure 6.12), in terms of P-S time, is very similar to the ACCP stack as shown in Figure 6.10. This suggests that a useful P-S DMO stack can be obtained in the new flow, even with a slight error in γ_{mig}.

Shown in Figure 6.13 is Harrison's P-S DMO (1992) with a γ of 2. Some of the diffraction patterns are lost in Figure 6.13. This may due to the fact that only one P-wave velocity function was supplied to the Harrison's DMO program, selected at the middle of the section.

In the next test, time-and-space variant γ_{ps} functions are used to approximate γ_{mig}. This γ_{ps} is obtained from matching the events between the P-P structural stack and the P-S ACCP stack (see equations 5.20 and 6.3). Figure 6.14 is the pseudo P-P shot gather using γ_{ps} for the transformation. After the transformation, the largest offset changes from 3250 m to about 5000 m. Figure 6.15 shows the limited offset version of Figure 6.14. In Figure 6.16, we now show the pseudo P-P CMP gather, again with limited offsets. Since γ_{ps} is used for the transformation, not only do all 4 events shown in Figure 6.16 look symmetric,
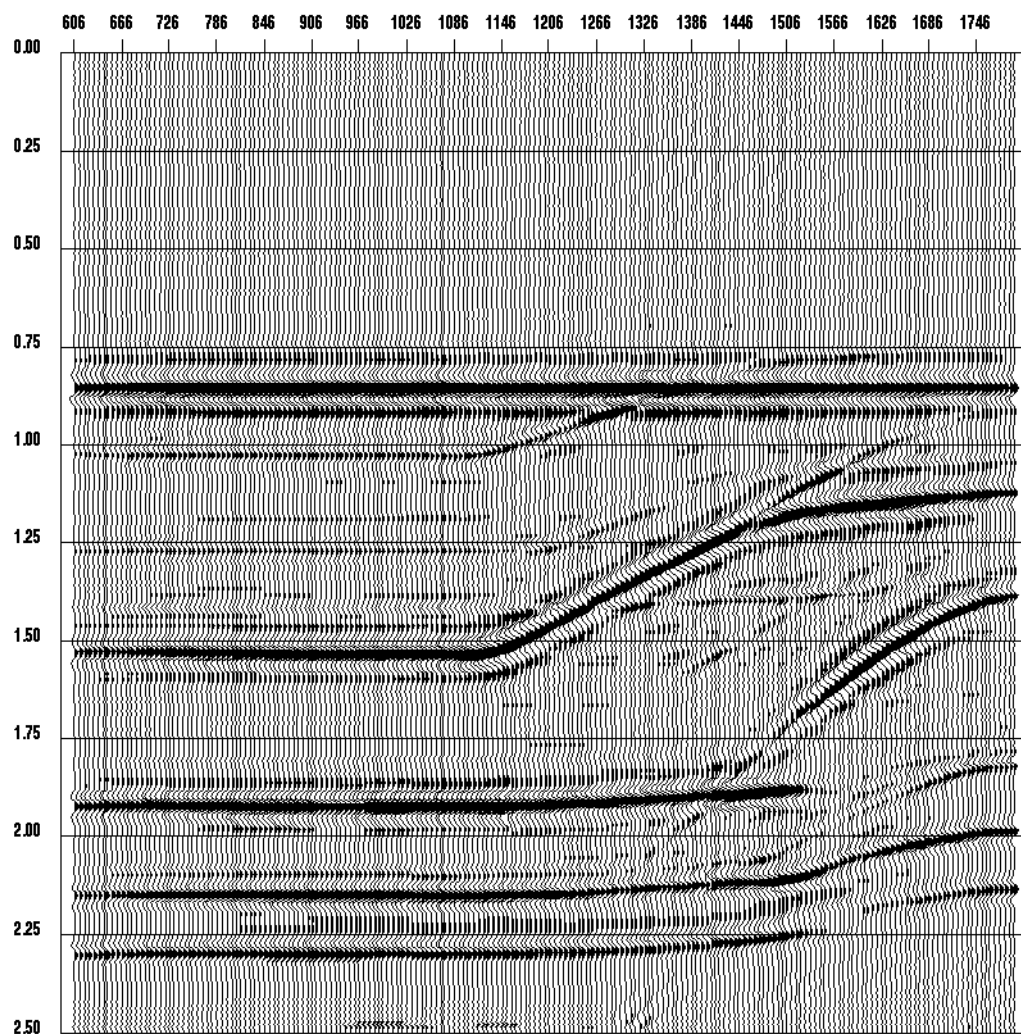
Fig. 6.11. Pseudo P-P DMO stack. A constant γ_{mig} = 1.8. is used for transformation. Note that the times of the events do not match with the true P-P DMO stack in Figure 6.8. Most of the strong artificial events are generated by P-P leakages and the artifact from the modeling program.
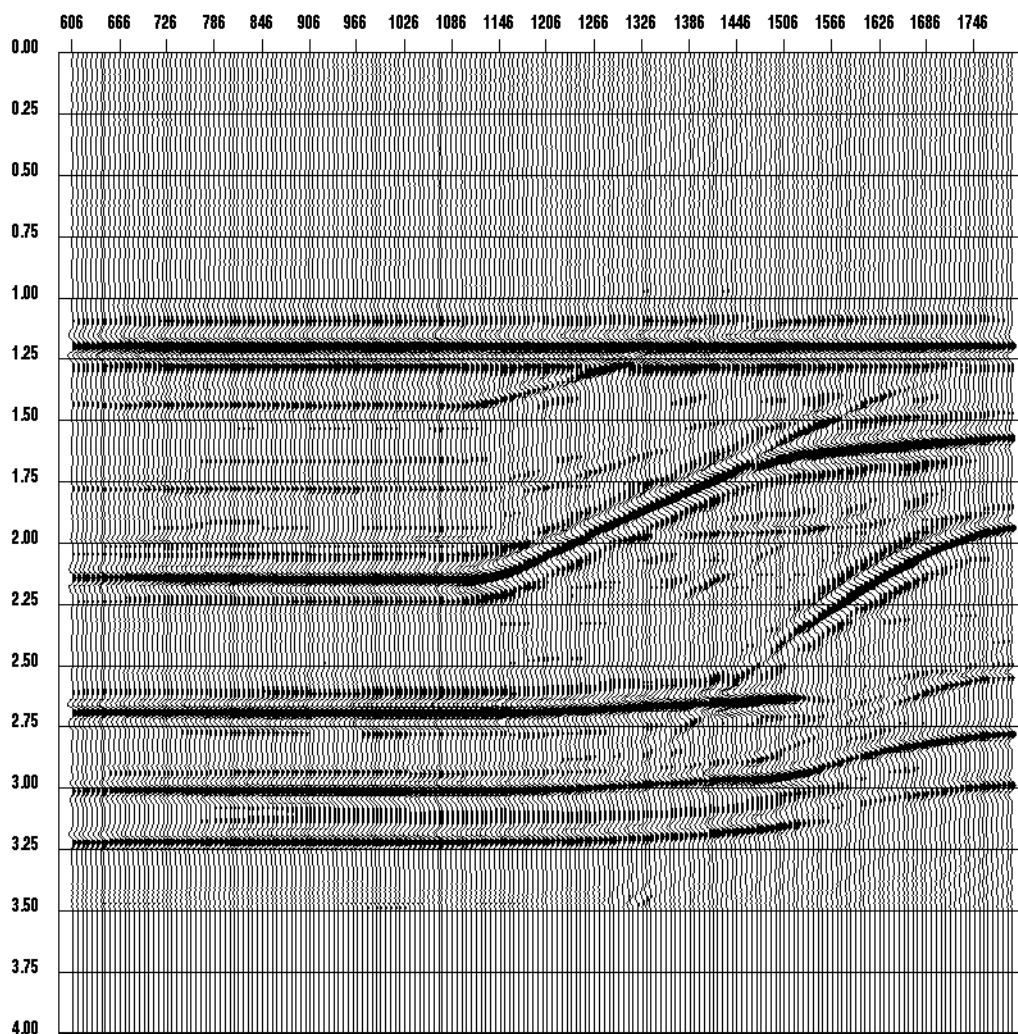
Fig. 6.12. The pseudo P-P DMO stack is vertically stretched in P-S time using γ_{ps} =1.8. The times of the events are similar to the ACCP stack in Figure 6.10.
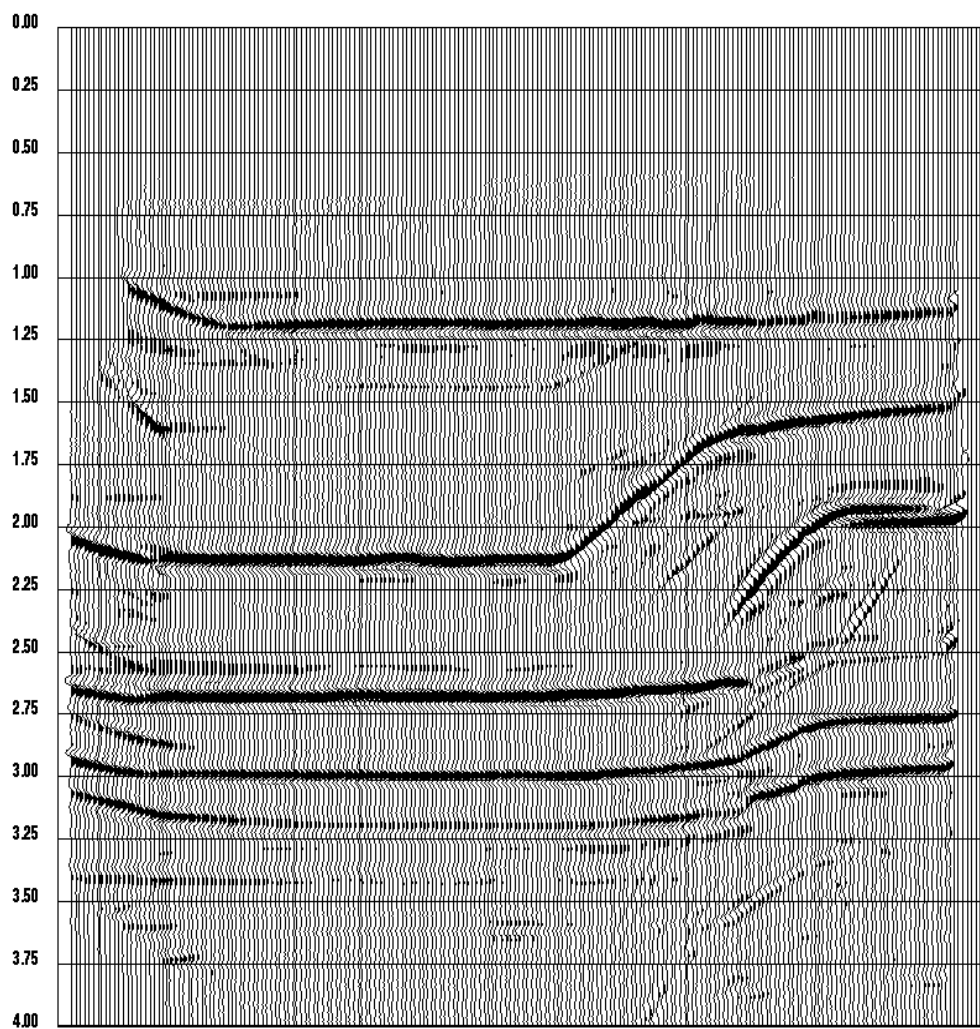
Fig. 6.13. Harrison's P-S DMO with γ=2.0. A single P-wave velocity function at the middle of the section is used.
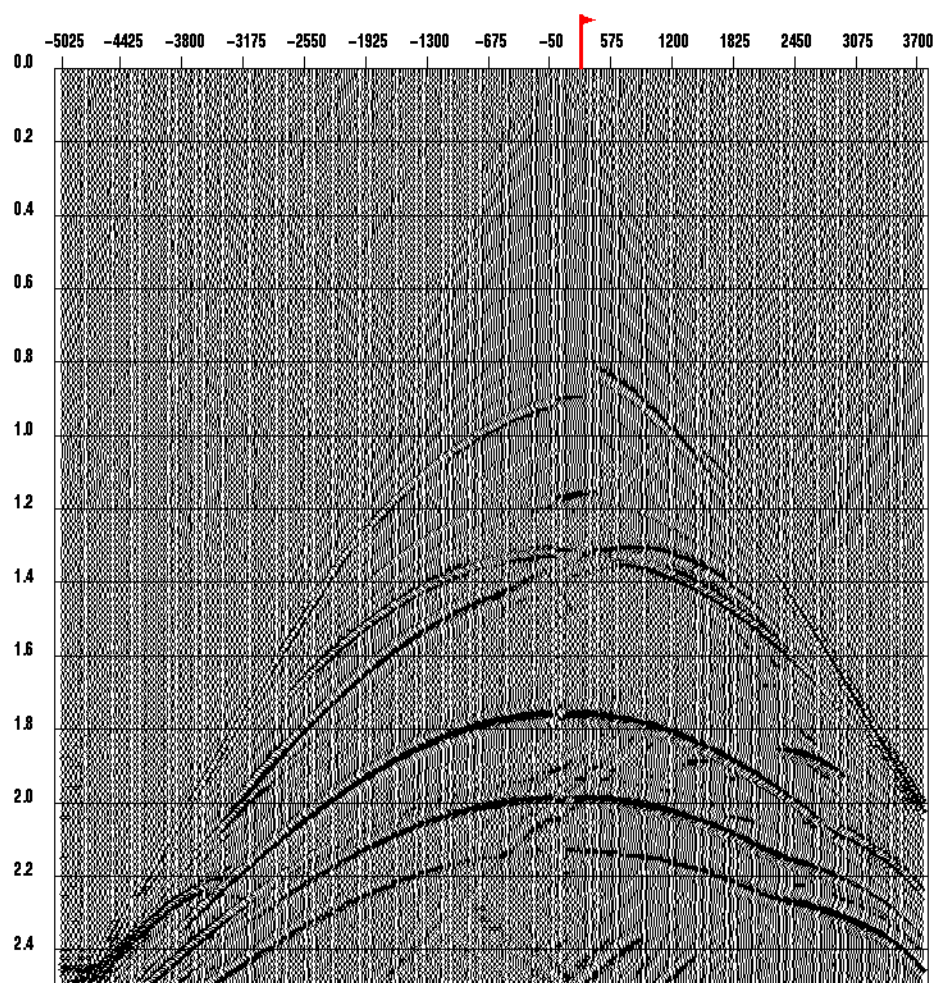
Fig. 6.14. The pseudo P-P shot gather at station 1200, using estimated γ_{ps} values.
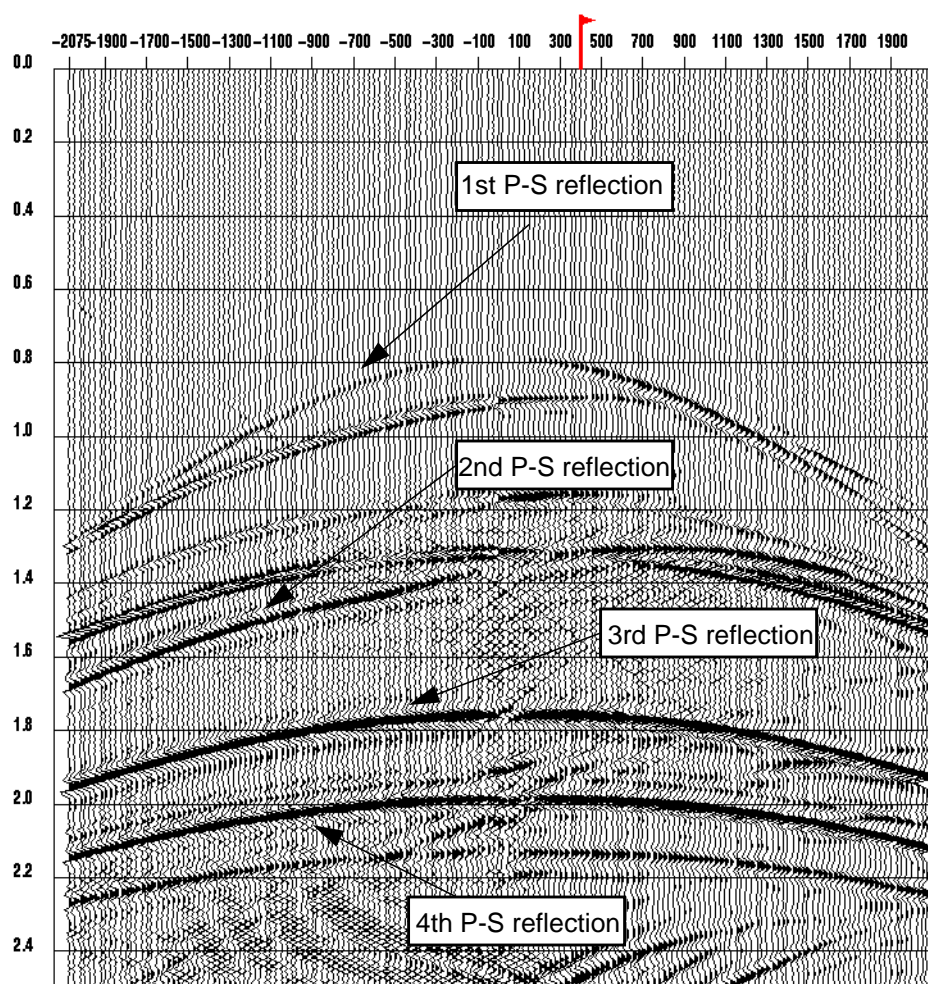
Fig. 6.15. Smaller offset range of Figure 6.14.
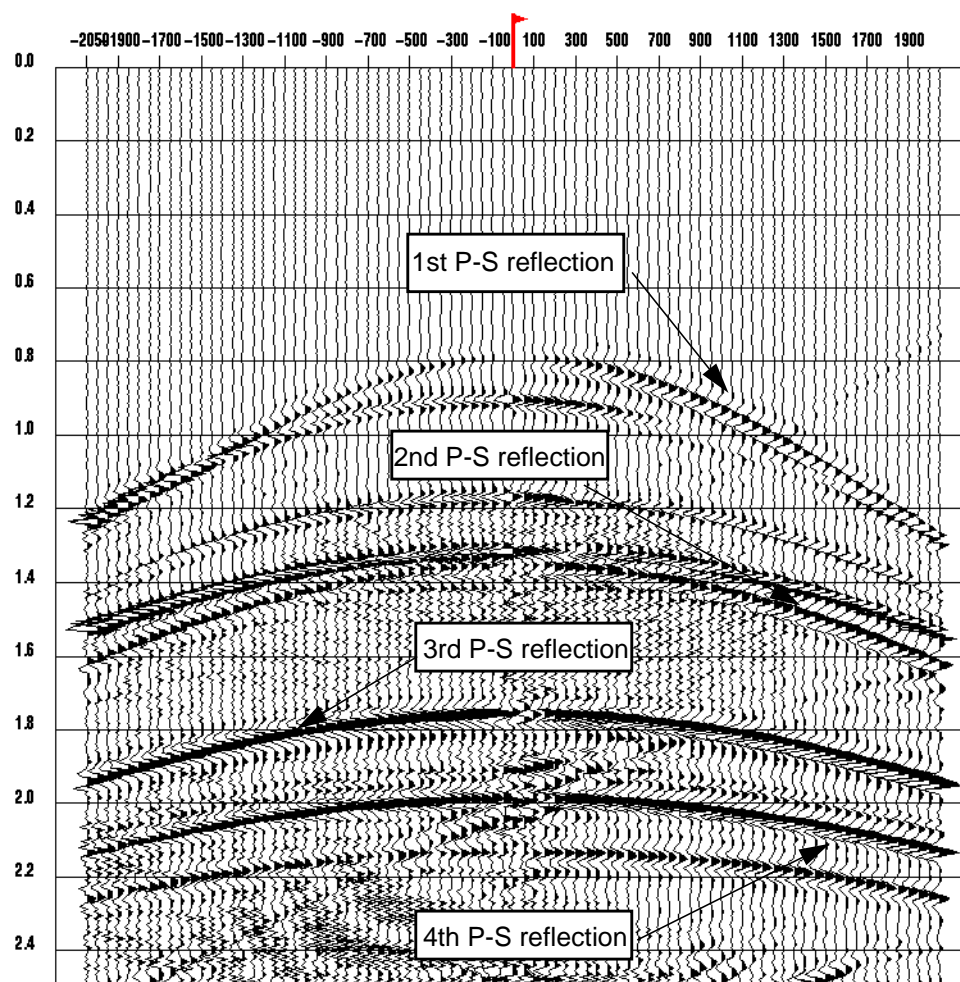
Fig. 6.16. The pseudo P-P CMP gather at station 1200. The reflection from the second layer is now symmetric.

but also the pseudo P-P times are in good agreement with the true P-P times (Figure 6.6).

Figure 6.17 is the new pseudo P-P DMO stack, and it is in general agreement with the true

P-P DMO stack (Figure 6.8). There are some mis-ties at around station 1606 for the last

layer where there is a significant lateral velocity variation. Figure 6.18 is the pseudo P-P

DMO stack stretched using the time variant γ_{ps} functions, and plotted in the P-S time. This

also represents the P-S DMO stack. The pseudo P-P prestack gathers are also migrated with

the P-P prestack time migration algorithm and the stack is shown in Figure 6.19.

The receiver version of the AMOC was also tested. Figures 6.20 and 6.21 are the pseudo

P-P receiver gathers at station 1194, and the pseudo P-P CMP gather at station 1200 respec-

tively, i.e., after AMOC. The resultant pseudo P-P DMO stack is shown in Figure 6.22. It

is similar to Figure 6.17 but it is noisier, especially on the top. This is may due to the loss

of offset after AMOC, indicating that and the far offset traces should possibly have been

muted before stack.

From the above tests, it is observed that the γ_{mig} values used for the AMOC are not un-

duly sensitive to errors. The reason is that during the final velocity analysis, optimum pseu-

do P -velocities, other than the original P-velocities, are picked to stack the pseudo P-P

gathers. However, it is important to understand that the quality of the stack is dependant on

the velocity we pick to stack, and the lateral conversion point curve with depth is affected

by the γ_{mig} we choose for the transformation.
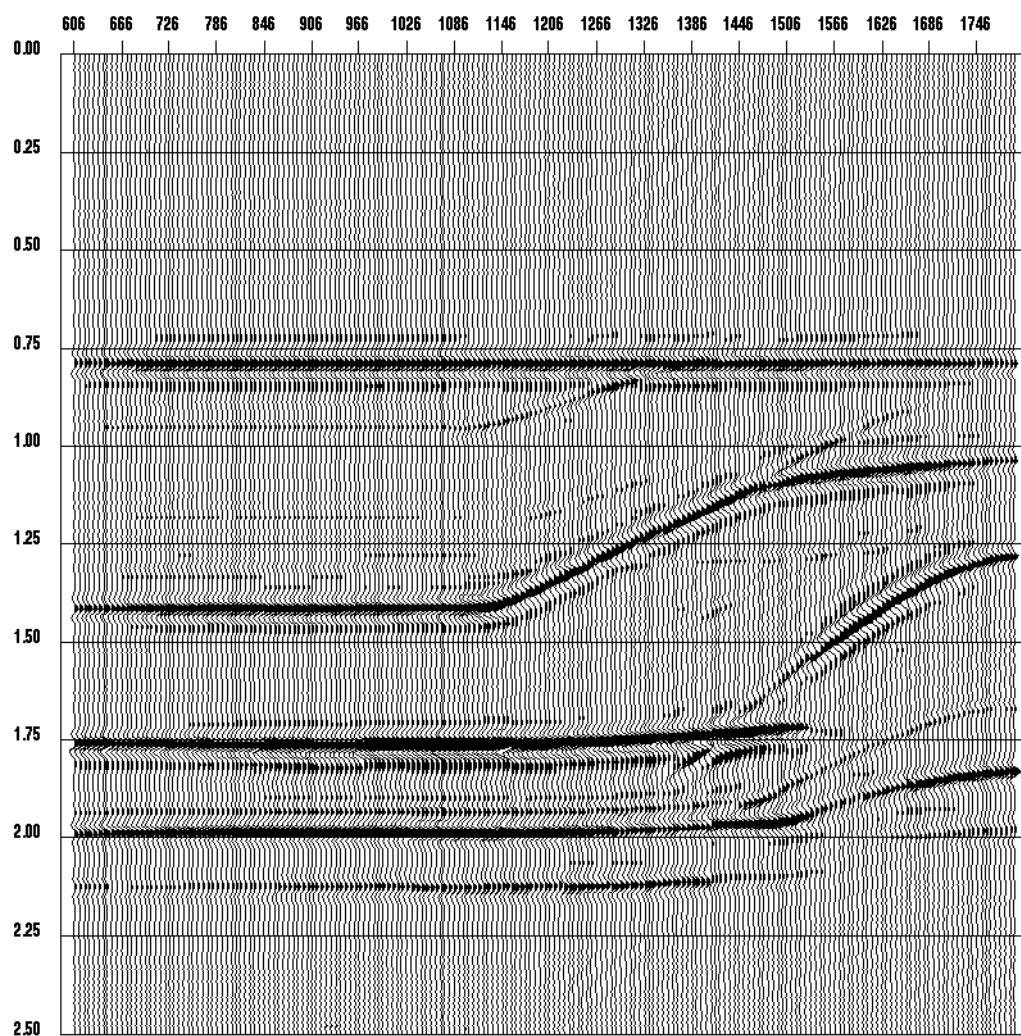
Fig. 6.17. The pseudo P-P DMO stack with time-and-space variant $\gamma_{mig} = \gamma_{ps}$ values. The times of the events match well with the true P-P DMO stack, except a slight mis-match of the layer occurs at around station 1606.
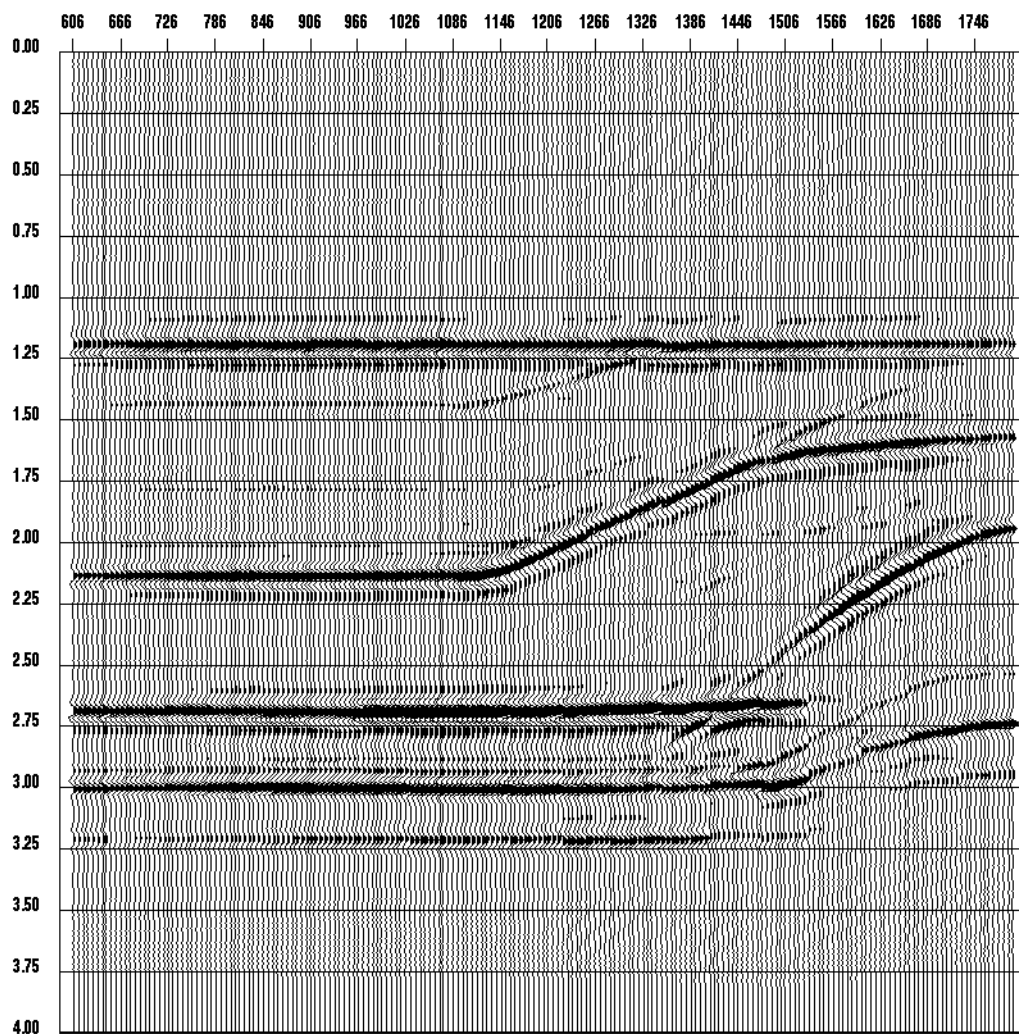
Fig. 6.18. The pseudo P-P DMO stack in P-S time. It is vertically stretched with the γ_{ps}. This stack also represents P-S DMO stack.
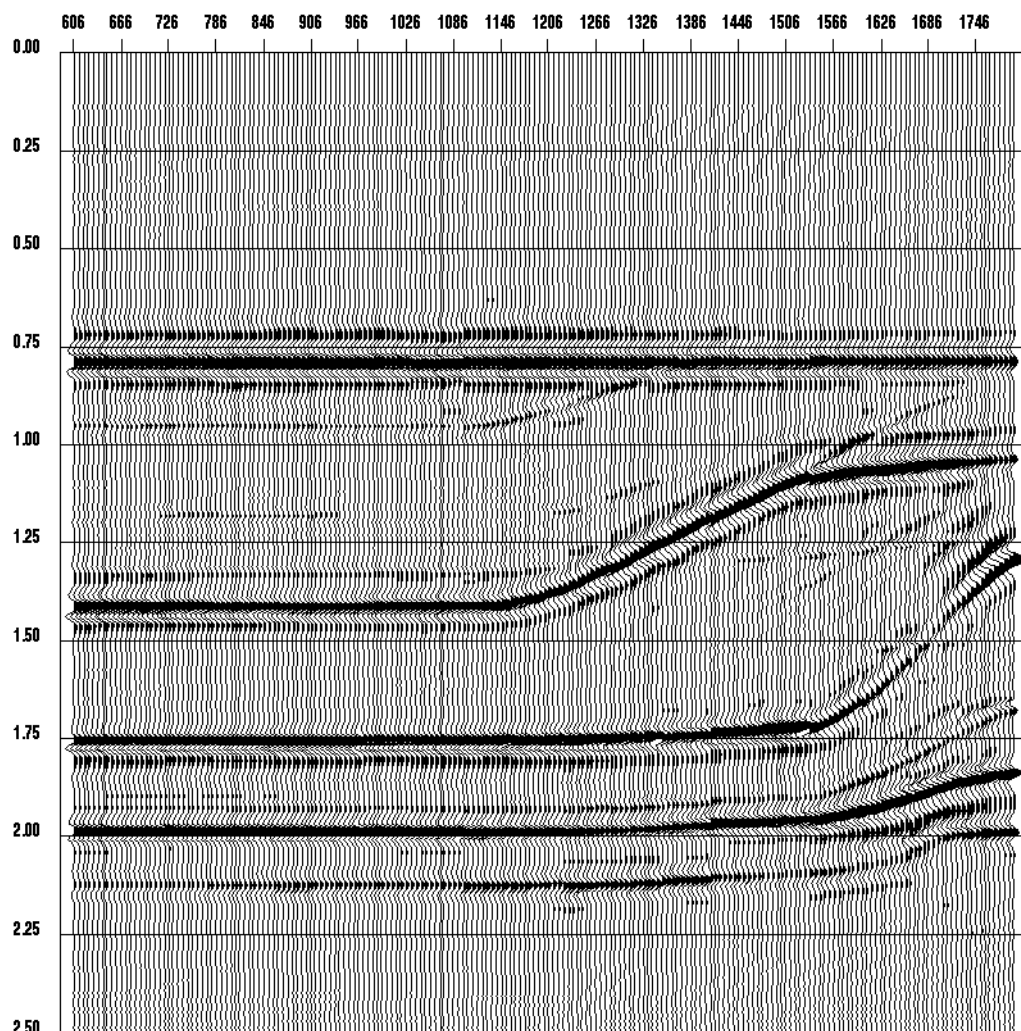
Fig. 6.19. The pseudo P-P prestack time-migrated stack. The events closely match those in Figure 6.9, the true P-P time-migrated stack.
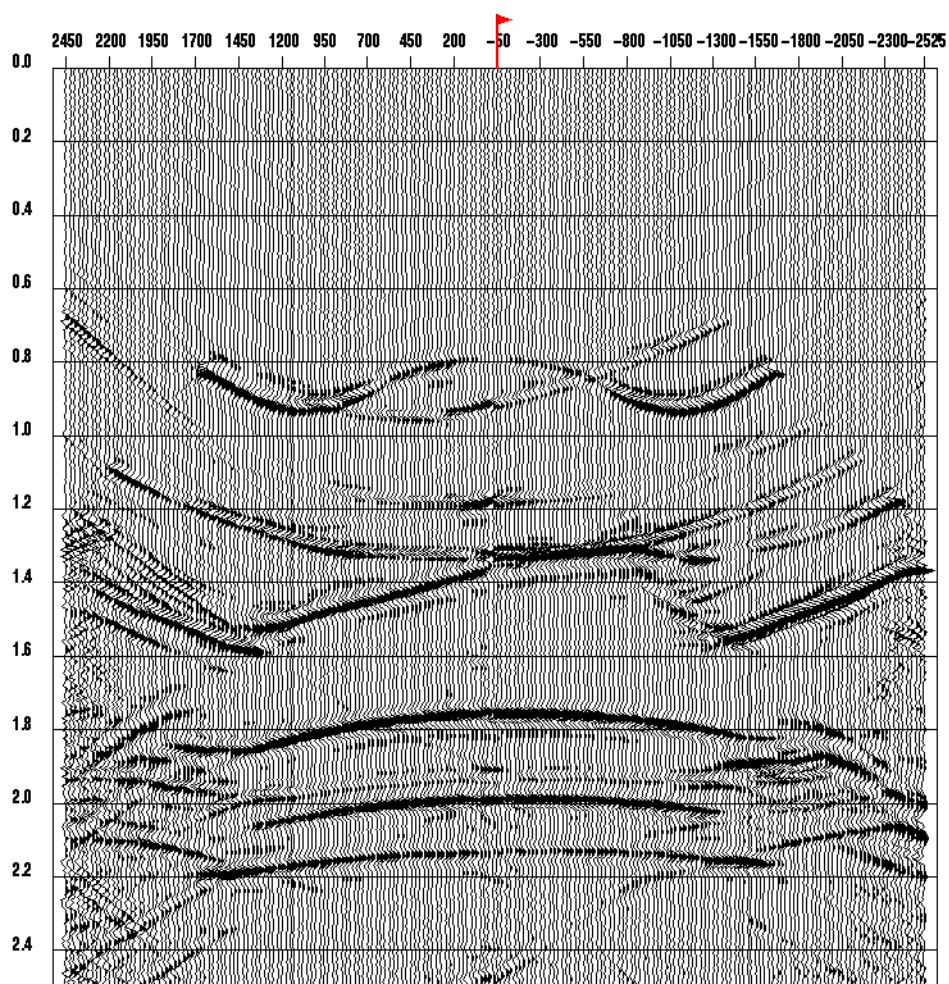
Fig. 6.20. The pseudo P-P receiver gather at station 1194. The AMOC is applied to common re-ceivers. Note that the valid offset of the events is less than the original gather.
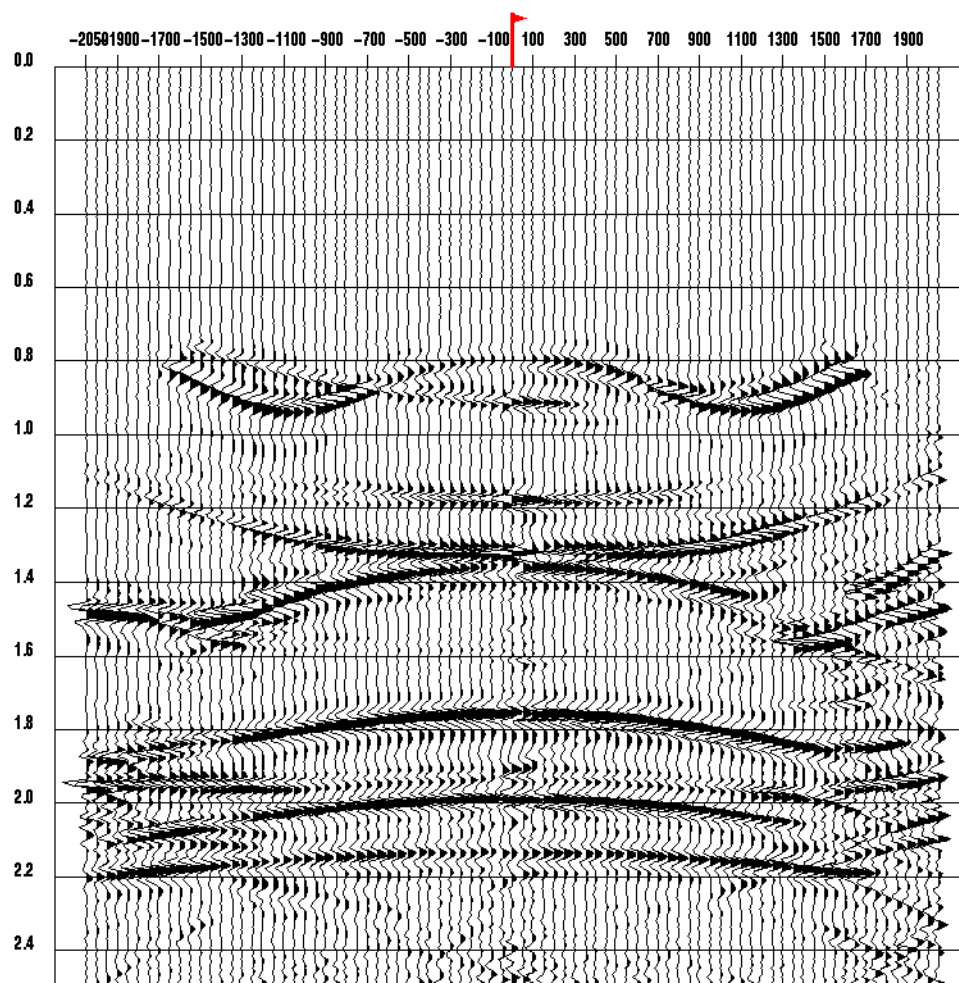
Fig. 6.21. The pseudo P-P CMP gather at station 1194. The AMOC is applied in receiver-domain.
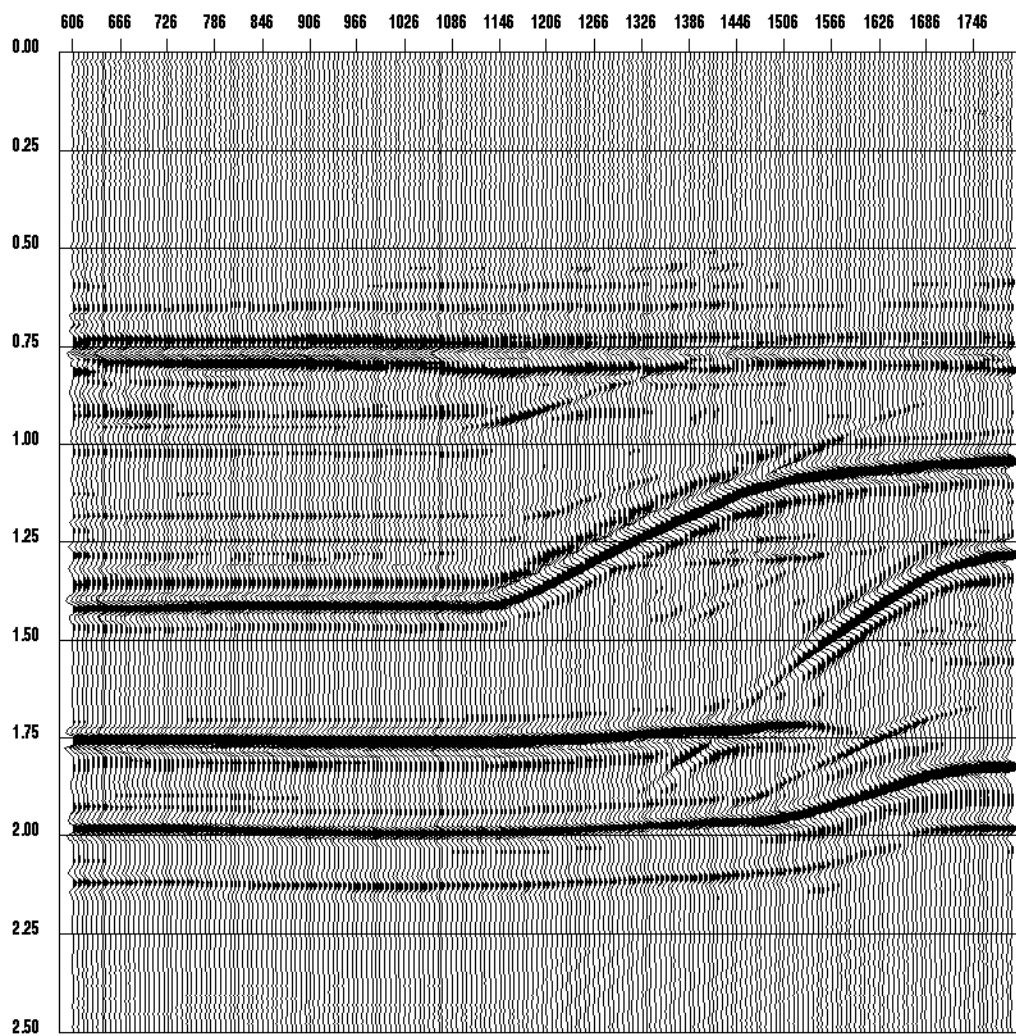
Fig. 6.22. The pseudo P-P DMO stack with the AMOC transformation applied in the receiver-domain.

6.4 Alternative processing of P-S data

After the transformation of P-S data into the pseudo-symmetric P-P data, it is shown that the pseudo data can be CMP binned and processed in the same manner as the normal P-wave data with existing P-wave processing tools. It is believed that, receiver statics determination and velocity analysis are easier after AMOC, especially for structural data. Unfortunately, the zero-offset, two-way pseudo P-wave traveltime cannot be used to correlate with the true P-wave time, unless γ_{mig} is very close to γ_{ps} (equation 6.2), or γ_{ps} is used for the transformation. However, the pseudo P-P stack section can be converted back to P-S zero-offset time by vertical stretch with the same γ_{mig} functions used for the transformation.

6.4.1 Statics

The conventional way of calculating the residual receiver statics for P-S data is from NMO-corrected ACCP gathers, in which no trace mixing has occurred because the conversion point is presumed time invariant. In the ACCP gather, the moveout curves can be corrected and stacked, assuming hyperbolic moveout, and form a pilot trace for the statics correlation. However, because of the wide lateral spread of the conversion point within an ACCP gather, when the earth is not flat, the ACCP stack may be poor quality.

Here, we suggest an improved approach using AMOC. To produce the pseudo P-wave

data, P-S data first have P-wave shot statics applied, followed by the receiver-domain AMOC (with $\gamma_{mig} = 2$ in the transformation). Because the transformation mixes traces among the shots only, but not the receivers, the transformed receiver gathers preserve the receiver surface consistency. The pseudo P-wave data are then sorted into the CMP domain, followed by velocity analysis and NMO correction. If the γ_{mig} used in the transformation was time variant, the statics would become dynamic after the transformation, due to a non-linear time stretch/squeeze operation. However, the problem can be solved by stretching the NMO-corrected CMP data into P-S time, using $\gamma_{ps} = \gamma_{mig}$. At this point, conventional surface-consistent statics routines can be followed to estimate the receiver statics.

Shown in Figure 6.23 are receiver statics, after applying the P-P shot statics, calculated from different methods on the Blackfoot example. The first trace is the f-x statics plotted at the appropriate receiver station numbers. The second group of the traces are 9 iterations of conventional statics from ACCP gathers, and the last group of the traces are 9 iterations of conventional statics from the receiver-domain AMOC pseudo CMP gather. It is observed that the statics calculated from the pseudo P-P gathers shows some correlation with f-x statics, and with little high frequency in AMOC statics. After the receiver-domain AMOC, the data at the far offset become pure noise. These far offset data should have been ignored during residual statics calculation, and the high frequency component of the statics may have been improved.
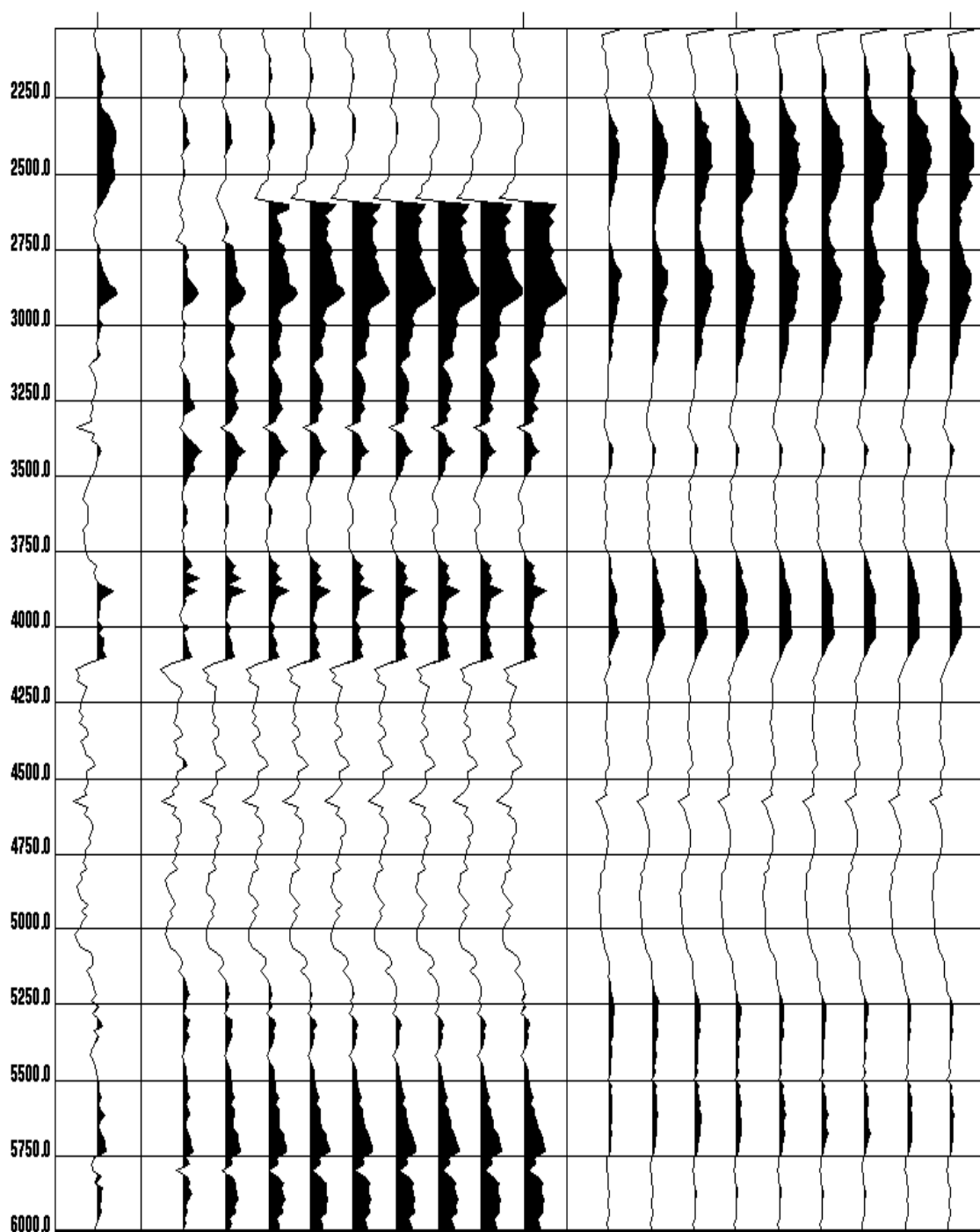
Fig. 6.23. The first trace is a plot of the f-x receiver statics. The second group contains 9 iterations of the receiver statics from the ACCP gather. The third group contains 9 iterations of the receiver statics calculated from the receiver-domain AMOC.

The next three figures show the comparison between the pseudo P-P receiver statics and the f-x statics applied to the shot at station 4810. Figure 6.24 is the shot at station 4810 without residual statics applied. Figure 6.25 is the same shot with pseudo P-P receiver statics applied and Figure 6.26 with the f-x statics applied. Both statics results show improvement over the shot without any receiver statics applied. It is observed that a small amount of long wavelength component difference is observed between the pseudo P-P AMOC receiver statics and the f-x statics.

Figure 6.27 is pseudo P-wave stack after applying the P-wave shot statics, but without receiver statics applied. Figure 6.28 has receiver statics applied in the manner outlined, while Figure 6.29 has previous calculated f-x receiver statics applied. Both stacks show more coherence than the one in Figure 6.27, suggesting that the statics have been improved. Only minor differences, mainly in the regional trend, are observed between Figure 6.28 and Figure 6.29.

For comparison, the statics calculated in the AMOC domain are applied to the ACCP stack (Figure 6.30). This is to be compared to the ACCP stack where shot and receiver statics have also been calculated in the conventional way (Figure 6.31, same as Figure 2.8). The major difference is due to the cycle skipping occurred in Figure 6.31.

It is also observed that the quality of the AMOC stack at the top is worse than the ACCP stack. It is believed that, at the top of the section, the usable offset range is reduced after the receiver-domain AMOC, causing reduced signal-to-noise ratio at the top after stack.
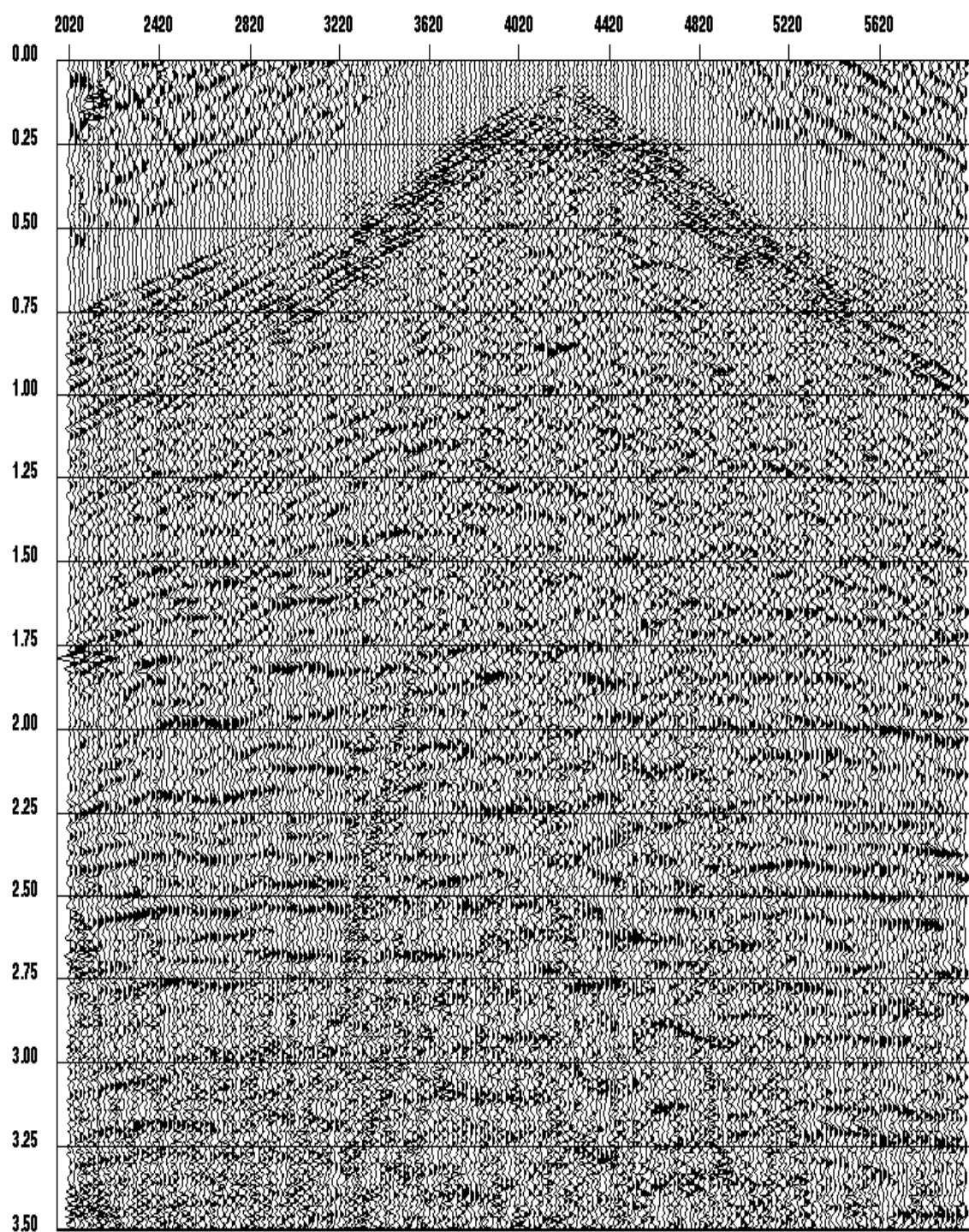
Fig. 6.24. Shot record at station 4810 without residual receiver statics applied.
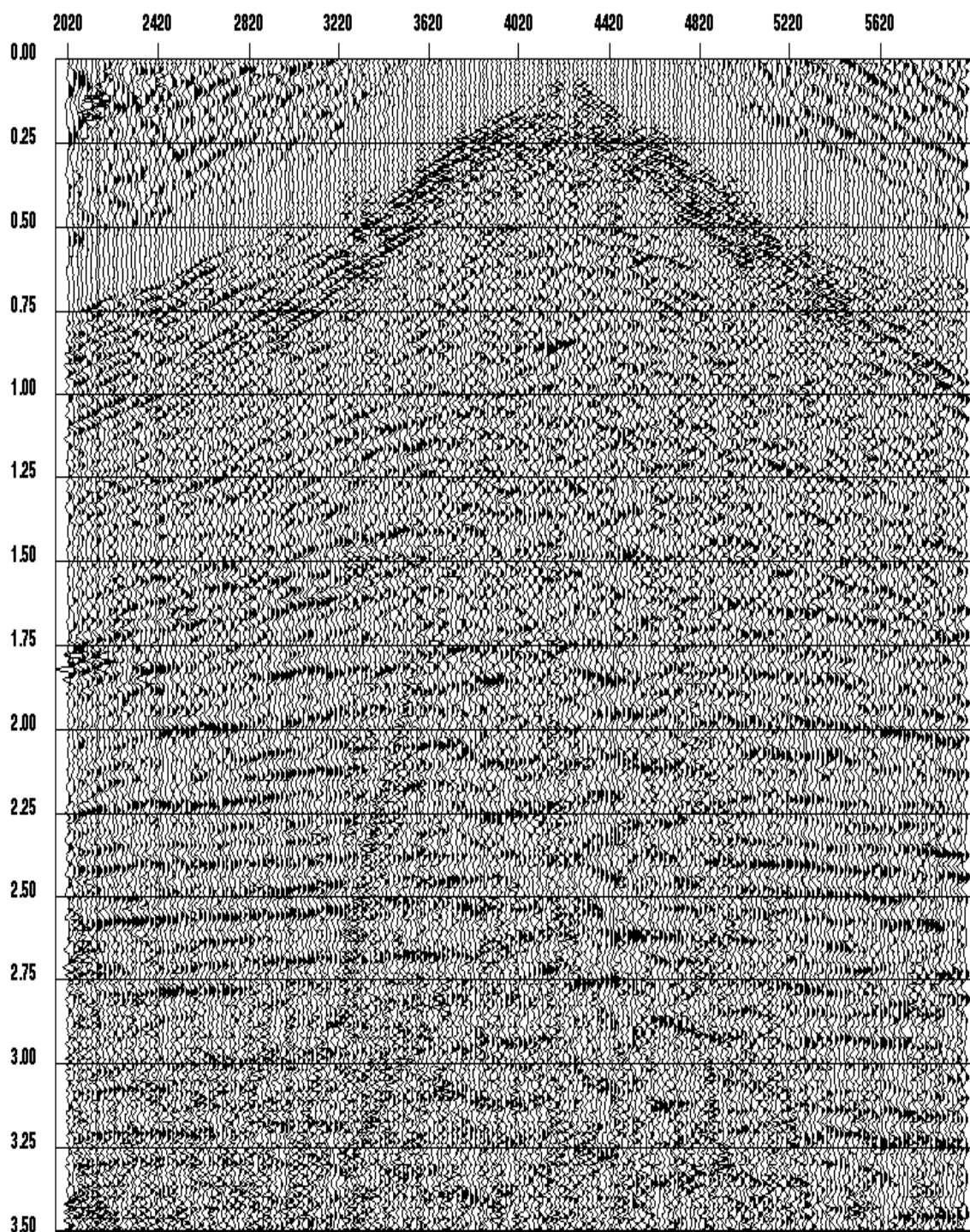
Fig. 6.25. Shot record at station 4810 with pseudo P-P AMOC residual receiver statics applied.
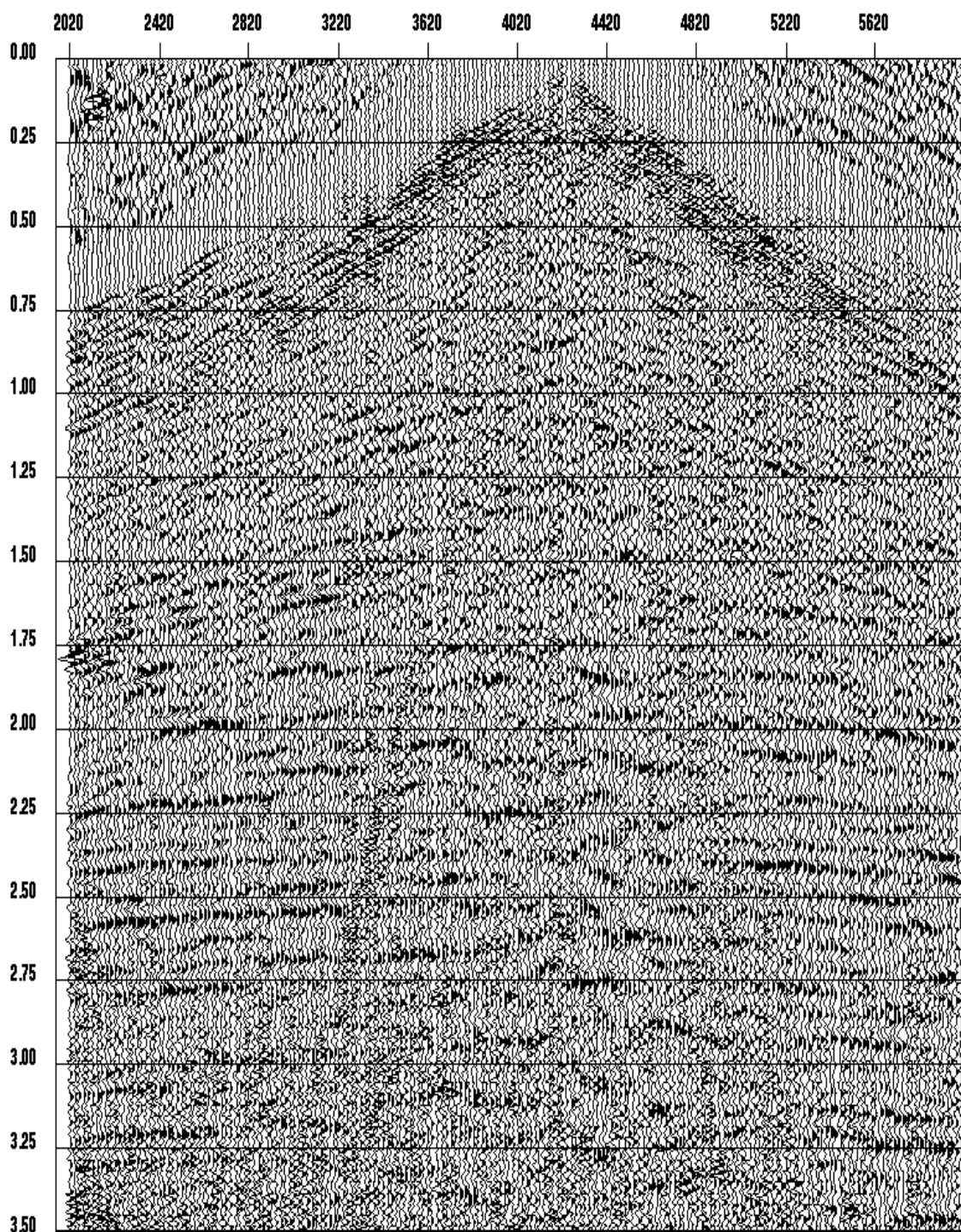
Fig. 6.26. Shot record at station 4810 with f-x statics applied.
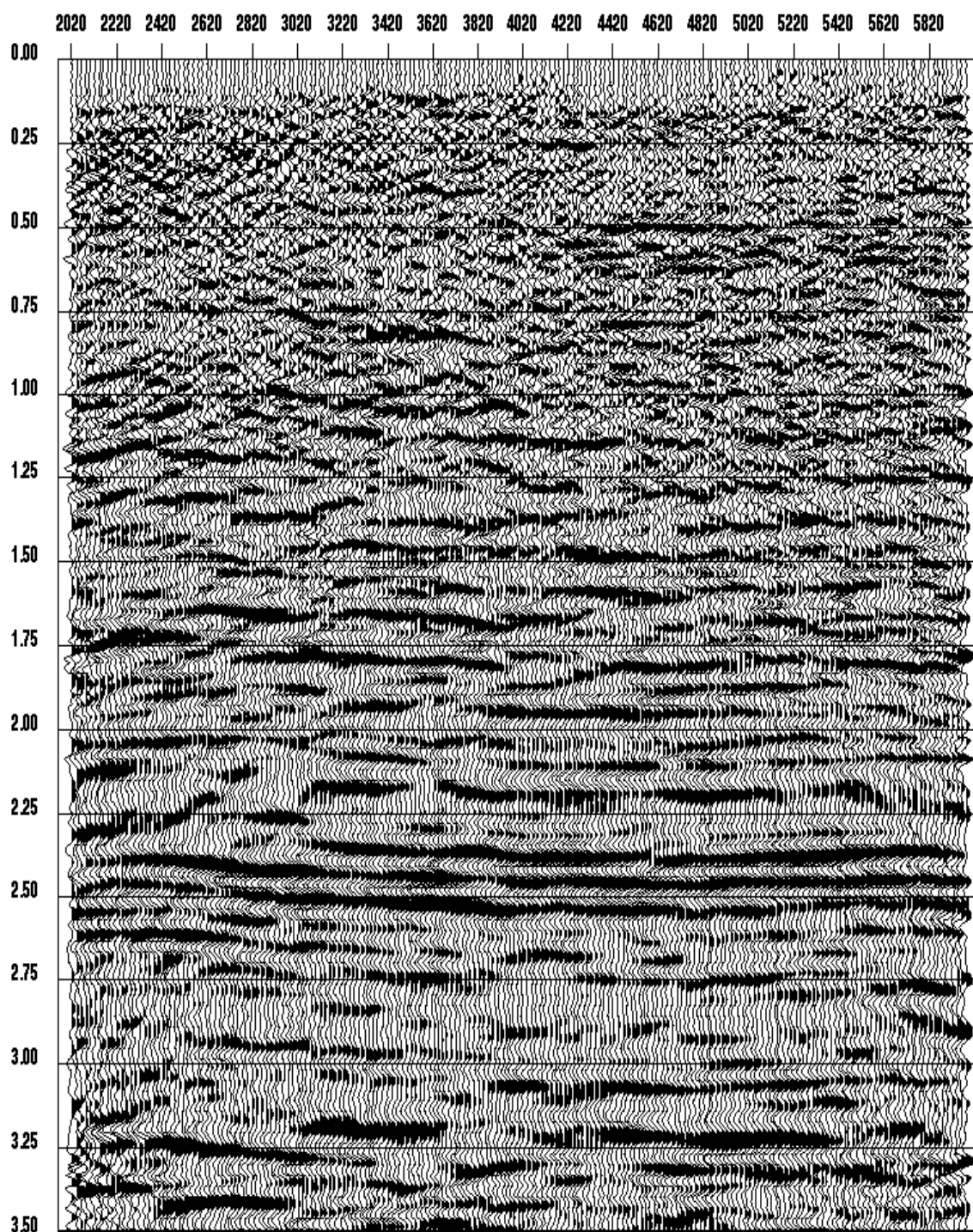
Fig. 6.27. Pseudo P-P stack after receiver-domain AMOC, without receiver statics.
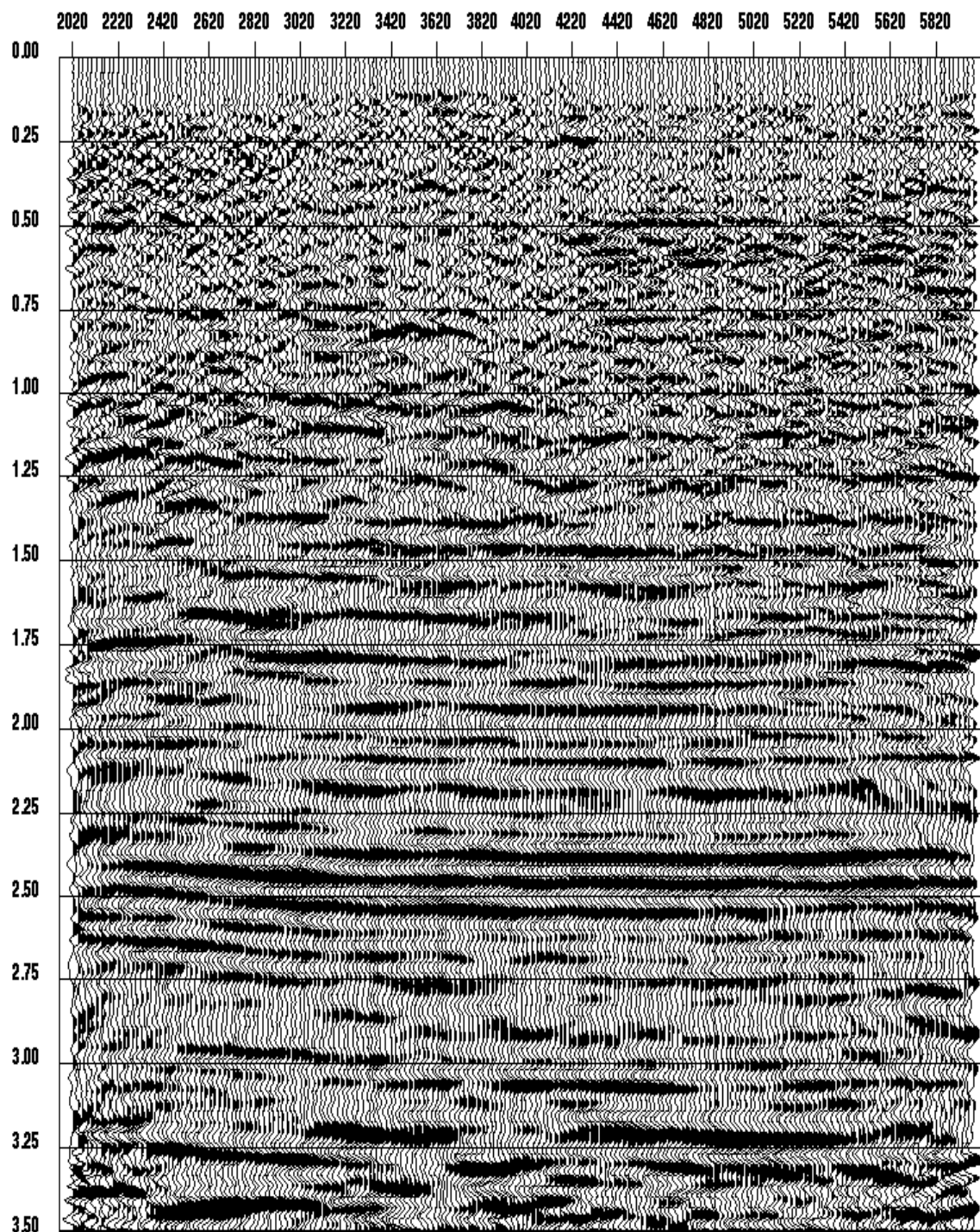
Fig. 6.28. Pseudo P-P stack after receiver-domain AMOC, with receiver statics solved after receiver-domain AMOC.
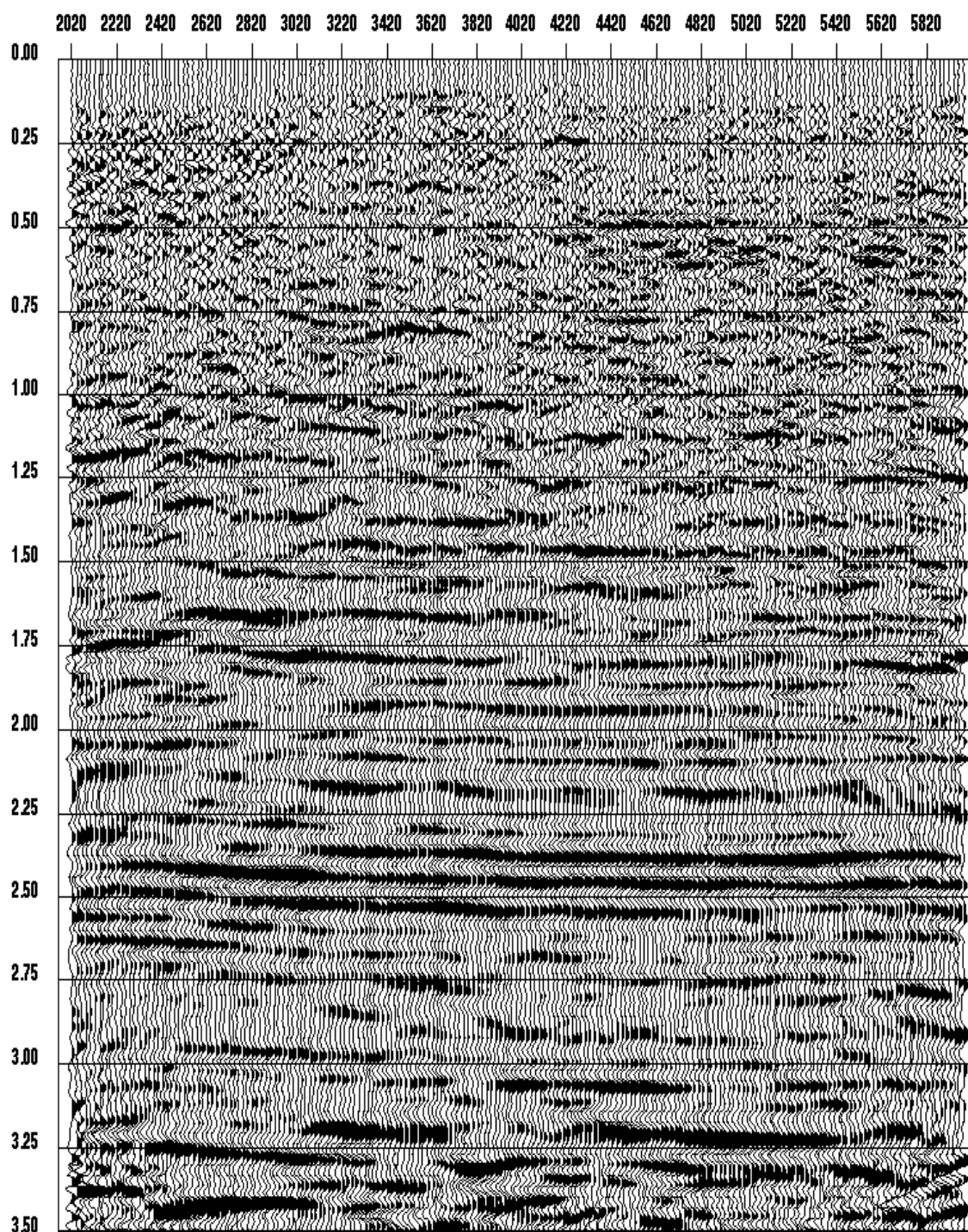
Fig. 6.29. Pseudo P-P stack after receiver-domain AMOC, with previous calculated f-x receiver statics applied.
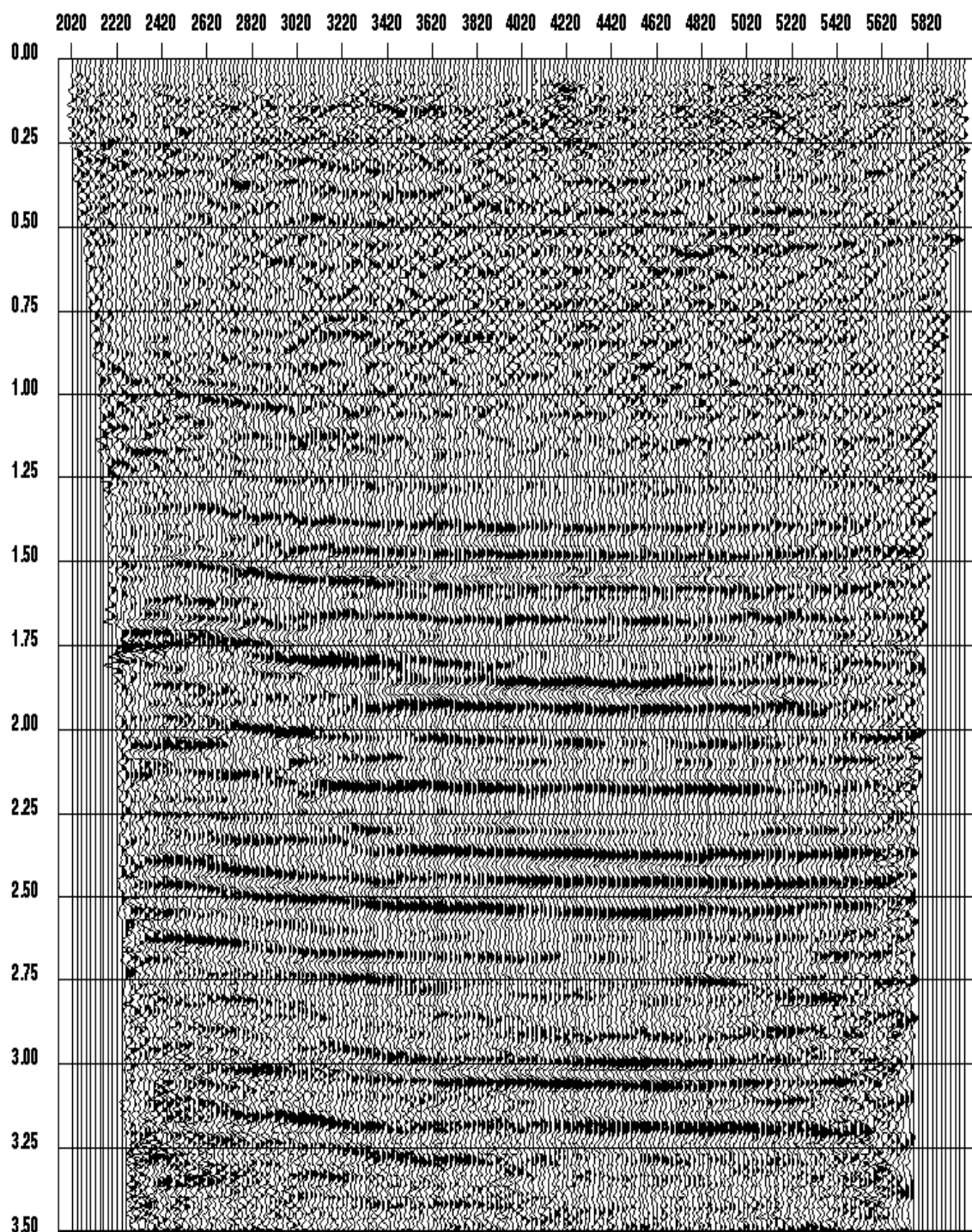
Fig. 6.30. ACCP stack with AMOC residual receiver statics applied.
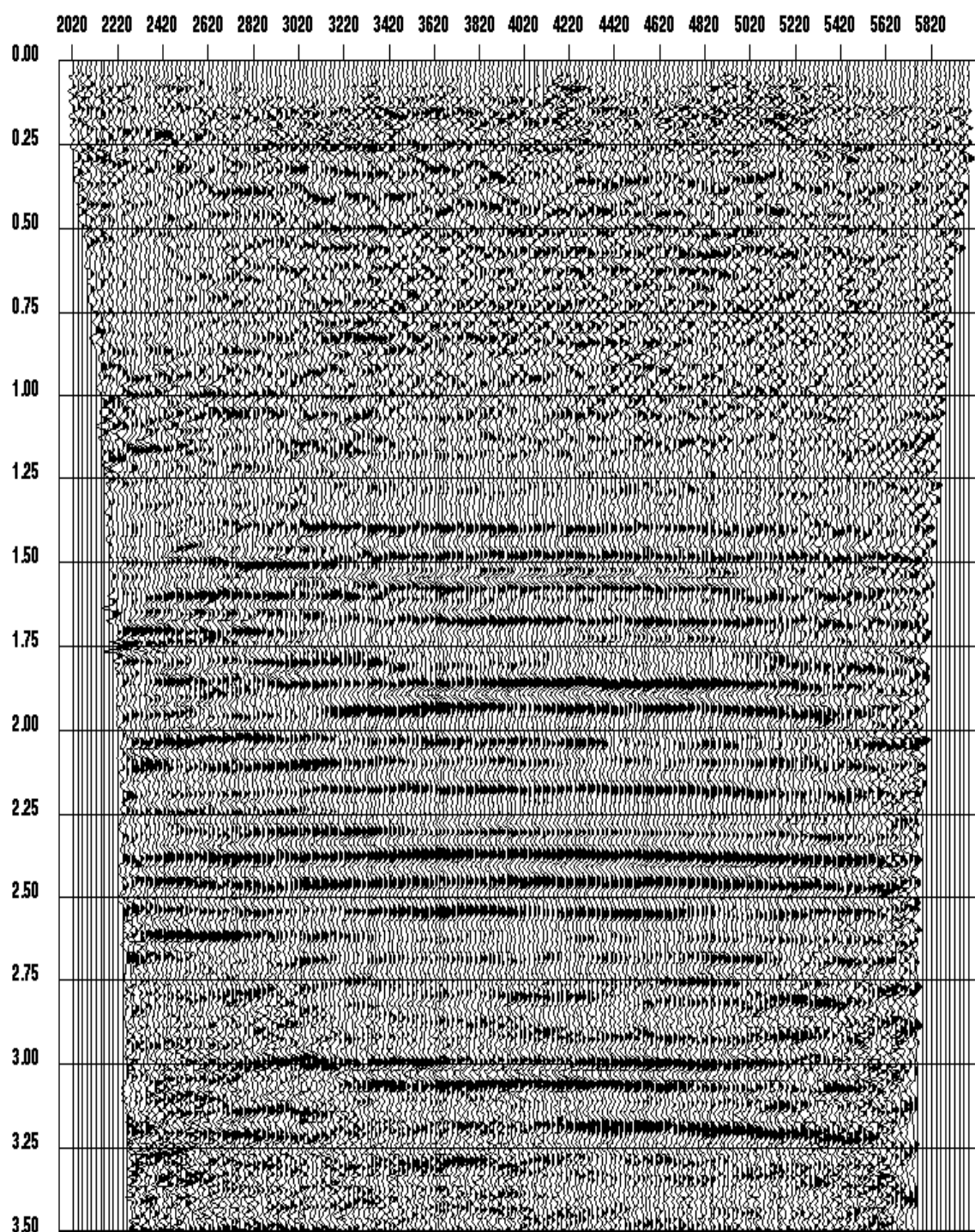
Fig. 6.31. ACCP stack with conventional residual receiver statics applied (same as Figure 2.8).

Nevertheless, the tests suggest that the statics can be calculated after the receiver-domain AMOC. The importance of the AMOC statics is that they can be applied to structural data, while the ACCP stack may not.

6.4.2 Structural stack

To get a better AMOC stack, we go back to the shot-domain AMOC.

After applying the shot and the receiver statics to the original P-S data, the shot-domain AMOC transformation is applied and the data are sorted into CMP gathers. At this point, we leave the data in the pseudo P-P domain, so a P-P velocity analysis can be done. If the proper γ_{mig} is used for the transformation, the velocity analysis will follow the same trend as the true P-wave velocity function. Figure 6.32 is the velocity semblance of the pseudo CMP gather at station 4310. The velocity function picked from the original CMP gather is overlain on the semblance. Although the contours are not focused on the original pick times (because T_{pp} and $\tilde{T}_{pp}$ are different), they follow a similar trend. The small difference between two trends can be considered as a residual correction term due to errors in the γ_{mig} used in the transformation. Structural stacks with the original P-P and new picked velocities are shown in Figure 6.33 and Figure 6.34 respectively. Both stacks show improvement on the top (above 0.75 s) over the receiver-domain AMOC stack, and the stack with new velocities shows overall better quality. (Note that after stack we have stretched the time axis back to P-S time).
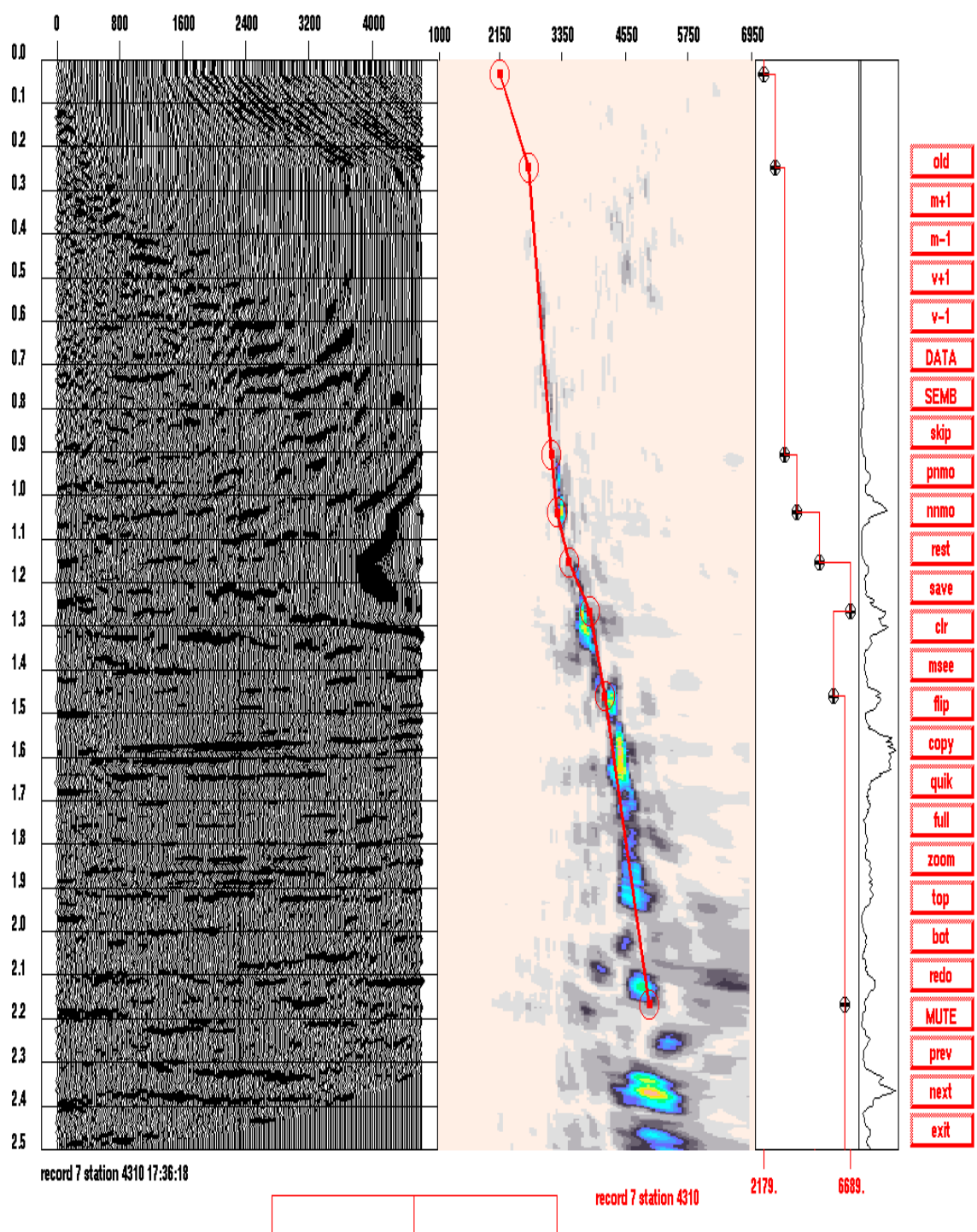
Fig. 6.32. Velocity semblance of pseudo P-P CMP gather at station 4310. The velocity picks are from the original CMP gather. The velocity function of the pseudo CMP shows similar trend.
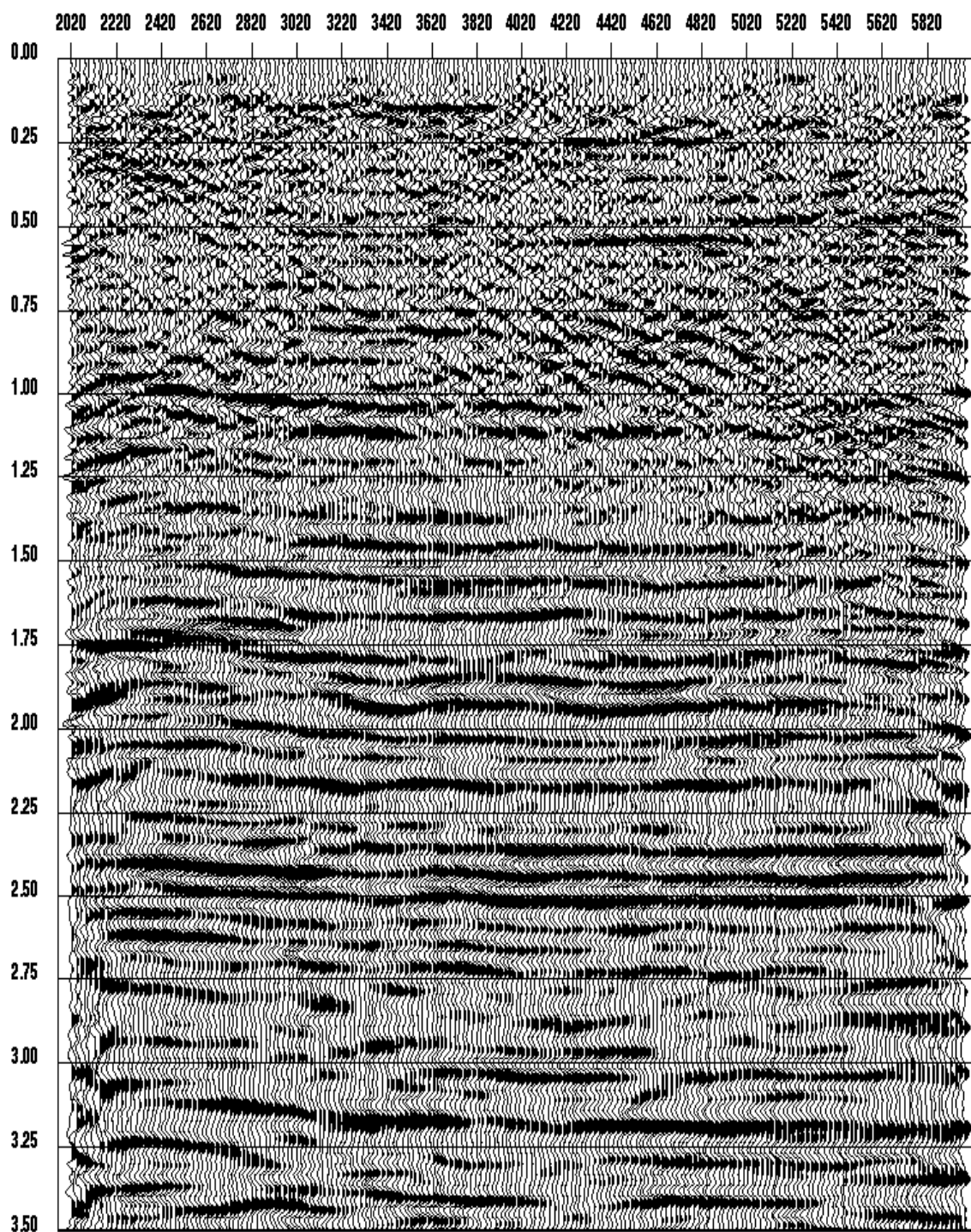
Fig. 6.33. Pseudo P-P stack in P-S time with shot-domain AMOC (with receiver statics from AMOC gathers). The stack has the same velocity function as original P-P stack. The top of the section is better than the receiver-domain version.
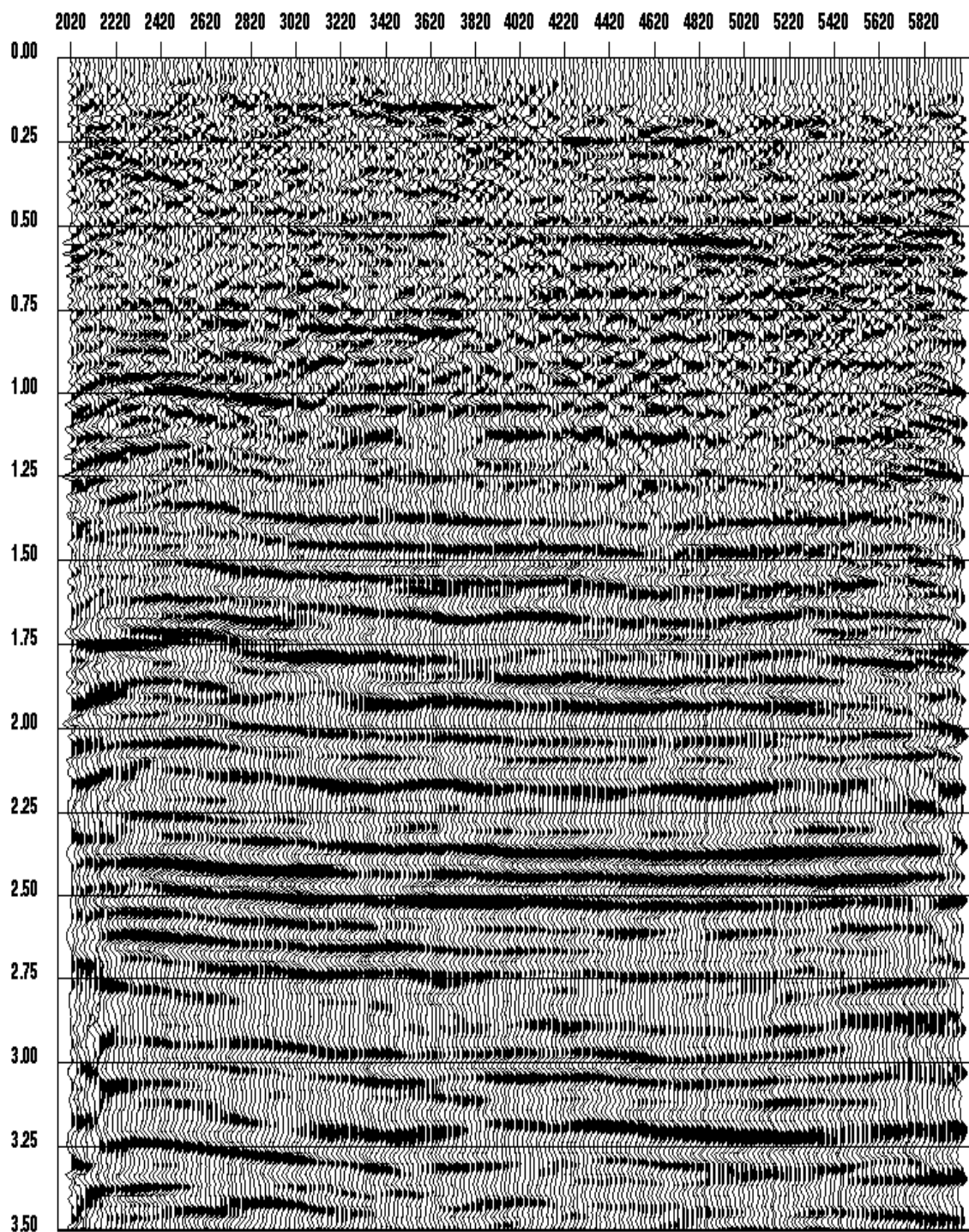
Fig. 6.34. Pseudo P-P stack in P-S time as in Figure 6.33, but with new velocity. The overall quality of image is improved over that in Figure 6.33.

6.4.3 DMO stack

The conventional approach for P-S DMO requires the application of NMO correction with the P-S RMS velocity to the data first (Harrison, 1990; Den Rooujen, 1991), followed by DMO. In the case of flat layers, Tessmer and Behle (1988) show that the P-S RMS velocity function can be estimated from velocity analysis on a CCP gather. However, for dipping layers, this procedure fails and the problem remains to choose the correct velocity for the NMO. The same problem is also present for P-P DMO algorithms that require NMO first. Deregowski (1986) proposes an iterative loop for P-P DMO application. Data are first corrected with NMO using stacking velocities, followed by DMO. Next, the initial NMO function is removed and a standard velocity analysis is applied again, followed by DMO and UN-NMO (normal moveout removal). The loop is continued until the velocity analysis shows insignificant differences from the initial NMO. To my knowledge, no literature discusses the application of Deregowski's loop to P-S data. The fact that P-S DMO is velocity dependent after NMO (unlike P-P DMO), may result in difficulty in applying the iterative loop for P-S DMO for structural P-S data.

Assuming γ is known, Alfaraj and Larner (1992) propose a kinematic P-S DMO before NMO, based on a similar construction as Forel and Gardner's (1988) P-P DMO. However, the Kirchhoff-style approach will need attention to avoid operator aliasing, and the assumptions of known constant γ, are limiting.

We show that once we have a reasonable γ_{mig} for the P-S to P-P transformation, Forel and Gardner's DMO for P-P data can be used on pseudo P-P data, before NMO. With this method, we avoid the possible difficulty of a Deregowski's loop approach, and can accomplish DMO with no operator aliasing. (Note that although it seems we are doing a prestack time migration to do DMO and then prestack time migration, in fact, the AMOC can be based on a crude γ_{mig} model, which the DMO and the prestack time migration can improve and correct.)

We proceed by applying Forel and Gardner DMO directly to the P-P pseudo data after the shot-domain AMOC transformation. Figure 6.35 is the velocity semblance of the pseudo P-P DMO gather at station 4310. The velocity picks are from the original P-P DMO gather, and they lie quite well on the coherent contours of the semblance. The DMO stack in P-S times with new velocity picks is shown in Figure 6.36.

6.4.4 Poststack migration

A kinematic definition of P-P poststack time migration is the summation along the zero-offset response of a point diffractor, and placement of the sum at its apex (Black and Brzostowski, 1994). Note that the CMP co-ordinate of the apex in the zero-offset plane matches the CMP co-ordinate of the apex of the same point diffractor for prestack data (i.e., in CMP-offset co-ordinates). As a result, both prestack and poststack migration collapse the point diffractor to the same point. The fact that the apex of the diffractor corresponds to the min-
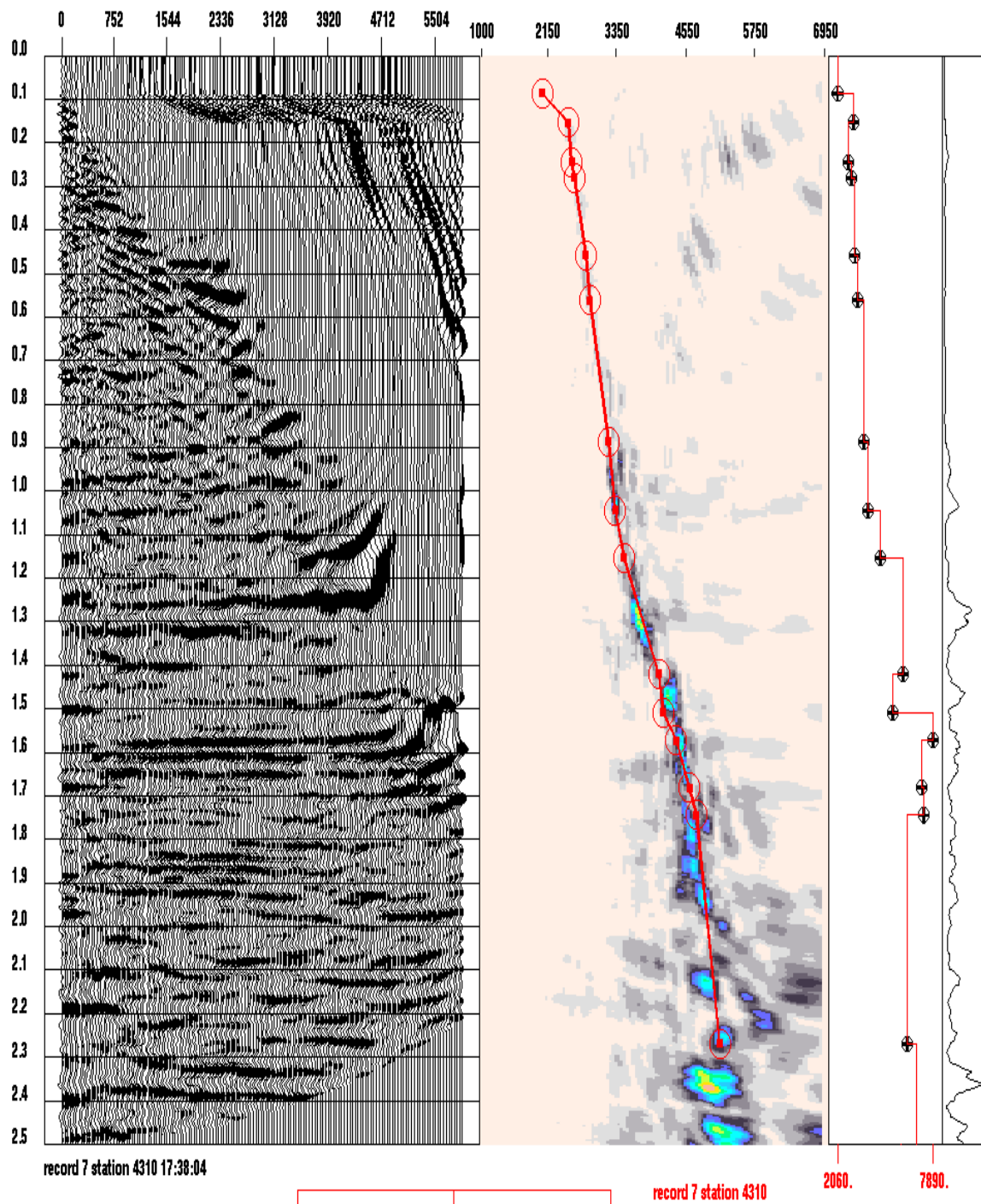
Fig. 6.35. Velocity semblance of pseudo P-P DMO gather at station 4310. The velocity picks are from the original P-P DMO gather. The velocity function of the pseudo P-P DMO shows a similar trend.
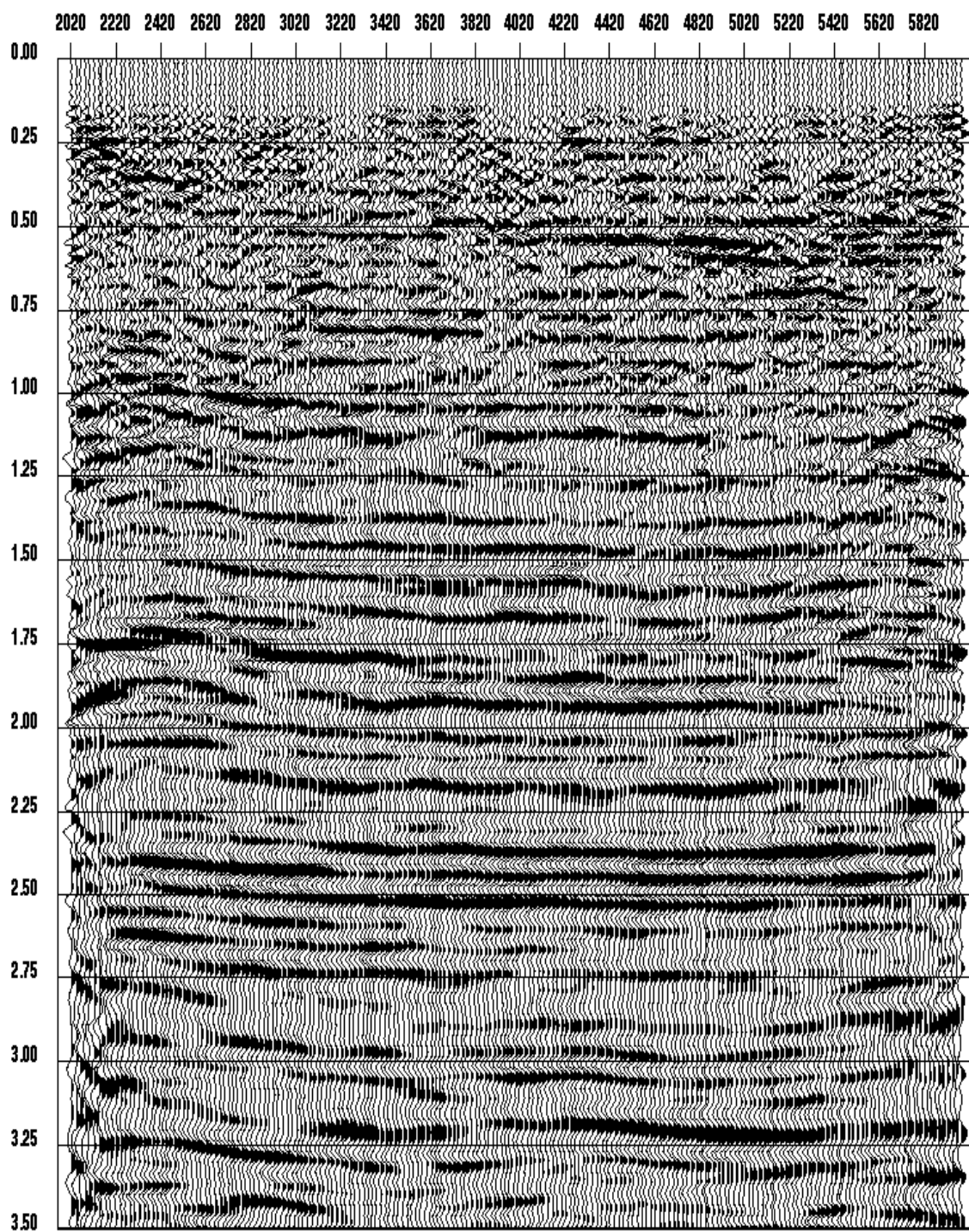
Fig. 6.36. P-S DMO stack in P-S times.

imum of the traveltime curve, suggesting that the actual location of the point diffractor at depth can be located with image ray ray-tracing (Hubral, 1977).

However, it is not generally true for P-S data that CMP location of the apex of the traveltime curve for a point at the zero-offset plane matches with the one in prestack data (CMP-offset co-ordinates). Therefore, even though, we could develop a poststack migration to collapse the P-S traveltime curve of a point response at the zero-offset to its apex, the result may not match the P-S prestack migration. Fortunately, for flat data or a constant γ medium, because both up- and down-going raypaths are identical, both apices coincide. Hence, the poststack and the prestack migrations will produce the same result.

Harrison (1992) shows that for flat layers, the P-S zero-offset diffraction curve can be approximated by a hyperbolic curve. Hence, it can be collapsed with conventional poststack migration algorithms. He also shows that the P-S migration velocity is different from the P-S RMS velocity, with normally the migration velocity being a few percent less than the P-S RMS velocity.

Alternatively, conventional poststack migration algorithms can be applied to the pseudo P-P DMO stack data. In fact, poststack migration for pseudo P-P data has some advantages over P-S data. For the dipping-layer model with variable γ, the P-S DMO stack is slightly different from the P-S DMO stack obtained from AMOC. When poststack migration is applied to the AMOC P-S DMO stack, the result of the events on poststack migrated stack have the same lateral position as the prestack migrated stack, because AMOC is based on

the prestack migration. Therefore, the pseudo P-P DMO stack can be viewed as a normal ray section of the corresponding P-P pseudo depth model and can be migrated with any P-P poststack migration algorithm

6.4.5 Prestack migration

Gardner et al. (1986) propose a migration scheme for P-P data (PreStack Imaging or PSI) that allows prestack data to be migrated without a priori velocity information. The advantage of this type of migration scheme is that it obviates iterative migration velocity analysis, as the final velocity analysis is performed after spatial collapse of the diffractor. After AMOC transformation to P-P pseudo gathers, the same migration scheme can be applied to P-S data. Figure 6.37 is the velocity semblance of the pseudo P-P PSI migrated gather at station 4310. The velocity picks are from the original P-P migrated gather, and they are positioned quite well on the coherent contours of the semblance plot. The result of P-S prestack migrated stack after converting back to P-S time is shown in Figure 6.38.

6.4.6 Alternative processing flows

In the conventional P-S processing flow, P-S processing follows after P-P processing. The processing sequence for the P-P data is then repeated for the P-S data, including the iteration between S statics and S velocity, the iterative P-S DMO velocity analysis and P-S DMO and the iterative P-S migration velocity analysis and P-S migration. With the help
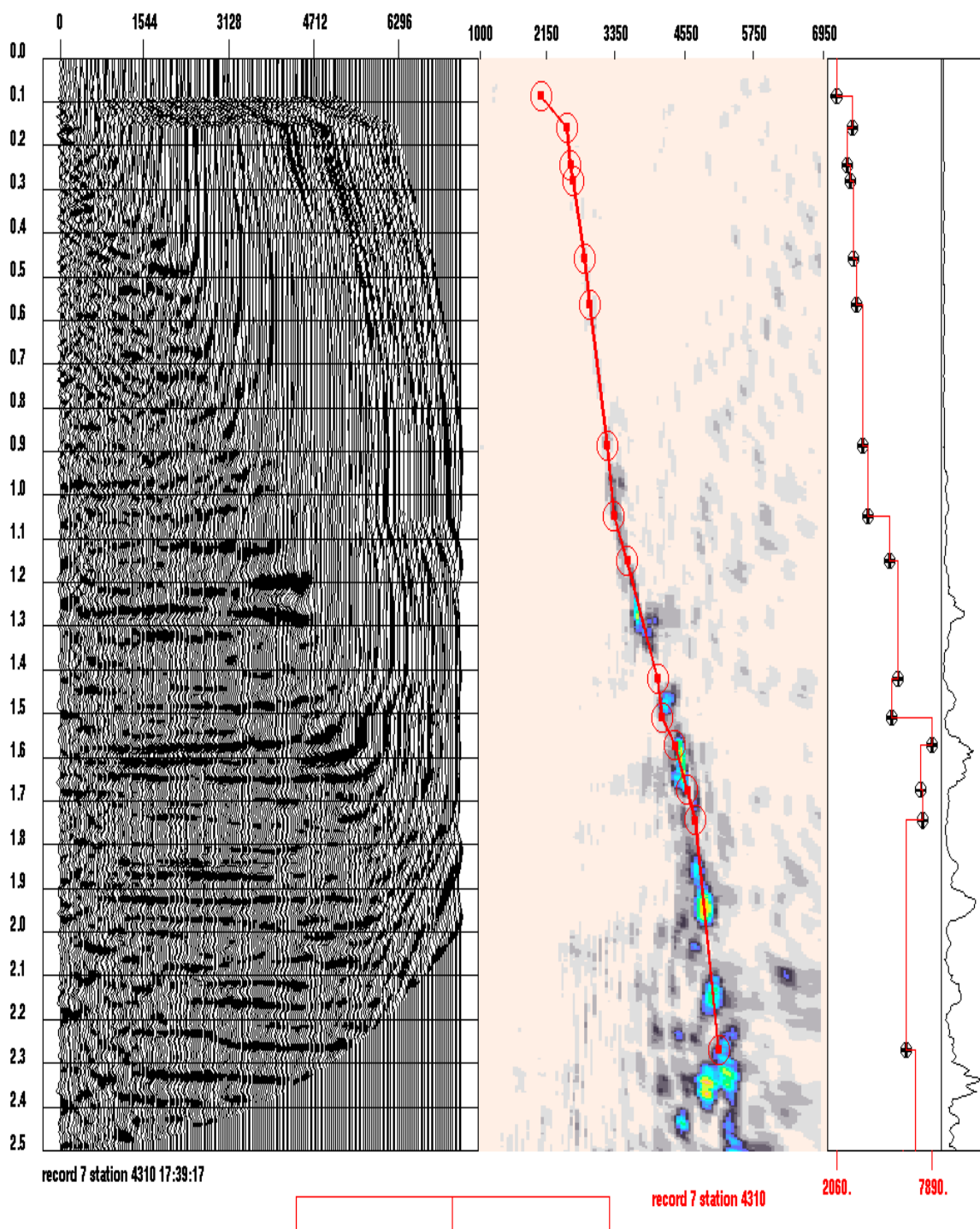
Fig. 6.37. Velocity semblance of pseudo P-P PSI migrated gather at station 4310. The velocity picks are from the original P-P PSI migrated gather. The velocity function of the pseudo P-P migrated CMP shows a similar trend.
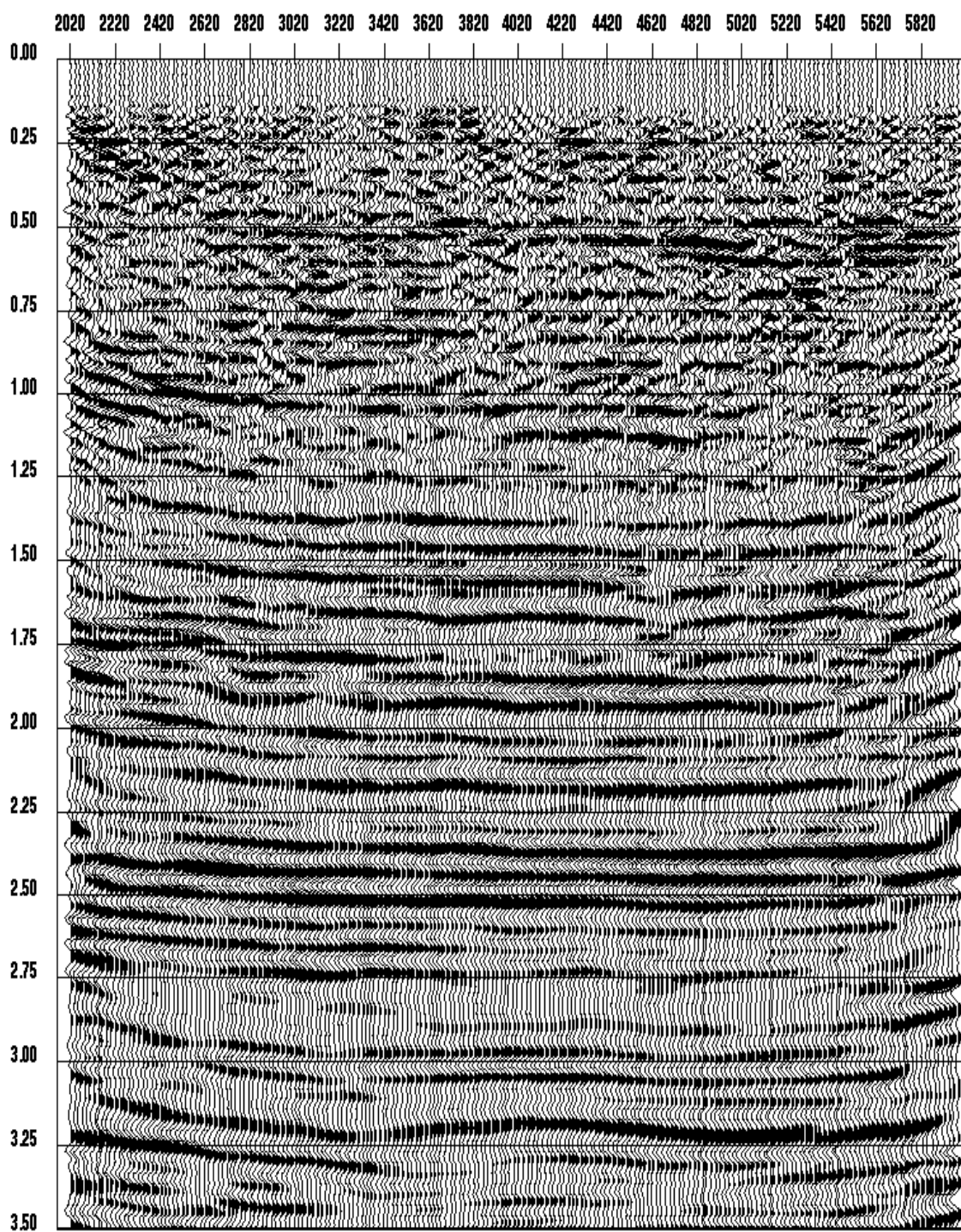
Fig. 6.38. P-S Prestack time-migrated stack in P-S time.

of the AMOC, the tedious iterative procedure can be minimized or even avoided.

Note that velocity and statics iterations may be required in solving S-wave receiver statics in AMOC method, similar to conventional residual statics estimation process. However in the non-iterative velocity processing flow, the step of calculating receiver statics is replaced by f-x technique described in chapter 4.

For comparison, residual receiver statics solution obtained from f-x technique are applied to the P-S data before the transformation. Figures 6.39 to 6.44 are different stacks with the f-x residual receiver statics applied and displayed in P-S time. Figures 6.39 and 6.40 are the pseudo P-P structural stacks with the new velocity function and the original P-P velocity function respectively. Figures 6.41 and 6.42 are the pseudo P-P DMO stack with the new velocity function and the original P-P velocity function respectively. Figures 6.43 and 6.44 are the prestack time-migrated stack with the new velocity function and the original P-P velocity function respectively. In general, the f-x statics gives better coherence stacks than the statics calculated in the receiver AMOC. The comparison also shows that the new velocity picked from the pseudo gathers produces similar result as the velocity function picked from the original P-P gathers. This suggests two new alternative processing flows for P-S data.

Flow 1:

    1) Complete P-P processing.

    2) Apply P-wave shot statics to P-S data.
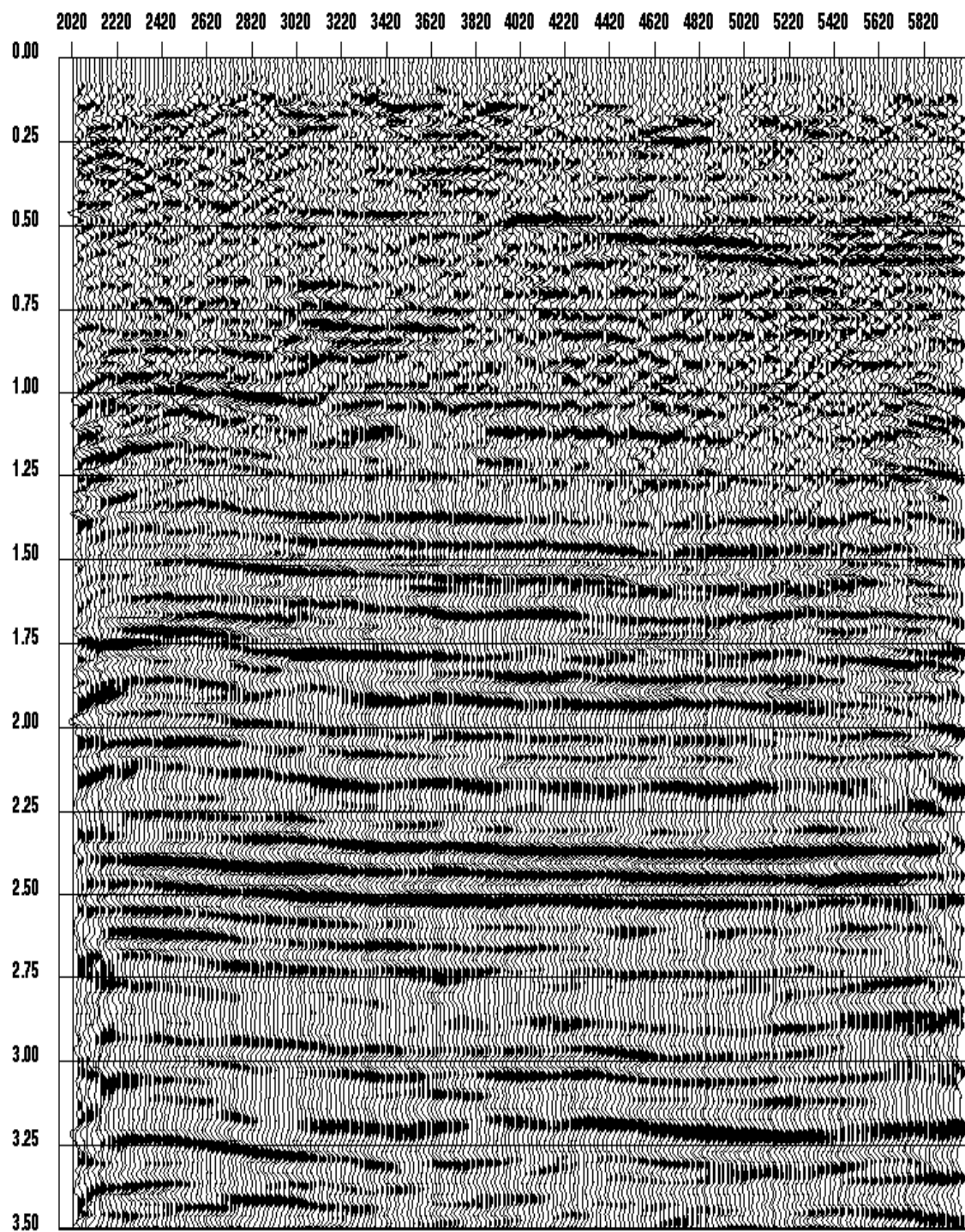
Fig. 6.39. Pseudo P-P structural stack in P-S time, with f-x residual receiver statics applied and new velocity.
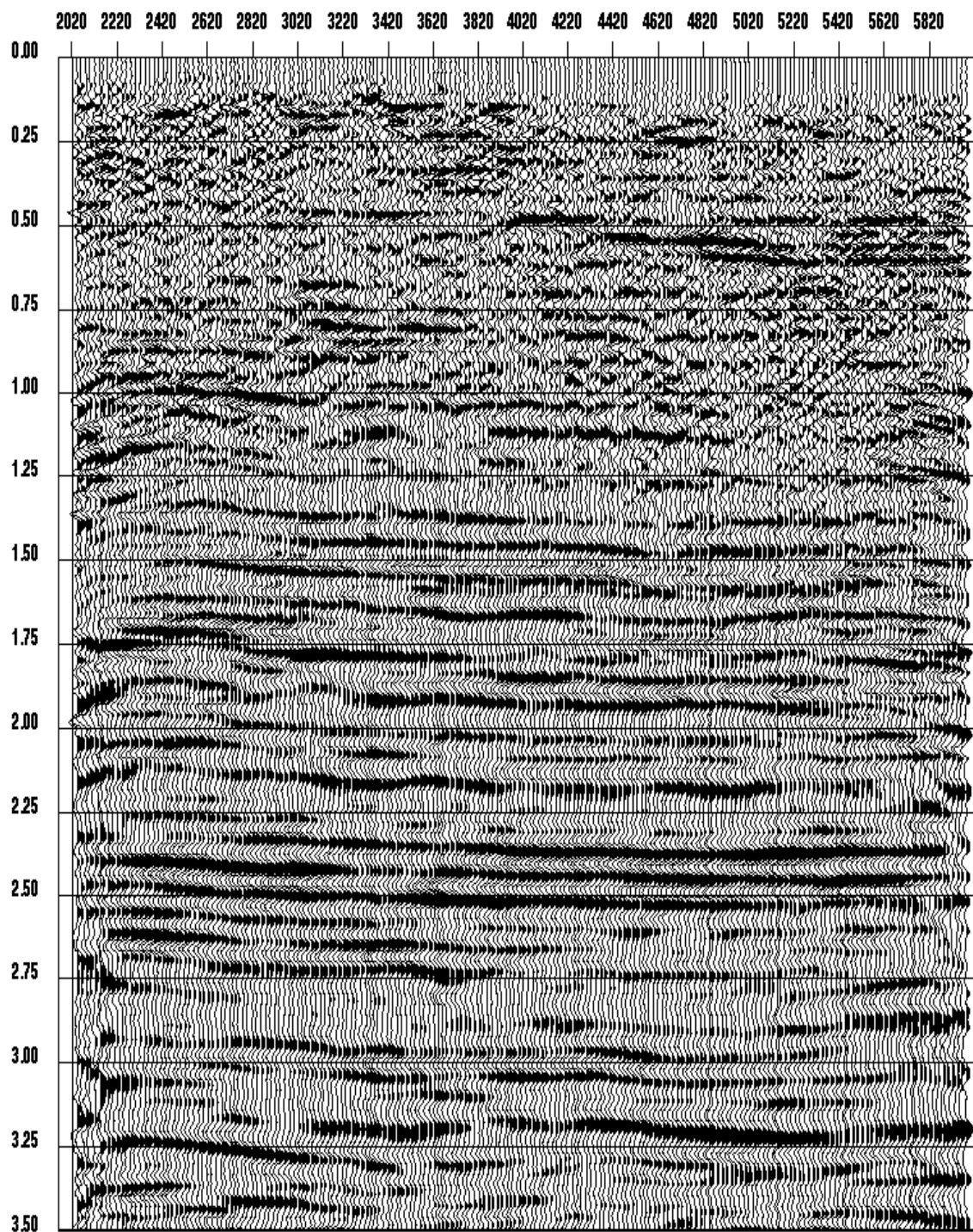
Fig. 6.40. Pseudo P-P structural stack in P-S time, with f-x residual receiver statics applied and P-P velocity.
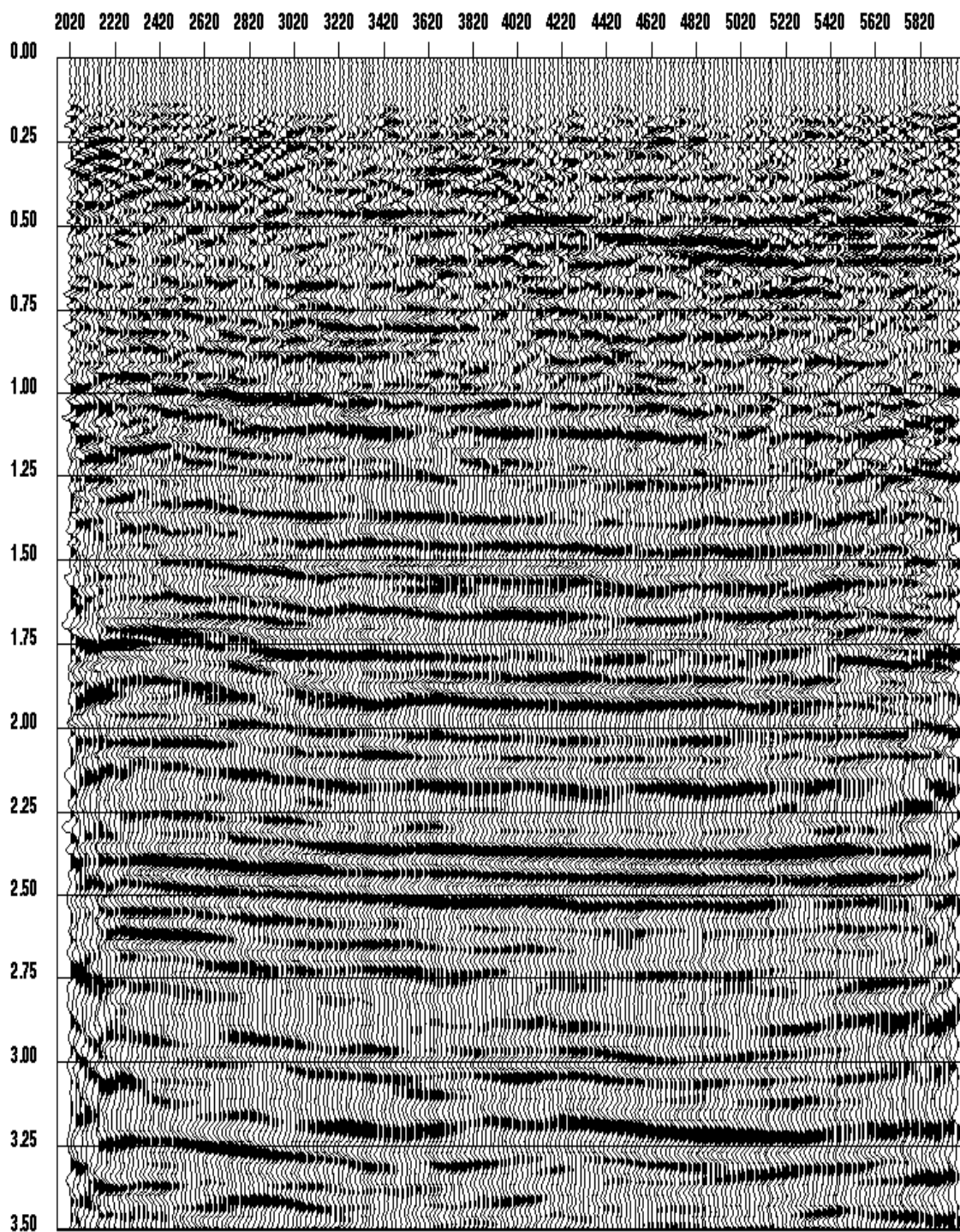
Fig. 6.41. Pseudo P-P DMO stack in P-S time, with f-x residual receiver statics applied and new velocity.
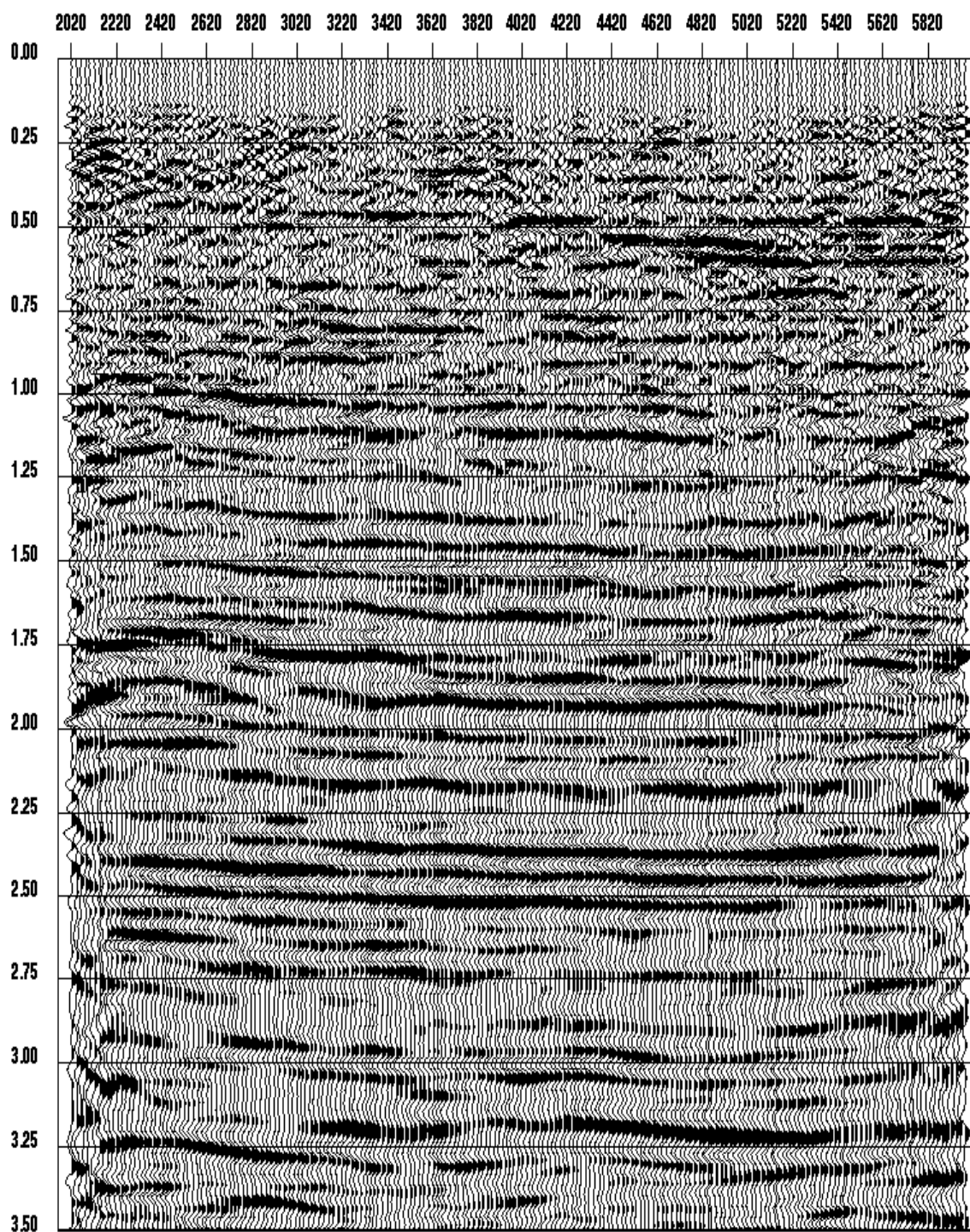
Fig. 6.42. Pseudo P-P DMO stack in P-S time, with f-x residual receiver statics applied and P-P velocity.
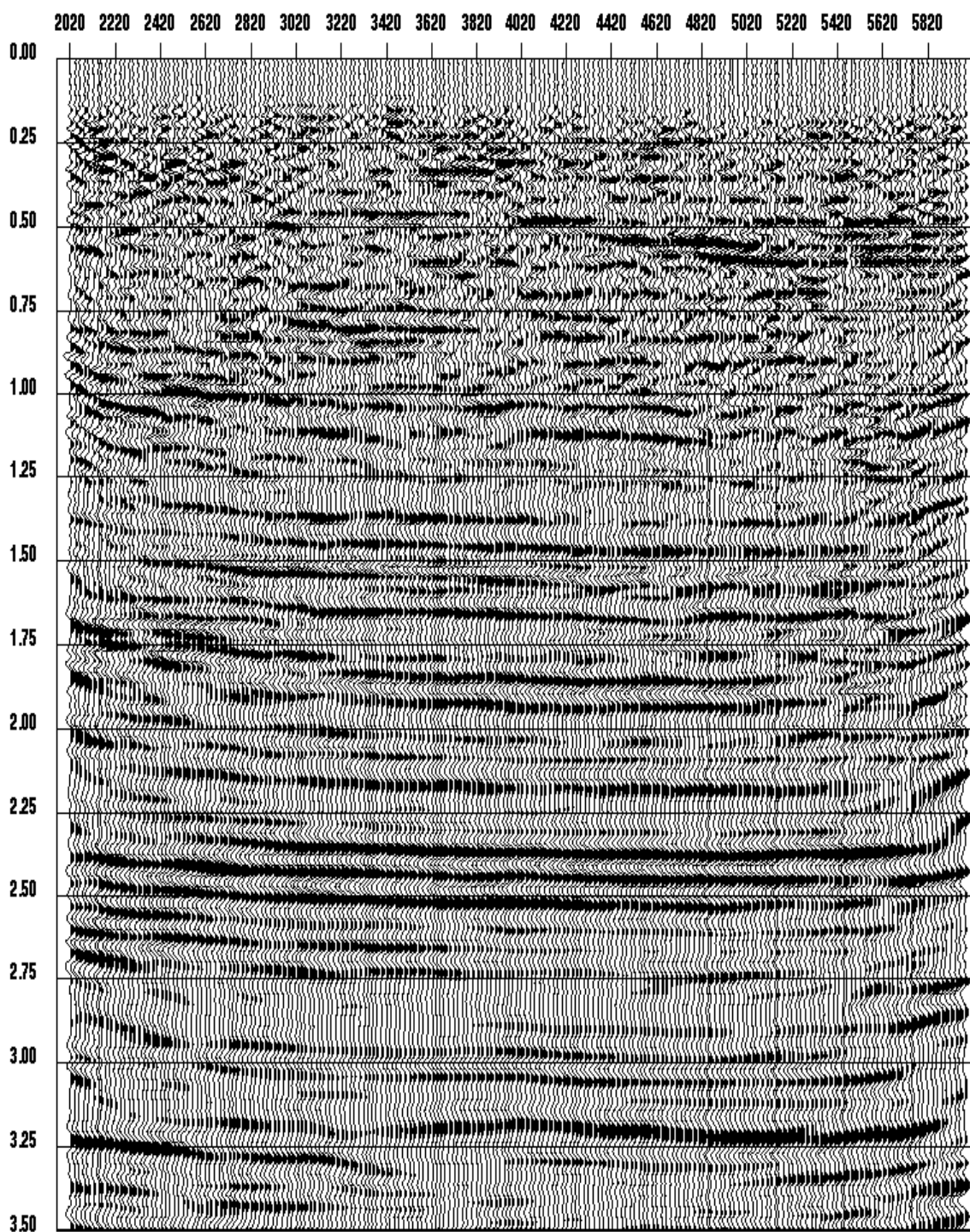
Fig. 6.43. Pseudo P-P prestack time-migrated stack in P-S time, with f-x residual receiver statics applied and new velocity.
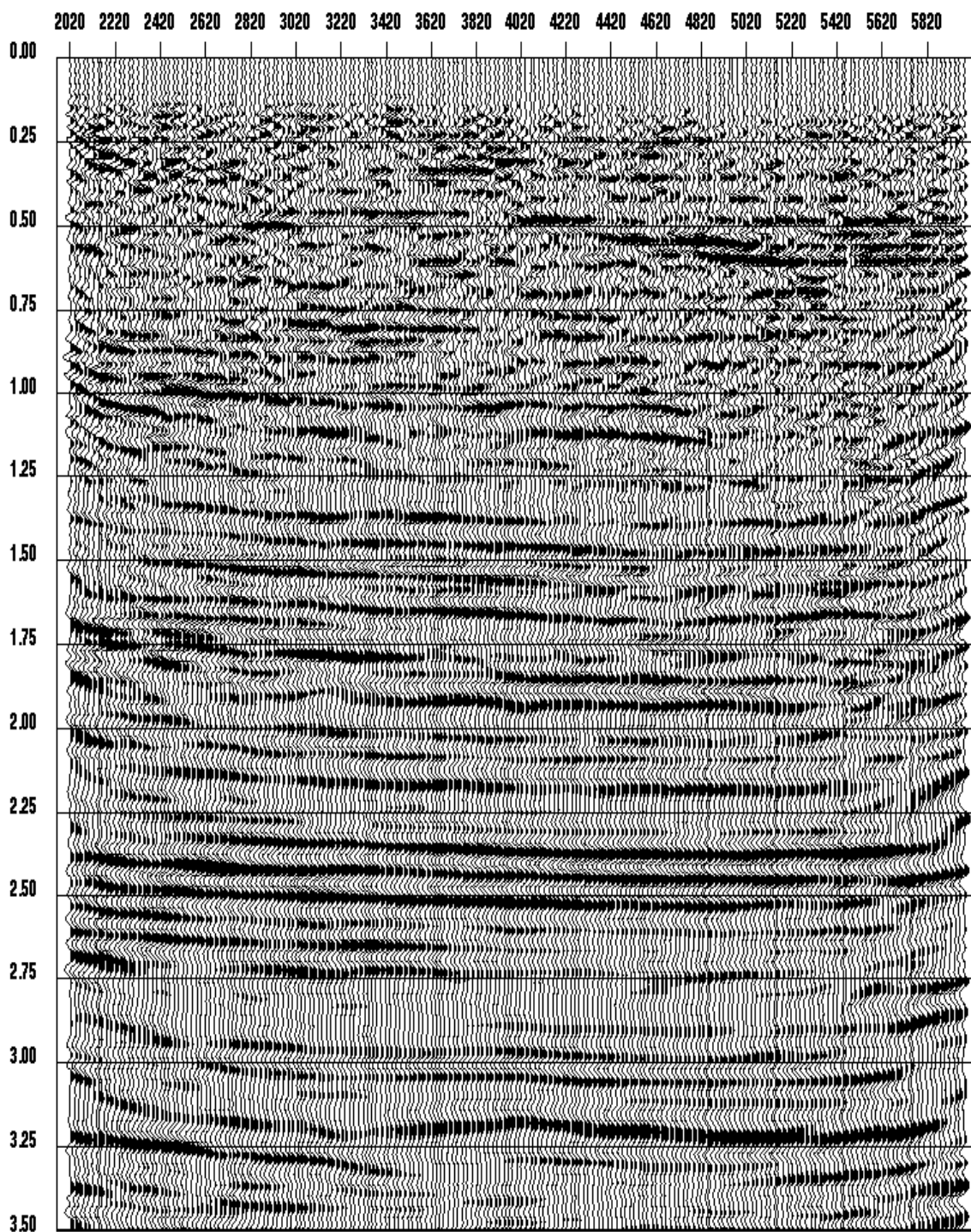
Fig. 6.44. Pseudo P-P prestack time-migrated stack in P-S time, with f-x residual receiver statics applied and P-P velocity.

3) Apply S-wave receiver residual statics obtained from f-x technique.

4) Apply AMOC transformation with $\gamma_{mig} = 2$.

5) Apply Forel and Gardner's DMO to the P-P pseudo data.

6) DMO velocity analysis and stack.

7) P-S DMO stack obtained from vertically stretched P-P pseudo DMO stack with

   $\gamma_{ps} = 2$.

8) PreStack Imaging (PSI) on P-P pseudo DMO data.

9) Migration velocity analysis and stack.

10) P-S prestack migrated stack obtained from vertically stretched P-P pseudo prestack migrated stack with $\gamma_{ps} = 2$.

Flow 2:

1) Complete P-P processing.

2) Apply P-wave shot statics to P-S data.

3) Apply S-wave receiver residual statics obtained from f-x technique.

4) Obtain γ_{mig} from migration velocity analysis at selected locations.

5) Apply AMOC transformation with proper γ_{mig}.

6) Apply P-DMO and stack with P-DMO velocity.

7) P-S DMO stack obtained from vertically stretched P-P pseudo DMO stack with

   $\gamma_{ps} = \gamma_{mig}$.

8) Apply P-prestack migration and stack with P-migrated velocity.

9) P-S prestack migrated stack obtained from vertically stretched P-P pseudo

prestack migrated stack with $\gamma_{ps} = \gamma_{mig}$.

The different between two flows is the first one does not required migration velocity analysis, but required non-iterative velocity estimation for DMO and prestack time migration. While the second one, after P-P processing, the only human intervention required to process the P-S data is to obtain the proper γ_{mig} from the migration velocity analysis at a few locations. Also, since γ_{mig} used for the transformation, in the second flow, is obtained from migration velocity analysis, and hence the second flow has less conversion point smearing problem.

6.5 Discussion

The motivation of this topic is two-fold. First, we would like to investigate the possibility of transforming P-S data into P-P. Secondly, we would like to see any advantages of processing the P-S data in the new transformed domain.

Unfortunately, the transform process I developed is a migration-like approach and hence it is rather expensive. Some other fast approaches may be possible if we could assume a constant γ medium. However, as we know the location of the conversion point is γ dependant, constant γ assumption may be significantly affected the conversion point smearing. Also special effort is needed to minimize the artifacts generated by the transformation.

There are several advantages of processing P-S data in the transformed domain that can

be summarized as follows:

1) we can solve S-wave receiver statics on structured models, in the receiver AMOC domain, where ACCP gathering may fail.

2) After transformation, no special P-S processing tools are required to process the

pseudo P-P data, other than the routine to stretch back into P-S time.

3) a non-iterative velocity processing flow can be developed.

Chapter 7   P-P and P-S mis-tie analysis

7.1 Introduction

A more complete recording of seismic experiments requires full vector measurement of three-component (3-C) motion of the received waves. Again, from these 3-C measurements, we can create independent converted-wave (P-S) images. Jointly interpreting P-P and P-S sections can significantly improve the description of the geological section and reservoir rocks. To facilitate this ultimate interpretation though, we need to correlate P-S data to P-P data. Ultimately, we will present both in either P-P time or depth.

For a simple horizontally layered earth, we may be able to use Dix's equation to convert P-P and P-S RMS velocities into interval velocities (Stewart and Ferguson, 1996) and obtain P-P to P-S correlation by vertically stretching both time sections into depth. Where structures are present, depth migration is needed to image the data in depth. However, to do depth migration, we need sophisticated graphic tools, intensive human intervention and knowledge of the geology, to simultaneously build P and S waves interval velocity models. Also, the processing velocity obtained from the depth migration velocity analysis may not be the right kind of velocity to image the same event on P-P and P-S data to the same depth. Difficulties may also arise if events show up clearly on one section and not on the other due to differences between P-P and P-S reflectivities. Furthermore, uncertainty in near surface velocities has major impact on both velocity model building and the imaging process.

Several mis-tie analysis techniques have been developed in the time domain. Garotta (1985) developed a method based on visual correlations between P- and S-wave data within small time windows. A time scale-factor guess of the average V_p/V_s ratio is applied to the S-wave data before cross-correlation. Behle and Dohr (1985) extracted T_{pp}/T_{ps} ratios from the combined velocity analysis between P and P-SV data for mis-tie analysis. This method, as shown in equation (5.20), is only valid when $g_\gamma \approx 1$. Lawton et al. (1992), and Miller et al (1994) used a forward modelling technique to create synthetic P-P and P-S offset stacks. Instead of correlating P-P to P-S real data directly, they correlated P-P to P-S synthetic offset stacks, followed by the correlation between P-P stack and P-P synthetic stack, and between P-S stack and P-S synthetic stack. If S-wave sonic log is not available, a set of P-S synthetic stacks are created based on a possible range of Vp/Vs ratios.

Unfortunately all the above methods will suffer, in different degrees, at least from 3 factors.

(1) Mis-correlation. Picking wrong cycles for the match due to the oscillatory nature (or limited bandwidth) of the seismic traces. The situation is improved if a large correlation window can be used. This implies that, as was suggested by Gaiser (1996), mis-tie analysis can only extract long wavelength component of Vp/Vs ratio and inversion is needed to extract short wavelength component of Vp/Vs ratio.

(2) Near-surface effects. The presence of the low-velocity zone requires datuming for the surface-seismic data. However, due to the uncertainty of replacement S-wave velocity,

P-S data may have a different datum than P-P data. The relative time shift, arising from the wrong datum, between P-P and P-S data needs to be determined and corrected. In fact, even for a model with constant Vp/Vs ratio, this shift must be corrected before a simple time scaling factor can be applied to P-S data for better visual correlation with P-P data.

Another problem with the near surface is that the γ value tends to be significantly higher than at depth. Even a γ value is constant at depth, the Vp/Vs time curve relative to the surface decreases slowly from a large Vp/Vs at the surface to a smaller constant Vp/Vs at depth. Therefore using a single time scaling to the P-S data may not be appropriate enough to tie with P-P data.

It is also known that much of the high frequency content of the seismic wave is lost as it propagates through the surface layer. As a result, the seismic trace becomes more cyclic in nature and is harder to correlate.

(3) Coherent noises. The presence of multiples and multimodes can confuse the quality of the match.

It is interesting to note that these 3 factors have less effect on VSP multi-component data than on surface-seismic data, because VSP data have a higher frequency content. This is because receivers are buried at depth, and the source signature can be easily removed by deconvolution. Gaiser (1996) demonstrated his correlation analysis on VSP data with good results. However, mis-tie analysis is not a major issue for VSP multi-component data, as the data have better depth control.

In this chapter, we propose two mis-tie analysis alternatives to the depth assignment approach. The first method is a semi-automatic procedure based on simulated annealing. It iteratively matches P-P and P-S time sections. The second technique is a simple but robust approach that matches P-P and P-S data in logarithmic time. Subsequent to section matching, interval velocity ratios can be derived from the correlated P-P and P-S time events. Also after the time correlation, we can update P- and S- wave velocities obtained from time processing to perform inversion of the P-S data. Once events are matched in time, we can safely perform depth migration velocity analysis and depth migration to properly position all events in depth.

7.2 Ray path assumption in P-P to P-S mis-tie analysis

Correlation between time domain P-P and P-S stacked traces assumes that both traces are measured along the same ray path. It is known that P-P DMO stack and P-P time-migrated stack are measured along the normal ray and the image ray respectively. However, from Snell's law, unless the earth model consists of horizontal layers or complex structures with a constant Vp/Vs ratio, the P-S DMO stack does not correspond to normal rays, and P-S time-migrated stack does not correspond to image rays. In spite of the former statement I assume that ray path discrepancies are small for most realistic earth models and continue to develop the following procedures.

7.3 Simulated annealing

Simulated annealing has long been used as a global optimization technique to solve problems in geophysics (Rothman, 1985; Sen and Stoffa, 1991; Chunduru et al., 1996; Jervis et al., 1996). Starting from an initial guess, the algorithm makes a change to the current solution and the optimization function is evaluated. Unlike other optimization techniques, (e.g. nonlinear simplex by Rowan, 1990), simulated annealing considers both favorable and unfavorable solutions during its search. By accepting non-favorable solutions occasionally, based on the Metropolis criteria (Metropolis et al., 1953), local optima can be escaped. As the optimization process proceeds, the change in the current solution becomes small, and the chance of accepting non-favorable solutions decreases. In principle, the algorithm has a reasonable chance to converge to the global optimum.

Correlation of events between P-P and P-S stacked traces is formulated as a global optimization problem. The functional value to be optimized is the zero-lag cross-correlation between the reference P-S trace and the stretched P-P trace in a selected time window. Using equation (5.20) with a set of γ_{ps} values, the corresponding set of correlation coefficients is calculated and searched to identify the value γ_{ps}^* which maximizes the correlation. Once γ_{ps}^* values are found at all desired time levels, they are used to squeeze the P-S traces to match P-P traces in P-P time.

7.4 Procedural issues

We know from equation (5.20) that the relationship between P-P and P-S times is expressed in terms of γ_{rms}/g_γ or γ_{ps}. Therefore the mis-tie analysis process can be constrained by the physically allowable values of γ_{ps}. We also know that the value of γ_{mig} is between γ_{rms} and γ_{ps}. Therefore γ_{mig} can be used in simulated annealing as the initial guess for γ_{ps}.

The number of γ_{ps} values to be estimated via the simulated annealing is an important issue. It is assumed that γ_{ps} values are smooth both in time and space. Therefore, it is wise to use as small a number of control points as possible provided that a reasonable P-P to P-S match is obtained. One logical choice of problem parameters is to pick time control points along key horizons (because γ is rather constant within a layer) and space controls at velocity analysis locations. Subsequently, γ_{ps} values in between control points are linearly interpolated as needed. Simulated annealing is done in two steps. In the first step, a spatial average γ_{ps} in space within each time horizon is sought. In the second step, simulated annealing is used to update the γ_{ps} value at each control point; allowing only a small deviation from the average found previously.

The procedure is summarized as follows:

- Obtain CMP-time velocity picks $T_{pp}^{i,j}$ of P-P data from horizon based velocity analysis, at i^{th} CMP velocity analysis location and j^{th} time horizon.

- Given $\gamma_{ps}^{i,j}$ (γ_{ps} at i^{th} CMP velocity analysis location and j^{th} time horizon), convert the P-P pick time $T_{pp}^{i,j}$ into the P-S pick time $T_{ps}^{i,j}$, based on equation (5.20), i.e.,

$$T_{ps}^{i,j} = \frac{1 + \gamma_{ps}^{i,j}}{2} T_{pp}^{i,j} \tag{7.1}$$

Similarly,

$$T_{ps}^{i,j+1} = \frac{1 + \gamma_{ps}^{i,j+1}}{2} T_{pp}^{i,j+1} \tag{7.2}$$

Assuming a constant γ within a time window, the mapping between $T_{pp}^{i,j}$ and $T_{pp}^{i,j+1}$ can be obtained from the linear interpolation between $T_{ps}^{i,j}$ and $T_{ps}^{i,j+1}$. That is, if $T_{pp}^{i,j+\delta}$ is between $T_{pp}^{i,j}$ and $T_{pp}^{i,j+1}$, then the corresponding P-S time, $T_{ps}^{i,j+\delta}$ satisfies the following equation:

$$\frac{T_{pp}^{i,j+\delta} - T_{pp}^{i,j}}{T_{ps}^{i,j+\delta} - T_{ps}^{i,j}} = \frac{T_{pp}^{i,j+1} - T_{pp}^{i,j}}{T_{ps}^{i,j+1} - T_{ps}^{i,j}}$$

$$= \frac{1 + \gamma}{2} \tag{7.3}$$

- Optimize the correlation between P-S data with stretched P-P data by iteratively up-

dating $\gamma_{ps}^{i,j}$ with simulated annealing.

Let $X_{ps}^{i,k}$ be P-S data sample at the ith CMP velocity analysis location and at time k, and $\tilde{X}_{ps}^{i,k}$ be stretched P-P data sample at the ith CMP velocity analysis location and at time k, then define $C_{i,j}$ as the cross-correlation value between P-S data and stretched P-P data at the ith CMP velocity analysis location and between j-1th and j^{th} time horizons, i.e.,

$$C_{i,j}\left(\gamma_{ps}^{i,j-1}, \gamma_{ps}^{i,j}\right) = \sum_{k=T_{ps}^{i,j-1}}^{T_{ps}^{i,j}} X_{ps}^{i,k}\tilde{X}_{ps}^{i,k} \qquad (7.4)$$

with $\gamma_{ps}^{i,0} = \gamma_{ps}^{i,1}$.

Define the objective function O_i at the ith CMP velocity analysis location as:

$$O_i\left(\gamma_{ps}^{i,1}, \gamma_{ps}^{i,2}, ..., \gamma_{ps}^{i,nhor}\right) = \sum_{j=1}^{nhor} C_{i,j}\left(\gamma_{ps}^{i,j-1}, \gamma_{ps}^{i,j}\right) \qquad (7.5)$$

where nhor is the total number of horizons.

The optimum set of $\gamma_{ps}^{i,1}, \gamma_{ps}^{i,2}, ..., \gamma_{ps}^{i,nhor}$ is searched with simulated annealing technique to maximize the objective function O_i with the following constraint:

$$\gamma_{ps}^{min} \le \gamma_{ps}^{i,j} \le \gamma_{ps}^{max} \qquad (\textbf{7.6})$$

where γ_{ps}^{min} and γ_{ps}^{max} are user defined minimum and maximum γ_{ps} values respectively.

To stabilize $\gamma_{ps}^{i,j}$ among CMP locations values, the search is done in two steps.

(1) Constrain $\gamma_{ps}^{i,j}$, such that, for the same horizon j, $\gamma_{ps}^{i,j}$ is same for all CMP velocity analysis location j, from 1 to nloc (total number of analysis location), i.e.,

$$\gamma_{ps}^{i,j} = \gamma_{ps}^{j} \qquad (\textbf{7.7})$$

This can be done by optimizing the average objective function $\overline{O}$,

$$\overline{O}\left(\gamma_{ps}^{1}, \gamma_{ps}^{2}, ..., \gamma_{ps}^{nhor}\right) = \frac{1}{nloc}\sum_{j=1}^{nhor}\sum_{i=1}^{nloc} C_{i,j}\left(\gamma_{ps}^{j-1}, \gamma_{ps}^{j}\right) \qquad (\textbf{7.8})$$

(2) Once the optimized set, $\gamma_{ps}^{1*}, \gamma_{ps}^{2*}, ..., \gamma_{ps}^{nhor*}$, is obtained, individual O_i is maximized with the following constraint,

$$\gamma_{ps}^{j} - \delta \le \gamma_{ps}^{i,j} \le \gamma_{ps}^{j} + \delta \qquad (\textbf{7.9})$$

where δ is the maximum deviation allowed from the γ_{ps}^{j}.

As mentioned before, there is a possibility that P-P and P-S data may have different

start times. To compensate for this time shift, we make δ for the first window larger, so that this time shift has less effect on the subsequent windows.

7.5 Synthetic example

The synthetic data used here is the same as that of chapter 6. The data consists of a P-P DMO stack (Figure 7.1) and a P-S DMO stack (Figure 7.2) obtained by the method discussed previously in Chapter 6. For reasons of clarity, only a subset of the data are used in the example as shown in Figure 7.3. To demonstrate the strength of the proposed approach we start the search at γ_{ps} =1.8, rather than the γ_{mig} value found previously, and show that simulated annealing can still converge to a proper solution. Figure 7.4 displays the result of the mis-tie analysis. The P-P DMO stack stretched to P-S time shows an overall good agreement with events present on the P-S DMO stack.

For these data, the match is straight forward as there are only four well separated main reflections and cycle-skipping (matching of un-related events) does not occur. Real data is much more cyclic in nature and hence cycle-skipping is easy to develop.

7.6 Blackfoot example

To evaluate the proposed mis-tie analysis procedure in field conditions, I use the P-P DMO stack in Figure 7.5 and the P-S DMO stack in Figure 7.6 (note that to match the po-
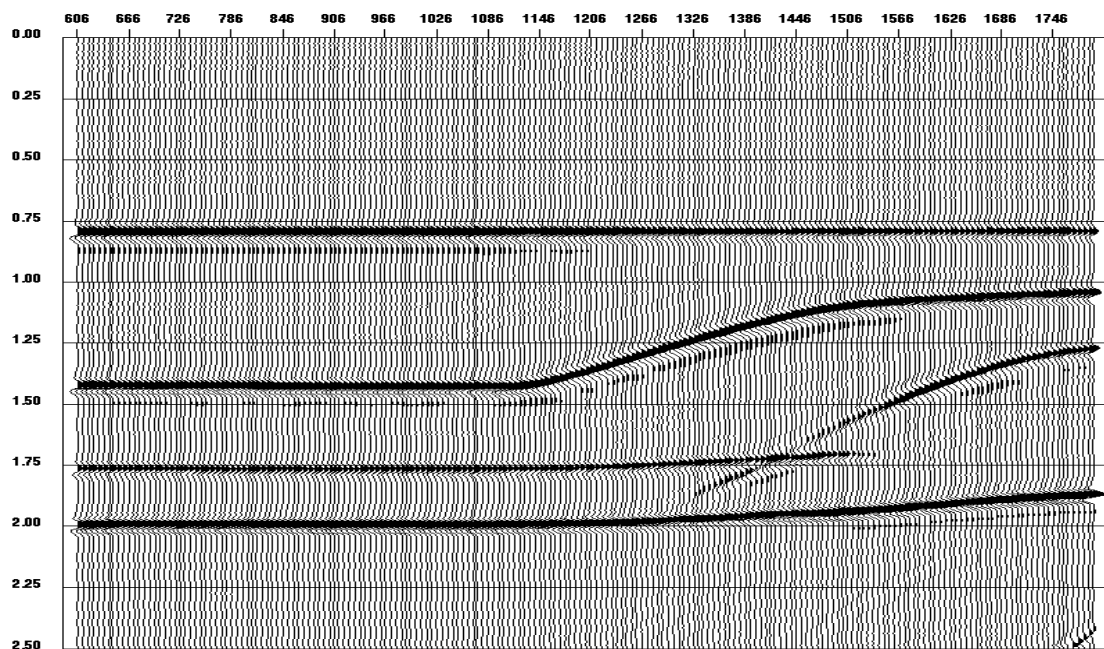
Fig. 7.1. P-P DMO stack.
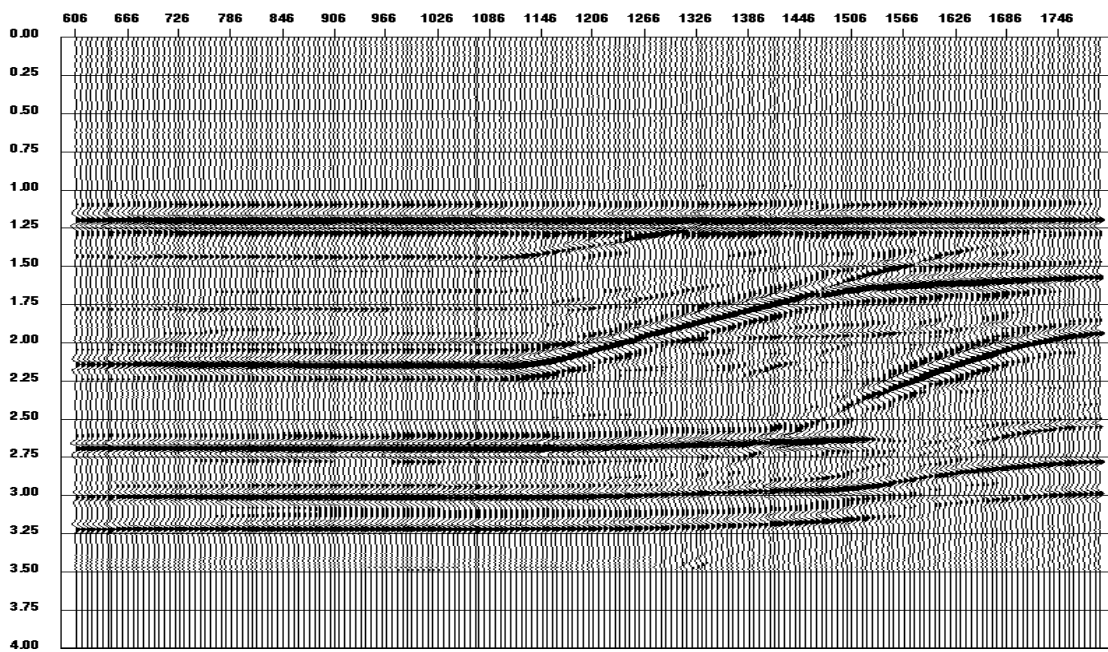
Fig. 7.2. P-S DMO stack.
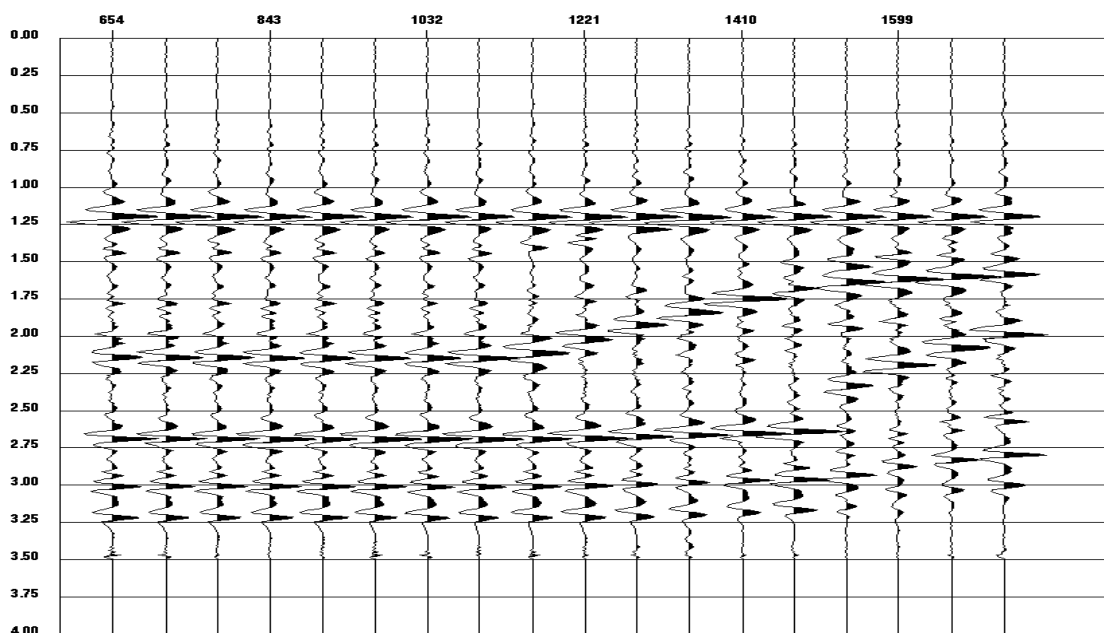
Fig. 7.3. A selected subset of reference P-S DMO stack traces to be used in mis-tie analysis.
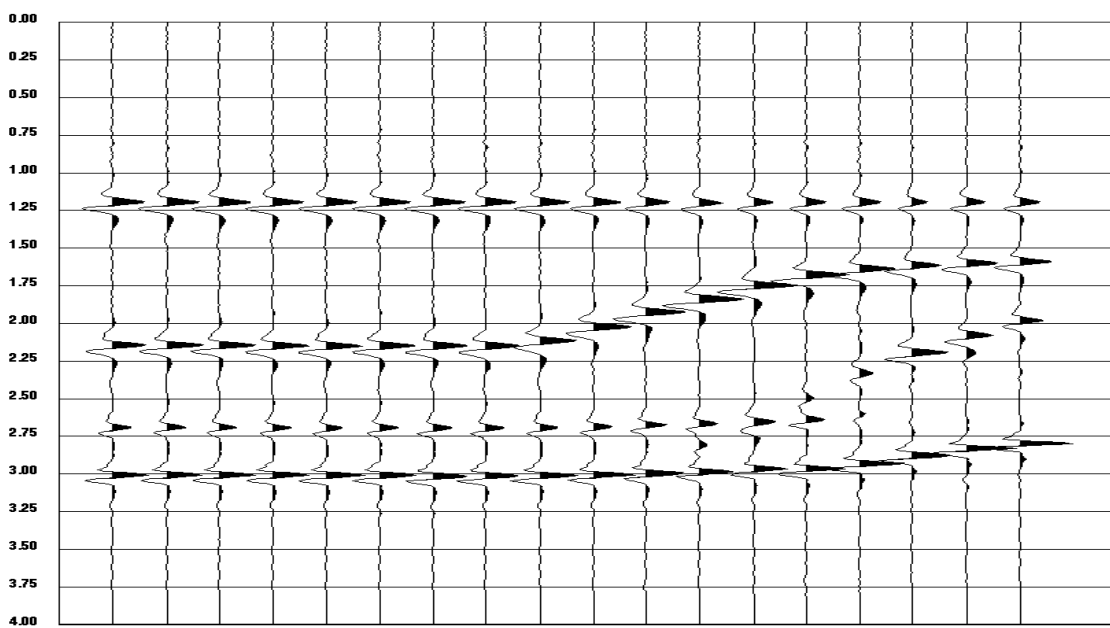
Fig. 7.4. The result of stretching the P-P DMO stack into P-S time using γ_{ps}^* estimated from simulated annealing.
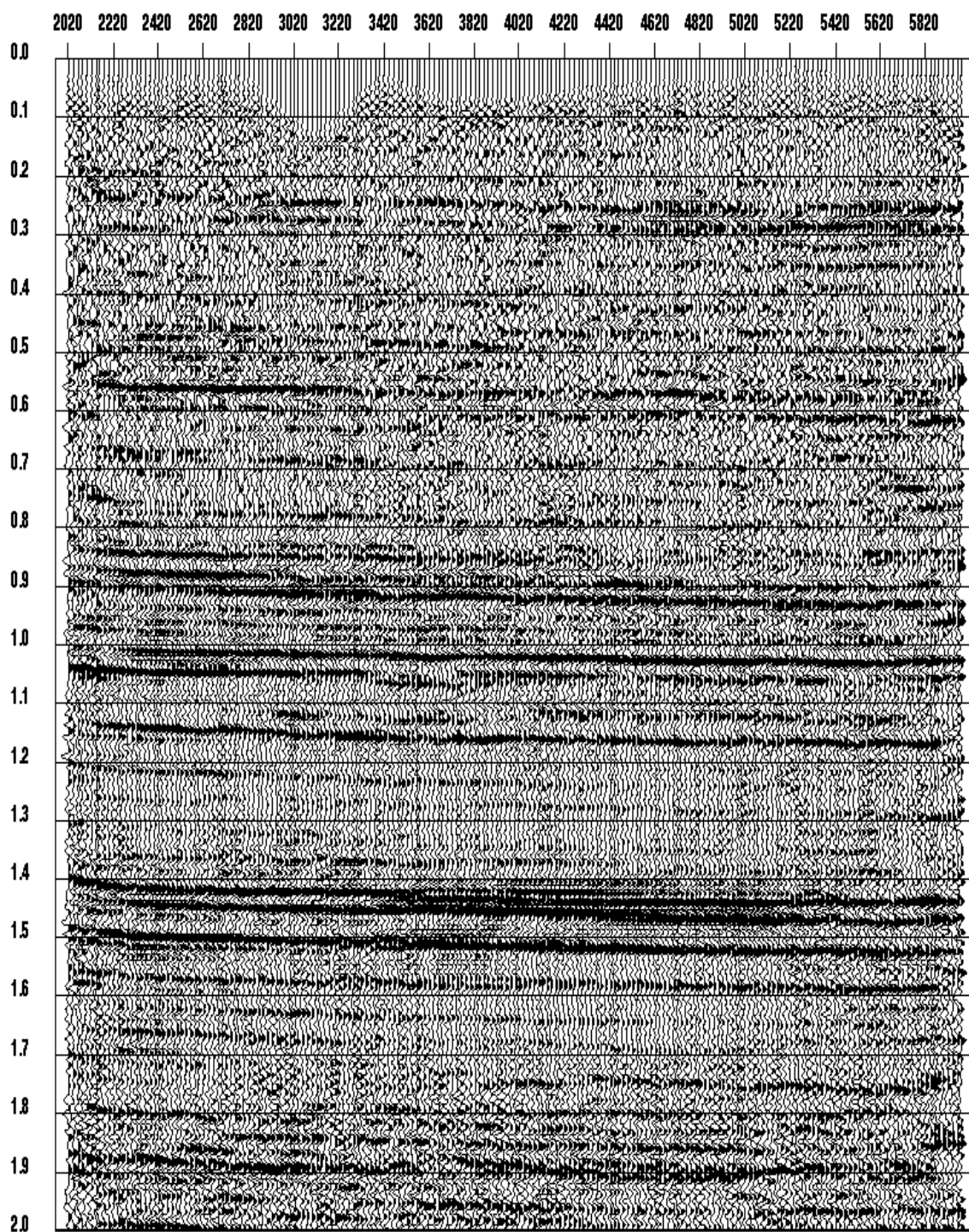
Fig. 7.5. P-P DMO stack.
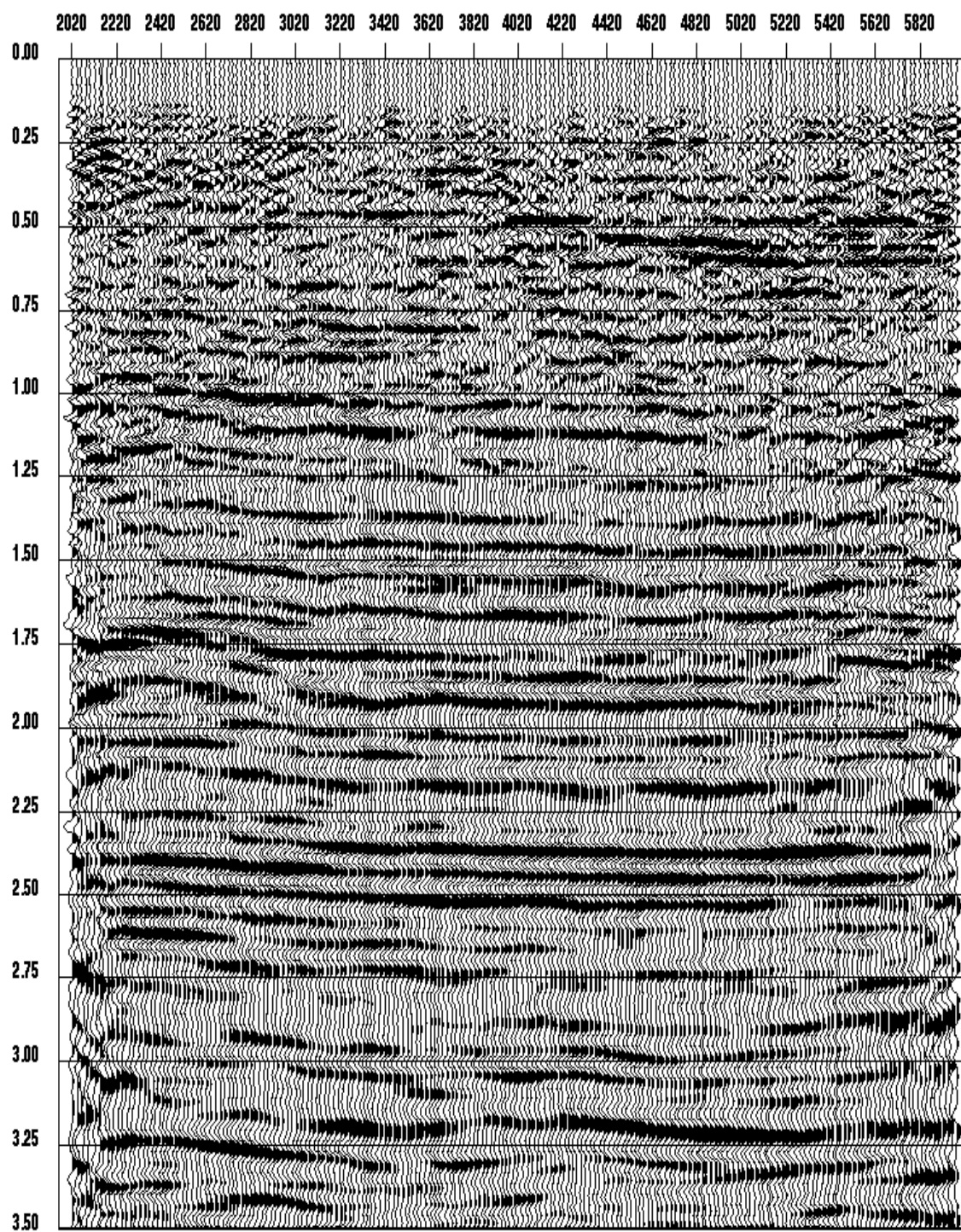
Fig. 7.6. P-S DMO stack.

larity of P-P DMO stack the polarity of the P-S DMO stack has been reversed). To stabilize the matching process, the P-P DMO stack is smoothed in time with a bandpass filter and space with a f-x filter and the result is shown in Figure 7.7.

Utilizing the results of the correlation analysis, the P-P DMO stack is stretched to P-S time and plotted in Figure 7.8. The analysis assumes an average γ_{ps}^{j} value for each time horizon picked j and resulted in a single time dependent γ_{ps} function for the whole data. The estimated $\gamma_{ps}^{j\,*}$ values are shown in Table 7.1. This function is then used to squeeze the P-S DMO stack into P-P time, and the result is shown in Figure 7.9. Further low-pass filtering of the P-P data to match the band-width of the P-S data resulted in Figures 7.10 and 7.11. Note that these figures contain both P-P and P-S data and facilitate easier evaluation of the matching procedure.

A time-and space-variant version of γ_{ps} function is also sought by restricting the deviation of γ_{ps} from the average function. The results are shown in Figures 7.12, Figure 7.13 and Figure 7.14. A slight improvement of the match between P-P and P-S data is seen.

As shown in Table 7.1, the last time control point for the simulated annealing analysis is at around 1.6 seconds, beyond this time, the quality of the mis-match may not be as good.
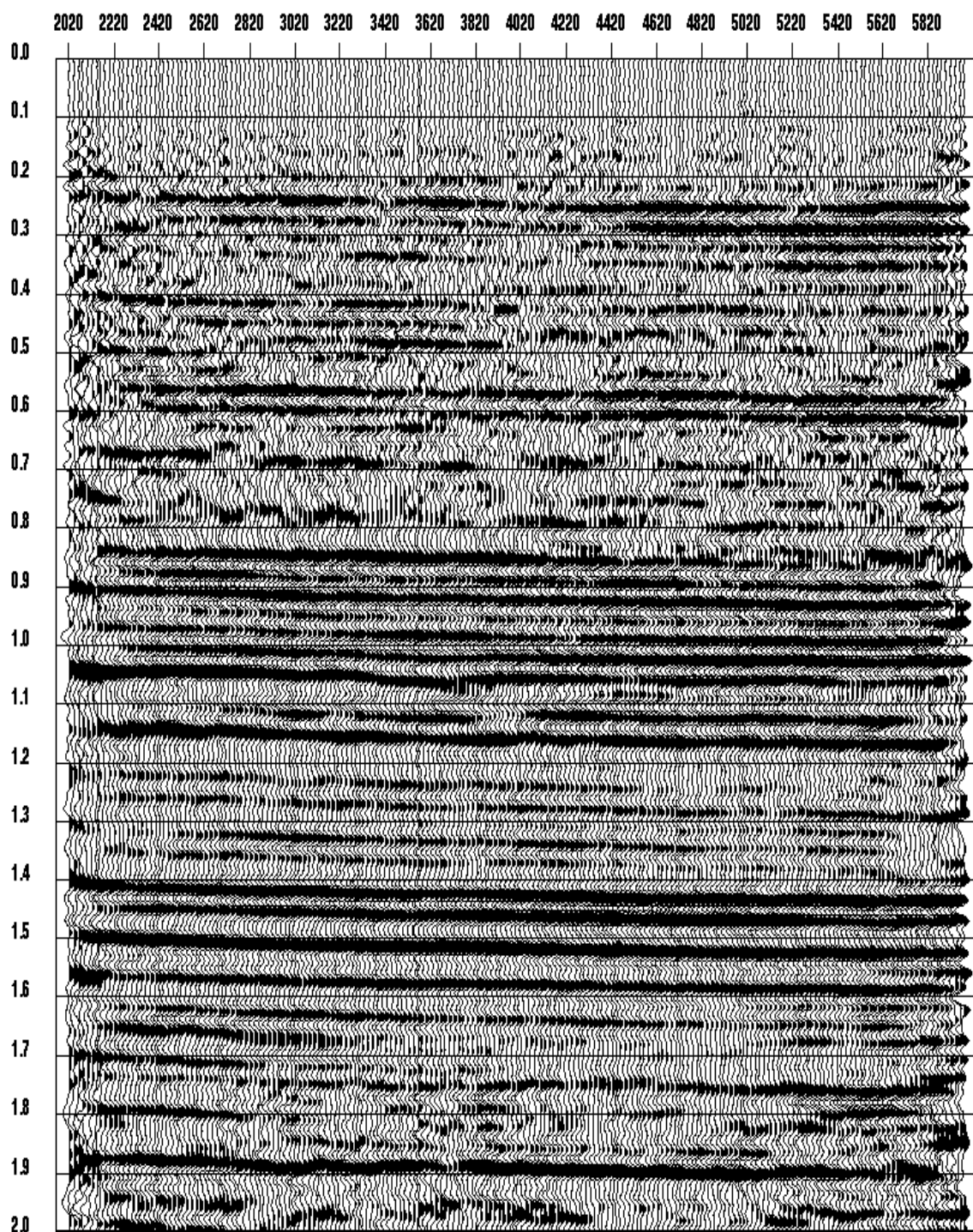
Fig. 7.7. P-P DMO stack with time and space smoothing.
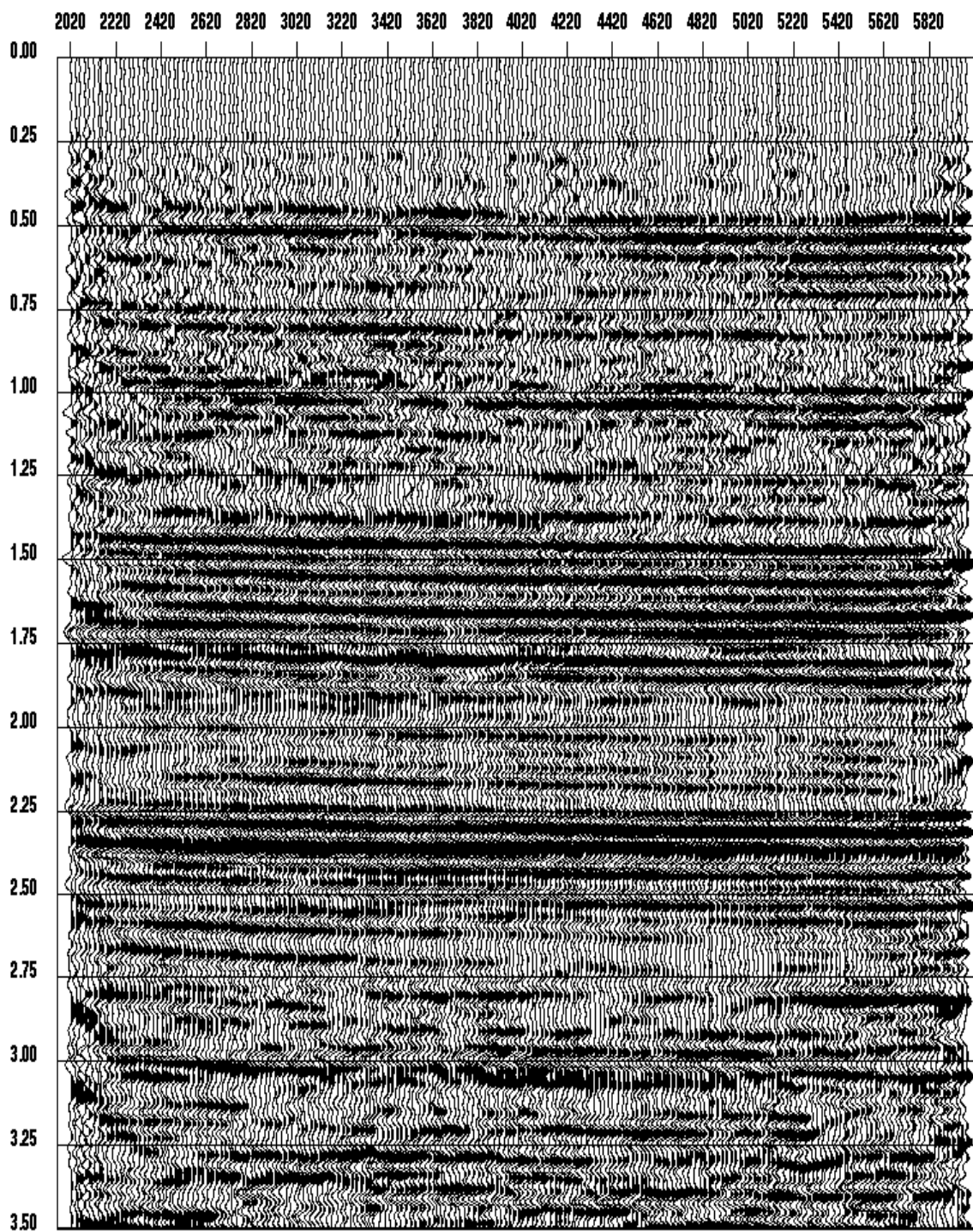
Fig. 7.8. Filtered version of P-P DMO stack in P-S time.
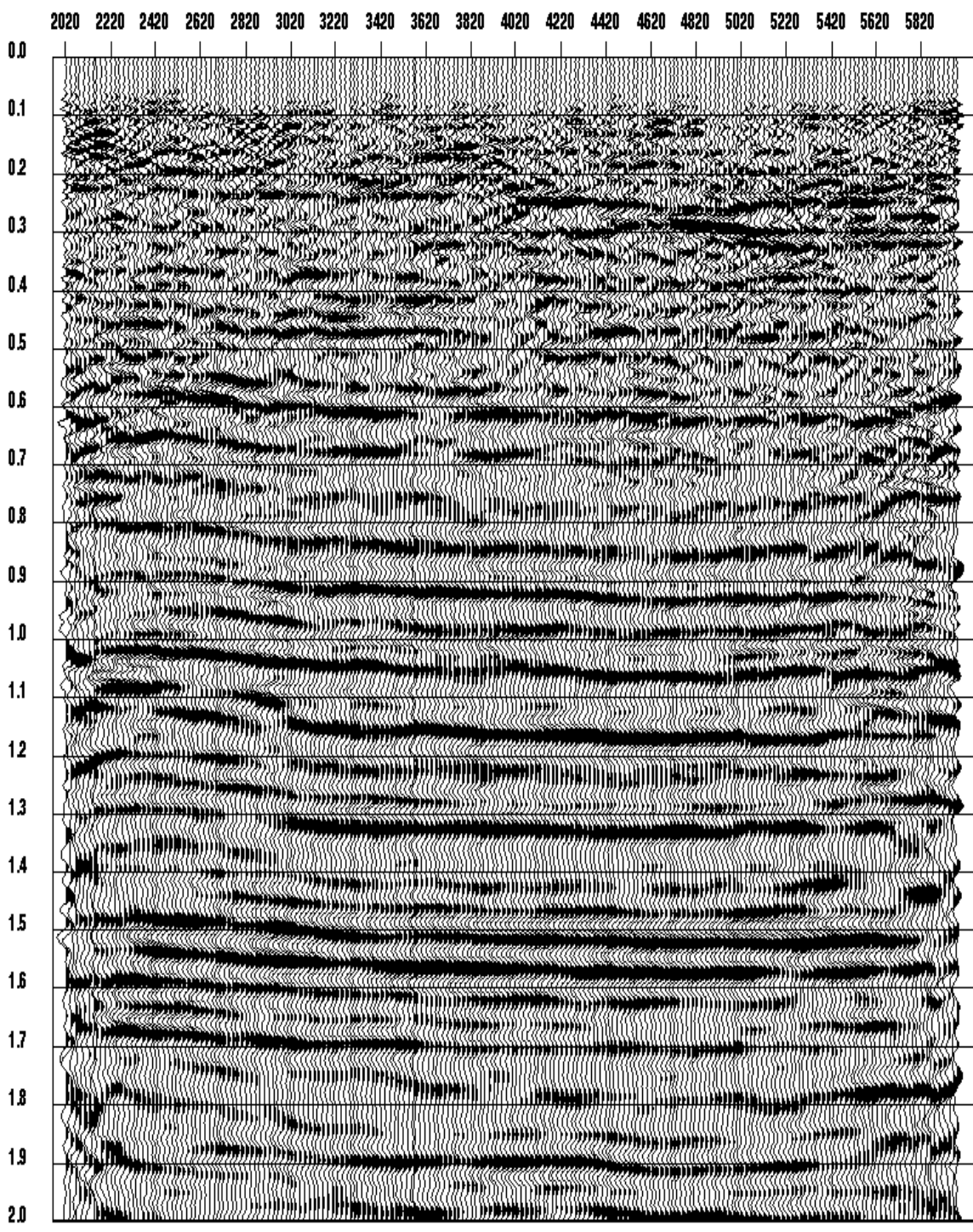
Fig. 7.9. P-S DMO stack in P-P time.
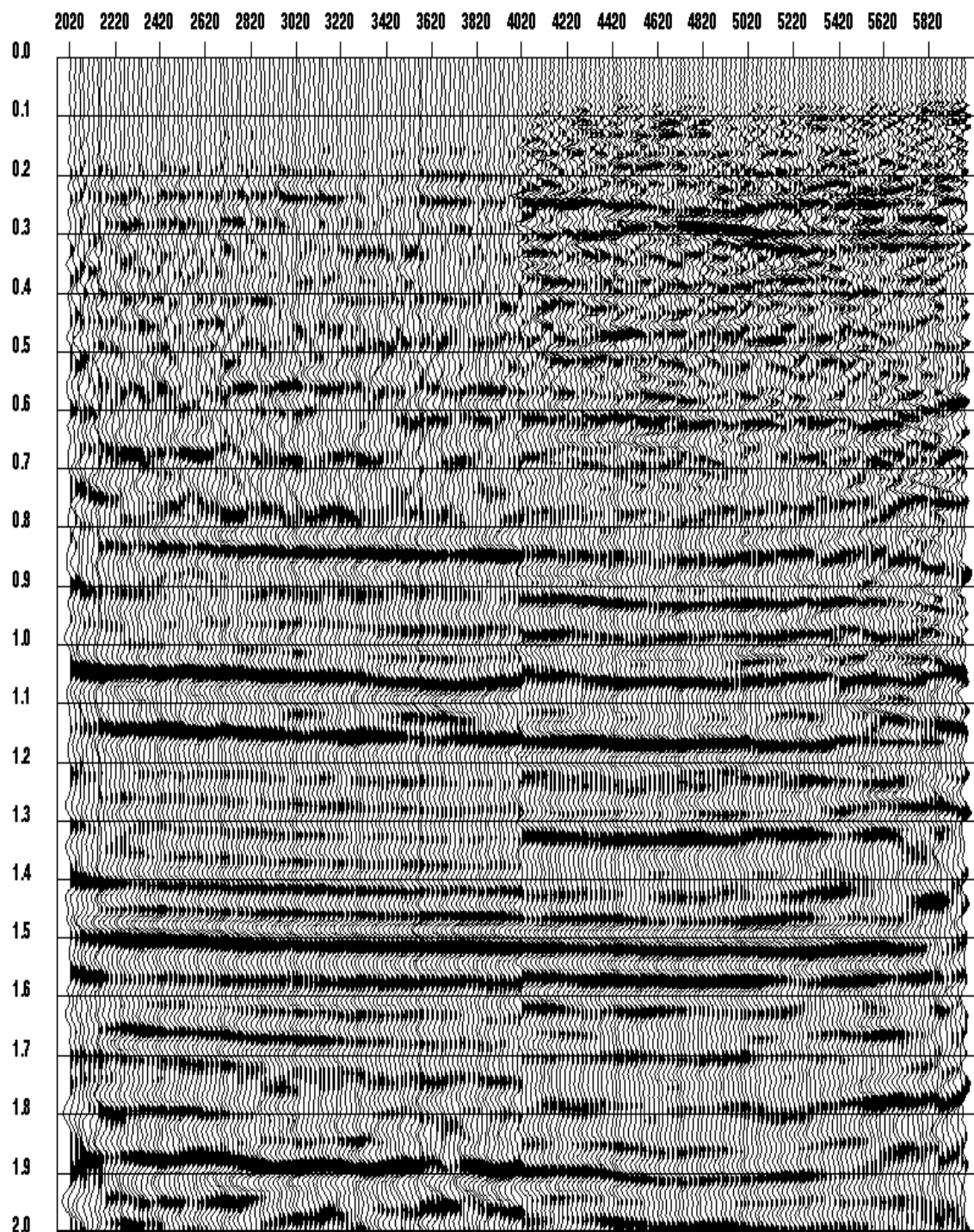
Fig. 7.10. The match between P-P and P-S DMO stacks. The first half is from the P-P data and the second half is from the P-S data stretched with a single γ_{ps} function.
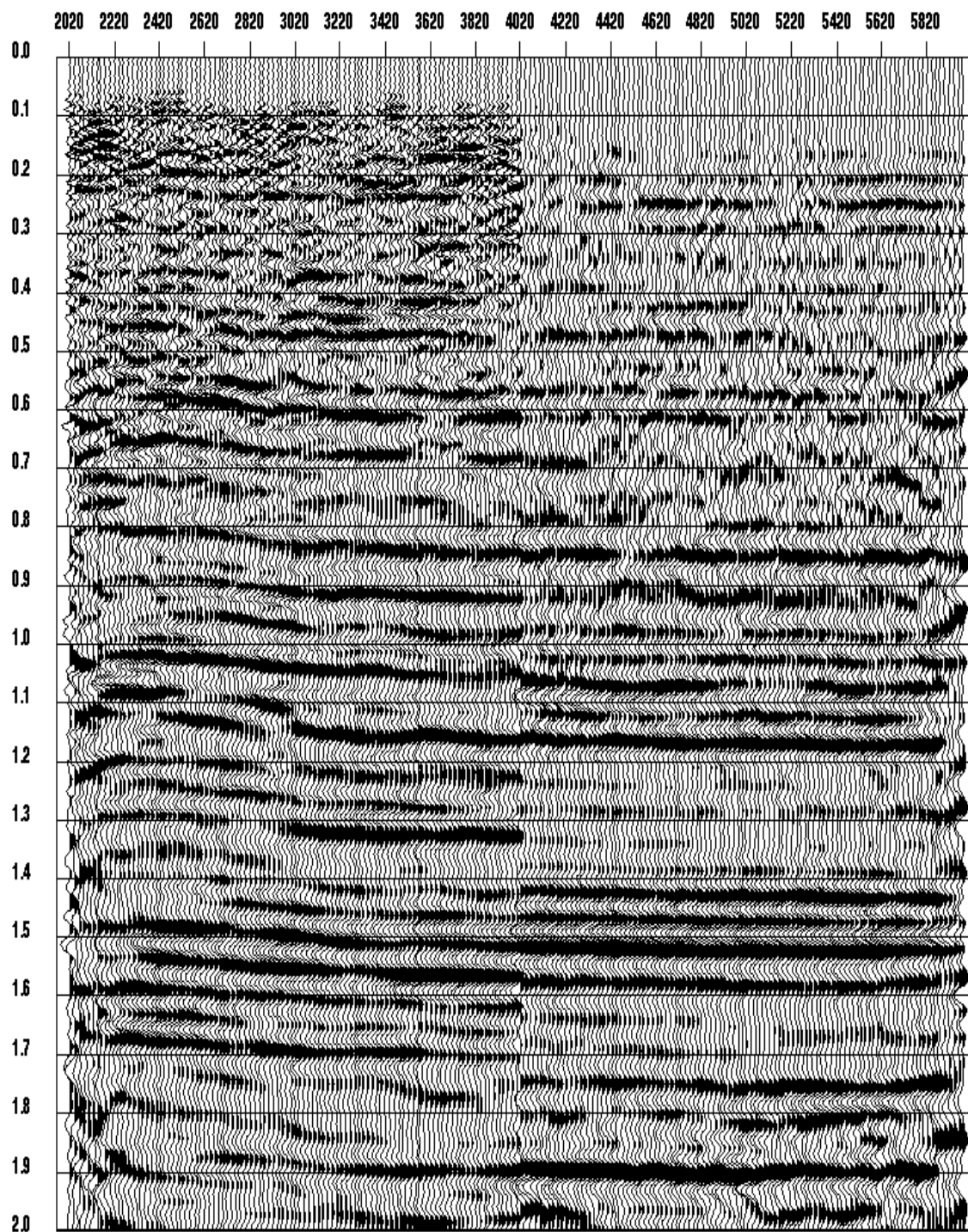
Fig. 7.11. The match between P-P and P-S DMO stacks. The first half record is from the P-S data stretched with a single γ_{ps} function. The second half is from the P-P data.
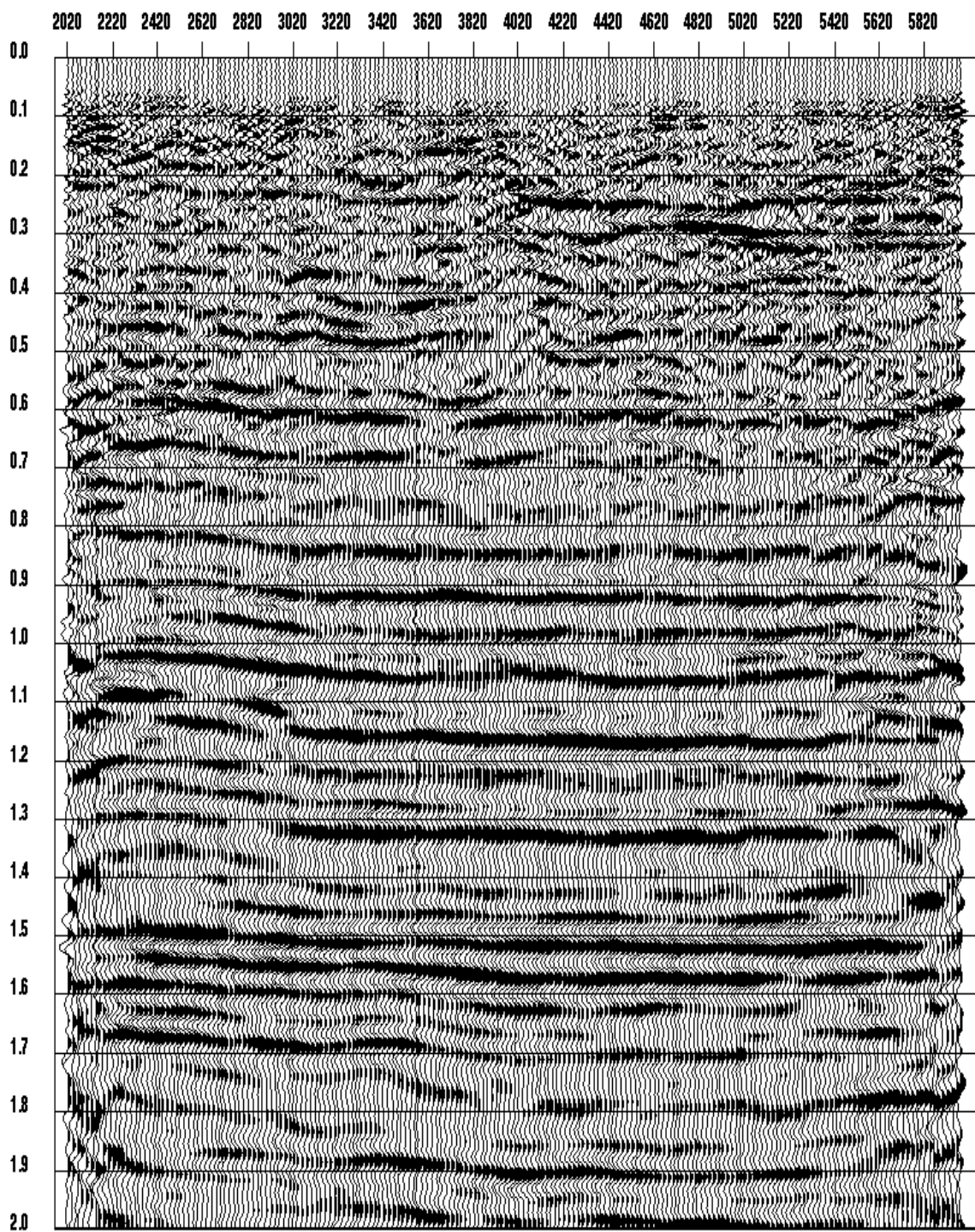
Fig. 7.12. P-S DMO stack in P-P time (squeezed with a time-and-space variant γ_{ps} function)
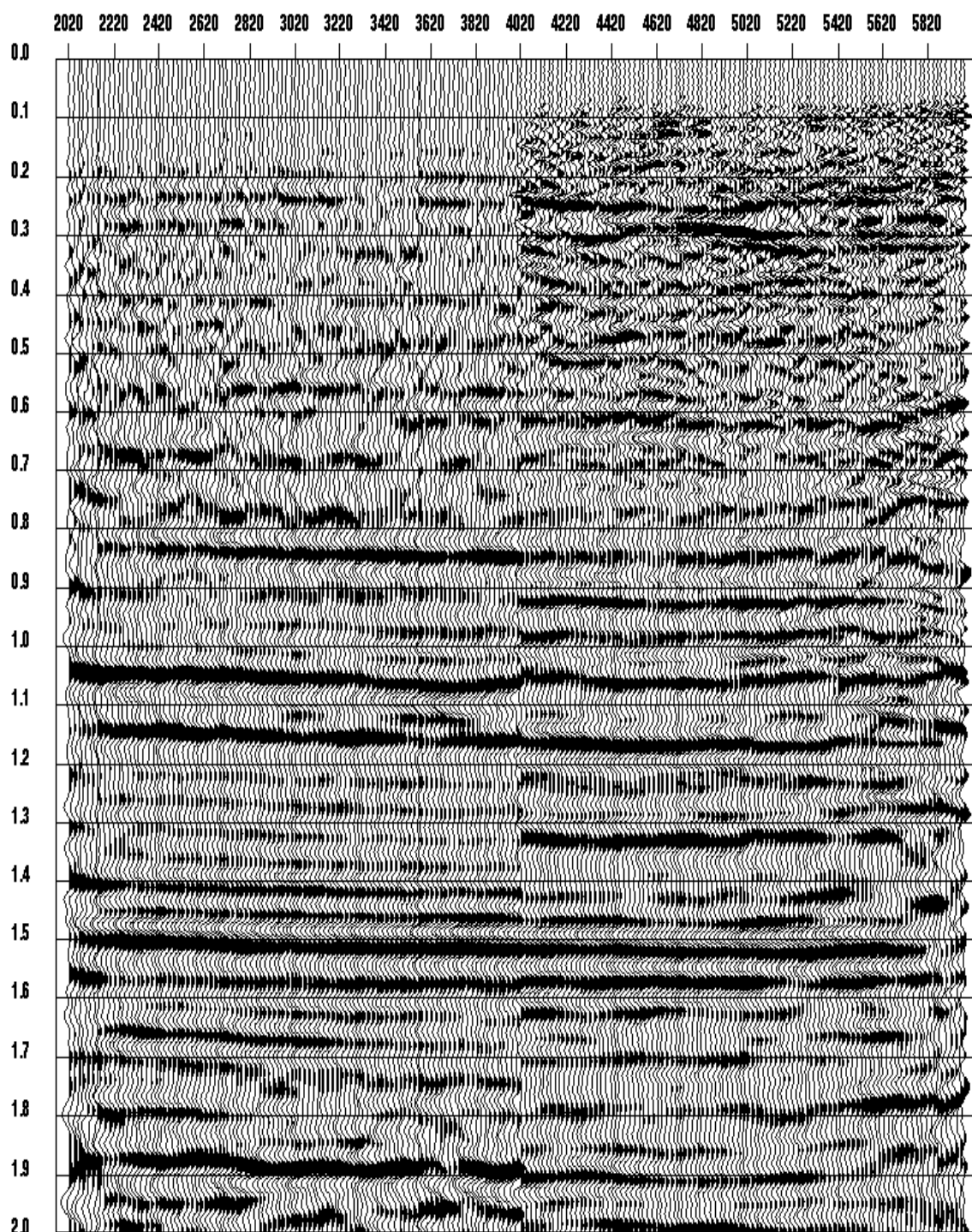
Fig. 7.13. The match between P-P and P-S DMO stacks. The first half is from the P-P data while the second half is from the P-S data squeezed with a time-and-space variant γ_{ps} function.
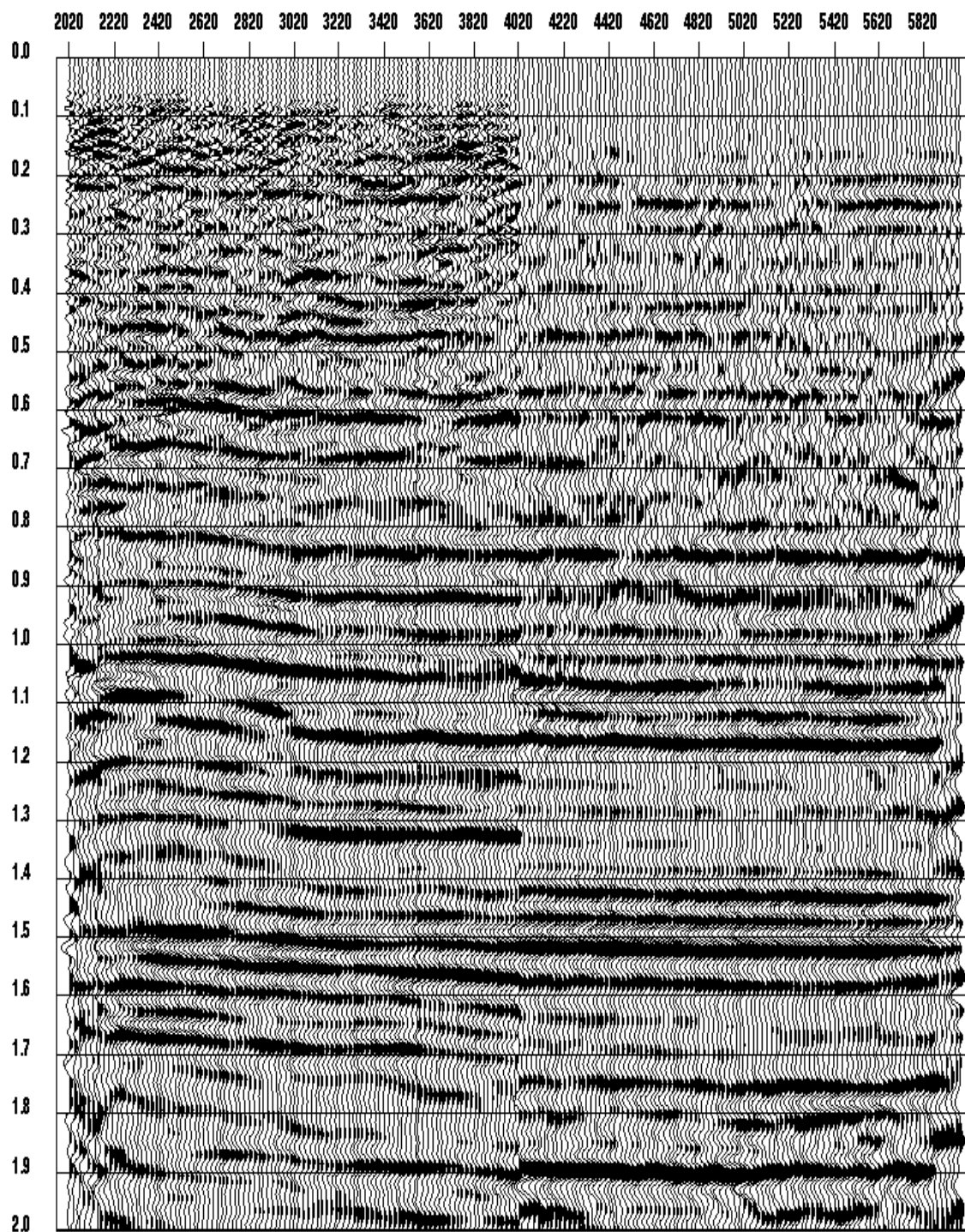
Fig. 7.14. The match between P-P and P-S DMO stack. The first half record is from the P-S data squeezed with a time-and-space variant γ_{ps} function. The second half is from the P-P data.

Time (s)	γ_{ps}^{j*}
0.1560000	3.135000
0.2445000	3.085859
0.2784000	2.954189
0.4620000	2.685732
0.5648000	2.529912
0.8940000	2.326451
1.051800	2.298005
1.160790	2.237987
1.428300	2.192411
1.515500	2.175910
1.578000	2.165394

Table 7.1. The γ_{ps}^{j*} functions from the correlation analysis.

7.7 Quick match

When the local geology exhibits minor variations in depth and in the horizontal co-ordinates, a fast mis-tie analysis procedure can be developed.

From equation (5.18),

$$\frac{T_{ps}}{T_{pp}} = \frac{1 + \gamma_{ps}}{2}$$
$$= k \qquad\qquad (7.10)$$

If γ_{ps} is nearly a constant within the seismic section, then k is also a constant. Taking the logarithms of both sides of equation (7.9), we have

$$\log T_{ps} - \log T_{pp} = \log k \qquad\qquad (7.11)$$

Equation (7.10) suggests that after log-stretching the time co-ordinate of both P-P and P-S

sections, events on the transformed sections are simply time shifted by the constant log k. This static shift can be estimated by searching for maximum cross-correlation lag between two log-stretched sections. Once this static shift is found for all traces in the section, an average $\overline{\gamma_{ps}}$ is estimated.

This method can also be applied in reversed time. That is if an event is identified in both P-P and P-S sections, the quick method can be used to estimate an average $\overline{\gamma_{ps}}$ above the event. To see that, let t_{pp} and t_{ps} denote 2-way traveltimes to the same event on P-P and P-S sections respectively. From equation (7.10), we have

$$
\begin{aligned}
t_{ps} - T_{ps} &= kt_{pp} - kT_{pp} \\
&= k\,(t_{pp} - T_{pp})
\end{aligned}
\tag{7.12}
$$

or

$$
T_{ps}' = k\,T_{pp}'
\tag{7.13}
$$

with

$$
T_{ps}' = t_{ps} - T_{ps}
\tag{7.14}
$$

and

$$
T_{pp}' = t_{pp} - T_{pp}
\tag{7.15}
$$

To produce acceptable results, this quick match requires a constant γ_{ps} medium. Since at depth, the Vp/Vs ratio may be considered constant, at least in RMS terms, the quick match is possible if γ_{ps} is measured relative to a deeper event on both P-P and P-S sections as per equation (7.11).

Note that γ_{ps} calculated by the quick match approach depends on analysis start time as defined by equation (7.11), and hence it may not agree with the value obtained by simulated annealing which always refers start time to time zero.

7.8 Quick match example

Shown in Figure 7.15 is the input to the quick match procedure prior to event re-alignment as per equation (7.11). From the previous result of simulated annealing, an event at time 0.479 seconds on the P-P DMO stack is identified as the event at 0.864 seconds on the P-S DMO stack.

To start the procedure both stacks are bulk shifted so that the same events now appear at time zero as shown in Figure 7.16.

Log-stretch transformation is applied to both stacks (Figure 7.17), and the corresponding P-P and P-S data are correlated. A reasonable match (Figure 7.18) is found after P-P DMO stack is shifted downwards by 0.4 (log-stretch domain units). The amount of shift is translated into an estimated γ_{ps} of 1.98.
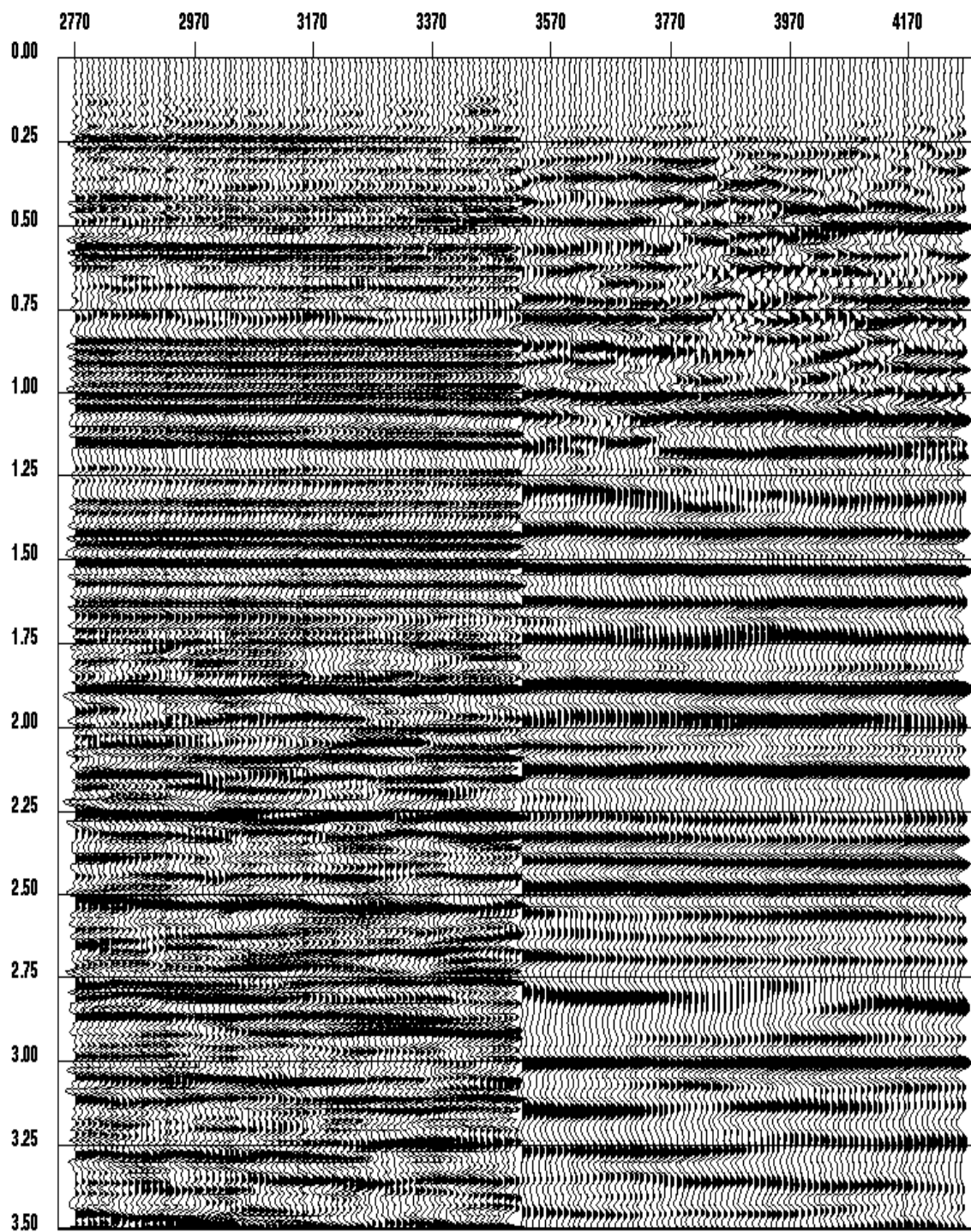
Fig. 7.15. P-P DMO and P-S DMO stacks. The first half of of the data is P-P DMO stack while the second half is P-S DMO stack.
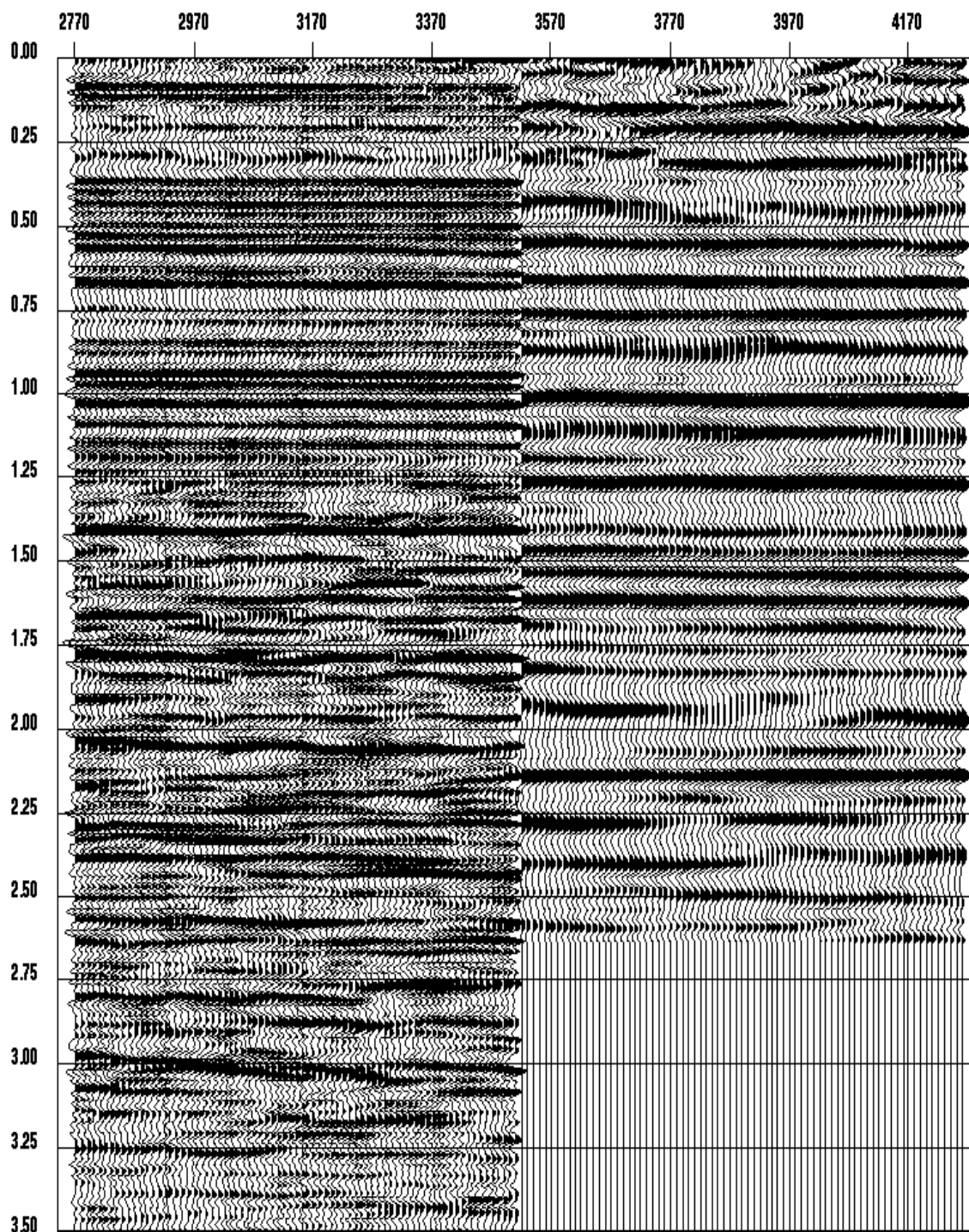
Fig. 7.16. The initial step in quick match procedure. The first half of these data is P-P DMO stack shifted by 0.479 seconds upwards. The second half is P-S DMO stack shifted by 0.864 seconds upwards.
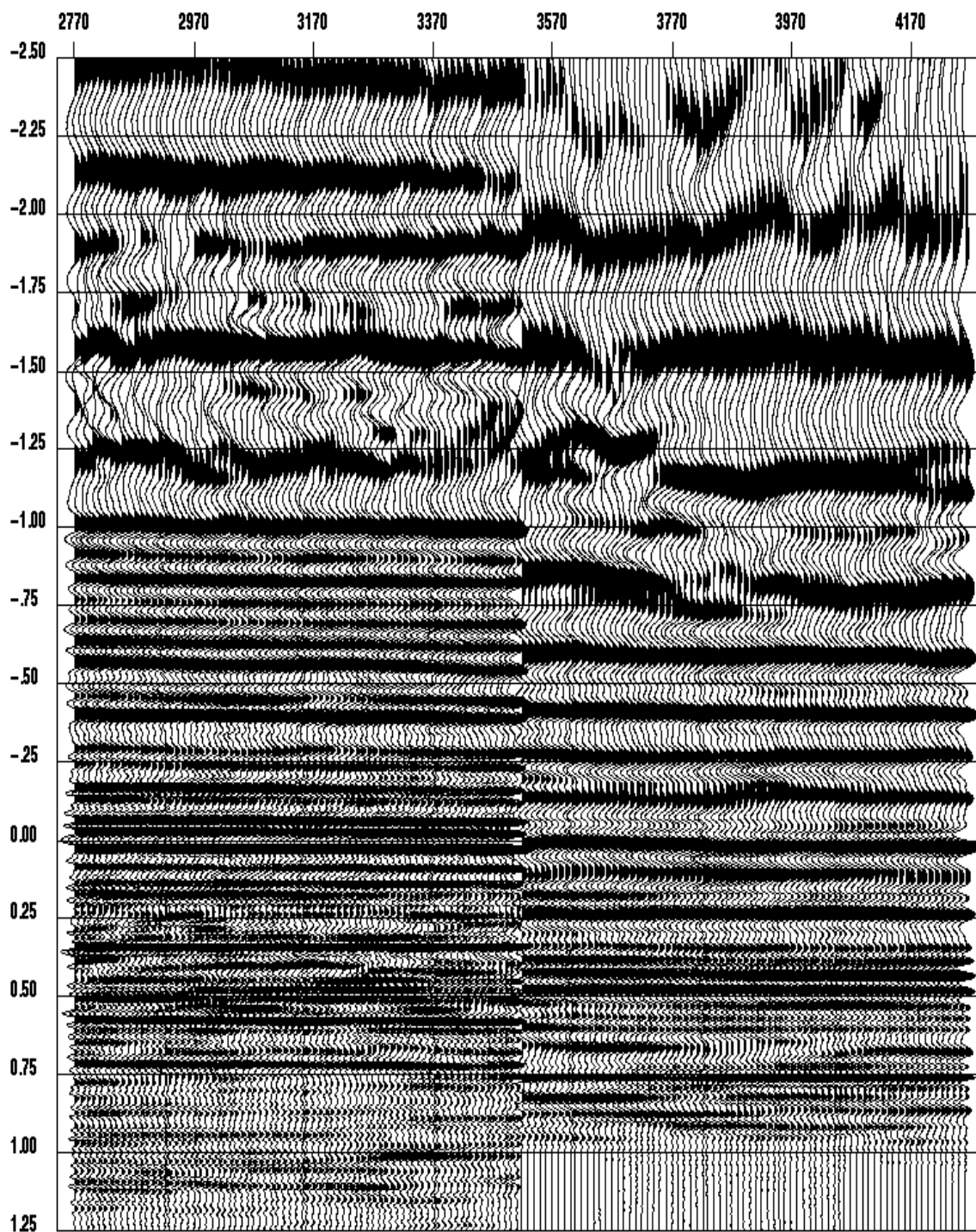
Fig. 7.17. The data in Figure 7.16 after log-stretch transformation.
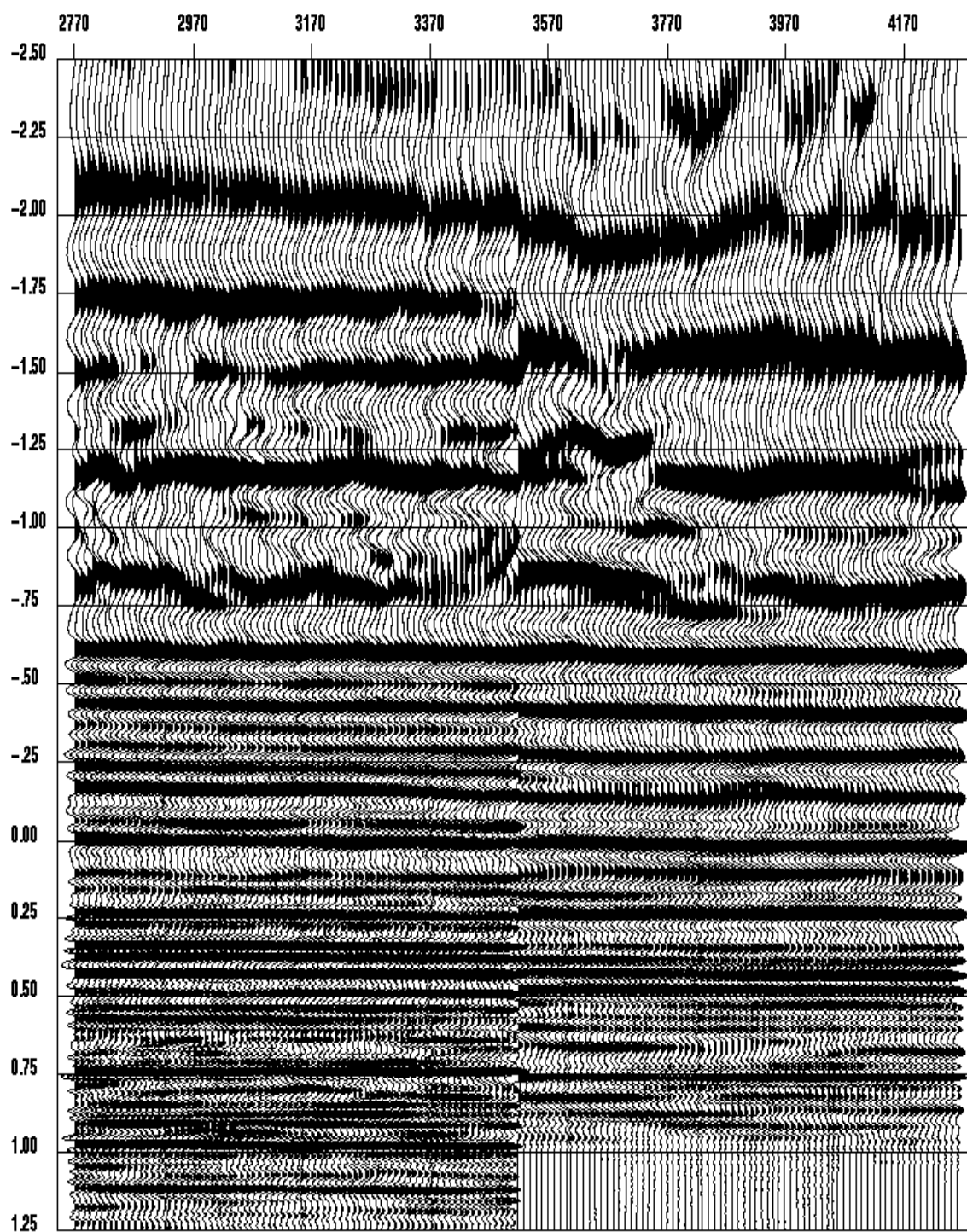
Fig. 7.18. Events are matched reasonably well in the log-stretch domain after P-P DMO stack (the first half of the data) are shifted by 0.4 downwards.

The P-S data of Figure 7.16 is squeezed with the estimated γ_{ps} to match P-P data in P-P time as shown in Figure 7.19. The final result of the quick match process after correction back to surface is shown in Figure 7.20. The overall match is good.

For comparison, the simulated annealing based time-and-space variant γ_{ps} function is utilized to squeeze the P-S data and the result is shown in Figure 7.21. Note that this data set has different scaling and band-width characteristics than the one shown in Figure 7.10. Both techniques give a very similar result, especially between 0.4 and 1.6 seconds. Outside this window, simulated annealing procedure gives a slightly better result as expected.

7.9 Discussion

To address P-P to P-S mis-tie analysis issues, I have developed two independent procedures. These techniques differ substantially from each other, and can be used in tandem to identify possible difficulties with the final matching results.

Although the quick match method is developed for constant γ_{ps} environment, the method can be applied repeatedly for different time windows, to obtain a time-variant γ_{ps}. For example, in Figure 7.20, P-P to P-S match starts to deteriorate at about 1.3 second. This implies that γ_{ps} is changing significantly as a function of time. Repeating the quick match procedure from 1.3 seconds onwards to obtain another γ_{ps} value will result in farther improvement of the overall match.
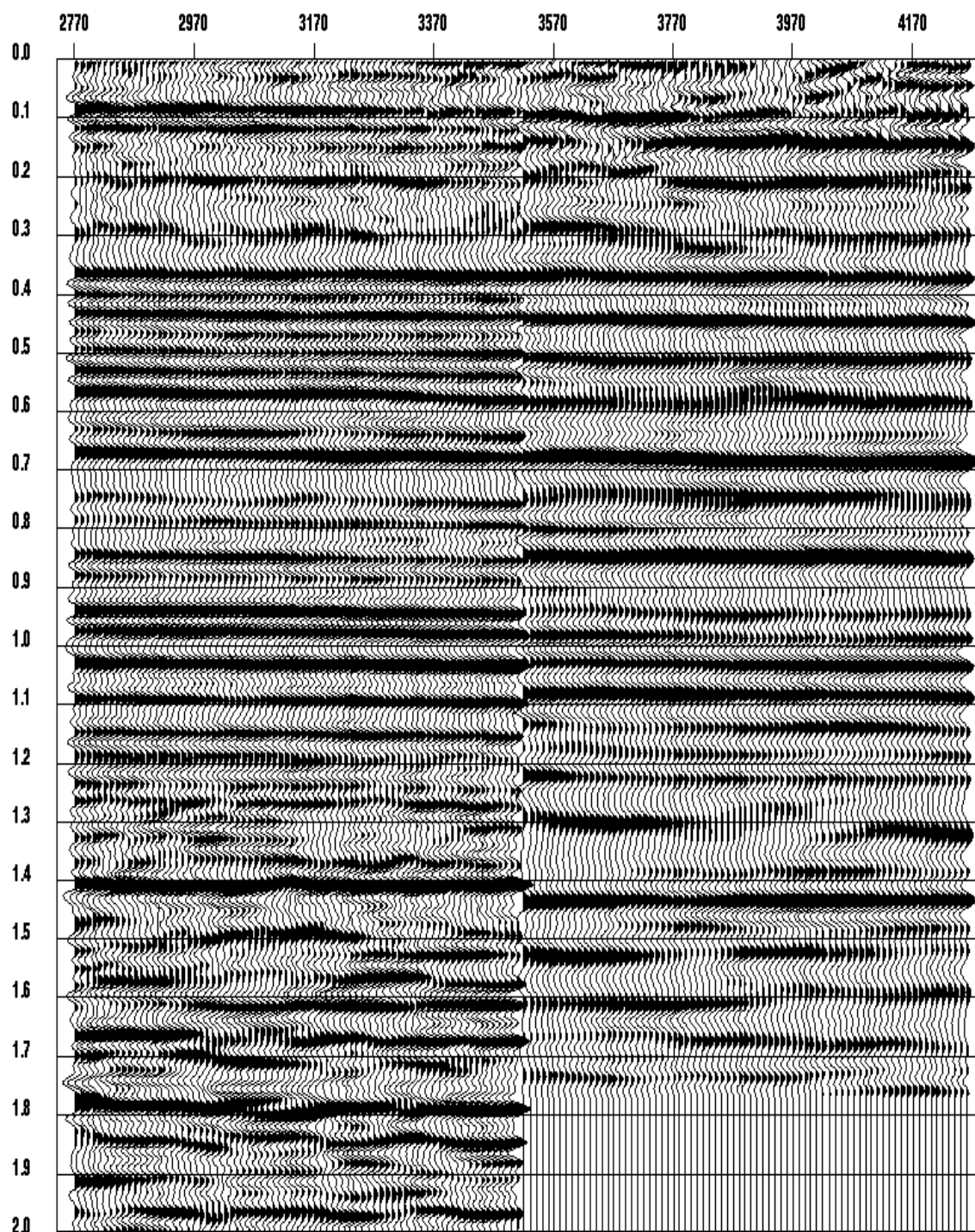
Fig. 7.19. P-P and P-S match in P-P time. The P-S data on the right has been squeezed with γ_{ps} =1.98 to match P-P data on the left.
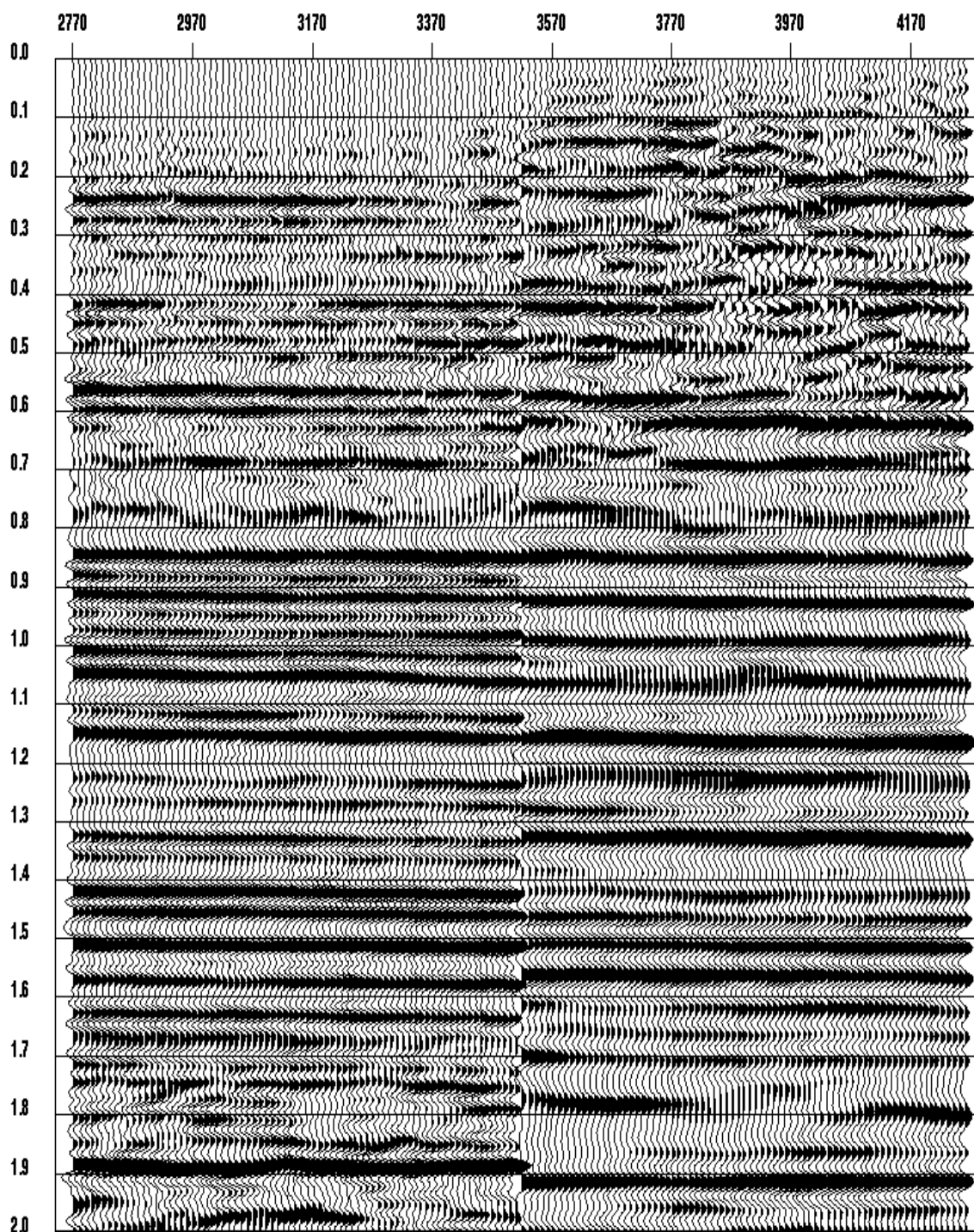
Fig. 7.20. P-P and P-S match in P-P time. Same as in Figure 7.19, except data are shifted down by 0.479 seconds to comply with the original start time.
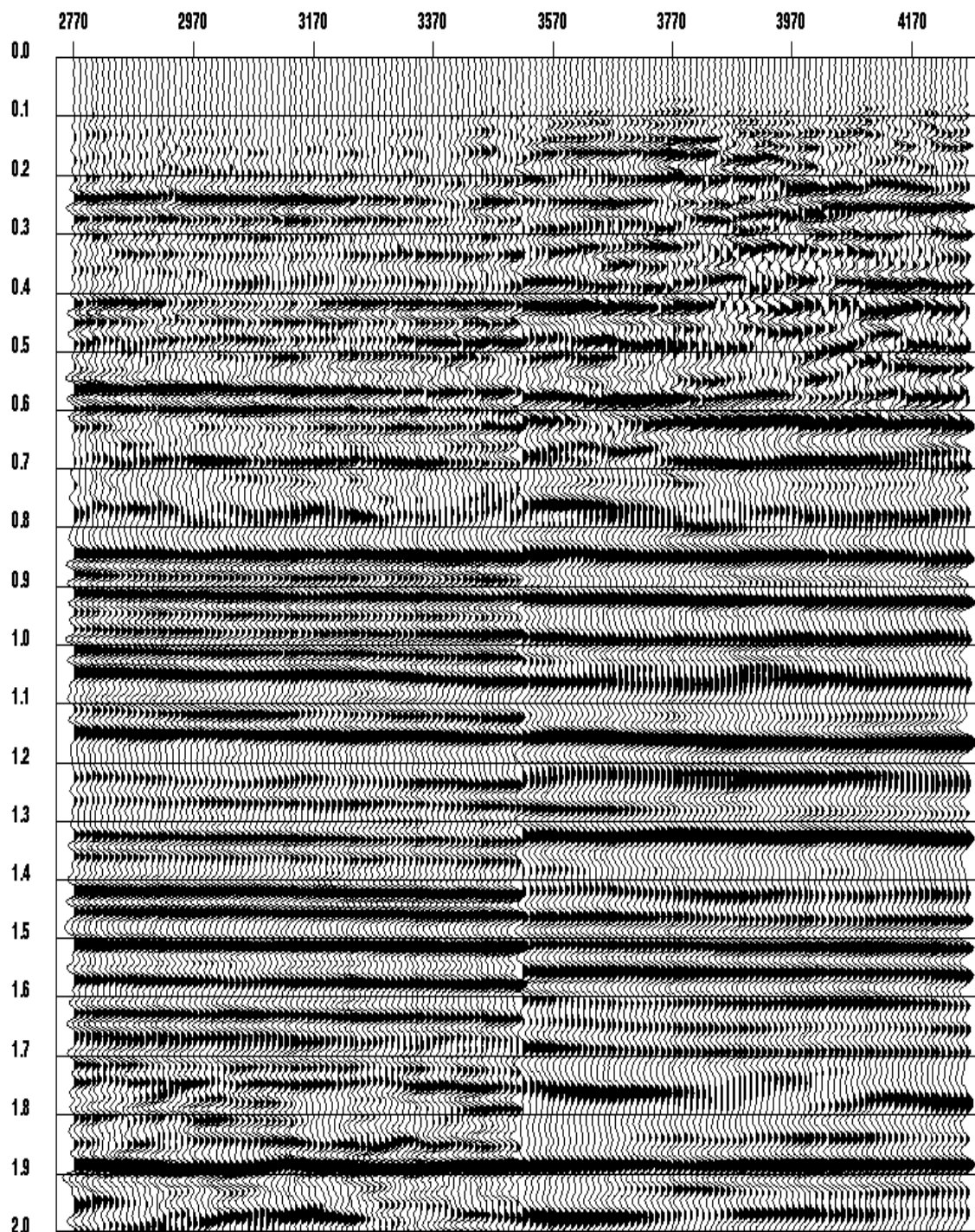
Fig. 7.21. P-P and P-S match in P-P time. P-S data are squeezed with the time-and-space variant γ_{ps} function sought previously from simulated annealing technique.

Finally, I point out that the quick match method is an ideal tool for interactive analysis. The algorithm is fast, and the result of the match in P-P time can be up-dated on the computer screen giving an interpreter the opportunity to identify the time (or geological horizon) where a change in γ_{ps} value is necessary. The analysis then proceeds to the next level.

Chapter 8   Dissertation summary

The purpose of this dissertation is to develop a converted-wave processing and interpretation algorithms and procedures aimed at structural data.

The conventional processing flows for P-P and P-S were discussed and summarized in chapter 2. Emphasis has been made on the processing due to the impact of the asymmetric P-S ray path.

Many multi-channel seismic algorithms assume that the input seismic data have a regular trace spacing. Unfortunately, this is not always so because of incomplete or noisy acquisition. This leads to difficulties in using procedures such as DMO and prestack migration to solve complex imaging problems. Aliasing caused by missing traces can corrupt the signal. The field example in chapter 3 shows that the proposed missing trace interpolation can lead to a considerable improvement in the final processed results.

In chapter 4, a new method of solving residual statics without a priori velocity information is introduced. It creates a new way to construct a pilot trace for statics correlation, and solves the issue of velocity and statics coupling. For converted-wave statics, it is very much depends on the ability of ACCP stack as a good pilot trace. Unfortunately, this may be a problem for complex structure. The new method is a good candidate for structural converted-wave data because it has an advantage of building pilot traces without a priori velocity information and a hyperbolic moveout assumption.

In chapter 5, fundamental equations for the kinematic converted-wave prestack time migration were derived, and three types of P-to-S velocity ratios (γ_{rms}, γ_{ps} γ_{mig}) are introduced for time-domain processing. The following points can be concluded from the equations:

1) The pseudo depths for P and S can be different. It depends on the velocity heterogeneity factors for P and S or g_γ.

2) The zero-offset times for P-P and P-S reflection from the same horizon are related to γ_{ps} rather than γ_{rms}. This implies that by just knowing the RMS velocities for P, S or even P-S of the same horizon are not enough to tie the P-P and P-S sections.

3) The single parameter (γ_{mig}) sought from the migration velocity analysis has no physical meaning (except when g_γ=1, then we have $\gamma_{mig}=\gamma_{rms}$), and its value is between γ_{rms} and γ_{ps}. It is a just a parameter that gives the best migrated image.

4) The lateral positions of events on P-P and P-S migrated may be different if g_γ is not 1, or the structure is complicated.

In chapter 6, a new technique called AMOC is developed to correct for the P-S asymmetric moveout. One of the advantages of this technique is that it provides another way to construct model traces (or pilot traces) for residual S-wave receiver statics for structural data. Also, after AMOC, P-S data can be processed like symmetric P-P data. Together with

f-x statics, two alternative processing flows for the P-S data are proposed. The advantage of the flows is we can use any P-P routines to process the pseudo P-P data, and more important, a non-iterative velocity analysis process is possible.

In chapter 7, two techniques are developed to tie both P-P and P-S sections, one is an automatic procedure incorporating simulated annealing to obtain an optimum match between the P-P and P-S sections. The other one is an interactive and recursive method to match both section in the logarithmic time domain. The importance of the match is that the interval P and S velocities between horizons can be derived, and they can provide a direct measurement of physical properties of the rocks

8.1 Future work

The f-x missing traces interpolation discussed in chapter 3 is also a very useful tool for 2-D analysis. It presents a problem in 3-D when we attempt to sort the data with irregular 3-D geometry into common-offset planes. The problem may be partly solved by first applying DMO to regularize the data. The data are followed by 2-pass 2-D f-x missing trace interpolation.

The f-x statics routine also has a problem in 3-D with irregular geometry. More research is needed to make f-x statics possible in 3-D geometries.

The migration velocity analysis and AMOC discussed in chapter 5 and 6 are mainly for

2-D data, more research is required to extend the idea to 3-D.

The mis-tie analysis discussed in chapter 7 is a highly non-linear problem. The more physical constraint we can put on the problem, the more confidence we will have in the results.The only constraint used in the simulating technique is the possible range of γ_{ps}. More work is needed to incorporate the velocity information to the mis-tie analysis. In the mis-tie analysis, the phase problem between P-P and P-S reflections is ignored. The results might be improved if the envelope of the reflections are used during the correlation.

Finally, the processing flow discussed in this dissertation should be evaluated on structural converted-wave data.

Chapter 9   References

Abma, R., Claerbout, J., 1995, Lateral prediction for noise attenuation by t-x and f-x techniques: Geophysics, 60, 1887-1896.

Al-Chalabi, M., 1974, An analysis of stacking, rms, average, and interval velocities over a horizontally layer ground: Geophys. Prosp., 22, 458-475.

Behle, A., and Dohr, G., 1985, Converted waves in exploration seismic, in Dohr, G., Ed., Seismic shear waves, Part B: Applications: Geophys. Press, 15B 178-223.

Canales, L. L., 1984, Random noise reduction: Presented at the 54th Ann. Internat. Mtg., Soc. Expl. Geophys., Expanded Abstracts, 525-527.

Canning, A. and Gardner, G.H.F., 1993, Two-pass 3-D prestack depth migration: Expanded Abst., 63 rd Ann. Intl. MTg., Soc. Expl. Geophys., 892-894.

Cary, P. W., 1994, 3-D converted-wave seismic processing: CREWES Research Report, v. 6, 31-1-31-10.

Cary, P. W. and Eaton, D. W. S., 1992, A simple method for resolving large converted-wave (P-SV) statics: Geophysics, 58, 429-433.

Chunduru, R. K., Sen, M. K., and Stoffa, P. L., 1996, 2-D resistivity inversion using spline parameterization and simulated annealing: Geophysics, 61, 151-161.

Deregowski, S. M., 1986, What is DMO? First Break, 4, 7, pp. 7-24.

Dufour, J. and Lawton, D. C., 1996, Determination of S-wave static corrections from S-wave refractions on P-S data: Presented at the 66nd Ann. Intl. Mtg., Soc. Expl. Geophys., Expanded Abstracts, 1551-1554.

Forel, D. and Gardner, G.H.F., 1988, A Three dimensional perspective on two dimensional dip moveout: Geophysics, 53, 504-610.

Gaiser, J.E., 1996, Multicomponent Vp/Vs correlation analysis: Geophysics, 61, 1137-1149.

Gardner, G.H.F., French, W.S., and Matzuk, T., 1974, Elements of migration and velocity analysis: Geophysics, 39, 811-825.

Gardner, G.H.F., Wang, S.Y., Pan, N.D., and Zhang, Z., 1986, Dip moveout and prestack imaging: OTC Ann. Mtg., Houston.

Garotta, R., 1985, Observation of shear waves and correlation with P events, in Dohr, G., Ed., Seismic shear waves, Part B: Applications: Geophys. Press, 15B 1-96.

Garotta, R., Marechal, P., and Magesan, M., 1985, Two-component acquisition as a routine procedure for recording P-waves and converted waves: Can. J. Expl. Geophys., 21, 40-53.

Goffe, B., Ferrier and Rogers, 1994, Jou. of Econometrics, vol 60, no. 1/2, Jan/Feb, 65-100.

Harrison, M., 1992, Processing of P-SV surface-seismic data: Anisotropy Analysis, Dip Moveout, and Migration: Dissertation of U of Calgary.

Jervis, M., Sen, M. K., and Stoffa, P. L., 1996, Prestack migration velocity estimation using nonlinear methods: Geophysics, 61, 138-150.

Lawton, D.C. and Howell, C.E., 1992, P-SV and P-O synthetic stacks: Presented at the 62nd Ann. Intl. Mtg., Soc. Expl. Geophys., Expanded Abstracts, 1344-1347.

Li, X. and Bancroft, J.C., 1997, Residual statics using CSP gathers: CREWES Research Report Vol. 9, 23-1-23-11.

Metropolis, N., Rosenbluth, A., Rosenbluth, M., Teller, A., and Teller, E., 1953. Equation of state calculations by fast computing machines, Journal of Chemical Physics, 21, 1081-1092.

Miller, S.L.M., Harrison, M. P., Lawton, D. C., Stewart, R. R., and Azata K. J., 1994, Analysis of P-P and P-SV seismic data from Lousana, Alberta: CREWES Research Report Vol. 6, 7-1-7-23.

Miller, S.L.M. and Stewart, R.R., 1990, The effect of lithology, porosity and shaliness on P- and S-wave velocities from sonic logs: Can J. Expl. Geophys., 26, 94-103.

Newman, P., 1973, Divergence effects in a layered earth: Geophysics, 38, 481-488.

Reshef, M., 1992, Structural imaging in complex geological areas. Presented at Ann. Nat. Mtg., Can. Soc. Expl. Geophys.

Ronen, J. and Claerbout, J., 1985, Surface-consistent residual statics estimation by power maximization: Geophysics, 50, 2759-2767.

Rothman, D. H., 1985, Nonlinear inversion, statistical mechanics, and residual statics estimation: Geophysics, 50, 2784-2796.

Rowan, T., 1990, Functional stability analysis of numerical algorithms: Ph.D. thesis, Department of Computer Sciences, University of Texas at Austin.

Simin, V., 1997, Post-stack attribute analysis of the 9C seismic survey-Olds, Alberta:

CREWES Research Report Vol. 9, 37.

Sen, M. K., and Stoffa, P. L., 1991, Nonlinear one-dimensional seismic wave form inversion using simulated annealing: Geophysics, 56, 1624-1638.

Soubaras, R., 1995, Prestack random and impulsive noise attenuation by f-x projection filtering: Presented at the 65th Ann. Internat. Mtg., Soc. Expl. Geophys., Expanded Abstracts, 711-714.

Spitz, S., 1991, Seismic trace interpolation in the F-X domain: Geophysics, 56, 785-794.

Stewart, R.R., and Ferguson, R.J., 1996. Shear-wave interval velocity form P-S stacking velocities: Can. J. Expl. Geophys., 139-142.

Taner, M.T., 1997, Common image stacking system: presented at the 49th Ann. Intl. Mtg., Soc. Expl. Geophys.

Taner, M.T. and Berkhout, A.J., 1997, Statics, a physical view: 59th Ann. Internat. Mtg., Eur. Ass. of Geosc. and Eng., Expanded abstracts.

Taner, M.T. and Berkhout, A.J., 1998, Dynamics of statics: Expanded Abst., 68 th Ann. Intl. MTg., Soc. Expl. Geophys., 1409-1412.

Taner, M.T. and Koehler, F., 1969, Velocity spectra - digital computer derivation and applications of velocity functions. Geophysics 34, 859-881.

Tessmer G., and Behle A., 1988, Common reflection point data-stacking technique for converted waves: Geophys. Prosp., 36, 671-688.

Wang, S., 1997, Three-component and three-dimensional seismic imaging: Thesis of U of Calgary.